Searches for Squarks and Gluinos in Supersymmetric Scenarios Including Prompt and Displaced Decays in pp Collisions at $\sqrt{s}$ = 13 TeV with the ATLAS Detector

Veronika Magerl

Fakultät für Mathematik und Physik
Albert-Ludwigs-Universität Freiburg

Searches for Squarks and Gluinos in Supersymmetric Scenarios Including Prompt and Displaced Decays in pp Collisions at $\sqrt{s}$ = 13 TeV with the ATLAS Detector

Dissertation

zur Erlangung des Doktorgrades der

Fakultät für Mathematik und Physik der

Albert-Ludwigs-Universität

Freiburg im Breisgau

vorgelegt von

Veronika Magerl

Supervisor

Prof. Dr. Gregor Herten

December 18, 2019

Veronika Magerl: *Searches for Squarks and Gluinos in Supersymmetric Scenarios Including Prompt and Displaced Decays in pp Collisions at $\sqrt{s}$ = 13 TeV with the ATLAS Detector*

Datum der mündlichen Prüfung: 20.02.2020

Dekan:	Prof. Dr. Wolfgang Soergel
Betreuer der Arbeit:	Prof. Dr. Gregor Herten
Koreferent:	Prof. Dr. Horst Fischer
Prüfer:	Prof. Dr. Gregor Herten
	Dr. Christian Weiser
	Prof. Dr. Stefan Dittmaier

To Fini … thank you for the motivating kicks

Abstract

Many extensions of the Standard Model of particle physics include heavy coloured particles, such as the gluinos and squarks predicted in Supersymmetry, which could be accessible at the Large Hadron Collider and detected by the ATLAS experiment. Depending on the specific assumptions of the underlying theoretical model, these supersymmetric particles are assumed to show different characteristics and decay modes.

Within the R-parity conserving Minimal Supersymmetric Model, gluinos and squarks may decay promptly into final states with quarks, leptons and substantial missing transverse momentum $E_{\mathrm{T}}^{\mathrm{miss}}$ carried away by the undetected Lightest Supersymmetric Particle (LSP), which is typically the lightest neutralino $\widetilde{\chi}_1^0$. A search for such supersymmetric particles targeting fully hadronic final states containing jets and $E_{\mathrm{T}}^{\mathrm{miss}}$, based on proton-proton collisions at $\sqrt{s}$ = 13 TeV corresponding to a total integrated luminosity of L=139 fb^{-1}, is presented in this thesis. No significant excess above the Standard Model was observed and results were interpreted in terms of simplified models describing gluino and squark production with subsequent direct or cascade decays, extending the exclusion limits provided by previous ATLAS searches.

Refraining from R-parity conservation gluinos and squarks decay promptly while the neutralino decays displaced. Varying the strength of the R-parity violating couplings results in a rich spectrum of simplified models. In Split-SUSY models, gluinos can be metastable massive particles which hadronise into R-hadrons. A reinterpretation of several searches for promptly decaying supersymmetric particles in these long-lived scenarios is discussed in this thesis. Exclusion limits are set on simplified models assuming pair-produced gluinos and stops as well as resonantly produced stops in scenarios with variable R-parity violating coupling strengths. Additional limits are provided for a simplified model describing pair produced metastable gluinos.

Zusammenfassung

Viele Erweiterungen des Standardmodells der Teilchenphysik beinhalten schwere Teilchen die eine Farbladung tragen, wie die in Supersymmetrie vorhergesagten Gluinos und Squarks, welche im Large Hadron Collider erzeugt und mit dem ATLAS Experiment nachgewiesen werden könnten. In Abhängigkeit der spezifischen Annahmen des zugrundeliegenden theoretischen Models weisen diese supersymmetrischen Teilchen verschiedene Charakteristika und Zerfallskanäle auf.
Innerhalb des R-Paritätserhaltenden Minimalen Supersymmetrischen Models können Gluinos und Squarks sofort in Endzustände mit Quarks, Leptonen und großem fehlendem transversalem Impuls $E_{\mathrm{T}}^{\mathrm{miss}}$ zerfallen, welcher vom leichtesten supersymmetrischen Teilchen (LSP), typischerweise das leichteste Neutralino $\widetilde{\chi}_1^0$, weggetragen wird. Eine Suche nach solchen supersymmetrischen Teilchen, die auf rein hadronische Endzustände mit Jets und $E_{\mathrm{T}}^{\mathrm{miss}}$ abzielt, wird in dieser Dissertation präsentiert. Der verwendete Datensatz hat eine integrierten Luminosität von L=139 fb^{-1} und wurde in Proton-Proton Kollisionen bei einer Schwerpunktsenergie von 13 TeV aufgenommen. Es wurde keine signifikante Abweichung von den Vorhersagen des Standard Models gefunden. Daher wurden die Ergebnisse anhand vereinfachter Modelle interpretiert, welche die Produktion von Gluinos und Squarks mit anschliessendem direktem oder kaskadischem Zerfall beschreiben. Dabei wurden die bestehenden Ausschlussbereiche früherer ATLAS Suchen signifikant erweitert.
Verzichtet man auf die Erhaltung der R-Parität, zerfallen Gluinos und Squarks prompt, das Neutralino zerfällt jedoch verzögert. Durch Variation der R-Paritätsverletzenden Kopplungsstärke ergibt sich ein breites Spektrum vereinfachter Modelle. Zu verzögerten Zerfällen kommt es auch in Split-SUSY Modellen, die metastabile Gluinos enthalten die zu R-Hadronen hadronisieren. Eine Reinterpretation mehrerer Suchen nach instantan zerfallenden supersymmetrischen Teilchen im Rahmen dieser langlebigen Szenarios wird in dieser Dissertation diskutiert. Obere Grenzwerte wurden für vereinfachte Modelle mit paarweise produzierten Gluinos und Stops sowie in Resonanz produzierten Stops mit variabler R-Paritätsverletzender Kopplungsstärke bestimmt. Darüber hinaus wurden Grenzwerte für ein vereinfachtes Modell paarweise produzierter metastabiler Gluinos präsentiert.

Contents

1 Introduction

The Standard Model (SM) of particle physics, formulated in the mid of the 20^{th} century, is one of the most successful theories in the history of physics. Its predictions have been experimentally substantiated one by one throughout the last decades with high precision. All elementary particles, comprised in the SM, were discovered in experiments conducted at higher and higher energies, last of which was the discovery of the Higgs boson at the Large Hadron Collider (LHC) located at the CERN research facilities in Switzerland.

Despite this enormous success, the SM leaves many phenomena observed in nature unexplained, for instance the stabilisation of the Higgs mass, known as "fine-tuning problem", or the origin of dark matter, to name only a few. The limitations of the SM gave rise to a plethora of theories, which try to solve or avoid these deficiencies by extending or replacing the SM theory. One of these Beyond the Standard Model (BSM) theories is Supersymmetry (SUSY), a generalisation of space-time symmetries, extending the SM by introducing a new set of particles, linked to the SM particles via a transformation, which alters their spin quantum number by one half. Regardless of the lack of experimental evidence for the existence of supersymmetric particles, SUSY is still a popular candidate for the description of new physics, as it is able to provide solutions for several of the SM limitations.

The basic idea of SUSY provides a theoretical framework, in which many different supersymmetric models can be constructed, covering a vast parameter space. These models can be driven by e.g. experimental constraints or considerations about conditions at very high energy scales, tuning the respective parameters of the theory and thus varying the phenomenological predictions at energy scales accessible by current collider experiments. Hence, searches for new physics in the context of SUSY, as conducted for instance by the ATLAS and CMS collaborations (operating the two multiple-purpose experiments at the LHC), are always designed with respect to the particular characteristics of the underlying theoretical model.

In models imposing the conservation of R-parity, a quantum number relating lepton number, baryon number and spin, the weakly interacting Lightest Supersymmetric Particle (LSP) is stable and escapes the experiment undetected, thus representing a suitable dark matter candidate. The detector signatures predicted by such models include quarks and leptons as well as missing transverse energy $E_{\mathrm{T}}^{\mathrm{miss}}$, a consequence of the stability of the LSP. A search targeting squarks (the scalar SUSY partners of the quarks) and gluinos (the supersymmetric equivalents of the gluons) predicted within the R-parity conserving Minimal Supersymmetric Model (MSSM), was performed based on data from proton-proton (pp) collisions recorded with the ATLAS detector during the full Run 2 data-taking period from 2015 to 2018, corresponding to an integrated luminosity of L=139 fb^{-1}. This search, the 0L (2-6jets) SUSY analysis, based on final states featuring a large amount of $E_{\mathrm{T}}^{\mathrm{miss}}$, multiple jets and the absence of leptons, is presented in this thesis, focusing in particular on the techniques employed to estimate the contribution of multijet background processes.

The majority of SUSY searches, published by the ATLAS collaboration, target supersymmetric models assuming full R-parity conservation (RPC) or maximal R-parity violation (RPV), resulting in prompt detector signatures with and without $E_{\mathrm{T}}^{\mathrm{miss}}$, respectively. However, many supersymmetric models predict the existence of long-lived (LL) SUSY particles, decaying non-promptly according

to their finite lifetime. The metastability of such supersymmetric particles is a consequence of the suppression of decay channels due to very heavy intermediate particles or due to small R-parity violating couplings, for instance. Depending on the specific underlying assumptions, detector signatures predicted in such scenarios can be similar to final states targeted by dedicated RPC or RPV SUSY searches.
Following these considerations, a reinterpretation of several ATLAS analyses, the so called RPC-meets-RPV analysis, was performed in the context of RPV models, assuming a variable strength of the R-parity violating couplings, and a pure RPC model spanning a large energy scale, featuring LL gluinos due to heavy mediators of gluino decays. The predecessor of the full Run 2 0L (2-6jets) SUSY analysis, based on a data-subset corresponding to an integrated luminosity of L=36.1 fb^{-1} collected in 2015 and 2016, contributed to this effort. The analysis was slightly modified in order to increase its sensitivity in such LL scenarios.
One of the major challenges in the RPC-meets-RPV analysis was to assess the impact of the displacement of jets, created in non-prompt decays, on the jet energy scale and resolution, giving rise to supplementary systematic uncertainties. The study of these effects and the estimation of the resulting systematics were the author's major contributions to the RPC-meets-RPV reinterpretation effort. The obtained uncertainties were applied in all incorporated analyses and the results of this study were made public separately.

This document is structured as follows:
An introduction to the SM and its theoretical basics is given in chapter 2, followed by a brief description of the main concepts of SUSY and a selection of different supersymmetric models as well as a discussion of the phenomenological implications. The analyses presented in this thesis are based on the ATLAS experiment at the LHC. The corresponding experimental setup is explained in chapter 3, while chapter 4 provides details about the processing and simulation of events recorded with ATLAS.
The techniques used to reconstruct and calibrate physics objects, as well as the computation of systematics uncertainties these objects are afflicted with, are described in chapter 5. Additionally, the main analysis concepts and tools are detailed in this chapter. Eventually, the 0L (2-6jets) SUSY analysis and the RPC-meets-RPV reinterpretation are presented in chapter 6 and chapter 7, respectively. The thesis concludes with a summary of these two analyses in chapter 8.

2 Theoretical Framework

Searches for new physics, described in this thesis, are designed based on predictions derived from particular theoretical models. Hence, a basic understanding of the underlying theory, describing the fundamental principles, the particle content and the interactions between these particles, is vital in order to conduct such a search and to understand the implications of its findings.
This chapter gives a short introduction to the Standard Model (SM) of particle physics (cf. section 2.1), which not only builds the basis of many new physics models but is also essential for understanding and modelling physics processes which appear as background in the searches performed in the context of this thesis. Additionally, the supersymmetric extension of the SM, i.e. the theoretical framework in which the models, targeted by said analyses, are constructed, is introduced in section 2.2. The phenomenological implications of this theory and the standard technique of model construction used in analyses, are discussed in section 2.3.

2.1 The Standard Model ...

The SM is the fundamental theoretical formulation of elementary particles and interactions observed in experiments, with the exception of gravity which could not be incorporated into the SM. Main parts of this theoretical framework were developed already by the mid of 20^{th} century and its implications can be briefly summarised as follows:

- matter consists of spin $\frac{1}{2}$ particles called fermions
- interactions between the fermions are mediated by spin 1 particles, the gauge bosons
- the mass of all fundamental particles is generated via electroweak symmetry breaking, referred to as *Higgs mechanism*
- fermions and bosons can be described as quantisations of the underlying quantum fields

The fundamental particles and forces of the SM are described in subsection 2.1.1, while subsection 2.1.2 introduces the formulation of the SM in the context of quantum field theories.
Even though the SM of particle physics is considered to be one of the most successful theories in physics, validated experimentally with a high precision, it cannot explain every phenomenon observed in nature. These limitations of the SM, which give rise to the intensive searches for new physics conducted at present at many research facilities around the globe, are discussed in subsection 2.1.3.

2.1.1 Fundamental Particles and Forces in the Standard Model

A schematic overview of the particle content of the SM is given in Figure 2.1. The nested annular structure in this sketch indicates the three groups of fundamental particles, mentioned above, which are distinguished by their spin quantum number. From the outer to the innermost ring these are:

Fermions (f): The fundamental constituents of matter, composed of leptons (l) and quarks (q) are further categorised into three generations. Each particle in the matter sector of the SM has an anti-matter partner, identical in all characteristics but of opposite charge. The (anti-)leptons - e, μ and τ carry negative (positive) elementary charge $\mp 1e$, while their associated neutrinos - ν_e, ν_μ and ν_τ - are neutral. Each quark generation holds an up-type (anti-)quark with a charge of $\pm\frac{2}{3}e$ (up, charm and top) and a down-type (anti-)quark with $\mp\frac{1}{3}e$ (down, strange and bottom). Unlike leptons, which can be observed as individual particles, quarks carry the so called colour-charge, the equivalent of the electric charge in the strong coupling sector, which forces them to form colourless bound states.

Gauge Bosons: The spin 1 carriers of the fundamental forces in the SM have masses ranging from 0 to above 90 GeV. The massless bosons - the photon γ, mediating the electromagnetic force, and the eight gluons g, the mediators of the strong force - are electrically neutral. So is the heaviest boson, the Z, while the $W^{\pm}$, which are almost as heavy as the Z, carry the elementary charge $\pm 1e$. $W^{\pm}$ and Z are associated with the electroweak interaction.

Higgs Boson: Placed in the centre of the figure, the spin 0 Higgs boson represents a scalar particle. It plays a central role in the Higgs mechanism that generates the masses of SM particles. In July 2012 the ATLAS and CMS collaborations announced the discovery of a new scalar particle with a mass of about 125 GeV, compatible with the Higgs boson predicted in the SM [1, 2].

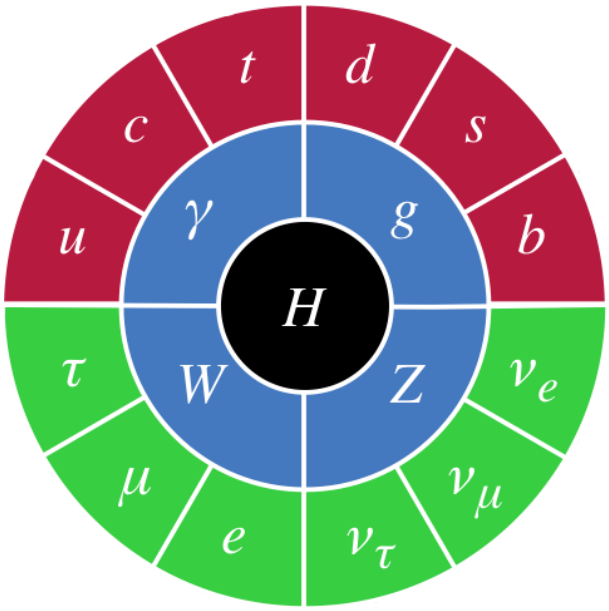

Figure 2.1: Schematic presentation of the particle content of the SM as shown in the film *"Particle Fever"* [3], depicting quarks in red, leptons in green, spin 1 bosons in blue and the Higgs boson in black.

Table 2.1 lists the fundamental interactions in the SM plus the gravitational force, together with their ranges, the respective force carrier, their source and the coupling constant.

Interaction	*Range*	*Mediator*	*Source*	*Coupling Constant*
strong	$\leq 10^{-15}$ m	gluon g	colour charge	$\alpha_s \approx 1$
weak	10^{-18} m	W- and Z-Boson $W^{\pm}$, Z^0	weak charge	$\alpha_W \approx 10^{-5}$
electromagnetic	∞	photon γ	electric charge	$\alpha_F \approx 137^{-1}$
gravitational	∞	(hypothetical) graviton	mass	$\alpha_G \approx 10^{-40}$

Table 2.1: Summary of the three fundamental interactions in the SM plus the fourth interaction observed in nature, the gravitational force [4].

2.1.2 Quantum Field Theory Description of the Standard Model

The mathematical formulation of the SM is based on relativistic quantum fields, where particles are described as the quanta of these fields. In this Quantum Field Theory (QFT) ansatz, the Lagrangian, comprising the kinetical and potential aspects of a theory, e.g. kinetic and potential energy in classical mechanics, is given as density, representing the propagation and interaction of the underlying field. The equation of motion of the respective particle is then determined by this Lagrangian density $\mathcal{L}$ and the *Euler-Lagrange equation*:

$$L = \int \mathcal{L}\, d^4x \qquad \frac{\partial \mathcal{L}}{\partial \phi} - \partial_\mu \frac{\partial \mathcal{L}}{\partial(\partial_\mu \phi)} = 0, \tag{2.1}$$

with $\partial_\mu = \frac{\partial}{\partial x^\mu}$ denoting the partial four-vector derivatives and ϕ being the quantum field.
The total SM Lagrangian includes contributions from several distinct QFTs discussed in detail below. The dimension and behaviour under local gauge transformation of the fields depend on the underlying symmetry of the respective theory.
Table 2.2 summarises the three fundamental symmetries in the SM, described by their gauge group, generator, gauge fields and coupling strength. The gauge group structure of the SM can be written as $SU(3)_C \otimes SU(2)_L \otimes U(1)_Y$, where $SU(3)_C$ is generated by the colour charge of the strong interaction and $SU(2)_L \otimes U(1)_Y$ is the unbroken symmetry of the unified electromagnetic and weak interactions.

Gauge Group	*Charge*	*Gauge Fields*	*Coupling Strength*
$SU(3)_C$	color	G^a_μ (gluon color octet $a \in [1, 8]$)	g_s
$SU(2)_L$	weak isospin	W^i_μ (iso triplet $i =, 2, 3$)	g
$U(1)_Y$	hypercharge	B_μ	g'

Table 2.2: Summary of the underlying gauge groups in the SM, listed together with their charge, gauge field and coupling strength.

Electromagnetic Interaction Quantum Electrodynamics (QED) is the quantum field formulation of the Maxwell theory, describing the electromagnetic interaction of particles. The equation of motion

for a free spin $\frac{1}{2}$ particle with mass m given in natural units ($\hbar = c = 1$) is derived from the Dirac Lagrangian

$$\mathcal{L}_{Dirac} = \bar{\Psi}\left(i\gamma^{\mu}\partial_{\mu} - m\right)\Psi, \tag{2.2}$$

where Ψ is the fermionic field, also known as *Dirac spinor*, and γ^{μ} represent the four Dirac matrices, which form an orthogonal basis for contravariant vectors. Like the Maxwell equations, $\mathcal{L}_{Dirac}$ is invariant under global gauge transformations. However, the Lagrangian is not invariant under local transformations of the $U(1)_{EM}$ (the unitarity group of the electric charge), which is defined by a space-time dependent function $f(x)$, acting on the fermion field

$$\Psi(x) \quad \rightarrow \quad \Psi'(x) = e^{iqf(x)}\,\Psi(x), \tag{2.3}$$

with a coupling strength q. Hence, the Lagrangian description of the electromagnetic interaction needs to be modified, in order to preserve gauge invariance under such transformations.
A new vector field A_{μ} is introduced, which transforms as

$$A_{\mu} \quad \rightarrow \quad A'_{\mu} = A_{\mu} + \partial_{\mu} f(x). \tag{2.4}$$

This new field interacts with the fermionic field ($q\bar{\Psi}\gamma^{\mu}A_{\mu}\Psi$), representing the interaction between the fermions and the quantum of A_{μ}, the photon.
The full QED Lagrangian is then

$$\mathcal{L}_{QED} = -\frac{1}{4}F_{\mu\nu}F^{\mu\nu} + i\bar{\Psi}\gamma^{\mu}\partial_{\mu}\Psi - m\bar{\Psi}\Psi + q\bar{\Psi}\gamma^{\mu}A_{\mu}\Psi, \tag{2.5}$$

with the field strength tensor $F_{\mu\nu} = \partial_{\mu}A_{\nu} - \partial_{\nu}A_{\mu}$ of the photonic field describing its kinetic aspects. The introduction of a mass term $mA_{\mu}A^{\mu}$ would once again violate gauge invariance. Hence, the gauge invariance of the QFT formulation of the electromagnetic interaction predicts a massless force mediator, observed in nature as photon.

Strong Interaction The QFT description of the strong interaction between quarks and gluons is called Quantum Chromodynamics (QCD). It is invariant under gauge transformations of the $SU(3)_C$ symmetry group generated by the colour charge C, which can assume three different values: red, blue and green.
Unlike the field strength tensor of the photon field in QED, the tensor of the gluonic field $G^a_{\mu\nu} = \partial_{\mu}G^a_{\nu} - \partial_{\nu}G^a_{\mu} - g_s f_{abc}G^b_{\mu}G^c_{\nu}$ has an additional term describing the self interaction of the gluons with the coupling strength g_s. The structure constant f_{abc} reflects the dimension of the colour space. However, similar to QED, a gluonic mass term would violate local gauge invariance resulting in eight massless quanta of the gluon field, the gluons.
The full QCD Lagrangian

$$\mathcal{L}_{QCD} = -\frac{1}{4}G^a_{\mu\nu}G_a^{\mu\nu} + i\bar{\mathbf{q}}_f\gamma^{\mu}\partial_{\mu}\mathbf{q}_f - m\,\bar{\mathbf{q}}_f\mathbf{q}_f - g_s\bar{\mathbf{q}}_f\gamma^{\mu}\lambda_a G^a_{\mu}\mathbf{q}_f, \tag{2.6}$$

includes the kinetic term of the gluon field, the Dirac term of $\mathbf{q}_f$ (the quark field of flavour f in a

vector representation in colour space) and the interaction term between quarks and gluons. This interaction term includes the Gell-Mann matrices λ^a which are related to the structure constant via $[\lambda^a, \lambda^b] = if^{abc}\lambda^c$ forming the algebra of the $SU(3)$ [5].
As a consequence of the particularities of the gluon self interaction, quarks and gluons are *confined* in colourless bound states and cannot be observed as individual particles. An additional effect associated to gluon self-coupling is the so called *asymptotic freedom*, which describes the reversion of the charge-screening process seen in QED, where the electric charge of e.g. an electron is screened by a cloud of virtual electron-positron pairs. In the context of QCD the same screening effect is present ($q\bar{q}$ pairs screen the colour charge of a quark) but additionally a cloud of gluons increases the colour charge, due to the gluon self interaction. This anti-screening is dominant and increases as a function of the distance. Although strongly interacting particles are confined at low energies, they appear free at high energies.

Electroweak Interaction Several phenomena observed in nature could not be explained in the context of QED, e.g. the β-decay, which was described by Enrico Fermi as a four point interaction [6]. However, this theoretical formulation of processes involving the weak interaction is valid only at low energies. Hence, in the 1970s Sheldon Glashow [7], Abdus Salam [8] and Steven Weinberg [9] developed a new theory based on the unification of the electromagnetic and the weak nuclear force. This new QFT describing the electroweak interaction is based on the symmetry group $SU(2)_L \otimes U(1)_Y$, mentioned above. $SU(2)_L$ describes the invariance under local rotations of the weak isospin, $U(1)_Y$ under the gauge transformation generated by the hypercharge Y. Two new quantum numbers are introduced, the third component of the weak isospin $I_3 = \pm\frac{1}{2}, 0$ and the weak hypercharge Y both of which are related to the electrical charge Q via $Y = 2(Q - I_3)$.
Table 2.3 lists the resulting chiral fermion fields, which are described as left-handed isospin doublets ($I_3 = \pm\frac{1}{2}$) and right-handed isospin singlets ($I_3 = 0$). Gauge transformations under $SU(2)_L$ act only on the left-handed chiral states, while $U(1)_Y$ applies to singlets and doublets alike. The left-handed

	first generation	*second generation*	*third generation*
leptons	$\begin{pmatrix} \nu^e \\ e^- \end{pmatrix}_L \quad e_R^-$	$\begin{pmatrix} \nu^\mu \\ \mu^- \end{pmatrix}_L \quad \mu_R^-$	$\begin{pmatrix} \nu^\tau \\ \tau^- \end{pmatrix}_L \quad \tau_R^-$
quarks	$\begin{pmatrix} u \\ d \end{pmatrix}_L \quad u_R,\, d_R$	$\begin{pmatrix} c \\ s \end{pmatrix}_L \quad c_R,\, s_R$	$\begin{pmatrix} t \\ b \end{pmatrix}_L \quad t_R,\, b_R$

Table 2.3: Summary of the fermionic fields in the SM showing the three generations of leptons and quarks. Neutrinos occur only as left-handed chiral states and are considered to be massless.

down-type quarks d_L, s_L and b_L in Table 2.3 are given as flavour eigenstates. The relation to their mass eigenstates is defined by the Cabibbo-Kobayashi-Maskawa matrix (CKM) [10] which describes the mixing of quark flavours under electroweak interaction.

Similarly to the QED, the requirement of local gauge invariance under the transformations in $SU(2)_L \otimes U(1)_Y$ demands the introduction of new vector fields $\mathbf{W}_\mu$ and B_μ.
The $\mathbf{W}_\mu = (W^1_\mu, W^2_\mu, W^3_\mu)$ couples to the weak isospin with the coupling strength g and B_μ to the hypercharge with strength g' (cf. Table 2.2). As it is the case for the photonic field in QED, the introduction of non-zero mass terms for $\mathbf{W}_\mu$ and B_μ would violate the local gauge invariance of the system. However, unlike the massless photon which mediates the electromagnetic interaction of infinite range, the short range of the weak force indicates that its mediators must be heavy. In order to correctly describe the electromagnetic and weak interactions observed at low energies, the electroweak symmetry is broken, preserving only the local gauge invariance under $U(1)_{EM}$ transformations.
After electroweak symmetry breaking W^3_μ and $B_\mu$are linearly combined to form the neutral boson fields of the Z

$$Z_\mu = \cos\theta_W W^3_\mu - \sin\theta_W B_\mu \tag{2.7}$$

and the photon

$$A_\mu = \sin\theta_W W^3_\mu + \cos\theta_W B_\mu, \tag{2.8}$$

while W^1_μ and W^2_μ mix to the form the charged electroweak boson fields of $W^\pm$

$$W^\pm_\mu = \frac{1}{\sqrt{2}}(W^1_\mu \mp W^2_\mu). \tag{2.9}$$

θ_W is the so called Weinberg angle and can be defined via the coupling constants as

$$\sin\theta_W = \frac{g'}{\sqrt{g^2 + g'^2}} \tag{2.10}$$

and

$$\cos\theta_W = \frac{g}{\sqrt{g^2 + g'^2}}. \tag{2.11}$$

A mechanism allowing to break the local gauge invariance while preserving the global one, is the *spontaneous electroweak symmetry breaking*, as it was developed by Robert Brout, François Englert and Peter Higgs [11, 12], consequently known by the name Brout-Engler-Higgs mechanism (BEH).

Generation of Mass The BEH allows to add mass terms for the fermions and massive bosons to the Lagrangian of the SM by introducing an additional $SU(2)_L$ doublet of complex scalar fields

$$\Phi = \begin{pmatrix} \phi^+ \\ \phi^0 \end{pmatrix}. \tag{2.12}$$

It has a potential of the form

$$V(\Phi) = \mu^2 |\Phi^\dagger \Phi| + \lambda (|\Phi^\dagger \Phi|)^2, \tag{2.13}$$

where the mass parameter μ and the quartic self-coupling λ are in principle free parameters. The stability of the vacuum requires λ to be positive and the sign of μ^2 defines the shape of the potential

$V(\Phi)$. A positive mass parameter squared would lead to a parabola with a global minimum at the origin, while $\mu^2 < 0$ results in the form sketched in Figure 2.2: the Higgs potential, also known as Mexican hat potential. In the latter case, the global minimum at the origin is transformed into a local maximum, rendering this choice unstable. Instead, a plethora of solutions minimises the potential, all of which are located on a circle in the complex plane. These solutions are equal and provide a non-vanishing vacuum expectation value (VEV) of the form $v = \sqrt{\frac{-\mu^2}{\lambda}}$, thus spontaneously breaking the electroweak symmetry.

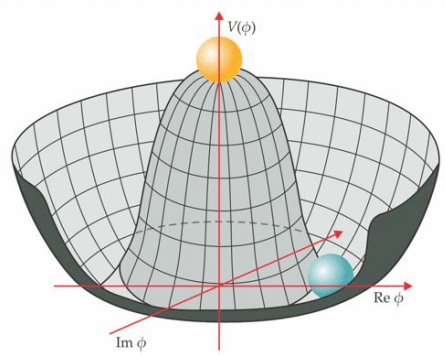

Figure 2.2: Illustration of the Higgs potential [13], with a stable, real and non vanishing ground state indicated by the blue pellet and the unstable vanishing VEV marked by the yellow pellet.

The ground state[1], indicated by the blue pellet in Figure 2.2, is

$$\langle \Phi \rangle_0 = \frac{1}{\sqrt{2}} \begin{pmatrix} 0 \\ v \end{pmatrix}, \tag{2.14}$$

which is modified in a perturbative ansatz by adding a small fluctuation $H(x)$ around the VEV

$$\langle \Phi \rangle = \frac{1}{\sqrt{2}} \begin{pmatrix} 0 \\ v + H(x) \end{pmatrix}. \tag{2.15}$$

The new scalar field $H(x)$ is the Higgs field, which gives rise to a new spin 0 particle, the SM Higgs boson and interacts with the bosonic fields of the electroweak theory. Thus, the Higgs Lagrangian $\mathcal{L}_{Higgs}$ includes the self interaction of the Higgs field resulting in a mass term for the Higgs boson $M_H^2 = 2\mu^2$. Additionally, $\mathcal{L}_{Higgs}$ incorporates the interaction of Φ with the electroweak fields, resulting in mass terms for the $W^{\pm}$ and Z, while the photon stays massless due to the preservation of the $U(1)_{EM}$ symmetry. The gauge bosons in the SM after the electroweak symmetry breaking are summarised in Table 2.4.

Unlike the masses of the spin 1 particles, the mass of the Higgs boson is not predicted in the theory, due to μ being a new degree of freedom. However, it has been measured to be about 125 GeV by the ATLAS and CMS collaborations [14, 15].
Another consequence of the electro weak symmetry breaking in the BEH are the masses of the SM fermions m_f. They are generated via the Yukawa terms, describing the interaction of the fermion

[1] in principle this choice is arbitrary, but reflects the usual convention

Interaction	*Boson Field*	*Boson*	*Mass*
charged weak	$W^{\pm} = \frac{1}{\sqrt{2}}(W^1_\mu \mp W^2_\mu)$	W^+, W^-	$M^2_W = \frac{1}{4} g^2 v^2$
neutral weak	$Z^0 = \frac{-g' B_\mu + g W^3_\mu}{\sqrt{g'^2 + g^2}}$	Z^0	$M^2_Z = \frac{1}{4}(g^2 + g'^2) v^2$
electromagnetic	$A_\mu = \frac{g' B_\mu + g W^3_\mu}{\sqrt{g'^2 + g^2}}$	γ	$M^2_\gamma = 0$

Table 2.4: Summary of the three bosonic fields included in the electroweak unification, their quanta and mass terms generated via spontaneous electroweak symmetry breaking.

fields with the Higgs doublet:

$$\mathcal{L}_{yukawa} = Y^u_{ij} (\bar{q}_i)_L \, \tilde{\Phi} \, (u_j)_R + Y^d_{ij} (\bar{q}_i)_L \, \Phi \, (d_j)_R + Y^e_{ij} (\bar{l}_i)_L \, \tilde{\Phi} \, (e_j)_R + Y^\nu_{ij} (\bar{l})_L \, \Phi \, (\nu_j)_R + h.c.. \tag{2.16}$$

The indices i and j indicate the families and the matrices Y_{ij} are the Yukawa couplings between the fermions and the Higgs field in the representations

$$\tilde{\Phi} = \begin{pmatrix} \phi^{0*} \\ -\phi^- \end{pmatrix} \qquad \Phi = \begin{pmatrix} \phi^+ \\ \phi^0 \end{pmatrix}. \tag{2.17}$$

Leptons and quarks interact differently with the Higgs field. The leptonic Lagrangian is simplified since neutrinos are considered to be massless within the SM. Thus, only one component of the lepton spinors interacts with Φ. This is not the case for the three generations of quark isospin doublets, where all components acquire masses via Yukawa interaction. Accordingly, the Lagrangian describing the Yukawa terms for one generation can be written as

$$\mathcal{L}_{yukawa} = y_u \bar{q}_L \, \tilde{\Phi} \, u_R + y_d \bar{q}_L \, \Phi \, d_R + y_e \bar{l}_L \, \tilde{\Phi} \, e_R + h.c.. \tag{2.18}$$

Choosing the ground state for the symmetry breaking

$$\Phi = \frac{1}{\sqrt{2}} \begin{pmatrix} 0 \\ v \end{pmatrix} \qquad \Rightarrow \qquad \tilde{\Phi} = \frac{1}{\sqrt{2}} \begin{pmatrix} v \\ 0 \end{pmatrix} \tag{2.19}$$

leads to the fermion masses given by the VEV and the respective Yukawa coupling

$$m_f = -\frac{y_f v}{\sqrt{2}}, \tag{2.20}$$

where f denotes the fermions of the generation, e.g. e, u and d.

2.1.3 Limitations of the Standard Model

The QFT formulation of the SM of particle physics is a powerful formalism, whose predictions were validated experimentally with a high level of precision. However, not all phenomena observed in nature can be described within this theory. This subsection discusses the most pressing deficiencies of the SM while possible solutions are given in section 2.2.

Unification of Gauge Couplings The SM itself is in principle not bound to a given energy scale and stays valid up to the Planck scale $E_{Planck} \approx 10^{19}$ GeV where effects of quantum gravity are expected to be non-negligible. However, to the present day no QFT formulation of gravity was included in the SM. In case the SM is considered to be valid only at the electroweak scale, it should be the low-energy representation of a more general theory valid at high energy scales. One possible realisation of such theories are the so called Grand Unification Theories (GUT), in which the SM gauge groups are unified to a single simple gauge group.
This idea is strengthened by the "running" of the gauge couplings, which depend on the energy scale of the respective interaction. These coupling constants (which are in fact not constant) and their order of magnitude at the electroweak scale are listed in Table 2.1. As already mentioned, the strong coupling α_s decreases with increased energy, as a consequence of the weakened gluon self-interaction at high energies. A similar behaviour is observed for the coupling of the weak force α_W, while the fine structure constant α_F shows an increase, due to the screening effect caused by vacuum fluctuations, which is less strong at high energies.
Hence, the couplings in the SM tend to converge at higher energies indicating a unification of the forces at the GUT scale $E_{GUT} \approx 10^{15}$ GeV. However, in the SM the couplings not quite coincide in a single point, rendering it a low-energy approximation of a potential unified high energy theory.

Neutrino Oscillations As mentioned above, in the SM neutrinos are considered to be massless particles of left-handed chirality, which occur in three different flavours. Contradictory, experimental results show that neutrinos are able to change their flavour. From observations of these neutrino oscillations the mass differences between the flavours are derived to be non-zero [16], indicating that neutrinos are in fact not massless. Similar to the CKM in the quark sector, the different neutrino flavour eigenstates can be described as a mixture of three different mass eigenstates. This mixing is defined by the Pontecorvo-Maki-Nakagawa-Sakata matrix [17], which contains the probabilities for oscillations between the different flavours.

Hierarchy Problem The term *hierarchy problem* refers to the energy hierarchy in the SM, i.e. the "smallness" of the electroweak scale with respect to the Planck scale.
In the QFT formalism, the SM parameters are calculated perturbatively, where higher order corrections occur as vertex corrections or self energy terms, realised as closed loops of virtual particles. Since these *loop corrections* lead to divergences, the calculations are renormalised. A physical quantity

$$x = x_{bare} - \delta x(\Lambda), \tag{2.21}$$

is described as an unmeasurable "bare" quantity x_{bare} screened by the virtual processes given as correction δx dependent on the energy scale Λ at which the parameter is probed.
Generally speaking, processes which require the bare quantity and the correction to be *finely tuned* in order to result in the observed physical quantity, are considered to be *unnatural*. The SM includes processes, where naturalness is provided by the intrinsic symmetries, e.g. the calculation of the electron mass in QED, where the large corrections due to self interaction are cured by the contributions of the positron, reducing the correction to $\delta m_e \sim \alpha_F m_e ln(\Lambda)$[2] .
The Higgs boson mass is not protected by such a symmetry and the radiative corrections include the Yukawa couplings to the fermions as well as the quartic Higgs coupling

$$\delta m_h^2 \sim \lambda \Lambda^2 - Y_f^2 \Lambda^2. \tag{2.22}$$

Thus, the cancellation necessary to gain an observed Higgs mass of 125 GeV, needs to happen with the high precision to cancel terms of the order of the cut-off scale.

Dark Matter and Dark Energy Cosmological observations show that matter as it is described in the SM can only account for about 5 % of the known universe (the "visible" matter). These observations, based on gravitational effects, indicate that roughly 25 % consist of invisible or dark matter (DM) while the remaining 70 % are referred to as dark energy (DE). A brief discussion of some of these experimental evidences is given below:

Observations by Fritz Zwicky: In 1933 a first evidence for the existence of DM was observed by Fritz Zwicky, investigating the Coma cluster [18]. Zwicky derived the mass of this galaxy cluster based on the velocity of the galaxies in the cluster and on the luminosity based on the *mass-to-light ratio*, known from single stars. A difference of two orders of magnitude was observed between both methods, indicating the existence of non-luminous matter increasing the mass of the galaxy cluster.

Galaxy Rotation Problem: Vera Rubin *et al.* investigated the rotational curves of galaxies, i.e. the rotational velocity of the stars in a galaxy as function of the radial distance to the galaxy centre [19]. It was found that stars in the outer regions of galaxies rotate much faster than expected from gravitational models based solely on the visible matter. Hence, it was concluded that invisible matter contributes to the galaxy mass.

Gravitational Lenses: In Einstein's general relativity gravity acts on the photons due to the space time curvature, resulting in so called gravitational lenses, i.e. the picture of light sources is distorted by large masses in the path of the light rays. This phenomenon can be applied to estimate the mass of galaxies or galaxy clusters, again showing a discrepancy between the mass derived form the visible matter and the gravitational potential of the object acting as lens [20].

[2] The higher order corrections in QFT are expanded as a power series in the respective coupling constant, that is α_F in QED.

Bullet Cluster: Observations of the collision of two galaxies, show a discrepancy in the distribution of mass derived from gravitational lensing and measured via x-ray emission. The x-ray sources in both galaxies interact electromagnetically while passing through each other, resulting in a smeared trace. The distribution including non-luminous matter, on the other hand, is unaffected by any inelastic interaction, indicating that DM, apart from gravitational interaction, can only interact weakly with the visible matter [21].

Following cosmological observations, DM is assumed to be electrical neutral, non-relativistic, stable with respect to the lifetime of the universe and massive. Many models of new physics predict either one or several particles as the source of DM and are currently the subject of many searches, conducted at CERN and elsewhere.

2.2 ...and beyond

A plethora of Beyond the Standard Model (BSM) theories was developed in order to extend or replace the SM to solve the deficiencies discussed in the previous section. One particular theory, developed in the 1970s simultaneously provides solutions for the majority of the problems in the SM. It is based on a new symmetry, relating fermions and bosons via a symmetry transformation, which changes the spin of each particle by $\frac{1}{2}$. Hence, this new theory, named Supersymmetry (SUSY) [22–30], assigns a supersymmetric partner to each particle, which has the same set of quantum numbers except the spin.
The basic concepts of SUSY and its solutions to the SM limitations are briefly discussed in this section. An overview of the basic supersymmetric extension of the SM and its particle content is given in subsection 2.2.1, followed by a couple of examples of more exotic SUSY models in subsection 2.2.2. An extensive pedagogical introduction can be found elsewhere [31].
Unlike in the SM, where space-time symmetries - mass, momentum, spin - and internal symmetries - quantum numbers representing the sources of the gauge groups - are independent, SUSY transformations combine these two symmetry classes. Consequently, fermions and bosons are not separated, as they are in the SM, but form so called supermultiplets.
The simplest way of relating fermionic and bosonic fields is the introduction of Weyl spinors Ψ, which are similar to Dirac spinors but without their chiral character, and operators $\mathcal{Q}$ acting on these spinors to describe the basic SUSY transformation,

$$\mathcal{Q}\,|\Psi_{boson}\rangle = |\Psi_{fermion}\rangle \qquad \mathcal{Q}^{\dagger}\,|\Psi_{fermion}\rangle = |\Psi_{boson}\rangle\,, \tag{2.23}$$

where $\mathcal{Q}$ ($\mathcal{Q}^{\dagger}$) increases (decreases) the spin quantum number by $\frac{1}{2}$. The Weyl spinors are included in the two supermultiplets extending the SM:

Chiral supermultiplets contain a complex scalar field and a Weyl fermion field. The SM fermions and their scalar superpartners form a chiral multiplet, as well as the only scalar in the SM, the Higgs boson, with its spin $\frac{1}{2}$ superpartners.

Vector supermultiplets correspond to the SUSY generalization of the SM gauge fields, composed

of a Weyl spinor, representing the so called "gauginos", the fermionic partners of the gauge bosons and a vector gauge field.

This formulation gives rise to a mass degeneracy of the supermultiplets, i.e. SUSY particles have the same masses as their SM partners. However, SUSY cannot be an exact symmetry, otherwise SUSY particles would have been detected experimentally. Within a low-energy effective QFT formulation, SUSY is broken via an additional term in the supersymmetric Lagrangian

$$\mathcal{L} = \mathcal{L}_{SUSY} + \mathcal{L}_{soft}, \tag{2.24}$$

explicitly breaking the symmetry. $\mathcal{L}_{SUSY}$ includes all interactions invariant under supersymmetric transformations, in particular gauge and Yukawa interactions among the supermultiplets, introducing nineteen parameters, in accordance with the nineteen parameters of the SM. $\mathcal{L}_{soft}$, on the other hand, adds a plethora of explicit SUSY breaking terms, giving rise to over one hundred new parameters, e.g. mass terms of scalar fermions, trilinear Higgs couplings, mixing angles, etc.
Within SUSY the hierarchy problem can be solved in a natural way. The new symmetry protects the mass of the Higgs boson against divergences since two new terms are introduced, each of which exactly cancels the corresponding term in Equation 2.22. The exact cancellation happens only if the bosonic and fermionic loop contributions are equal. Hence, the soft term in Equation 2.24 needs to be constructed, such that the remaining one-loop radiative corrections to the Higgs mass are of the form

$$\delta m^2 \sim m_{soft}^2 \ln\left(\frac{\Lambda}{m_{soft}}\right). \tag{2.25}$$

If the typical scale of the SUSY breaking parameter m_{soft} is not too far from the electroweak scale, the radiative corrections and the bare Higgs mass cancel without any large fine tuning.
In supersymmetric theories the coupling strength of the fundamental interactions included in the SM are affected such that they unify automatically at the GUT scale. Figure 2.3 shows the inverse strength of these interactions as a function of the energy scale and the particle distance, respectively, comparing the evolution of the coupling constants in the SM (left) and in a weak-scale SUSY scenario (right).
Additionally, SUSY may provide a candidate for a particle source of DM. This supersymmetric particle, or *sparticle*, is a direct consequence of the conservation of an additional symmetry, often introduced in supersymmetric theories. This symmetry is represented by a new quantum number, the so called R-parity [33]

$$P_R = (-1)^{3(B-L)+2s}, \tag{2.26}$$

which relates the baryon number B, the lepton number L and the spin s, such that R-parity is positive for SM and negative for SUSY particles. The concept of R-parity is introduced in order to preserve the SM conservation of B and L, which is violated due to the gauge invariance of the supersymmetric Lagrangian. Furthermore, general formulations of SUSY allow for a possible (experimentally unobserved) proton decay, which is suppressed by requiring conservation of R-parity. Under this assumption sparticles can be produced and annihilated pairwise only. Thus, the Lightest Supersymmetric Particle (LSP), which can be chosen to be electrically neutral and only weakly

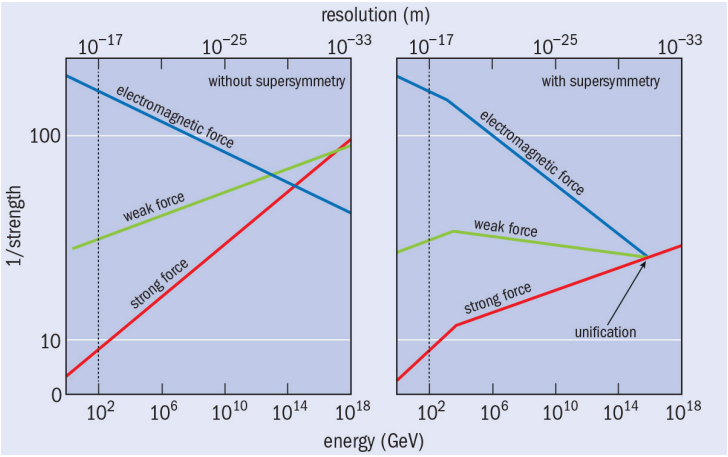

Figure 2.3: Comparison of the running of the inverse couplings α_F^{-1}, α_W^{-1} and α_S^{-1} in the SM and modified in SUSY [32].

interacting, is rendered a stable particle, being a suitable DM candidate. In a hadron collider such particles are manifested as *missing transverse energy* $E_{\mathrm{T}}^{\mathrm{miss}}$ (cf. subsection 5.1.4), since they escape the experiments undetected.

Many supersymmetric models assume RPC. However, there are also popular RPV models, as discussed in subsection 2.2.2.

2.2.1 The Minimal Supersymmetric Standard Model

The Minimal Supersymmetric Model (MSSM) is the most basic supersymmetric extension of the SM, which provides solutions to many of its deficiencies (the hierarchy problem, the problem of DM and force unification), while introducing a minimum of new particles and preserving the SM group structure $SU(3)_C \otimes SU(2)_L \otimes U(1)_Y$. In order to extend the SM, chiral supermultiplets include the left-handed SM quarks and their scalar partners the *squarks* (Q) as well as the left-handed SM leptons together with their bosonic partners the *sleptons* (L). The right-handed fermions and their superpartners, generalised as *sfermions*, form the singlets $\bar{\mathrm{u}}$, $\bar{\mathrm{d}}$ and $\bar{\ell}$. In order to avoid gauge anomalies, two complex $SU(2)$ Higgs doublets, H_U and H_D are introduced, coupling to up-type and down-type quarks, respectively. Table 2.5 summarises these chiral supermultiplets.

The vectorial supermultiplets contain the SM gauge fields (the gluon field and the electroweak fields $W_\mu^\pm$ and B_μ) and their fermionic superpartners.

Interactions between these superfields can be summarised in the *superpotential*

$$\mathcal{W}_{MSSM} = \mathcal{W}_{RPC} + \mathcal{W}_{RPV}, \tag{2.27}$$

which is composed of two parts, reflecting the RPC and RPV terms.

The RPC superpotential can be written as

$$\mathcal{W}_{RPC} = Y_{up}\bar{\mathrm{u}}Q\mathrm{H}_U - Y_{down}\bar{\mathrm{d}}Q\mathrm{H}_D - Y_{lep}\bar{\ell}L\mathrm{H}_D - \mu\mathrm{H}_U\mathrm{H}_D, \tag{2.28}$$

Names	*Supermultiplet*	*spin* $\frac{1}{2}$	*spin 0*
three families	Q	$\begin{pmatrix} \mathrm{u}_L \\ \mathrm{d}_L \end{pmatrix}$	$\begin{pmatrix} \widetilde{\mathrm{u}}_L \\ \widetilde{\mathrm{d}}_L \end{pmatrix}$
of (s)quarks	$\overline{\mathrm{u}}$	$\overline{\mathrm{u}}_L \sim (\mathrm{u}_R)^c$	$\widetilde{\overline{\mathrm{u}}}_L$
	$\overline{\mathrm{d}}$	$\overline{\mathrm{d}}_L \sim (\mathrm{d}_R)^c$	$\widetilde{\overline{\mathrm{d}}}_L$
three families	L	$\begin{pmatrix} \nu_L \\ \mathrm{e}_L \end{pmatrix}$	$\begin{pmatrix} \widetilde{\nu}_L \\ \widetilde{\mathrm{e}}_L \end{pmatrix}$
of (s)leptons	$\bar{\ell}$	$\bar{\ell}_L \sim (\ell_R)^c$	$\widetilde{\bar{\ell}}_L$
higgs(inos)	H_U	$\begin{pmatrix} \widetilde{\mathrm{H}}^+_U \\ \widetilde{\mathrm{H}}^0_U \end{pmatrix}$	$\begin{pmatrix} \mathrm{H}_U{}^+ \\ \mathrm{H}_U{}^0 \end{pmatrix}$
	H_D	$\begin{pmatrix} \widetilde{\mathrm{H}}^0_D \\ \widetilde{\mathrm{H}}^-_D \end{pmatrix}$	$\begin{pmatrix} \mathrm{H}^0_D \\ \mathrm{H}^-_D \end{pmatrix}$

Table 2.5: Summary of the chiral multiplets in the MSSM listing their fermionic (spin $\frac{1}{2}$) and bosonic (spin 0) components.

Names	*spin* 1	*spin* $\frac{1}{2}$
gluons, gluinos	g	$\widetilde{\mathrm{g}}$
W bosons, winos	$\mathrm{W}^\pm, \mathrm{W}^0$	$\widetilde{\mathrm{W}}^\pm, \widetilde{\mathrm{W}}^0$
B boson, bino	B	$\widetilde{\mathrm{B}}$

Table 2.6: Summary of the gauge multiplets in the MSSM showing the SM gauge bosons and their superpartners, the gauginos.

where the Y denote matrices representing the Yukawa couplings of the left-handed up- and down-type (s)quarks Q and (s)fermions L. The parameter μ, which is similar to the Higgs mass parameter in the SM, is called higgsino mass, following the naming convention of adding the suffix "-ino" to the name of spin $\frac{1}{2}$ partners of SM bosons.

The lepton number violating couplings in the RPV superpotential,

$$\mathcal{W}_{RPV} = \frac{\lambda_{ijk}}{2} L_i L_j \bar{\ell}_k + \lambda'_{ijk} L_i Q_j \overline{\mathrm{d}}_k + \frac{\lambda''_{ijk}}{2} \overline{\mathrm{u}}_i \overline{\mathrm{d}}_j \overline{\mathrm{d}}_k + \kappa_i L_i \mathrm{H}_U, \tag{2.29}$$

are λ and λ', while λ'' gives the baryon number violation. Quark and lepton generation indices are denoted i, j, and k. Consequently, L_i and Q_i are the (s)quark and (s)fermion superfields of generation i. Singlet chiral superfields are $\bar{\ell}_i$, $\overline{\mathrm{d}}_i$ and $\overline{\mathrm{u}}_i$ and H_U denotes the Higgs superfield coupling to up-type quarks. The last term with the dimensional mass parameter κ is again lepton number violating.

Similar to the SM, the SUSY fields mix, in order to form the mass eigenstates of the particles. In

case of the scalar fermions these are $\widetilde{f}_1$ and $\widetilde{f}_2$ ($m_{\widetilde{f}_1} < m_{\widetilde{f}_2}$), defined by the mixing angle $\theta_{\tilde{f}}$ via

$$\begin{pmatrix} \widetilde{f}_1 \\ \widetilde{f}_2 \end{pmatrix} = \begin{pmatrix} \cos\theta_{\tilde{f}} & -\sin^*\theta_{\tilde{f}} \\ \sin\theta_{\tilde{f}} & \cos\theta_{\tilde{f}} \end{pmatrix} \begin{pmatrix} \widetilde{f}_L \\ \widetilde{f}_R \end{pmatrix} \tag{2.30}$$

diagonalising the sfermion mass matrix

$$\mathbf{M}_{\tilde{\mathrm{f}}}{}^2 \approx \begin{pmatrix} M_{(\tilde{f}_L^*\tilde{f}_L)}{}^2 & \propto Y_f \\ \propto Y_f & M_{(\tilde{f}_R^*\tilde{f}_R)}{}^2 \end{pmatrix}, \tag{2.31}$$

in the respective term of the soft Lagrangian

$$\mathcal{L}_{m(\tilde{f})} = -\begin{pmatrix} \widetilde{f}_L^* & \widetilde{f}_R^* \end{pmatrix} \mathbf{M}_{\tilde{\mathrm{f}}}{}^2 \begin{pmatrix} \widetilde{f}_L \\ \widetilde{f}_R \end{pmatrix}. \tag{2.32}$$

The off-diagonal elements of the mass matrix are proportional to the respective Yukawa coupling, thus neglected in case of light-flavoured sfermions. Consequently, only third generation squarks (stops and sbottoms) and sleptons are assumed to show a substantial mixing of their left- and right-handed components.

Gluinos occur as colour octet fermions, which do not mix with any other multiplet. The two Higgs doublets, H_U and H_D, each of which comprises four real scalar fields, represent eight degrees of freedom: three for the SM bosons $\mathrm{W}^{\pm}$ and Z and five to form additional physical scalar particles. These are the equivalent of the SM Higgs boson - a neutral scalar h^0 - plus four additional particles extending the Higgs sector - another neutral scalar H^0, a neutral pseudo-scalar A^0 as well as two charged scalars H^+ and H^-.

The neutral gauge eigenstates $\widetilde{\mathrm{B}}^0$, $\widetilde{\mathrm{W}}^0$, $\widetilde{H}_U^0$ and $\widetilde{H}_D^0$ mix to form four weakly interacting neutralinos of increasing mass: $\widetilde{\chi}_1^0$, $\widetilde{\chi}_2^0$, $\widetilde{\chi}_3^0$ and $\widetilde{\chi}_4^0$. The lightest neutralino $\widetilde{\chi}_1^0$ is typically considered the LSP, which is stable in RPC scenarios.

In the gauge eigenstate basis, the mass matrix of the neutralinos can be written as

$$\mathbf{M}_{\widetilde{\chi}^0} = \begin{pmatrix} M_1 & 0 & -m_Z s_W c_\beta & m_Z s_W s_\beta \\ 0 & M_2 & m_Z c_W c_\beta & m_Z c_W s_\beta \\ -m_Z s_W c_\beta & m_Z c_W c_\beta & 0 & -\mu \\ m_Z s_W s_\beta & -m_Z c_W s_\beta & -\mu & 0 \end{pmatrix}, \tag{2.33}$$

where $s_W = \sin\theta_W$, $c_W = \cos\theta_W$ with the mixing angle θ_W and $c_\beta = \cos\beta$, $s_\beta = \sin\beta$ with $\tan\beta = \frac{v_U}{v_D}$ denoting the ratio of the higgs VEVs. M_1, M_2 and M_3 are the gaugino mass parameters. $\mathbf{M}_{\widetilde{\chi}^0}$ is diagonalised by means of the unitary matrix $\mathbf{N}$, in order to obtain the mass eigenstates

$$\widetilde{\chi}_i^0 = N_{i1}\widetilde{\mathrm{B}}^0 + N_{i2}\widetilde{\mathrm{W}}^0 + N_{i3}\widetilde{\mathrm{H}}_D^0 + N_{i4}\widetilde{\mathrm{H}}_U^0. \tag{2.34}$$

The components of $\mathbf{N}$ represent the admixture of the individual gauge eigenstates to the i^{th} neutralino,

$$f(\widetilde{\mathrm{B}}^0) = |N_{i1}|^2, \quad f(\widetilde{\mathrm{W}}^0) = |N_{i2}|^2, \quad f(\widetilde{\mathrm{H}}^0) = |N_{i3}|^2 + |N_{i4}|^2. \tag{2.35}$$

Similarly, the charged gauge eigenstates $\widetilde{H}_U^+$, $\widetilde{H}_D^-$, $\widetilde{W}^+$ and $\widetilde{W}^-$ form the charginos $\widetilde{\chi}_1^\pm$ and $\widetilde{\chi}_2^\pm$. Neutralinos and charginos are often referred to as electroweakinos or eweakinos, representing the supersymmetric extension of the electroweak sector of the SM.
Table 2.7 lists the particle content of the MSSM, grouped into mass eigenstates with positive R-parity, these are the SM particles and their R-parity negative SUSY partners.

Names	*mass eigenstates* ($P_R = +1$)	*spin*	*mass eigenstates* ($P_R = -1$)	*spin*
quarks, squarks	$u_{L,R}$, $d_{L,R}$, $c_{L,R}$, $s_{L,R}$, $t_{L,R}$, $b_{L,R}$	$\frac{1}{2}$	$\widetilde{u}_{L,R}$, $\widetilde{d}_{L,R}$, $\widetilde{c}_{L,R}$, $\widetilde{s}_{L,R}$, $\widetilde{t}_{1,2}$, $\widetilde{b}_{1,2}$	0
leptons, sleptons	$e_{L,R}$, ν_{e_L}, $\mu_{L,R}$, ν_{μ_L}, $\tau_{L,R}$, ν_{τ_L}	$\frac{1}{2}$	$\widetilde{e}_{L,R}$, $\widetilde{\nu}_{e_L}$, $\widetilde{\mu}_{L,R}$, $\widetilde{\nu}_{\mu_L}$, $\widetilde{\tau}_{1,2}$, $\widetilde{\nu}_{\tau_L}$	0
gluons, gluinos	g^A	1	$\widetilde{g}^A$	$\frac{1}{2}$
bosons, eweakinos	h^0, H^0, A^0, $H^\pm$, $W^\pm$, Z^0	0, 1	$\tilde{\chi}_1^0$, $\tilde{\chi}_2^0$, $\tilde{\chi}_3^0$, $\tilde{\chi}_4^0$, $\tilde{\chi}_1^\pm$, $\tilde{\chi}_2^\pm$	$\frac{1}{2}$

Table 2.7: Summary of the particle spectrum in the MSSM, represented by R-parity positive and R-parity negative mass eigenstates.

The large number of free parameters introduced by the electroweak symmetry breaking can be reduced by applying experimental constraints, in particular CP-violating processes and flavour changing neutral currents are suppressed. The resulting model is called phenomenological Minimal Supersymmetric Model (pMSSM).
In order to stabilise the lightest Higgs mass at the experimentally obtained value of 125 GeV without introducing new sources of fine tuning, the mass spectrum of the SUSY particles is expected to extend down to the electroweak scale. A typical SUSY mass spectrum in a natural pMSSM scenario is shown in Figure 2.4.

2.2.2 Non-vanilla SUSY Models

The majority of searches for SUSY conducted by the ATLAS collaboration is based on the RPC MSSM. However, the existence of non-zero RPV couplings, given in Equation 2.29, is not disproved experimentally [35, 36].
Allowing one or several of the RPV couplings λ, λ' and λ'' to be non-zero, gives rise to decays of the LSP via the respective interactions in Equation 2.29. Depending on the strength of the coupling, the timescale of these decays can vary greatly. The resulting lifetime of the LSP, τ_{LSP}, additionally depends on the masses of the sfermions involved in the decay. In case of large RPV couplings, τ_{LSP} can become arbitrarily small, while for moderate coupling strength and a high sfermion mass scale, the LSP has a non-negligible lifetime, fundamentally changing the expected phenomenological implications of the theory.
In case of RPV models particular assumptions need to be made in order to avoid the decay of the proton, which is suppressed by imposing R-parity in RPC models, e.g. ensuring lepton number conservation is sufficient to satisfy proton stability bounds. An example of such considerations is called Minimal Flavour Violation (MFV) [37, 38], which essentially links all flavour and CP-violating

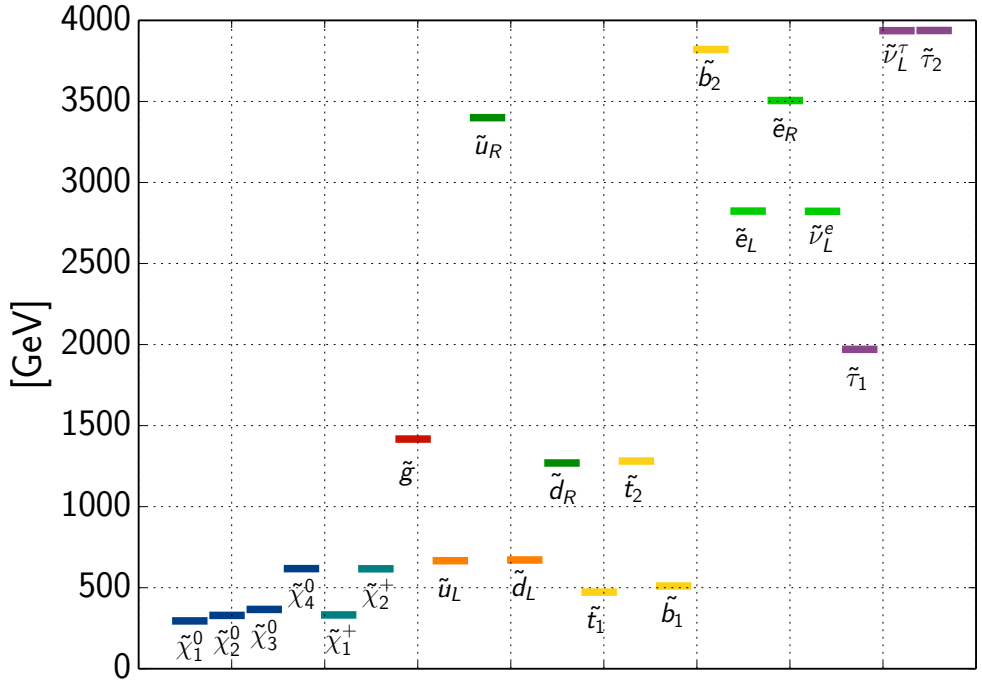

Figure 2.4: A typical low fine tuning pMSSM mass spectrum [34].

interactions present in the RPV model to the SM structure of the Yukawa couplings.
Abandoning the concept of naturalness, models can be constructed where the supersymmetry breaking not necessarily occurs at the electroweak scale. Such a model is *Split-SUSY* [39], where the symmetry breaking occurs at mass scales of the order of PeV. Hence, decays involving intermediate scalar particles, e.g. gluino decays via squarks, are suppressed. In this case, gluinos would have a non-negligible lifetime and hadronise with quarks and gluons resulting in composite states, called *R*-hadrons. The mass spectrum of such colourless bound states depends to a large extent on their composition, in particular they can be baryonic, mesonic or glueball-like [40]. Moreover, they can alter their composition as well as their charge, in case the gluino is sufficiently long-lived, thus strongly affecting the expected phenomenology at collider experiments.
A search dedicated to such non-vanilla SUSY models is presented in chapter 7.

2.3 SUSY at the LHC

Supersymmetric particles might be produced in proton-proton (pp) collisions at the LHC, leading to distinct signatures in the ATLAS detector systems. The search for such signatures in different underlying supersymmetric scenarios is the subject of this thesis. Thus, the production and decay mechanisms of sparticles, in particular in the RPC MSSM, are described in the following.

2.3.1 Production of Sparticles

At a hadron collider such as the LHC, the production of SUSY particles is dominated by the strong interaction, resulting in a larger production cross-section for strongly coupling sparticles than

for eweakinos and sleptons. Figure 2.5 shows these cross-sections for the coloured and for the electroweak sector, as they are used in many SUSY searches published by the ATLAS collaboration.

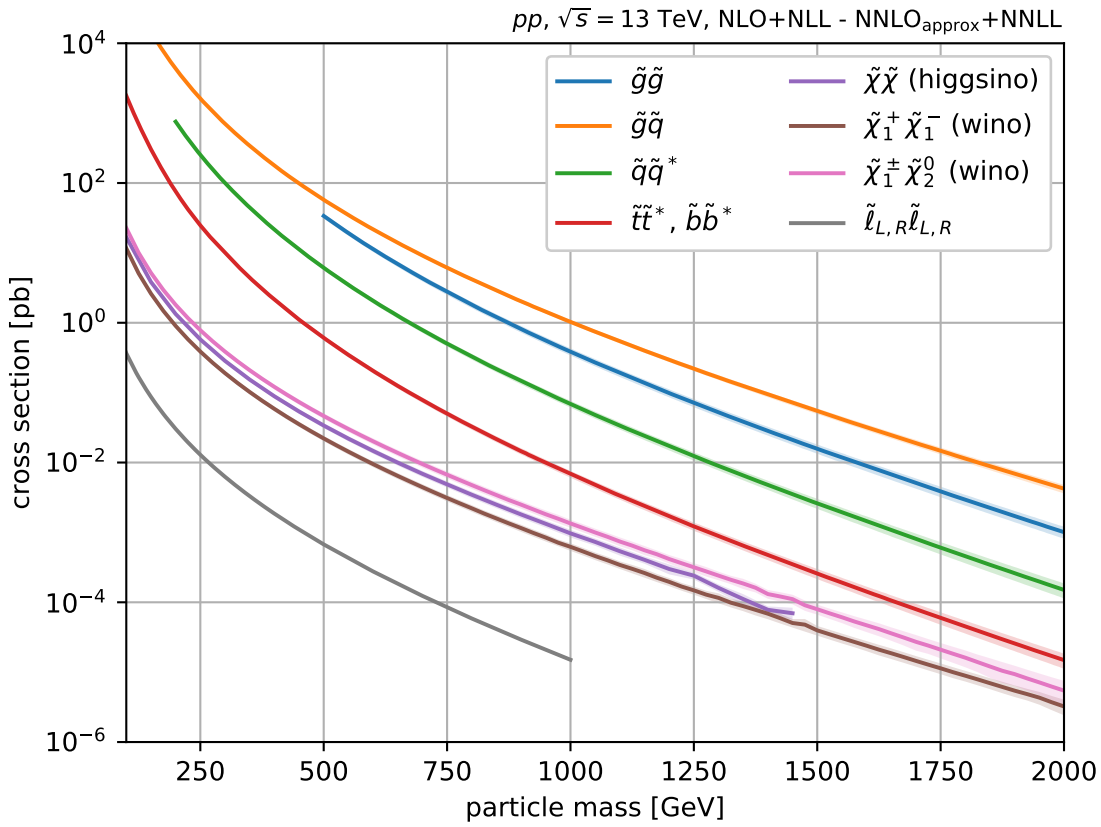

Figure 2.5: Comparison of the production cross-section of strongly and weakly coupling sparticles at $\sqrt{s} = 13$ TeV provided by the *LHC SUSY Cross Section Working Group* [41], computed at next-to-leading plus next-to-leading-logarithmic order in case of sleptons and eweakinos and using a next-to-next-to-leading approximation in the coloured sector.

The predominant production modes for sparticles underlying strong interactions in SUSY scenarios assuming RPC are listed in Equation 2.36 and depicted in Figure 2.6a. These processes are fully valid only for light-flavoured squarks. For third generation squarks ($\tilde{t}$ and $\tilde{b}$) on the other hand, production modes involving initial quarks (bottom row of Figure 2.6a) are heavily suppressed.

$$\begin{aligned} gg &\to \tilde{g}\tilde{g}, \tilde{q}\bar{\tilde{q}} \\ gq &\to \tilde{g}\tilde{q} \\ q\bar{q} &\to \tilde{g}\tilde{g}, \tilde{q}\bar{\tilde{q}} \\ qq &\to \tilde{q}\tilde{q} \end{aligned} \tag{2.36}$$

The second group of SUSY particles which can be produced at the LHC is comprised of weakly interacting sparticles, i.e. charginos, neutralinos and sleptons. Figure 2.6b shows the leading production modes for eweakinos via quark-antiquark annihilation. These production mechanisms as well as the production of charged and neutral sleptons are as follows:

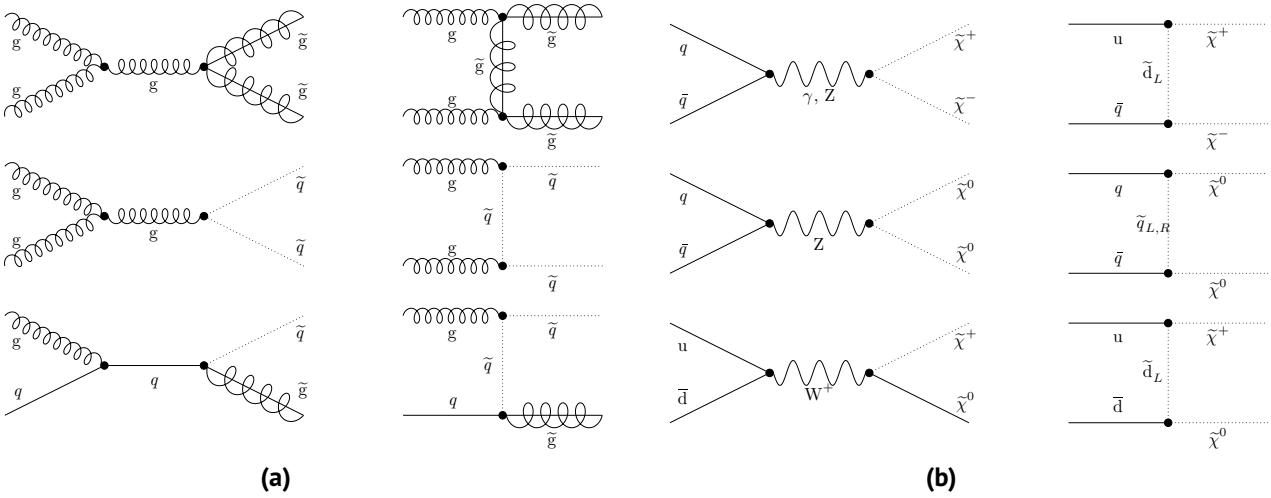

Figure 2.6: Feynman graphs describing s- and t-channel production for the main strong and electroweak supersymmetric production mechanisms at the LHC. Gluinos and squarks are mainly produced via gluon gluon and gluon quark fusion (Figure 2.6a), while quark-antiquark annihilation is dominant in case of chargino and neutralino production (Figure 2.6b).

$$
\begin{aligned}
q\bar{q} &\rightarrow \widetilde{\chi}^{\pm}\widetilde{\chi}^{\mp},\ \widetilde{\chi}^{0}_{2}\widetilde{\chi}^{0}_{2},\ \widetilde{\ell}^{\pm}\widetilde{\ell}^{\mp},\ \widetilde{\nu}_{L}\widetilde{\nu}_{L} \\
u\bar{d} &\rightarrow \widetilde{\chi}^{+}\widetilde{\chi}^{0}_{2},\ \widetilde{\ell}^{+}_{L}\widetilde{\nu}_{L} \\
d\bar{u} &\rightarrow \widetilde{\chi}^{-}\widetilde{\chi}^{0}_{2},\ \widetilde{\ell}^{-}_{L}\widetilde{\nu}_{L}
\end{aligned}
\tag{2.37}
$$

2.3.2 Decay Modes of Sparticles

SUSY particles are not stable, with the exception of the LSP in RPC scenarios, and will decay leading to distinct signatures. The possible decay channels depend on the nature of the decaying sparticle which may vary according to the underlying theoretical assumptions defining the respective scenario. This section gives a few examples of such processes.

For weakly interacting sparticles the branching ratios are mainly driven by the admixture of electroweak gaugino eigenstates ($\widetilde{W}^{\pm}$, $\widetilde{W}^{0}$ and $\widetilde{B}$) determining the coupling strength. Figure 2.7 depicts the main decay channels of charginos and neutralinos via on- or off-shell SM vector bosons or scalar fermions. In case of a dominant higgsino admixture, decays into third generation quark-squark pairs can be enhanced du to the large Yukawa coupling of the top quark to the neutral higgsino gauge eigenstate. The description of the nature and decay modes of eweakinos is crucial not only in searches dedicated to the electroweak SUSY sector but also in searches for coloured sparticles in scenarios assuming RPV or RPC models including cascade decays.

Figure 2.8 shows a selection of diagrams describing possible gluino decay modes. These processes, dictated by the strong interaction, depend mainly on the mass hierarchy in the coloured sector. In case the mass scale of the gluino and the squarks is of the same order of magnitude, on- and off-shell decays via intermediate squarks of all three generations, as summarised in Equation 2.38, are possible.

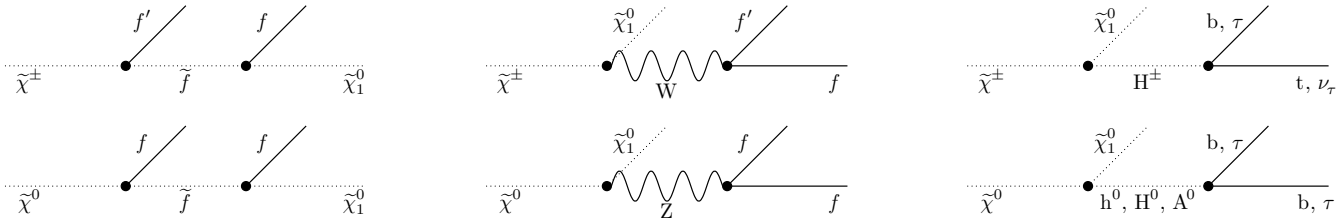

Figure 2.7: Main decay modes of neutralinos and charginos with the lightest neutralino as stable LSP. Sparticles undergo two or three body decays via intermediate on- or off-shell scalar or vector bosons. The fermions f and f' comprised in one $SU(2)$ multiplet can be leptons or quarks.

$$\begin{aligned} \widetilde{g} &\to \widetilde{q}^{(*)} q \\ \widetilde{g} &\to \widetilde{t}^{(*)} t \\ \widetilde{g} &\to \widetilde{b}^{(*)} b \end{aligned} \tag{2.38}$$

The subsequent decay of the intermediate (on- or off-shell) squark will result in possibly long and complicated cascade decays. However, there are supersymmetric scenarios, for instance split-SUSY mentioned above, where the mass difference between gluinos and squarks becomes large enough to effectively suppress the decay of the gluino.

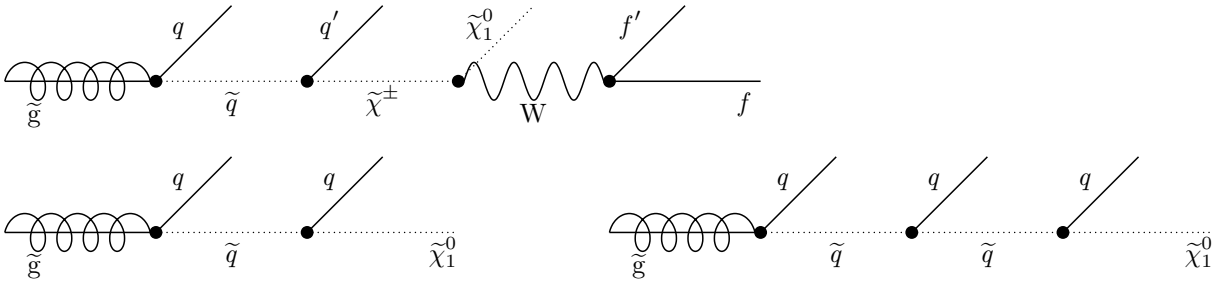

Figure 2.8: Example gluino decays via on- or off-shell squarks assuming the lightest neutralino to be the stable LSP.

The same principles apply if the squark is the initial sparticle, such that $\widetilde{q} \to \widetilde{\chi}^0 q$ and $\widetilde{q} \to \widetilde{\chi}^{\pm} q'$ are the dominant decays in the decoupling limit ($m_{\widetilde{g}} \gg m_{\widetilde{q}}$).

2.3.3 The Simplified Model Approach

Generally, a full BSM model like the MSSM or the pMSSM described in section 2.2, includes a large number of potential observables, e.g. a full mass spectrum of the sparticles listed in Table 2.7. In order to design a search for new physics based on particular final states predicted in the given BSM scenario, these observables have to be taken into account, as well as the kinematics and possible decay patterns. However, this procedure can be arbitrarily complex and the results of such an analysis would depend largely on the underlying theoretical model. Furthermore, modern high energy BSM searches make use of simulated signal and background processes, as detailed in chapter 4. The simulation of all possible signal processes included in a full BSM model is infeasible due to limited computational resources. Hence a strategy was developed, which allows to heavily

reduce the number of parameters taken into account. This technique is called the *simplified model approach* or Simplified Model Spectra (SMS) description [42].
Based on the fact that the phenomenologies predicted by a wide range of different BSM theories are very similar, SMS are used to decompose a full theoretical model. In particular in SUSY scenarios, the complicated and long decay chains, shown for instance in Figure 2.8, lead to very similar final states. This similarity gives rise to the idea, that the simplest process can be used to constrain general parameters of the underlying theory. Consequently, a simplified model is constructed by choosing a small set of sparticles which are assumed to be light, while all other SUSY particles are decoupled, i.e. their masses are set to values far above the energy scale probed by the underlying experiment. The branching ratio for one particular decay channel involving these light sparticles is set to 100 %. Hence, the number of signal events observed in the analysis is interpreted to originate solely from this decay. Results interpreted in such a way are less dependent on the underlying model assumptions, than in case of a full theoretical model. Therefore they can easily be applied to constrain different BSM scenarios (cf. chapter 7).
The SUSY searches presented in this thesis make use of simplified models, exemplified in Figure 2.9, describing strongly interacting sparticles predicted in different underlying SUSY models.

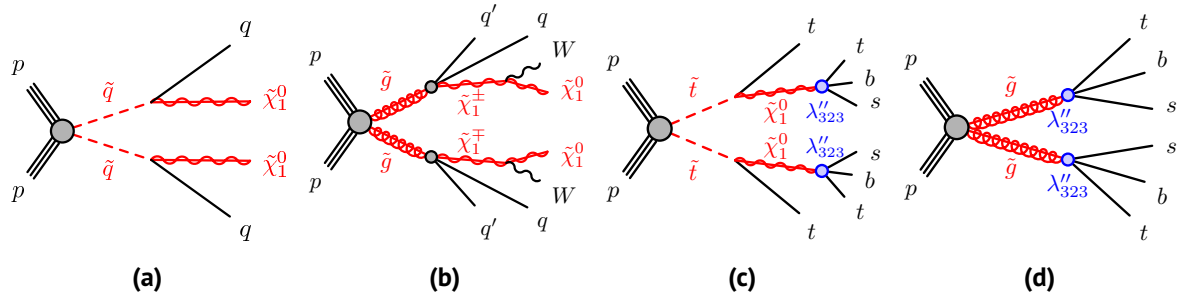

Figure 2.9: Examples of simplified model topologies describing strongly produced sparticles in an RPC scenario (Figure 2.9a, Figure 2.9b) and an RPV scenario assuming moderate (Figure 2.9c) and maximal (Figure 2.9d) baryon number violation.

3 The Large Hadron Collider and the ATLAS Detector

In order to conduct searches for new physics as presented in this thesis a large amount of pp collision data is needed. The pp collisions were produced at the LHC [43] and recorded by the ATLAS (A Toroidal LHC ApparatuS) detector experiment. This chapter gives an overview of these sophisticated machineries and their working principles.

3.1 The Large Hadron Collider

CERN (Conseil Européenne pour la Recherche Nucléaire), a leading institution for fundamental physics research, was founded in 1954. Its research facilities located near Geneva in Switzerland host amongst many other experiments the largest and most powerful hadron collider in the world, the LHC. It was built into the 27 km long tunnel about 100 m beneath the ground, originally constructed for the Large Electron Positron Collider (LEP) operating from 1989 until 2000 [44].
The LHC, a pp-collider, consists of two beam pipes encapsulating the two counter-rotating proton beams using superconducting magnets. The protons, hydrogen atoms stripped of their electrons by an electric field, need to be pre-accelerated before they can be injected as bunches into the LHC. This chain of pre-accelerator steps shown in Figure 3.1 pushes the proton energies to higher and higher levels as summarised in Table 3.1. Starting with the LINAC2, a linear accelerator, the particles acquire energies of roughly 50 MeV, before they are inserted into the Proton Synchrotron Booster and the subsequent Proton Synchrotron where the energy of the beam is increased to roughly 25 GeV. From there the protons are fed into the Super Proton Synchrotron gaining up to 450 GeV and eventually injected into the LHC's two beam pipes, where they are accelerated further reaching their peak energy of 3.5 and later 4 TeV in Run 1 (data taking between 2010 and 2012) and 6.5 TeV in Run 2 (between 2015 and 2018).

Accelerator	*Energy of the proton*
LINAC 2	50 MeV
Proton Synchrotron Booster (PSB)	1.4 GeV
Proton Synchrotron (PS)	25 GeV
Super Proton Synchrotron (SPS)	450 GeV

Table 3.1: The four pre-acceleration steps for the LHC and the respective proton energy reached in each step.

Each concentrated bunch of protons in the LHC consists of roughly 10^{11} protons travelling at almost the speed of light. These bunches collide at the four interaction points, where the main experiments ALICE [45], ATLAS [46], CMS [47], and LHCb [48] are located.

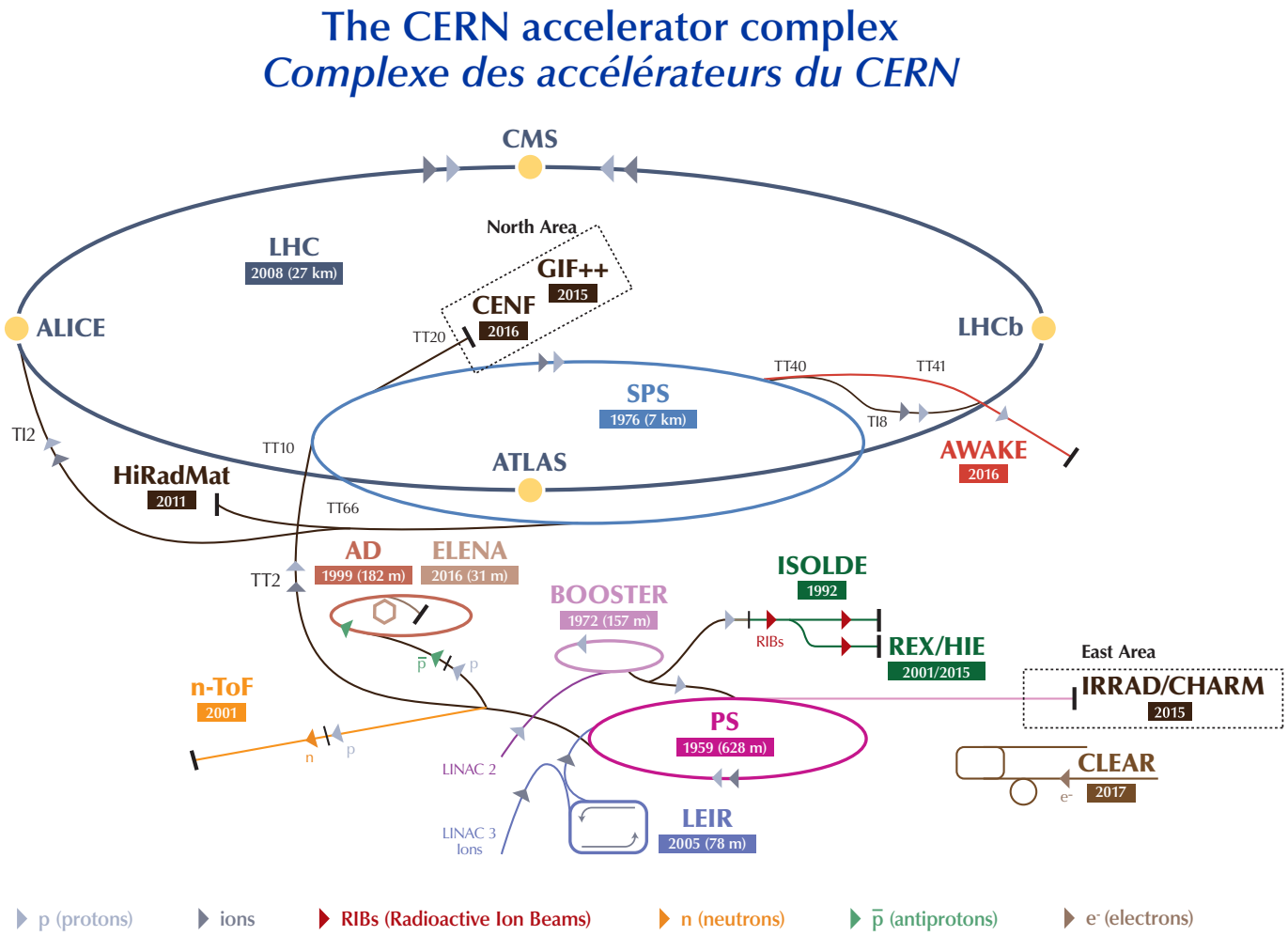

LHC - Large Hadron Collider // SPS - Super Proton Synchrotron // PS - Proton Synchrotron // AD - Antiproton Decelerator // CLEAR - CERN Linear Electron Accelerator for Research // AWAKE - Advanced WAKefield Experiment // ISOLDE - Isotope Separator OnLine // REX/HIE - Radioactive EXperiment/High Intensity and Energy ISOLDE // LEIR - Low Energy Ion Ring // LINAC - LINear ACcelerator // n-ToF - Neutrons Time Of Flight // HiRadMat - High-Radiation to Materials // CHARM - Cern High energy AcceleRator Mixed field facility // IRRAD - proton IRRADiation facility // GIF++ - Gamma Irradiation Facility // CENF - CErn Neutrino platForm

Figure 3.1: Schematic illustration of the whole accelerator complex at CERN. The protons (*p*) undergo the four pre-accelerating structures of the LHC: LINAC2, PSB, PS and SPS [49].

3.2 The ATLAS Experiment

Being one of the LHCs two multiple-purpose detectors, ATLAS was designed to investigate a wide range of SM and BSM physics. With a diameter of about 25 m, a length of about 44 m and a weight of 7000 tonnes ATLAS is by far the biggest high energy particle detector ever built. A sketch of the detector layout and its subsystems, positioned as layers around the interaction point (IP), is shown in Figure 3.2.

The combination of these subsystems allows for an inclusive measurement of the momentum and the energy of particles that is produced in a collision. In case of charged particles their trajectory is recorded additionally. The collision point represents the centre of the detector. It is surrounded by the innermost subsystem, the Inner Detector (ID) [50, 51], which consists of three layers of trackers. That are the Pixel Detector, the Semi-Conductor Tracker (SCT) and the Transition Radiation Tracker (TRT). The paths of the particles exiting the beam pipe and traversing the ID are bent by a solenoid magnet providing an axial magnetic field of 2 T located between the ID and the second subsystem, the calorimeter system. This system consists of a liquid argon high granularity electromagnetic calorimeter [52], followed by a scintillator-tile calorimeter [53] for measuring the energy of electromagnetic (EM) particles like electrons or photons and hadrons, respectively. The calorimeter is surrounded by the eponymous toroid magnet, which generates a magnetic field of 0.5 T in the central and 1 T in the forward regions. This field bends the track of charged particles which are not stopped inside the calorimeter[1] in the subsequent muon spectrometer (MS) [54], the outermost subsystem of ATLAS.

A more detailed description of these three subsystems as well as of the main detector variables is given below.

3.2.1 ATLAS' Coordinate System

In order to identify the particles produced in the pp collisions, their position inside the ATLAS detector needs to be determined. A cylindrical coordinate system best matches the detector geometry, where the origin is located at the nominal IP as sketched in Figure 3.3. The z-axis points along the beam pipe and (r, ϕ) are used in the perpendicular plane with ϕ being the azimuthal angle around and θ the polar angle with respect to this axis. The polar angle in this description is not invariant under Lorentz transformation in the z-direction. Therefore θ is conveniently substituted by the boost invariant *pseudo-rapidity*

$$\eta = -\ln\left[\tan\left(\frac{\theta}{2}\right)\right]. \tag{3.1}$$

The usage of η allows to define the Lorentz invariant angular separation between two given objects as

$$\Delta R \equiv \sqrt{(\Delta\eta)^2 + (\Delta\phi)^2}. \tag{3.2}$$

Due to the residual boost of the collision products in the beam direction, the projections of the

[1] these are ideally only muons

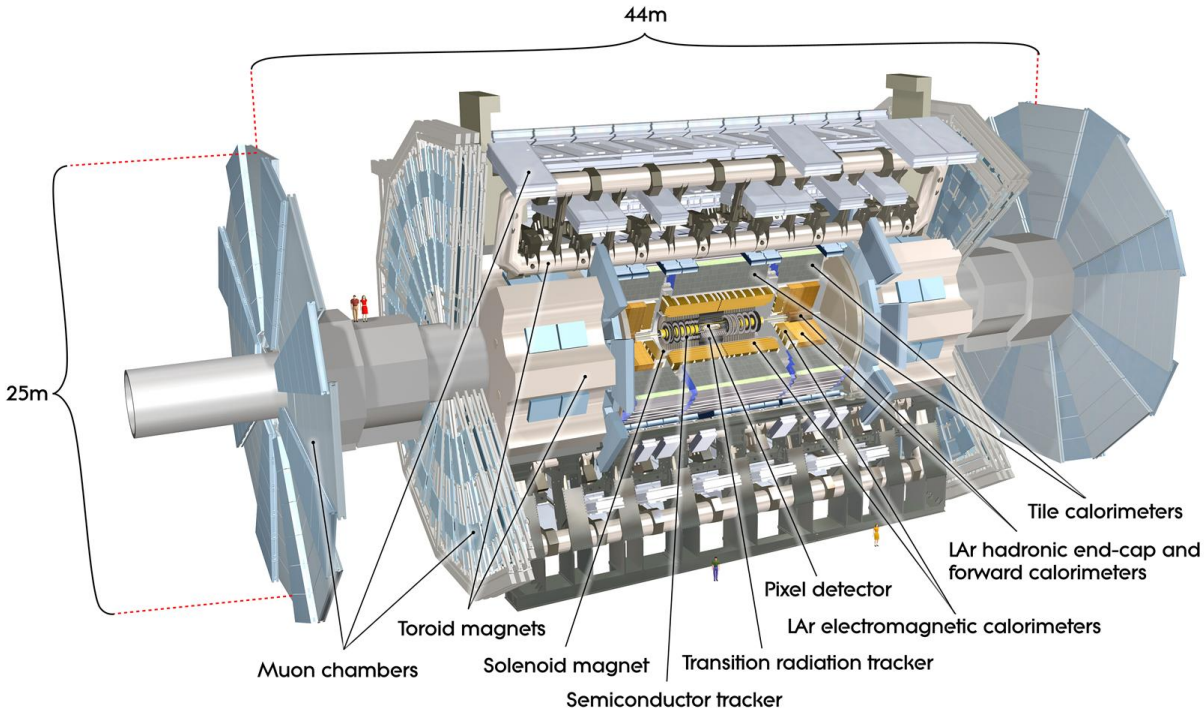

Figure 3.2: Scheme of the ATLAS detector [46].

particle momentum $\vec{p}$ and energy $\vec{E}$ onto the transversal $x-y$ plane, the transverse momentum p_T and energy E_T,

$$p_T = \sqrt{(p_x)^2+(p_y)^2} \quad \text{and} \quad E_T = \sqrt{(E_x)^2+(E_y)^2} \tag{3.3}$$

are used as kinematic variables rather than $\vec{p}$ and $\vec{E}$.

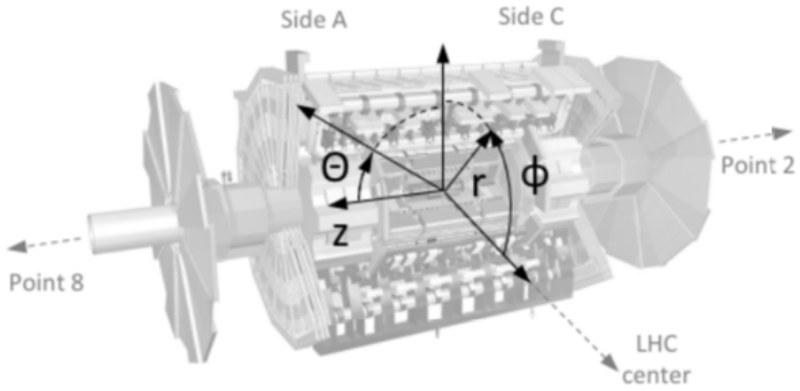

Figure 3.3: Scheme of the ATLAS coordinate system [55].

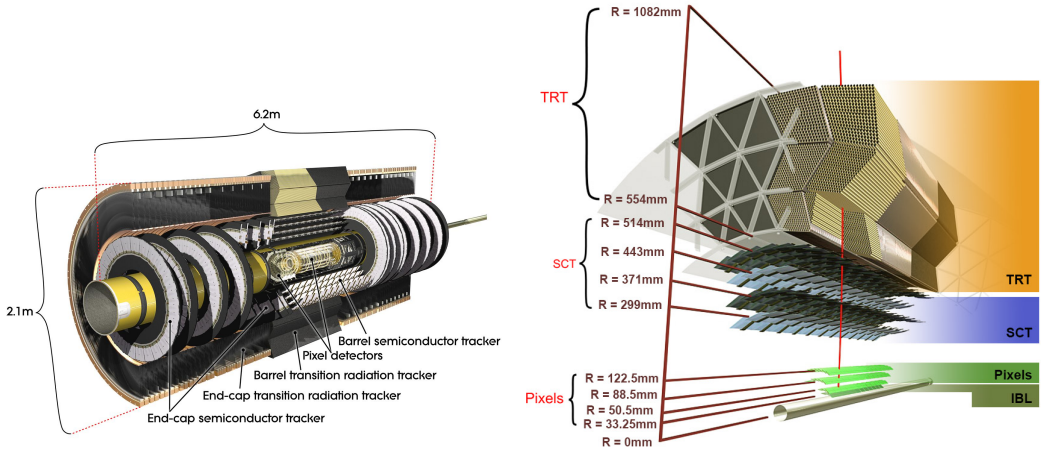

Figure 3.4: Scheme of the inner detector of ATLAS (left) and detailed view of the included subsystems (right) [56].

3.2.2 The Inner Detector

The innermost detector subsystem surrounding the beam pipe measures the charges and momenta of charged particles and allows to reconstruct their tracks as well as their track vertices. The technical layout of this 6.1 m long tracking system with a diameter of 2.1 m is shown in Figure 3.4a. The tracking system itself consists of several subsystems, thus covering a pseudo-rapidity range of $|\eta| \leq 2.5$ and providing an overall momentum resolution of about $\sigma_{p_T}/p_T \approx 0.05\%\ p_T \oplus 1\%$. A detailed overview of these subsystems - the Pixel Detector (including the insertable B-layer (IBL)), the SCT and the TRT - is shown in Figure 3.4b.

Pixel Detector and Insertable B-layer The Pixel Detector (Pixels) consists of three cylindrical layers of pixel sensors of about 250 µm $\times$ 50 µm $\times$ 400 µm. In order to improve the track reconstruction precision, as it is needed in particular for the identification of jets originating from B-hadrons (b-tagging), and to scope with the increased luminosity in Run 2, the IBL was installed between the Pixels and the beam pipe during the first long shut-down (LS1) of the LHC between Run 1 and Run 2. With its more than twelve million 250 µm $\times$ 50 µm pixels the IBL covers a pseudo-rapidity of up to $|\eta| = 2.9$.

SCT The layout of the SCT is very similar to the one of the Pixels, namely four cylindrical barrels surrounding the beam pipe equipped with silicon micro-strip sensors instead of pixel sensors. The barrels are completed by nine planar end-cap discs increasing the covered range of pseudo-rapidity from $|\eta| \leq 1.5$ to $|\eta| \leq 2.5$ with an area of about 63 m^2. The micro-strips are arranged tilted to one another such that an optimal resolution of the position of charged particles is achieved, thus allowing a very good reconstruction of the particle momentum.

TRT The outermost layer of the ID is the TRT, a combined straw tracker and transition radiation detector consisting of more than 300000 straw tubes of 4 mm diameter. These tubes are filled with

a gaseous mixture of 70% Xe, 27% CO_2 and 3% O_2. A thin gold-plated tungsten wire in the centre of the tube collects the ionisation charge generated by traversing particles. The TRT not only provides further tracking information of charged particles but also measures the transition radiation of these particles thus allowing to distinguish between electrons and charged hadrons. This is achieved by means of polymer fibres and foils placed between the tubes, causing electrons transitioning from one material to the other to radiate transition photons. These photons amplify the ionisation in the straw tubes allowing to identify the original particle passing through.

3.2.3 The Calorimeter System

Subsequent to the inner solenoid, surrounding the ID, follows the calorimetric system which covers a total range of pseudo-rapidity up to $|\eta| = 4.9$. A cutaway view of the two calorimetric sub-systems, the ElectroMagnetic Calorimeter (EMcal) and the Hadronic Calorimeter (Hcal), is shown in Figure 3.5. The EMcal and Hcal provide measurements of the energy deposited in the active detector material from EM and hadronic showers, respectively. Thus playing a vital role in the determination of particle energies and $E_{\mathrm{T}}^{\mathrm{miss}}$.

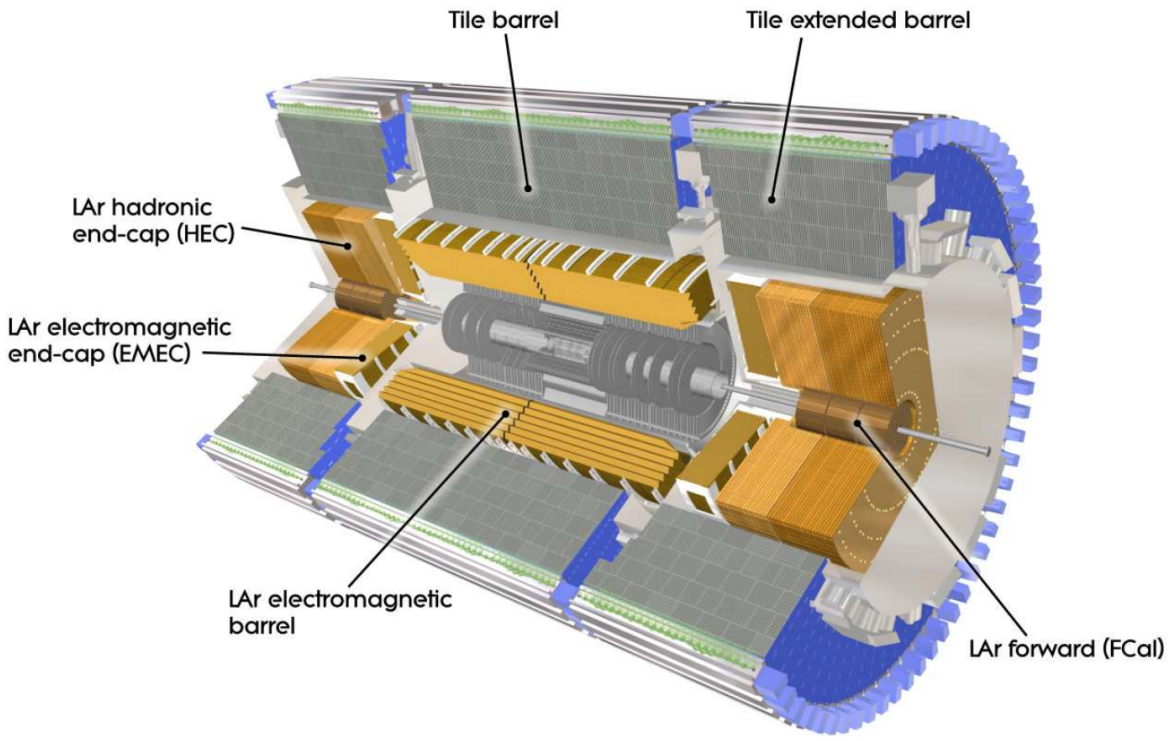

Figure 3.5: Scheme of the calorimeter system of ATLAS [46].

EMcal The inner part of the calorimetric system is a high-granularity liquid Argon (LAr) sampling calorimeter. It is composed of a barrel section and two end-caps each of which uses intermediate lead plates as absorbing material. Incoming electrons, positrons and photons will create an EM shower in the active material of the EMcal provided their energy exceeds a threshold of 1 GeV. This

active material, the LAr, is characterised by a large radiation length X_0, i.e. the length in which an EM particle is reduced to $1/e$ of its original energy via Bremsstrahlung and pair-production. The region between the barrel and the end-caps ($1.37 \leq |\eta| \leq 1.52$), the so called "crack region" shows only limited performance and is therefore excluded in many analyses.
The barrel section has a thickness of about 22 X_0 and the end-caps of even 24 X_0 ensuring that EM showers are contained within the calorimeter. The EMcal provides a high energy resolution of about $\sigma_E/E \approx 10\% \sqrt{E} \oplus 0.7\%$.

Hcal Due to the average interaction length of hadronic showers being much larger than the one of EM showers, the Hcal is located outside the EMcal. It is vital for the measurement of energy and direction of *hadronic jets* created by the hadronisation of quarks and gluons and the reconstruction of $E_{\mathrm{T}}^{\mathrm{miss}}$, as is described in greater detail in chapter 5. The Hcal comprises three parts in order to cover the total range of pseudo-rapidity:

- The barrel section is covered by the *Tile Barrel* ($|\eta| \leq 1.0$) and the *Tile Extended Barrel* ($0.8 \leq |\eta| \leq 1.7$) using plastic scintillators as active material and steel as absorbing medium forming an accordion-shaped sandwich calorimeter. It consists of three layers with a granularity of $\Delta\eta \times \Delta\phi = 0.1 \times 0.1$ in the first two and $\Delta\eta \times \Delta\phi = 0.2 \times 0.1$ in the last layer.
- Intermediate values of pseudo-rapidity between 1.5 and 3.1 are covered by the *LAr Hadronic EndCap (HEC)* in which the steel-interlayers are replaced with copper. The granularity is the same as in the first two layers of the barrel for small values of pseudo-rapidity but only half as fine for $|\eta| \geq 2.5$.
- In the very forward region ($3.1 \leq |\eta| \leq 4.9$) the *LAr Forward Calorimeter (FCal)* relies on tungsten as absorbing material. This specific sub-system is also sensitive to EM showers.

While the energy resolution in the barrel and the end-caps is about $\sigma_E/E \approx 50\% \sqrt{E} \oplus 3\%$, it is only $\sigma_E/E \approx 100\% \sqrt{E} \oplus 10\%$ in the forward region.
The construction principle of the Hcal provides a coverage of more than 10 X_0 such that hadronic showers up to very high energies are contained entirely within the Hcal. A passive layer of brass completing the outside of the FCal further minimises the number of hadronic particles escaping the calorimeter and contaminating the muon system ("punch-through").

3.2.4 The Muon System

The technical design of ATLAS' MS is shown in Figure 3.6 designating all four types of gaseous detector systems and their position within the MS. The basic shape is again a barrel region and a number of end cap discs covering a pseudo-rapidity range of up to 2.7. Muons are not stopped by the inner detector systems, hence the MS is the outermost part of ATLAS.
The barrel layers embrace the toroid magnet bending the tracks of charged particles in order to measure their momentum. In addition three vertical wheels build the end caps of the MS. The innermost disc is the *small wheel* with a diameter of about 10 m, followed by the so called *big wheel* (23 m) and completed by the *outer wheel*, the biggest of the three with a diameter of 25 m.

With its volume of about 20 000 m^3 the MS builds up almost 90% of the total volume of ATLAS. These large dimensions are essential for the precise measurement of the muon tracks. The overall momentum resolution σ_{p_T}/p_T for soft muons (p_T below 200 GeV) lies around 2-4% and drops with increased p_T to 10% at the upper threshold of p_T = 1 TeV.
Different types of chamber technologies are used in the MS: Monitored Drift Tubes (MDT) and Cathode Strip Chambers (CSC) provide tracking information and Resistive Plate Chambers (RPC) as well as Thin Gap Chambers (TGC) are used as muon trigger.

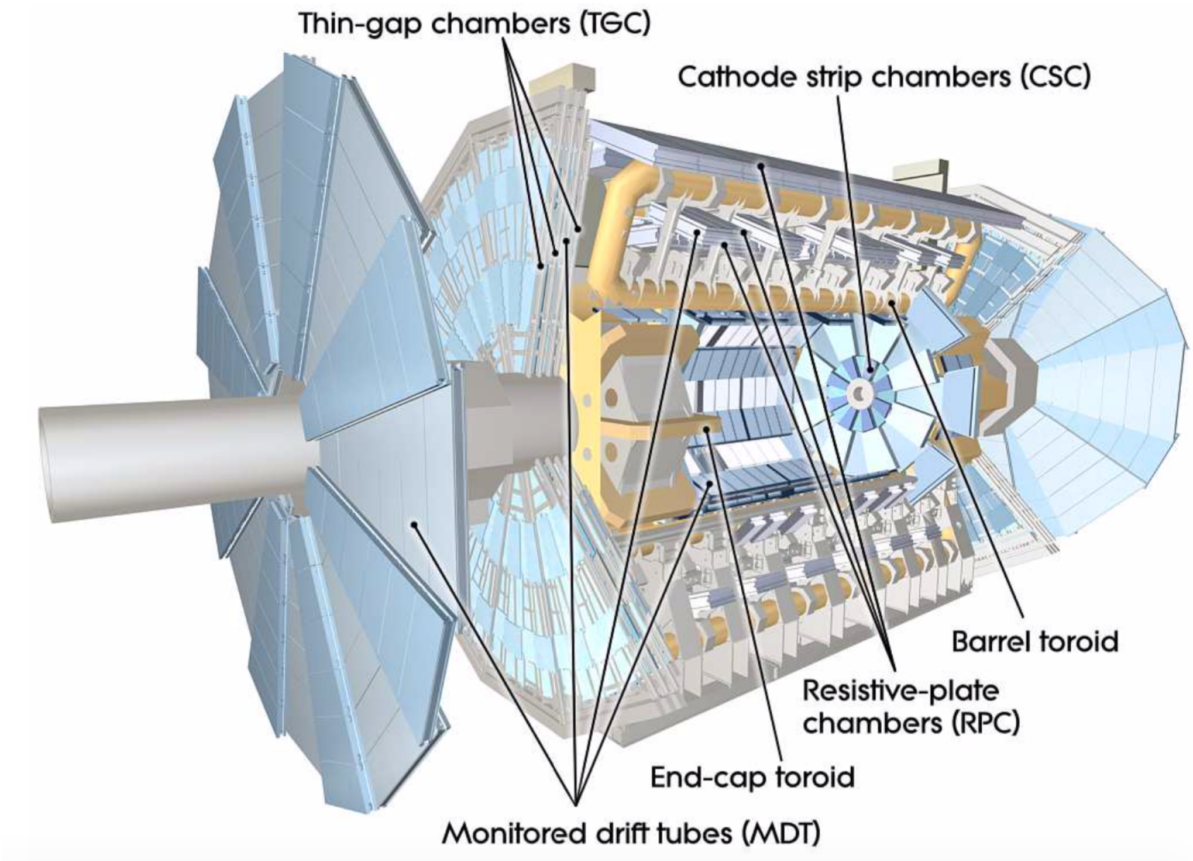

Figure 3.6: Scheme of the muon system of ATLAS [46].

3.2.5 The Trigger System

The trigger system [57], composed of a hardware based and a software based trigger is needed in order to reduced the rate of events to a recordable level. This event rate amounts to a total of 1 GHz if the LHC runs at its designed performance[2]. However, most of these events are of no or only limited interest for physics analysis and thus are discarded. An overview of the trigger system as used in Run 2 is given in Figure 3.7.
The first stage is the hardware based Level 1 (L1) using information delivered by the calorimeters and the MS. The L1 decides within 2.5 µs on "regions of interest (ROIs)" reducing the rate to about

[2] expected 40 millions of bunch crossings inside ATLAS per second, each with 20 collisions on average

100 kHz. These ROIs are fed into the software based second level, the High Level Trigger (HLT), which sorts events based on possible *physics objects* present in the ROI. The naming schema of the HLTs refers to the respective object they trigger on, e.g. HLT_xeXX triggering on $E_{\mathrm{T}}^{\mathrm{miss}}$ or HLT_jXX requiring at least one jet, where XX refers to the p_{T} online threshold of the given object. A detailed description of the exact definition of these objects and how they are reconstructed is given in chapter 5.

In order to reduce the rate further to about 1 kHz not every single event selected by the fast algorithms of the HLT can be recorded. This is true in particular for so called "soft objects", i.e. physics objects with a low p_{T} which are produced very frequently. L1 triggers as well as HLTs targeting these soft objects are "prescaled" where the prescale factor corresponds to the fraction of events that are actually recorded[3].

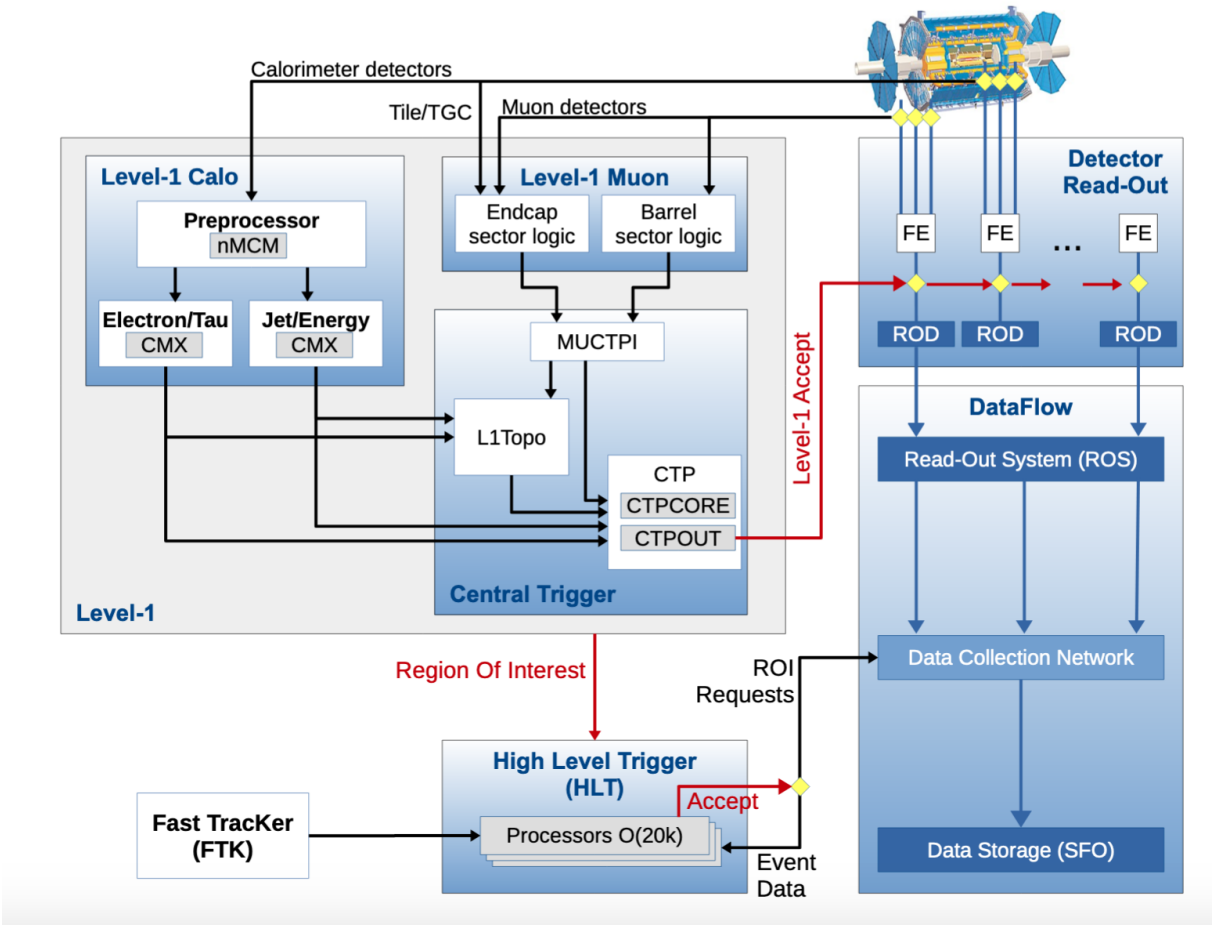

Figure 3.7: Scheme of the trigger system of ATLAS used in Run 2 [57].

[3] if only 1 in 100 events triggering the respective HLT is recorded, this trigger is said to be prescaled by a factor of 100

4 Hadron Collider Phenomenology

A deeper understanding of the processes taking place in a collider like the LHC is necessary to analyse and interpret pp collision data. The fundamental principles of the phenomenology of these elastic and inelastic scatter processes are explained in this chapter, followed by a more detailed description of event and detector simulation, in particular in the context of searches for SUSY as they are conducted at the LHC.

4.1 Particle Production in Hadronic Collisions

When two counter circulating beams at the LHC are brought to collision in one of the four experiments, two bunches of protons overlap in the so called "bunch crossing" giving rise to elastic and inelastic scattering. New particles are produced in inelastic or hard scatter processes with a rate determined by the cross-section of the respective production process and the LHC's luminosity, as described below.

4.1.1 Luminosity

The performance of the LHC is measured by the number of instantaneous collisions that can be used for physics analysis. This quantity is conveniently characterise using the *luminosity* $\mathcal{L}$ or *integrated luminosity* L which is given by a set of beam parameters:

$$L = \int \mathcal{L} dt = f n \frac{N_1 N_2}{A} \tag{4.1}$$

where f is the revolution frequency, n is the number of bunches in each beam, N_1 and N_2 are the numbers of protons in each bunch and A denotes the crossing area of the two beams which is related to the normalised beam emittance and the β function at the IP.
$\mathcal{L}$ allows to derive the expected rate of events $R_{process}$ for a give process with a cross-section $\sigma_{process}$ as

$$R_{process} = \frac{dN_{process}}{dt} = \mathcal{L}\sigma_{process}. \tag{4.2}$$

The overall luminosity delivered by the LHC and recorded by ATLAS in Run 1 and Run 2 is shown in in Figure 4.1.

4.1.2 Hard Scattering and Parton Distribution

Following Equation 4.2 the precise measurement of the luminosity as well as the correct prediction of $\sigma_{process}$ is of significant importance in order to predict the expected production rate. This cross-section, given independently from the experimental setup as

$$\sigma_{process} = \int \frac{d\sigma}{d\Omega} d\Omega = \int \frac{1}{f} |M_{if}|^2 dQ \tag{4.3}$$

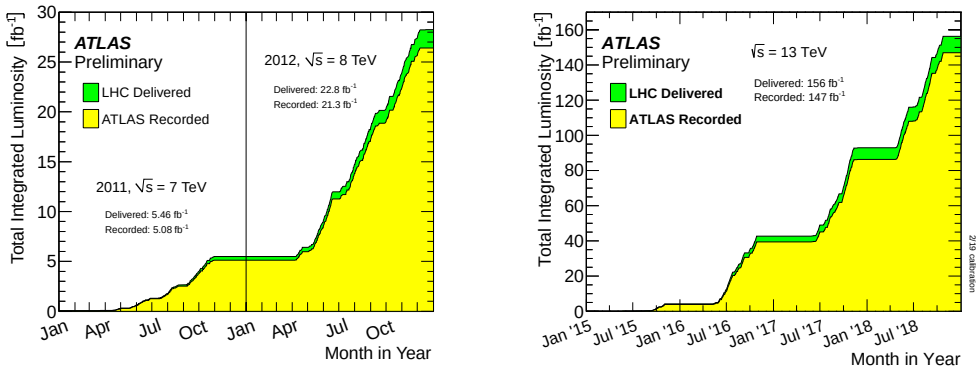

Figure 4.1: Total integrated luminosity as function of time delivered by the LHC (green), and recorded by ATLAS (yellow) during data taking in Run 1 (left) [58] and Run 2 (right) [59].

is defined solely by the scattering amplitude, that is the matrix element M_{if} between the initial (i) and the final (f) state of the process and the particle flux f in the given element of kinematic phase space dQ.

The difficulty in deriving the total cross-section for a hard scatter process at a hadron collider lies in the fact, that rather than being point-like particles, protons are compound states of so called partons, i.e. three valence quarks (two up and one down quark) as well as gluons and "sea quarks" that are created due to vacuum fluctuation. Since all these constituents are involved in the interaction, it is necessary to quantify their individual contribution.

The parton distribution function (PDF) $f_a(x, Q^2)$ gives the probability to find a parton of flavour a with a fraction x of the momentum of the proton in an interaction taking place at the energy scale Q. In order to calculate σ_{total} the parton level cross-section is convoluted with the respective PDF. The shapes of PDFs cannot be predicted from perturbative QCD calculations, due to the nature of the strong interaction strength α_s which is increasing at low energy scales. However, the *Factorisation Theorem* [60] allows to obtain the PDFs experimentally at a fixed scale. This theorem states that the cross-section of a given process can be factorised into a term describing the short-range interaction of the hard scatter (calculable perturbatively) and a term describing the long-distance interaction including infrared and collinear divergences. The latter is absorbed in the PDFs and is independent of the underlying scattering process. Hence, the PDFs can be measured by fitting data from experimental observables in different processes occurring for example in deep inelastic scattering in $e^{\pm}p$ or e^+e^- collisions. They can be extrapolated to the given energy scale Q^2 and ported to pp collisions [60–62], such that the total cross-section can be described as $\sigma_{total} = \sigma_{HardScatter} \times PDFs \times FragmentationFunction$.

Figure 4.2 shows a set of PDFs for gluons and the quark flavours $u, \bar{u}, d, \bar{d}$ and $s = \bar{s}$ for two different energy scales.

4.1.3 Event and Detector Simulation

The basic of every physics analysis is a profound knowledge and a reliable simulation of the involved SM and - in case of searches for new physics - of the expected BSM processes. Therefore, Monte Carlo (MC) simulation is used starting from the fundamental hard scatter which is basically described

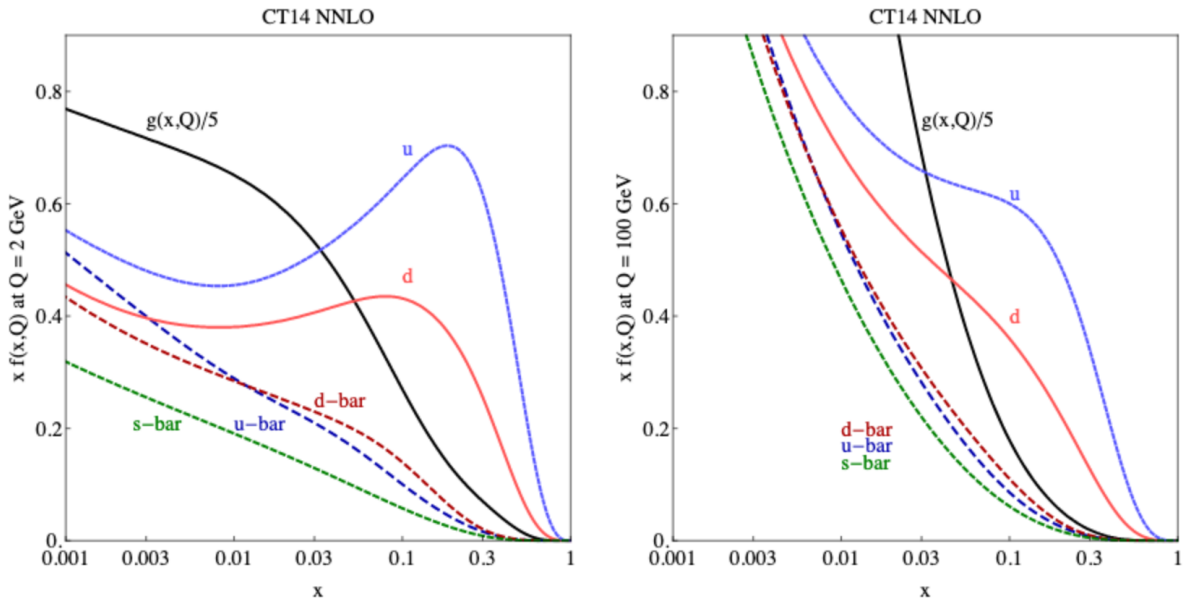

Figure 4.2: PDFs determined at two different energy scales (Q=2 GeV on the left and Q=100 GeV on the right) for gluons and various quark flavours [63].

by the given matrix element. In a next step the Parton Shower (PS) as well as the EM and hadronic showers are simulated. The last step in this simulation chain are the final decays and the detector response to the final state particles. A plethora of different algorithms, so called event generators, is available. Searches for new physics usually combine several of these programs.
The full simulation chain as depicted in Figure 4.3 is described step by step in this section.

Hard Scatter The main interaction in a particle collision is the hard scatter in which new particles are produced. Its cross-section $\sigma_{HardScatter}$ is calculated perturbatively as an expansion series of the strong coupling α_s. Since tree-level precision or leading order (LO) proofed to be insufficient for many applications, the current state of the art is to include at least one-loop diagrams. These next-to-leading order (NLO) calculations include extra radiation and provide a fairly good description of the kinematics involved in the hard scatter.

Parton Showering A PS describes the fragmentation of partons produced in the main interaction. These particles are highly accelerated due to the large transfer of momentum in the hard scattering. The underlying principle of the simulation of PSs is the simulation of the branching of one external parton into two under local conservation of the four momentum and the flavour. There are two possible consequences of such a parton splitting:

- QCD radiation, the emission of a gluon or the production of a quark anti-quark pair, creates a hadronic shower.
- QED radiation, the creation of a lepton anti-lepton pair from photon radiation caused by scattered charges, is referred to as EM shower. These showers are smaller than the hadronic

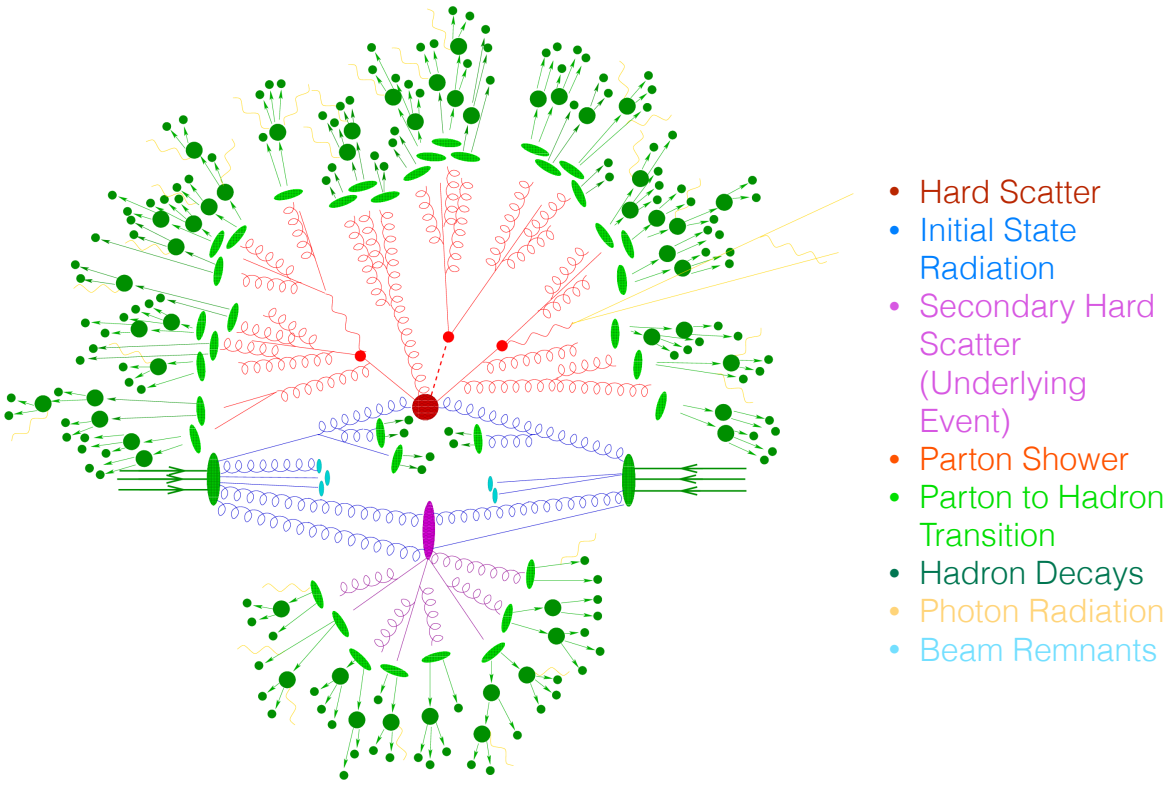

Figure 4.3: Illustration of the simulation of a pp collision as produced in a MC event generator [64].

ones since the photon, unlike the gluon, is not self-interacting.

The emission of a parton by the incoming parton before it takes part in the hard scatter is referred to as Initial State Radiation (ISR) and Final State Radiation (FSR) if it is radiated by a parton produced in the hard scatter.
The simulation of a PS starts at the main interaction and from there sequentially walks through the evolution of the splitting processes to lower and lower momentum until the cut-off scale is reached and the perturbative calculations break down. Thus, PSs can be seen as an approximation schema for higher order corrections of the hard scatter which can not be calculated.

Secondary Hard Scatter The rest of the hadronic activity in the collision, not accounted for in the hard scatter or ISR and FSR is often called the Underlying Event (UE). This secondary hard scatter comprises interactions such as re-scattering, multi-parton interaction and interactions involving the beam remnants. The UE activity of a pp collision can not be calculated and is simulated in many generators by tuning the simulation parameters to experimental data.

An additional undesirable contribution to the event structure is the so called *pile-up*, i.e. the overlap of multiple events, summarising the additional interactions occurring in the bunch-crossing (in-time pile-up) $\langle\mu\rangle$ and the presence of particles created in previous collisions (out-of-time pile-up). The

disturbing impact of pile-up depends largely on the luminosity as can be seen in Figure 4.4 which shows $\langle\mu\rangle$ as a function of the recorded luminosity for all data-taking periods in Run 2.

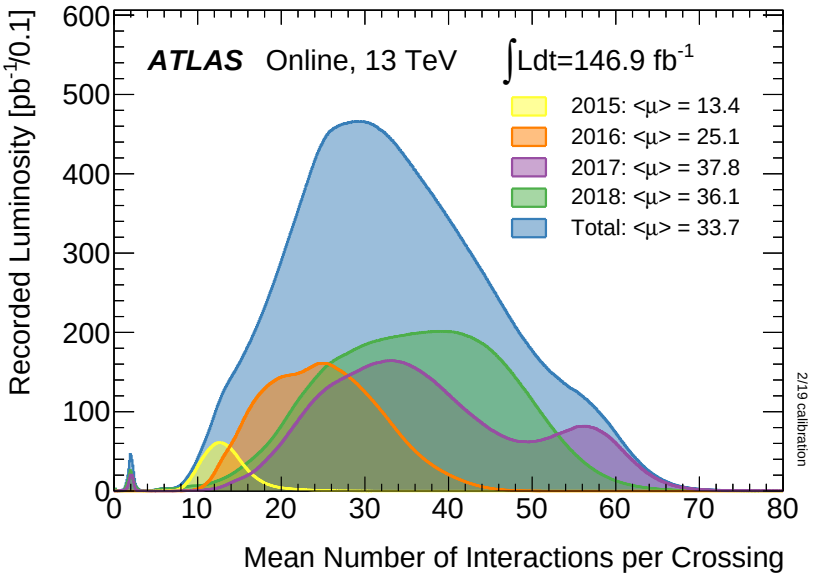

Figure 4.4: The average number of interactions per bunch-crossing $\langle\mu\rangle$ weighted with the respective luminosity for pp collision data collected at $\sqrt{s}$ = 13 TeV [65].

Parton to Hadron Transition When the showering reaches the cut-off scale the hadronisation process takes place. This formation of colourless bound-states is simulated using non-perturbative approaches.

- In the *cluster hadronisation model* [66] as it is used for instance in the generators HERWIG [67] and SHERPA [68], gluons split into quark anti-quark pairs. Nearby quarks are clustered to form hadrons, that further decay.
- The *Lund string model* [69] uses a linear effective potential in order to define the end of the iterative quark anti-quark pair splitting. This hadronisation model is used in the PYTHIA [70] event generator.

Independently of the method used, these algorithms provide an approximation of the hadronisation process, rather than an exact description. Thus, the results need to be tuned using experimental data.
Searches for new physics typically use a combination of different generators in order to model their SM background processes as well as their expected BSM signals. The 0L (2-6jets) SUSY analysis - described in great detail in chapter 6 - for example uses SHERPA2.2 [68] for the simulation of background processes including SM bosons (vector bosons plus jets and di-boson processes), POWHEG-BOX V2 [71] to describe top anti-top pair and single top processes and MADRAPH5 [72] for all signal SUSY processes.

Hadron Decay and Photon Radiation The hadrons produced in the condensation of the PS are mostly unstable and subsequently decay into stable particles like leptons. The characteristics of such stable final states, in particular the spin configuration and the mass, are in principle determined by the matrix element of the decay process but again need to be tuned using data from experiments. With the exception of the SHERPA program many of the generators used in BSM searches rely on the EVTGEN [73] algorithm to simulate this last step in the event generation chain.

Interaction with the Detector Material In order to use a simulated event in a physics analysis one last ingredient is needed: the response of the ATLAS detector systems to the final state particles created from the full simulation of an event. Within the ATLAS collaboration two different frameworks are used to simulate the interaction of the active detector material with the stable charged and neutral particles:

GEANT4 [74] includes a full reconstruction of the detector geometry and provides an accurate simulation of the response of the tracking and the calorimetric subsystem. Furthermore it takes into account not only the entire material in the detector but also the trigger system and the working condition of the readout electronics. This high level of accuracy comes at the price of an extended consumption of computational resources (CPU time, disc space, etc.).

ATLASFASTII [75] was developed to have a faster simulation of the detector response for processes where the high accuracy of GEANT4 is not needed. In particular it is used to produce MC samples to describe SUSY processes. The reduction in computing time is achieved by using a parametrised calorimeter response while fully simulating the ID and the MS based on GEANT4.

5 Analysis Tools

The recording of real collision data was detailed in chapter 3 and the generation of physics processes as well as the simulation of the detector response of major processes was described in chapter 4. Consequently these events - simulated and real ones - are passed through the same reconstruction software. This procedure ensures that the reconstructed physics objects used in the data analysis coming from real or simulated events are treated in the same way. Figure 5.1 gives an overview of the data processing needed to get from the data collected by the ATLAS detector (*raw data*) and the simulated detector response to events generated in a MC production, respectively, to the results published by searches as they are the subject of this thesis.

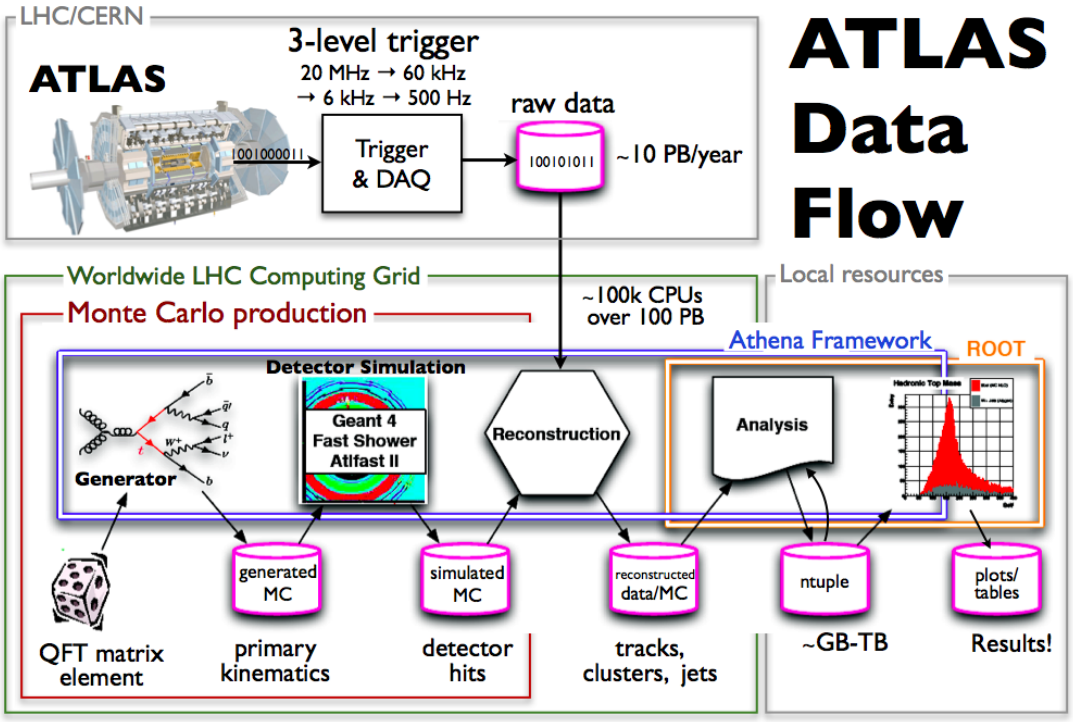

Figure 5.1: A schematic overview of the data flow for recorded collision data and simulation used by the ATLAS collaboration [76].

The main building blocks of such an analysis are not only the physics objects, which are the result of the reconstruction process, but also the systematic uncertainties these objects are afflicted with. Furthermore, the event information retrieved from the conversion of the detector response to such objects needs to be corrected against double counting, negative influence of detector effects and shortcomings of the simulation process. In order to allow for a consistent interpretation of the results found in an analysis, a set of standardised statistical tools and procedures is needed. This chapter describes the object reconstruction, the event corrections and the statistical interpretation of the analysis results as utilized in the analyses presented in this document.

5.1 Physics Object Reconstruction

The reconstruction of leptons, photons, jets and $E_{\mathrm{T}}^{\mathrm{miss}}$ as detector level objects exploits techniques and algorithms, which can differ greatly depending on the respective physics object. This section details the reconstruction of jets and $E_{\mathrm{T}}^{\mathrm{miss}}$ and discusses leptons and photons more briefly.

5.1.1 Tracks and Vertices

Charged particles traversing the ATLAS detector leave traces in the ID that can be reconstructed as tracks arising from one or more joint vertices. Although tracks and vertices themselves are not considered to be stand-alone physics objects, they form the basis for the reconstruction of jets and leptons.
The reconstruction of tracks combines hits in the different layers of the ID to build the most probable path of a particle produced in the IP using two complimentary approaches [77]:

Outside-In uses hits in the outer subsystem of the ID, the TRT, as seeds for track candidates and walks inwards through the subsequent layers adding hits in the silicon. This approach is used particularly for the reconstruction of tracks caused by secondary interactions or decays of particles with a non-negligible lifetime.

Inside-Out is the primary strategy of track finding. It starts from hits in the pixel detector, the innermost layer of the ID, and moves outwards.

In the presence of large pile-up, as was the case during Run 2 (cf. Figure 4.4), it is vital to resolve ambiguities between track candidates which share the same hits in the detector material. For this purpose an iterative procedure is used. A quality measure is assigned to each track which is based on the number of hits, holes (a missing hit where one is expected) and outliers (a hit where non is expected). If two track candidates share the same hit, the one with more holes and outliers is discarded.
The tracks that survive this procedure are extrapolated to the beam-axis in order to identify their centre of origin, that is their production vertex. Typically several such vertices are identified in a given event, one of which represents the initial pp collision. This Primary Vertex (PV) is characterised by the maximal sum of the squared transverse momenta of all tracks associated to this vertex.

5.1.2 Jets

Particles produced in the hard scatter process form collimated sprays of hadrons interacting with the detector material. These particle sprays are encapsulated in *jets*, hadronic physics objects with a well defined size, mass and energy. Several different approaches of jet definition, reconstruction and calibration are used by the collaborations of the LHC experiments. This section focuses on the technique most widely used by the ATLAS collaboration, the so called *EMtopo jets*.

Jet Reconstruction The reconstruction of EMtopo jets uses as input three dimensional, mass-less topological clusters of cells in the EMcal with an energy deposit exceeding a given threshold, referred to as topoclusters. These clusters, which are measured at the EM scale, are subjected to combinatoric principles forming a *jet reconstruction algorithm*.

Experimentalists and theorists alike should be able to use the same algorithm to mutually profit from each others work. Hence, such an algorithm needs to be easy to implement in experimental analyses as well as in theoretical calculations. It has to be valid at any order of perturbation theory, result in finite cross sections and be as insensitive to hadronisation as possible. In particular it has to be infrared and collinear (IRC) safe, i.e. the addition of a soft gluon or the radiation of a collinear parton should not change the result of the jet finding. The top row of Figure 5.2 shows an example for a jet reconstruction algorithm that is not infrared safe, while the bottom row depicts the violation of collinear safety.

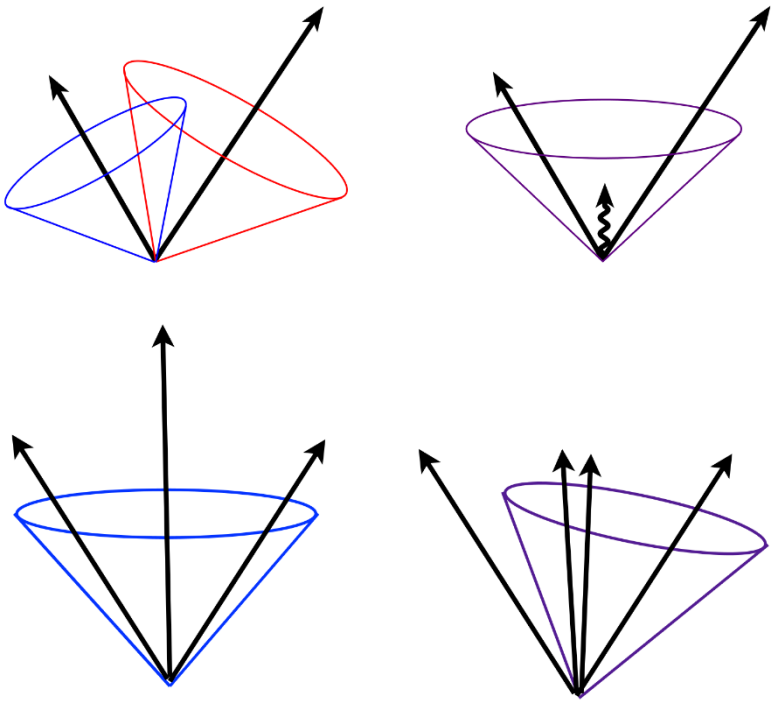

Figure 5.2: Examples for IRC violating jet reconstruction: soft emission of a parton changes the number of jets (top) and splitting of one parton changes the constituents of a jet (bottom) [78].

The algorithm of choice in the analyses described in this document is the anti-k_t algorithm [79] that is implemented in the software package FastJet [80]. The anti-k_t algorithm is based on a pairwise recombination of topoclusters using the distance of a given cluster to the beam-axis d_{iB} and the relative distance of two such clusters

$$d_{ij} = min(k_{ti}^{2p}, k_{tj}^{2p}) \times \frac{\Delta R_{ij}^2}{R^2} \quad \text{with} \quad \Delta R_{ij}^2 = (y_i - y_j)^2 + (\Phi_i - \Phi_j)^2 \quad \text{and} \quad d_{iB} = k_{ti}^{2p} \tag{5.1}$$

where k_{ti} denotes the transverse momentum of the particle. The parameter R defines the cone size

of the resulting jet and the parameter p is set to -1 to ensure that the algorithm starts from the objects with the largest momentum. In case $d_{ij} < d_{iB}$ the 4-vectors of the two clusters i and j are combined, otherwise the topocluster i is taken as new jet candidate. This process is repeated until all topoclusters are combined to jet candidates, leading to well defined circular shaped jet cones clustered around the hardest objects in the event, as can be seen in Figure 5.3.

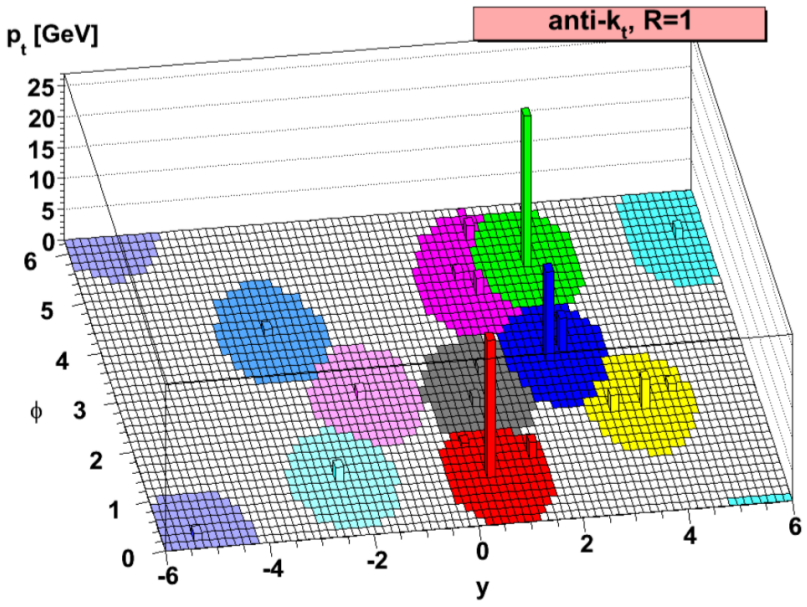

Figure 5.3: Example for jet reconstruction with the anti-k_t algorithm using a simulated parton-level event with additional soft activity [79].

In order to suppress hadronic contributions from pile-up, the jet candidates are associated with reconstructed tracks from the PV. In Run 2 this is achieved using the so called "ghost association" [81] which treats tracks as infinitesimal small four-vectors associated to the jet. Jets are then subjected to a multivariate approach, the Jet Vertex Tagger (JVT) calculating the likelihood that a given jet comes from the initial hard scatter using a set of track-based variables [82].

Jet Calibration Reconstructed EMtopo jets have four-vectors based on the energy measurement of the topoclusters at the EM scale. Thus, they need to be calibrated in order to define the jet energy and momentum at the particle scale. This procedure, the Jet Energy Scale (JES) calibration, includes several calibration and correction steps, which can be either MC based or rely on *in situ* methods. MC based techniques are used to correct the four-momentum of reconstructed jets to match simulated stable final state particles enclosed in *truth jets*, i.e. simulated particle level jets subjected to the same reconstruction algorithm as "real" detector level jets. Truth jets do not include neutrinos pile-up particles and muons, which can be misidentified as jets. This method allows to account for effects from pile-up, detector features and the reconstruction algorithm.
In situ methods, on the other hand, are used to derive residual corrections of the four-momentum from the difference of the detector response in data and simulation.
Figure 5.4 gives an overview of the full sequence of jet calibration steps applied to EMtopo jets:

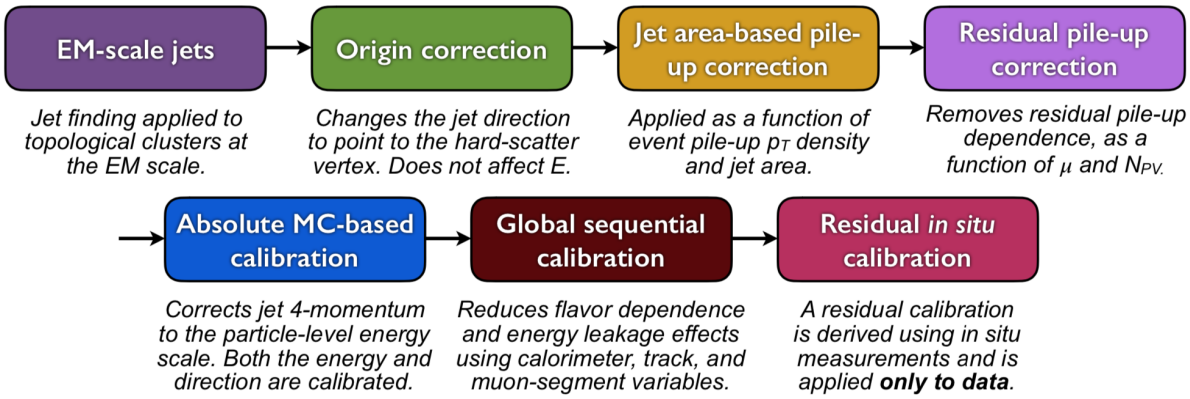

Figure 5.4: Full jet calibration sequence applied on EMtopo jets [83].

Origin Correction: The direction of the jet is altered to point back at the PV rather than the centre of the detector. This calibration step improves the η-resolution of the jets but keeps the jet energy unchanged.

Pile-up Corrections: There are two subsequent steps applied to reduce the contributions from pile-up. The contribution to the transverse momentum of each jet is removed event-per-event using the area based p_T density of each jet in the $\eta - \Phi$ plane [81]. In order to correctly cover the pile-up sensitivity in the forward direction, in particular for hard jets, a MC based residual correction is derived in the second step.

MC based Calibration: This is the main JES calibration step, that corrects the four-momentum of the reconstructed jets to the one from truth jets, which are assigned via a geometric matching procedure for isolated jets with a distance parameter ΔR = 0.3 A detailed description of this method, including the effects of the isolation and the calculation of the correction itself will be given in section 7.3. Additionally, the JES calibration corrects the pseudo-rapidity of the jets to account for a bias that is introduced by e.g. the transition between different calorimeter technologies or different calorimeter granularity.

Global Sequential Calibration (GSC): The GSC further improves the jet calibration by using additional information from the ID, the calorimeter system and the MS. This method covers dependencies of the JES on spatial features of the jet and the sensitivity of the response to the constituents of the jet as well as the energy distribution within a jet.

In situ Calibration: In a last step residual corrections are applied to data only. These are derived from energy ratios in well measured reference objects (e.g. γ + jets or Z + jets events) or measured in forward direction and in the central region (the so called η-intercalibration) as well as differences between the ratios in data and MC simulation.

b-Tagging The physics objects referred to as jets can be divided into subgroups according to their origin, e.g. jets from light quarks, gluon jets etc. among which the so called b-jets play a special role. These b-jets originate form the decay of b-hadrons with a lifetime of the order of 10^{-12} s. If

the p_T of such a particle is large enough it will travel a short distance before it decays creating a *Secondary Vertex (SV)*, as shown in Figure 5.5. PV and SV can be discriminated using the transverse impact parameter d_0 (the distance from the PV to the closest approach of the associated tracks in the R-Φ plane) and the longitudinal impact parameter z_0 (the z-coordinate of the point of closest approach).

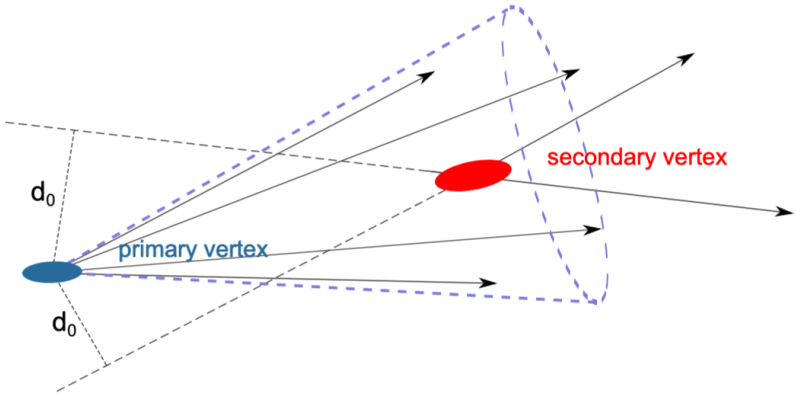

Figure 5.5: Schematic picture of vertex and track reconstruction in a jet originating from a b-hadron [84].

A standardised procedure is used in many analyses in order to identify b-jets, the so called *b-tagging*. It combines the output of three b-tagging algorithms - based on the significance of the impact parameter, the tagging of a secondary vertex and the identification of multiple vertices - in a neural network based multivariate analysis (MVA), the MV2c10 [85, 86].

5.1.3 Leptons and Photons

Electrons and positrons ($e^{\pm}$) as well as photons (γ) create EM showers which are measured in the EMcal as described in subsection 3.2.3. The reconstruction of these so called "E-Gamma physics objects" is based on the energy deposition in the EMcal. Leptons and photons are identified by the reconstruction of the EM shower associated with a track in the ID. This shower reconstruction is based on the clustering of calorimeter cells in the different layers of the EMcal, the so called "towers". A sliding-window algorithm [87] locates such a tower of EMcal cells, which is used as a seed to build a cluster of cells exceeding the given energy threshold. If tracks from the ID which have a pseudo-rapidity of $|\eta| < 2.47$ and lie within a distance of ΔR = 0.3 to the cluster are matched to this cluster, the reconstructed object is considered to be an electron (positron). Additional information from the SCT and the TRT can be used to further distinguish between $e^{\pm}$ and γ.
The reconstruction of muons (μ) relies on the tracks detected in the MS, described in subsection 3.2.4. Such muon candidates are further categorised according to the additional information from other detector subsystems.

- Combined muons (CB) are defined by tracks reconstructed in the MS in combination with tracks from the ID.

- Calorimeter-Tagged muons (CT) are based on the matching of reconstructed tracks from the ID to energy deposits in the calorimeter. Although CT have a low purity, they are useful in particular in the very central region ($|\eta| \approx 0$) to compensate the lack of instrumentation of the MS in this region.
- Extrapolated muons (ME) are complementary to the CT type since this type allows to reconstruct muons in the forward region ($2.5 < |\eta| < 2.7$) that is not covered by the ID. Thus the ME rely solely on the reconstruction of a track in the MS which can be extrapolated to the IP.
- Segment-Tagged muons (ST) are similar to CB but the reconstructed track in the ID can be matched to only one segmented track in the MS.

5.1.4 Missing Transverse Momentum

As already briefly discussed in chapter 2, the missing transverse momentum which is equivalent to the $E_{\mathrm{T}}^{\mathrm{miss}}$ is one of the key quantities in searches based on RPC supersymmetric scenarios. Since transverse momentum, i.e. the momentum in the plane transverse to the beam-axis is conserved in collider experiments, it is possible to identify the amount of energy that is "missing" due to the production of particles which only interact weakly, e.g. SM neutrinos or stable supersymmetric neutralinos.
Additional sources of $E_{\mathrm{T}}^{\mathrm{miss}}$ are miss reconstructed particles, beam-halo objects, detector inefficiencies, etc. The reconstruction of $E_{\mathrm{T}}^{\mathrm{miss}}$ makes use of all reconstructed and calibrated physics objects. Hence, the composition of $E_{\mathrm{T}}^{\mathrm{miss}}$ can be written as

$$E_{\mathrm{T}}^{\mathrm{miss}} = E_{\mathrm{T}}^{\mathrm{miss},\,\gamma} + E_{\mathrm{T}}^{\mathrm{miss,\,e}} + E_{\mathrm{T}}^{\mathrm{miss},\,\mu} + E_{\mathrm{T}}^{\mathrm{miss,\,jets}} + E_{\mathrm{T}}^{\mathrm{miss,\,soft}} \tag{5.2}$$

The last term of Equation 5.2 $E_{\mathrm{T}}^{\mathrm{miss,\,soft}}$ is estimated from unmatched tracks which are associated with the PV, the so called Track Based Soft Term (TST) [88].

5.2 Event Corrections

A reconstructed event, composed of the physics objects described in section 5.1, generally does not accurately describe the actual physics of the collision but includes many different unfavourable effects, e.g. overlap of the reconstructed objects, inaccuracies in the MC simulation, information from inefficiently working areas of the detector or different trigger prescale factors. In order to correct the reconstructed events for these effects a number of modifications is applied onto the physics objects and the reconstructed event.

5.2.1 Quality Criteria and Overlap Removal

As described in the previous section the methods used to reconstruct various physics objects are based on the same or at least very similar information from the detector sub-systems. Hence, it is crucial to resolve any possible ambiguities between these objects in order to avoid double counting.

Additionally, these reconstruction techniques might lead to incompletely or mis-reconstructed objects which need to be removed. Thus, physics objects are required to fulfil certain quality criteria. These requirements are individually adapted by a given analysis and are exemplified in this section by means of the 0L (2-6jets) SUSY analysis discussed in detail in chapter 6.

Jets The quality criteria for jets are described in detail in [89]. In order to reject jets reconstructed from detector noise or non-collision background, events are removed if jets fail to satisfy the *"LooseBad"* criteria or if at least one of the two leading jets in the event does not fulfil the *"TightBad"* criteria.

Leptons Two different lepton categories are used in the 0L (2-6jets) SUSY analysis. *Baseline leptons* are used to place a lepton veto to select events potentially including signal processes and *high purity leptons* are used to define selections dedicated to cover particular SM background processes, as detailed in section 6.2.

baseline leptons: The reconstruction of baseline muons relies on the information from the MS and the ID [90], in particular CB and ME muon categories are used. Baseline electrons, on the other hand, are reconstructed from isolated energy deposits in the EMcal which can be matched to one track using a loose likelihood based identification [91].

high purity leptons: Requirements are placed on the significance of the transverse impact parameter and the longitudinal impact parameter defined in Equation 5.3, where the threshold x is 3 (5) for high purity muons (electrons) and y is 0.5 mm. In addition a set of η- and p_{T}-dependent isolation criteria which rely on tracking variables and calorimeter based variables are applied. In particular, muons must satisfy the "FCTight" isolation requirements [90] and electrons the "Tight" selection criteria [91].

$$\frac{|d_0^{PV}|}{\sigma(d_0^{PV})} < x \quad \text{and} \quad |z_0^{PV} sin\Theta| < y \tag{5.3}$$

Overlap Removal Ambiguities between physics objects, e.g. between a jet and an electron reconstructed from the same track and energy deposits in the calorimeter system, are resolved by a standardised procedure based on the distance parameter ΔR.

- If a jet lies within a distance of ΔR = 0.2 to a baseline electron, the electron is kept and the jet discarded.
- In case the distance between a lepton and a jet that passes the JVT lies between ΔR = 0.2 and ΔR = min(0.4, 0.04 + 10 GeV/p_{T}^{ℓ}) the lepton is discarded.
- If a muon and a jet are found within ΔR = 0.2, the jet is removed if it has assigned less than three tracks with a p_{T} > 0.5 GeV. Otherwise the jet is kept and the muon removed.

- A track shared by an electron and a muon is interpreted as muon unless it is reconstructed as CT muon.

These basic rules of Overlap Removal (OR) are often tuned and completed by additional requirements to meet the individual needs of the respective analysis, as will be discussed in subsection 6.1.2.

5.2.2 Event Cleaning

An additional cleaning step is applied to events used in a physics analysis. This so called *event cleaning* includes a set of cuts which are designed to suppress undesired effects in particular from detector effects:

Good Run List (GRL): For each data taking period an official GRL is defined listing all recorded events which are of high enough quality to be used in a physics analysis, i.e. events with sufficient beam-quality and functionality of all detector systems.

Vertex cleaning: A valid event must contain at least one PV with more than 1 associated tracks.

Non-Collision Background (NCB) suppression: Events are removed if they contain fake jets, which originate from NCB, i.e. "halo muons" or noise bursts in the calorimetric systems, i.e. jets need to fulfil the quality criteria stated above.

Dead-Tile cleaning: Jets involving calorimeter cells which lie in mal-functioning or non-operating areas of the calorimeter are a possible source of fake $E_{\mathrm{T}}^{\mathrm{miss}}$. Events are removed if they include such jets aligned with the $E_{\mathrm{T}}^{\mathrm{miss}}$ ($\Delta\phi(j, E_{\mathrm{T}}^{\mathrm{miss}}) < 0.3$).

Negative-Energy cleaning: Another source of fake $E_{\mathrm{T}}^{\mathrm{miss}}$ are calorimeter cells with entries of negative energy due to data-corruption. Events including jets reconstructed from such cells are vetoed.

5.2.3 Reweighting the Simulation

In the beginning of this chapter it was explained, that recorded and simulated events are treated in the same way during the objects reconstruction and event cleaning steps, in order to make them indistinguishable from an analysis point of view. However, the weights of the simulated events need to be rescaled to correctly reflect the actual data-taking conditions.
Run 2 comprises three different data-taking periods each of which is characterised by the luminosity and the pile-up distribution. Table 5.1 summarises these periods, their luminosity as well as the respective MC production campaign. Simulating a large number of events for various different physics processes is computationally expansive and very time consuming. Thus, the MC samples were prepared in advance, before the actual data-taking conditions were known. Hence, the simulation needs to be scaled in order to reflect the correct pile-up distribution and luminosity observed in data. MC16a events are reweighted using the average number of interactions per bunch-crossing $\langle\mu\rangle$ while for MC16d and MC16e the actual pile-up distribution μ was used.

period	int. luminosity [fb^{-1}]	MC campaign
2015 + 2016	36.20	MC16a
2017	44.31	MC16d
2018	58.45	MC16e

Table 5.1: Summary of luminosities for the Run 2 data-taking periods with the corresponding MC production campaigns .

Additional scale factors account for effects like flavour tagging efficiencies, differences in the trigger efficiencies in data and MC or lepton reconstruction efficiencies.

5.3 Systematic Uncertainties

The calibration of physics objects as well as the cleaning and reweighting of simulated events partially uses *in situ* techniques which are based on measurements. Thus, the systematic uncertainties on the experimental quantities used in these methods need to be taken into account. Furthermore, MC simulation used in the calibration is afflicted with systematic uncertainties which also need to be accounted for.
The 1.7% uncertainty on the total Run 2 integrated luminosity of 139 fb^{-1} is one example, the uncertainties introduced by the reconstruction of leptons and photons are another. The biggest contributions to the overall experimental uncertainties in an all-hadronic BSM search, like the 0L (2-6jets) SUSY analysis, are the systematics arising from the calibration of jets, in particular the uncertainties on the Jet Energy Scale (JES) and the Jet Energy Resolution (JER).

5.3.1 Uncertainties on the Jet Energy Scale

The full calibration sequence, described in subsection 5.1.2, comprises several methods giving rise to a set of 80 different JES systematic uncertainties [83].
Figure 5.6 shows the combination of all these uncertainties (*total uncertanties*) for a subset of the full Run 2 data recorded from 2015 to 2017 as a function of the transverse momentum for central jets (η = 0.0) and as a function of the pseudo-rapidity for jets with p_T = 60 GeV. In addition, the contributions of the main uncertainty groups are shown:

Absolute in situ JES: The majority of the 80 individual uncertainties comes from *in situ* calibration steps based on reference objects. This group accounts for assumptions made in the event selection, the effects from MC simulation and the uncertainties propagated from the energy scales of reconstructed leptons and photons in the reference samples.

Relative in situ JES: These uncertainties arise from the η-intercalibration which is based on the p_T-balance of dijet events in certain areas of the detector. The uncertainties cover a possible

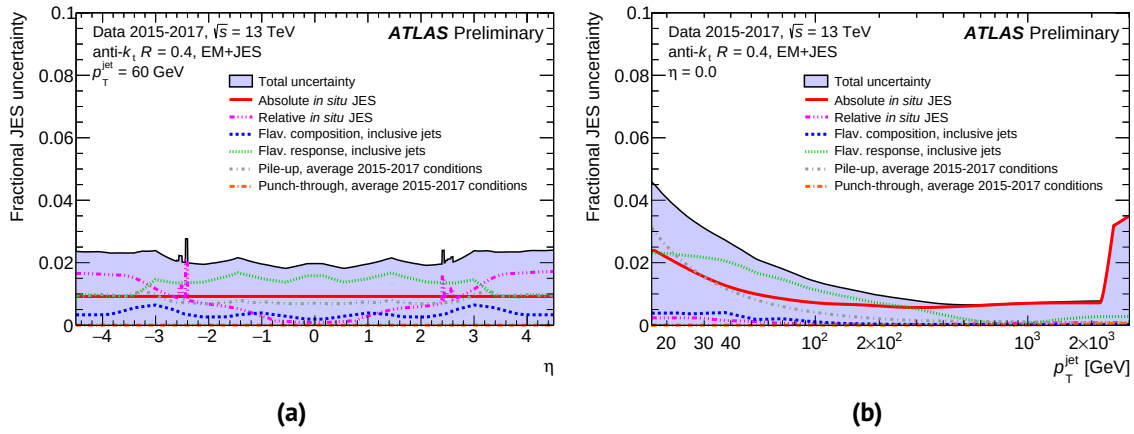

Figure 5.6: Combined uncertainties on the JES and the contribution from the individual subgroups described in [83] for the combined 2015-2017 dataset as a function of η for jets with a fixed p_T (Figure 5.6a) and as a function of the p_T for central jets only (Figure 5.6b) [92].

physics mismodelling of the dijet samples, statistical uncertainties and a non-closure of the calibration method observed in the region between η = 2.0 and η = 2.6.

Falvour composition: The relative amount of quark and gluon jets usually depends on the particular phase-space, probed by an analysis. Hence, this composition has to be derived individually or is assumed to be 50% gluons and 50% quarks with a conservative uncertainty of 100%.

Flavour response: The general jet reconstruction does not distinguish between jets seeded by light quarks, gluons or b-quarks all of which will differ in their jet response.

Pile-up: The pile-up uncertainties account for potential mismodeling of the pile-up distribution in MC simulation.

Punch-through: The GSC includes a correction for jets not fully contained in the calorimetric system leading to tracks in the MS, the punch-through jets. This correction is afflicted with an uncertainty based on the difference between the jet response in MC and data depending on the number of involved track segments in the MS.

Although the full set of 80 JES systematics gives the most accurate description of the total uncertainty on the JES it is difficult to implement in an actual analysis. Furthermore, the level of precision and detailed understanding of the JES systematics and their correlations provided by the full set, will not necessarily lead to an improvement of the analysis. The usual practice to simplify the application of JES uncertainties in the statistical interpretation of analysis results, is to make use of one of the various available reduction schemas which heavily reduce the number of individual JES uncertainties while seeking to preserve their η- and p_T-correlations.

5.3.2 Uncertainties on the Jet Energy Resolution

The reconstruction of jets is based on energy deposits in the calorimeters which have a finite granularity. Accordingly, the measurement of the calibrated jet energy is of finite resolution. The JER is reflected by the width of the response function, as will be described in greater detail in section 7.3. The jet response is studied by constructing

$$\mathcal{A} = \frac{p_{\mathrm{T}}^{probe} - p_{\mathrm{T}}^{ref}}{1/2(p_{\mathrm{T}}^{probe} + p_{\mathrm{T}}^{ref})}, \tag{5.4}$$

the p_{T}-asymmetry of dijet events in well calibrated regions of the detector (p_{T}^{ref}) and regions that should be probed (p_{T}^{probe}). The asymmetry function $\mathcal{A}$ gives a measure for the imbalance of the transverse momentum, which arises from differences in the detector response in different calorimeter regions. The width of this function

$$\sigma(\mathcal{A}) = \frac{\sqrt{\sigma(p_{\mathrm{T}}^{probe})^2 - \sigma(p_{\mathrm{T}}^{ref})^2}}{1/2\,(p_{\mathrm{T}}^{probe} + p_{\mathrm{T}}^{ref})} \tag{5.5}$$

is used to calculate the JER.

This method is afflicted with uncertainties covering the measurement of the jet response as well as the modelling of dijet events in MC, the assumptions in the selection of the dijet topologies and the effect of additional quark and gluon radiation. Figure 5.7 shows the uncertainties on the JER derived for the 2017 dataset.

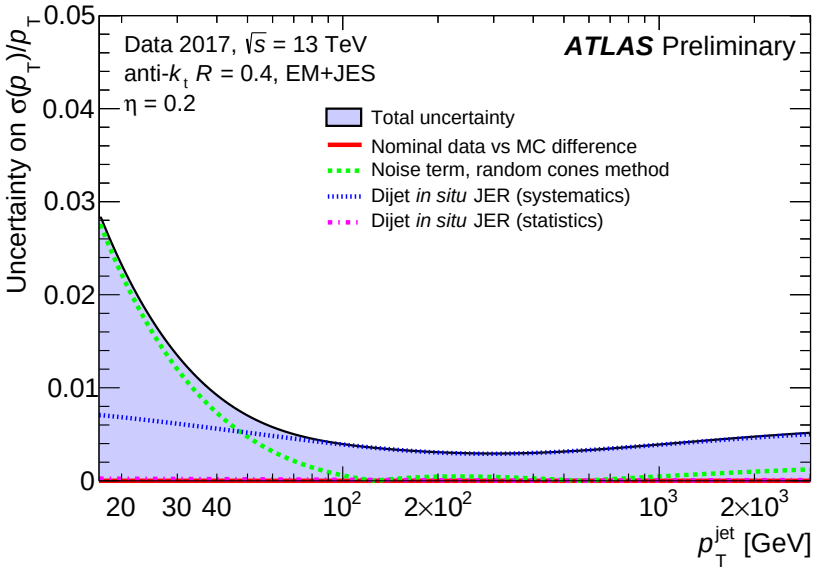

Figure 5.7: Combined uncertainties on JER and the contribution from the individual subgroups as a function of the p_{T} for central jets only, derived from the 2017 data-set [93].

5.4 Tools for Statistical Interpretation

The processing of collision data and simulated events depicted in Figure 5.1 was described above with the exception of the last step, the final results obtained from a data analysis. This section gives an overview of the main concepts typically used in searches for new physics.

5.4.1 Basic Analysis Procedure

The very basic of each BSM search is the counting of events which show a detector signature predicted in the BSM model that is searched for. The resulting event yield n_{obs} is then compared to the number of events expected from SM processes which form the background of the analysis. This background contribution cannot be measured in the region of phase-space expected to contain signal events from the hypothetical BSM process, the so called signal region (SR). Instead a region of phase-space is chosen for each background, the control region (CR), which is enriched with the respective SM process. The CR selections need to be kinematically close but orthogonal to their respective SR .
The event yield of each background in the respective CR (n_{SM}^{CR}) is obtained from fully data-driven methods or MC simulation normalised to the observed event count in the same region (n_{obs}^{CR}) using a "background-only" fit, as described in subsection 5.4.3. The normalised event yield is then extrapolated into the SR by means of a *transfer factor (TF)*

$$n_{SM}^{SR} = n_{SM}^{CR} \times \mathrm{TF}_{SM}. \tag{5.6}$$

The validity of the extrapolation is tested in regions of the phase-space which are kinematically close to the SRs as well but still expected to contain very few signal events, called validation region (VR). Ideally, the VRs are orthogonal to the SRs and the CRs.
The final comparison of the estimation of SM background yields in the SR (n_{SM}^{SR}) to the observed event counts (n_{obs}^{SR}) is then interpreted using common statistical techniques as described in the following.

5.4.2 Basic Statistical Concepts

In order to interpret the number of observed events in the context of a BSM search, two hypotheses are formulated:

H_0 the background-only hypothesis states that $n_{obs} = n_{SM}$

H_1 the alternative hypothesis assumes the existence of new physics $n_{obs} = n_{SM} + n_{BSM}$

Both hypotheses can be represented by a probability density function (PDF) $f_0(x)$ and $f_1(x)$, respectively.
In order to test H_0 a significance level α is computed which would be predefined in a formal theory but depends on the signal strength assumed in the alternative hypothesis in a real application. The

p-value that can be calculated from the PDF as

$$p_0 = \int_{x=n_{obs}}^{\infty} f_0(x)\, dx \tag{5.7}$$

conveys the probability to get a result at least as extreme as the observed one under the assumption that H_0 is true. This value can be translated into a measure for the significance of an observed deviation from the nominal prediction under H_0

$$p_0 = 1 - \Phi(\alpha) \tag{5.8}$$

using the cumulative Gaussian distribution

$$\Phi(\alpha) = \frac{1}{\sqrt{2\pi}} \int_{-\infty}^{\alpha} \exp(\frac{-t^2}{2})\, dt. \tag{5.9}$$

By convention a 3σ significance ($\alpha \geq 3$) is required for a fluctuation to be considered an evidence for new physics, while at least 5σ are necessary to be classified as discovery.
Similarly a p-value p_1 can be defined for the signal hypothesis H_1. In a hypothesis test H_1 is rejected by deriving an upper limit (UL) on the signal using the so called confidence level (CL_s) prescription [94], where the CL_s is defined as

$$CL_s = \frac{p_1}{1 - p_0} \tag{5.10}$$

A particular signal model is considered to be excluded at *95% CL* if $CL_s \leq 0.05$.
Based on this convention an UL on the number of signal events can be derived via a variation of the signal strength assumed in H_1, until exclusion is reached. Such an UL on the event count can be translated into an UL on the production cross-section of a specific BSM process in a specific analysis

$$\sigma_{BSM} = \frac{n_{BSM}}{L \times (\mathcal{A} \times \epsilon) \times BR} \tag{5.11}$$

where L is the integrated luminosity, $\mathcal{A}$ the detector acceptance, ϵ the analysis efficiency and BR denotes the branching ratio of the respective BSM process.
In order to apply these basic concepts in a more realistic interpretation of analysis results, cross correlations between different regions of phase space have to be taken into account as well as systematic and statistical uncertainties. Thus, the p-value computation uses PDFs constructed from Poissonian distributions describing the numbers of observed events in various analysis regions which are afflicted with systematic uncertainties. These systematics are taken into account by a convolution with a set of Gaussian PDFs constraining the nuisance parameters (NP) representing the uncertainties.
A technique to deal with such a complex statistical model, widely used in high-energy physics, is based on the application of likelihood (LH) functions $\mathcal{L}(\mu, \theta)$ [95], which associate the signal strength parameter μ, i.e. the signal normalisation, with the set of NPs $\theta = (\theta_1, \theta_2, \theta_3, \ldots)$. The LH functions are used in testing the hypotheses in the context of the *profile likelihood ratio (LHR)* method

where the LH ratio for an observed measurement x is defined as

$$\lambda(\mu) = \frac{\mathcal{L}(\mu, \theta''(\mu)|x)}{\mathcal{L}(\mu', \theta'|x)}. \tag{5.12}$$

The LH in the nominator of Equation 5.12 is maximised for a specific value of μ. Hence, θ'', the *conditional maximum likelihood (ML) estimator* of θ, is a function of μ. The denominator holds the unconditionally maximised LH function. Thus, $\lambda(\mu)$ describes the smearing of the profile of the LH by the NPs depending on the respective signal strength reflecting the reduction of information due to the systematic uncertainties.
In a statistical interpretation of an analysis result the LHR is then used to calculate the p-values and subsequently the CL_s in the fitting procedure.

5.4.3 Fit Methods

Three different fit procedures are typically used in a BSM search all of which are based on the LHR method described above:

The **background-only fit** is used to normalise the expected SM event yield in the CRs to data.

The **discovery fit** is a model-independent fit. It is very similar to the background-only fit but uses the yields in the CRs to constrain the prediction of background contribution in the SRs. Thus, the level of agreement of observed and predicted yields in the SRs can be quantified by testing H_0. In a second step, a generic signal model is included in the fit procedure to test the signal hypothesis H_1 and derive UL at *95% CL* on the visible cross-section of BSM processes $\sigma_{vis} = \sigma_{BSM} \times (\mathcal{A} \times \epsilon)$ in each SR.

An **exclusion fit** replaces the generic signal model with specific BSM models the search is designed for. It includes the predicted event yields of the specific model in the SRs as well as possible signal contaminations in the CRs. Additionally, it takes into account correlations between systematics associated to background and signal processes and experimental systematics on the signal yields from detector effects.

The fit procedures briefly outlined here are implemented in a common software framework, the HistFitter program [96]. Their application in the 0L (2-6jets) SUSY analysis is detailed in section 6.5.

6 Search for Squarks and Gluinos in a Pure RPC Scenario

The general aspects and fundamental principles of SUSY are detailed in section 2.2 and the phenomenology of supersymmetric particle production and decay at a hadron collider - in particular under the assumption of RPC - is described in section 2.3. Figure 2.5 shows that the production cross-sections for strongly coupling sparticles, namely gluinos ($\tilde{g}$) and light-flavoured squarks ($\tilde{q}$), are expected to be dominant, making these sparticles a chief target for SUSY searches at the LHC. In RPC scenarios these particles have a negligible lifetime and decay promptly into final states including a stable LSP, leading to signatures with a substantial amount of E_T^{miss}. The decay modes with the highest branching ratio are the all hadronic channels (cf. subsection 2.3.2). Hence, the 0L (2-6jets) SUSY analysis [97], which targets exactly these hadronic signatures, is often referred to as the "flagship" of the ATLAS SUSY search program. This chapter is dedicated to this analysis using the full Run 2 data-set.

6.1 The ATLAS inclusive Zero Lepton Analysis

The 0L (2-6jets) SUSY analysis is a search for squarks and gluinos based on the RPC MSSM. This particular supersymmetric parameter space includes a plethora of different models due to the large number of free parameters (cf. section 2.2).
Within the RPC MSSM squarks and gluinos can be produced in pairs ($\tilde{g}\tilde{g}$, $\tilde{g}\tilde{q}$, $\tilde{q}\tilde{q}$). A selection of their simplest decay channels are summarised in Equation 6.1. In particular, these are direct decays into quarks and the lightest neutralino ($\tilde{\chi}_1^0$), the stable LSP, or cascade decays via an intermediate chargino ($\tilde{\chi}_1^\pm$) which subsequently decays into a W-boson ($W^\pm$) and the LSP. In case of cascade decays the overall possibility to find hadronic final states is further enhanced by the branching ratios of the $W^\pm$ which are about 70% for $W^\pm \to qq$ and only about 30% for $W^\pm \to \ell^\pm \nu$.

$$\begin{aligned} \tilde{g} &\to q\bar{q}\tilde{\chi}_1^0 \\ \tilde{q} &\to q\tilde{\chi}_1^0 \\ \tilde{g} &\to q\bar{q}\tilde{\chi}_1^\pm \to q\bar{q}W^\pm\tilde{\chi}_1^0 \\ \tilde{q} &\to q\tilde{\chi}_1^\pm \to qW^\pm\tilde{\chi}_1^0 \end{aligned} \tag{6.1}$$

The production modes and decay channels considered in the 0L (2-6jets) SUSY analysis are implemented as the five simplified model topologies (cf. subsection 2.3.3) reflecting the processes in Equation 6.1 and depicted in Figure 6.1.
In order to suppress SM background processes including leptonic W decays (e.g. W boson plus jets and top anti-top pair and single top), which produce neutrinos contributing to the E_T^{miss}, events including a baseline lepton ($e^\pm$, $\mu^\pm$) are rejected in the three different analysis approaches condensed in the 0L (2-6jets) SUSY analysis. The *multi-bin (MB)* search, an advanced extension of the *cut and count* method used in the previous version of the analysis [98], simultaneously fits multiple bins. The *boosted decision tree (BDT)* analysis is a MVA based on the TMVA framework [99] which exploits

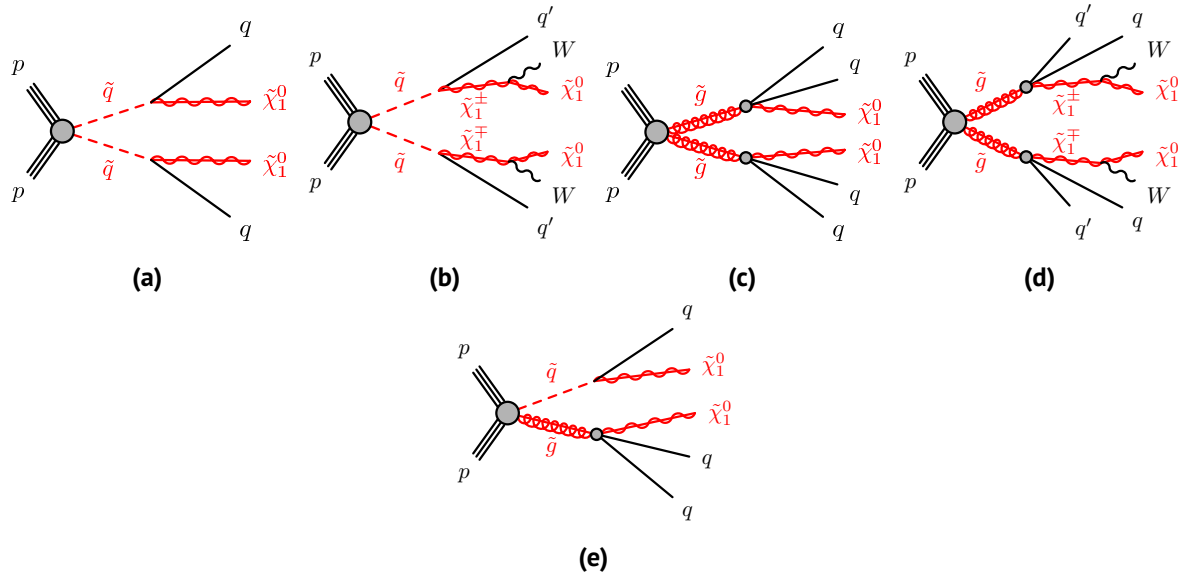

Figure 6.1: The simplified model topologies considered in the inclusive 0L search, describing pair produced squarks (Figure 6.1a, Figure 6.1b) and gluinos (Figure 6.1c, Figure 6.1d) decaying directly or via one-step cascades as well as a squark-gluino production (Figure 6.1e) with both sparticles decaying directly.

the correlations between certain observables. In addition, a set of *cut and count* selections are used to obtain model-independent limits. These three approaches are detailed in section 6.2.
The inclusive 0L search makes use of MC simulation of several background processes to estimate the expected background contributions, as described in section 6.3. Simulated signal processes, given by the topologies depicted in Figure 6.1, are used in the final interpretation of the analysis results (cf. section 6.5). The simulation of event samples as well as the underlying data-set are discussed in subsection 6.1.1, followed by a detailed definition of the physics objects in subsection 6.1.2.

6.1.1 Simulated and Recorded Event Samples

The full Run 2 data-set was analysed enclosing the collision data recorded with the ATLAS detector between 2015 and 2018 at $\sqrt{s}$ = 13 TeV with a bunch-crossing rate of 25 ns, corresponding to a total integrated luminosity of L=139 fb^{-1} with an uncertainty of 1.7%. The average number of pp collisions as well as the individual luminosity of each data taking period in Run 2 is given in Table 6.1.

Standard Model Background Samples The main SM background processes in the inclusive 0L search are the production of vector bosons (W and Z) in association with jets, diboson production, processes including single top and $t\bar{t}$ production as well as QCD processes with multiple jets. The latter is difficult to model effectively using MC simulation, as detailed in subsection 6.3.1, while all other processes are simulated. Processes involving the production of photons (γ) are used to constrain the irreducible background from invisible Z decays (cf. section 6.3). Table 6.2 summarises these SM background samples, the respective event generator used, the precision at which the

Period	*Luminosity* [fb^{-1}]	*Relativ uncertainty* [%]	*Pile-up* $\langle\mu\rangle$
2015	3.22	2.1	20
2016	32.97	2.2	20
2017	44.31	2.4	38
2018	58.45	2.0	37

Table 6.1: Summary of luminosities, their relative uncertainty and the respective pile-up condition for all Run2 data-taking periods.

cross-sections were calculated, the PDFs and generators for the PS as well as the set of tuning parameters for ISR, FSR and UE parameters.

Physics process	*Generator*	*Cross-section normalization*	*PDF set*	*Parton shower*	*Tune*
$W(\rightarrow \ell\nu)$ + jets	SHERPA2.2.1 [100]	NNLO [101]	NNPDF3.0NNLO [102]	SHERPA [103]	SHERPA
$Z/\gamma^*(\rightarrow \ell\bar{\ell})$ + jets	SHERPA2.2.1	NNLO	NNPDF3.0NNLO	SHERPA	SHERPA
γ + jets	SHERPA2.2.2	NLO	NNPDF3.0NNLO	SHERPA	SHERPA
$t\bar{t}$	POWHEG-BOX V2 [71]	NNLO+NNLL [104, 105]	NNPDF2.3LO [106]	PYTHIA8.230 [70]	A14 [107]
Single top (Wt-channel)	POWHEG-BOX V2	NNLO+NNLL [108, 109].	NNPDF2.3LO	PYTHIA8.230	A14
Single top (s-channel)	POWHEG-BOX V2	NLO [110, 111]	NNPDF2.3LO	PYTHIA8.230	A14
Single top (t-channel)	POWHEG-BOX V1	NLO	NNPDF2.3LO	PYTHIA8.230	A14
$t\bar{t}+W/Z/H$	MG5_aMC@NLO2.2.3 [72]	NLO [112, 113]	NNPDF2.3LO	PYTHIA8.210	A14
$t\bar{t}+WW$	MG5_aMC@NLO2.2.2	NLO	NNPDF2.3LO	PYTHIA8.210	A14
WW, WZ, ZZ, Wγ, Zγ	SHERPA2.2.1	NLO	NNPDF3.0NNLO	SHERPA	SHERPA
QCD MC	PYTHIA8.1 [114]	NLO	NNPDF2.3LO	PYTHIA8.1	A14

Table 6.2: MC simulated samples of the SM background processes relevant in the 0L (2-6jets) SUSY analysis. Details about the generators, cross-section precision, PDFs, showering and tunes are shown.

Signal Samples SUSY signal samples are generated by varying the free parameters of the respective simplified model, creating a grid of signal points. In case of the squark and gluino pair-production followed by a direct decay into SM particles, shown in Figure 6.1a and Figure 6.1c, respectively, the free parameters are the masses of the respective initial SUSY particle, $m(\tilde{q})$ or $m(\tilde{g})$ and the LSP mass, $m(\tilde{\chi}_1^0)$. The one-step decay models in Figure 6.1b and Figure 6.1d feature in principle three free parameters, i.e. the masses of the involved sparticles, $m(\tilde{q})$ or $m(\tilde{g})$, $m(\tilde{\chi}_1^\pm)$ and $m(\tilde{\chi}_1^0)$. However, in order to be able to produce two-dimensional results, two slices of the respective parameter space are considered, where one of the free parameters is fixed. In particular either $m(\tilde{\chi}_1^\pm)$ is varied with a fixed $m(\tilde{\chi}_1^0)$ = 60 GeV or $m(\tilde{\chi}_1^0)$ is free with the chargino mass fixed between the initial sparticle mass and $m(\tilde{\chi}_1^0)$ via $m(\tilde{\chi}_1^\pm)$ =$1/2(m(\tilde{q}/\tilde{g}) + m(\tilde{\chi}_1^0))$.
A less simplified model considered in the 0L (2-6jets) SUSY analysis, includes processes exemplified in Figure 6.1a, Figure 6.1c and Figure 6.1e. It is also referred to as *phenomenological squark-gluino production* since, unlike pure squark or gluino models, the parameter space accessible by the LHC is assumed to contain both, $\tilde{q}$ and $\tilde{g}$, allowing a joint production of these two sparticles ($\tilde{q}\tilde{\bar{q}}$, $\tilde{g}\tilde{g}$,

$\widetilde{q}\widetilde{q}/\bar{\widetilde{q}}\bar{\widetilde{q}}$, $\widetilde{q}\widetilde{g}$) as well as on-shell decays from one to the other, depending on the kinematics of the respective signal point. Hence, the signal grid for the phenomenological squark-gluino production is created by varying $m(\widetilde{g})$ and $m(\widetilde{q})$. The third free parameter in this model is the mass of the LSP which is fixed to 0 GeV, 995 GeV and 1495 GeV, forming three slices of the parameter space. The non-decoupling of $\widetilde{g}$ and $\widetilde{q}$ enhances the production cross-section for this particular topology by opening up the t- and u-channel for gluino and squark pair-production and including the production process $\widetilde{g}\widetilde{q}$.
Following the simplified model prescription, discussed in subsection 2.3.3, all other sparticles, including the third generation squarks ($\widetilde{t}$ and $\widetilde{b}$), are decoupled. Models with direct decays assume an eightfold degeneracy of light-flavoured squarks ($\widetilde{u}$, $\widetilde{d}$, $\widetilde{s}$ and $\widetilde{c}$). For the one-step cascade decays, on the other hand, a fourfold degeneracy is assumed. The $\widetilde{\chi}_1^0$ is a pure bino state in all models.
The production cross-sections for all signal samples are calculated to approximate next-to-next-to-leading order (NNLO) in α_s with additional resummation of soft gluon emission at next-to-next-to-leading-logarithmic order (NNLL) [115–122].
MG5_aMC@NLO interfaced with PYTHIA8 is used to simulated the matrix-level generation, parton showering and fragmentation for all signal processes. For the inclusive model the branching ratios of on-shell decays of the form $\widetilde{q} \to q\widetilde{g}$ and $\widetilde{g} \to q\widetilde{q}$ are calculated with SUSY-HIT [123]. Additionally, ISR and FSR as well as the UE parameters are taken into account using the *A14 tune* with the NNPDF2.3LO PDF set.

The detector response for all MC samples used in the inclusive 0L search was simulated with GEANT4 for SM processes and ATLASFASTII for signal samples. They are overlaid with a number of additional pp collisions and reweighted to match the respective pile-up conditions as described in subsection 5.2.3.

6.1.2 Object Definition

Simulated as well as recorded data events are subjected to the full physics objects reconstruction detailed in section 5.1. Additional requirements are placed on the transverse momentum and the pseudo-rapidity:

- Jet candidates in the inclusive 0L search are the standard anti-k_t jets with a cone size of R = 0.4 subjected to the full correction and calibration sequence, as well as the quality criteria stated in subsection 5.2.1. Furthermore, they are required to have a p_{T} larger than 20 GeV and lie within a region of $|\eta| < 2.8$. Jet candidates with $p_{\mathrm{T}} < 120$ GeV and $|\eta| < 2.4$ are discarded if the JVT is below 0.59, in order to suppress jets from pile-up. This requirement is loosened to 0.11 if the pseudo-rapidity is between 2.4 and 2.5.

- The MV2c10 algorithm is used to tag b-jets as described in subsection 5.1.2 using a 77% efficiency working point. Candidate b-jets are retained if they have $p_{\mathrm{T}} > 50$ GeV and $|\eta| < 2.5$.

- Baseline muons are required to posses $p_{\mathrm{T}} > 6$ GeV and $|\eta| < 2.7$. For baseline electrons these requirements change to $p_{\mathrm{T}} > 7$ GeV and $|\eta| < 2.47$.

- Reconstructed photons are retained if their p_T is above 25 GeV and $|\eta| < 2.37$ excluding the transition region, or "crack region" between the end-cap and the barrel of the EMcal. In addition, photons are required to satisfy the photon shower shape, the electron rejection criteria and they need to be isolated [124].

Ambiguities between these objects are resolved following the OR strategy discussed in subsection 5.2.1 with additional rules applied in CRs including photons:

- If a baseline lepton and a photon are located inside a cone of $\Delta R = 0.4$, the photon is discarded and the lepton is kept.
- A photon that lies within $\Delta R = 0.4$ of a jet is retained and the jet is removed.

6.2 Analysis Strategy

The basic analysis strategy, as it is followed by the 0L (2-6jets) SUSY analysis and many other BSM searches, is introduced in subsection 5.4.1. Preselected events are subjected to three different analysis approaches. These approaches differ mainly in the method of constructing the SRs but are all based on the same observables.

6.2.1 Physics Observables

Physics observables, or variables, used to discriminate between signal and background, exploit certain kinematic and geometric aspects of the expected event structure created by hadronic SUSY processes. This section gives an overview of the most important variables used to define SRs, CRs and VRs in the inclusive 0L search.

- E_T^{miss} is a measure for the imbalance in the reconstructed transverse momentum of an event. It is one of the key variables since signal events are characterised by a large amount of E_T^{miss} due to the LSP which escapes undetected in RPC scenarios (cf. section 2.2 and subsection 5.1.4).
- N_j denotes the multiplicity of jets with $p_T > 50$ GeV used to increase the sensitivity to a given topology.
- $p_T(j)$ is the transverse momentum of each jet present in the event.
- m_{eff}, the inclusive effective mass, is the main discriminating variable used in the inclusive 0L search. It is a very powerful discriminator due to the high mass scales expected for the SUSY models considered in this analysis. m_{eff} is defined as the scalar sum of the p_T of all n jets with $p_T > 50$ GeV in an event plus the E_T^{miss}[1]

$$m_{eff} = \sum_{i=1}^{n} |\mathbf{p}_T^i| + E_T^{miss}. \tag{6.2}$$

[1] in CRs with a lepton requirement, the p_T of the lepton is also added to the m_{eff}

In regions placing a requirement on N_j this variable can be modified to take into account the respective leading jets only

$$m_{\text{eff}}(N_j) = \sum_{i=1}^{N_j} |\mathbf{p}_{\text{T}}^{\text{i}}| + E_{\text{T}}^{\text{miss}}. \tag{6.3}$$

- H_{T} measures the jet activity in an event and is defined as $m_{\text{eff}} - E_{\text{T}}^{\text{miss}}$.

- $E_{\text{T}}^{\text{miss}}/\sqrt{H_{\text{T}}}$ is called the significance of the missing transverse momentum. It is used to suppress multijet background events where jet energy mis-measurement generates fake missing transverse momentum (fake $E_{\text{T}}^{\text{miss}}$). This variable is particularly sensitive to processes arising from $\tilde{q}\tilde{q}$ production. It compares the value of $E_{\text{T}}^{\text{miss}}$ to the hadronic energy resolution in the event.

- $E_{\text{T}}^{\text{miss}}/m_{\text{eff}}(N_j)$ is another variable that is used to suppress contributions from events with fake $E_{\text{T}}^{\text{miss}}$. It is most effective in regions with a high jet-multiplicity.

- $\Delta\phi(j_{1,2,(3)}, \mathbf{p}_{\text{T}}^{\text{miss}})_{\text{min}}$ is a geometric variable which also serves the purpose of discriminating between real and fake $E_{\text{T}}^{\text{miss}}$. It denotes the minimal azimuthal angle between the directions of the (up to) three leading jets and $\mathbf{p}_{\text{T}}^{\text{miss}}$. $\Delta\phi$ is powerful in rejecting multijet background events since the fake $E_{\text{T}}^{\text{miss}}$ coming from mis-measured jet energies is likely to be aligned with the axis of the jet. In regions where more than three jets are present, $\Delta\phi(j_{i>3}, \mathbf{p}_{\text{T}}^{\text{miss}})_{\text{min}}$ is taken into account separately.

- Aplanarity, another geometric variable, distinguishes between signal and background based on the shape of the event [125]. It is defined via λ_3 the smallest eigenvalue of the normalised momentum tensor of the jets in the event

$$\mathcal{A} = \frac{3}{2}\,\lambda_3. \tag{6.4}$$

- m_{T}, the transverse mass, is only used in certain CRs which require the presence of a lepton and is defined as

$$m_{\text{T}} = \sqrt{2p_{\text{T}}^{\ell} E_{\text{T}}^{\text{miss}} \left(1 - \cos\left[\Delta\phi(\ell, \boldsymbol{p}_{\text{T}}^{\text{miss}})\right]\right)}. \tag{6.5}$$

6.2.2 Event Selection

Events used as input to the three different analysis strategies are selected by imposing the preselection cuts summarised in Table 6.3.

In order to be sensitive to RPC SUSY processes events need to have a $E_{\text{T}}^{\text{miss}}$ of at least 300 GeV[2], a hard leading jet with $p_{\text{T}} > 200$ GeV and a sub-leading jet with $p_{\text{T}} > 50$ GeV. To further increase the sensitivity to high-mass SUSY signals, events are rejected if the effective mass is below 800 GeV. A

[2] This requirement also ensures, that the $E_{\text{T}}^{\text{miss}}$-trigger used to select candidate events, is working at the trigger plateau.

Lepton veto	No baseline electron (muon) with $p_T > 7$ (6) GeV
E_T^{miss} [GeV]	> 300
$p_T(j_1)$ [GeV]	> 200
$p_T(j_2)$ [GeV]	> 50
$\Delta\phi(j_{1,2,(3)}, \mathbf{p}_T^{miss})_{min}$ [rad.]	> 0.4
m_{eff} [GeV]	> 800

Table 6.3: The 0L preselection criteria common to the MB, the BDT and the model-independent search included in the analysis.

basic rejection of the multijet background is guaranteed by requiring $\Delta\phi$ to be above 0.4. In addition, events are vetoed if they contain at least one baseline lepton.
The preselected data-set is then subjected to additional and tightened selection cuts, the SR selections, which are used to differentiate between the signal models shown in Figure 6.1. A direct decay of a $\tilde{q}$ for instance will add a jet to the final state, while a $\tilde{g}$ will decay into two jets. Consequently the jet-multiplicity is expected to increase with the length of the decay chain. The decay structure of the respective topology will also affect the kinematic characteristics of the event. Hence, several SRs are defined for each different search included in the 0L (2-6jets) SUSY analysis, optimised to maximise the *95% CL* limits for the respective model. These search strategies as well as their SR definitions are explained in the following.

6.2.3 Multi-Bin Search

The MB analysis targets three different scenarios. The MB-SSd and MB-GGd are optimised for direct decays of pair-produced squarks (SS-direct) and gluinos (GG-direct) each with a large mass-splitting between the initial sparticle and the LSP, while the MB-C targets compressed mass spectra for all topologies. All three MB channels have very similar sets of preselection cuts listed in Table 6.4. Each MB channel is composed of a set of orthogonal bins, defined based on the jet-multiplicity, effective mass and significance of missing transverse momentum.

variable	*MB-SSd*	*MB-GGd*	*MB-C*
N_j	≥ 2	≥ 4	≥ 2
$p_T(j_1)$ [GeV]	> 200	> 200	> 600
$p_T(j_{i=2,\ldots,N_{j_{min}}})$ [GeV]	> 100	> 100	> 50
$\lvert\eta(j_{i=1,\ldots,N_{j_{min}}})\rvert$	< 2.0	< 2.0	< 2.8
$\Delta\phi(j_{1,2,(3)}, \mathbf{p}_T^{miss})_{min}$	> 0.8	> 0.4	> 0.4
$\Delta\phi(j_{i>3}, \mathbf{p}_T^{miss})_{min}$	> 0.4	> 0.2	> 0.2
Aplanarity	-	> 0.04	-
$E_T^{miss}/\sqrt{H_T}$ [GeV$^{1/2}$]	> 10	> 10	> 10
m_{eff} [GeV]	> 1000	> 1000	> 1600

Table 6.4: Additional preselection criteria imposed on the three different MB channels.

The MB-SSd regions require a minimum of two jets obeying a tighter η selection than the basic 0L preselection, a leading jet with a p_{T} of at least 200 GeV and all other jets with $p_{\mathrm{T}} > 100$ GeV. Furthermore, the cut on $\Delta\phi(j_{1,2,(3)}, \mathbf{p}_{\mathrm{T}}^{\mathrm{miss}})_{\mathrm{min}}$ is tightened to 0.8 and $\Delta\phi(j_{i>3}, \mathbf{p}_{\mathrm{T}}^{\mathrm{miss}})_{\mathrm{min}}$ must be larger than 0.4. Bins in this channel are constructed by varying N_j, m_{eff} and $E_{\mathrm{T}}^{\mathrm{miss}}/\sqrt{H_{\mathrm{T}}}$ and are partially merged, as indicated in Table 6.5.

N_{j}=[2, 3]		m_{eff} [TeV]					
		[1.0, 1.6)	[1.6, 2.2)	[2.2, 2.8)	[2.8, 3.4)	[3.4, 4.0)	[4.0, ∞)
$E_{\mathrm{T}}^{\mathrm{miss}}/\sqrt{H_{\mathrm{T}}}$ [GeV$^{1/2}$]	[10, 16)						
	[16, 22)						
	[22, 28)						
	[28, ∞)						
N_{j}=[4, ∞)		m_{eff} [TeV]					
		[1.0, 1.6)	[1.6, 2.2)	[2.2, 2.8)	[2.8, ∞)		
$E_{\mathrm{T}}^{\mathrm{miss}}/\sqrt{H_{\mathrm{T}}}$ [GeV$^{1/2}$]	[10, 16)						
	[16, 22)						
	[22, ∞)						

Table 6.5: Summarised bins in the MB-SSd channel with the last bin in each case being inclusive.

Due to the larger number of jets in final states origin from gluino decays, the MB-GGd channels require at least one leading and three additional jets with a p_{T} above 100 GeV. The cuts on the two $\Delta\phi$ variables are slightly looser than in case of the MB-SSd selections but an additional requirement on the Aplanarity is placed. The MB-GGd bins, listed in Table 6.6, are constructed based on m_{eff} and $E_{\mathrm{T}}^{\mathrm{miss}}/\sqrt{H_{\mathrm{T}}}$, while the jet-multiplicity is kept inclusive.

N_{j}= [4, ∞)		m_{eff} [TeV]					
		[1.0, 1.6)	[1.6, 2.2)	[2.2, 2.8)	[2.8, 3.4)	[3.4, 4.0)	[4.0, ∞)
$E_{\mathrm{T}}^{\mathrm{miss}}/\sqrt{H_{\mathrm{T}}}$ [GeV$^{1/2}$]	[10, 16)						
	[16, 22)						
	[22, ∞)						

Table 6.6: The m_{eff} and $E_{\mathrm{T}}^{\mathrm{miss}}/\sqrt{H_{\mathrm{T}}}$ boundaries of the bins in the MB-GGd channel with the last bin in each case being inclusive.

Compressed mass-spectra, which the MB-C is designed for, are generally difficult to cover. Hence, the MB-C regions require a high energetic ISR jet ($p_{\mathrm{T}} > 600$ GeV) against which the entire system is recoiling, while keeping the cuts on all additional jets at the preselection level. This channel requires a higher value for the lower boundary of the m_{eff} bins, as summarised in Table 6.7.

N_j= [2, 3]; 4; [5, ∞)		m_{eff} [TeV]		
		[1.6, 2.2)	[2.2, 2.8)	[2.8, ∞)
$E_T^{miss}/\sqrt{H_T}$ [GeV$^{1/2}$]	[16, 22)			
	[22, ∞)			

Table 6.7: MB-C bin boundaries with inclusive last bins.

6.2.4 BDT Search

The BDT analysis approach uses the value of the BDT score obtained from a training process of BDTs implemented in the TMVA framework[3], to further separate between signal and background exploiting the correlations of various input variables. Single bin SRs are then constructed including the optimal BDT score. This approach specifically targets signal models describing the direct (GG-direct) and one-step (GG-onestep) decay of pair-produced gluinos.
The BDT training categories for each topology are chosen based on the mass-splitting $\Delta m(\tilde{g}, \tilde{\chi}_1^0)$ of the respective signal grid point, since the kinematic aspects of phase-space targeted by the BDTs are mainly driven by the mass configuration of the involved sparticles. Hence, for each training category several grid points with very similar Δm are combined to one input signal sample, increasing the number of available signal events in the training.
Four different BDTs are trained for each topology all of which use preselected events obtained from the respective combined signal sample and from all MC simulated background samples as input. These events are randomly divided into two sets such that the BDTs can be trained on each set individually. The BDT score obtained from one set is then applied onto the other set and vice versa. This standard procedure ensures, that the full statistics available can be used as input for the signal and background evaluation.
A set of variables is used as input for each BDT which are selected based on detailed studies on the impact of each individual variable. These variable sets, comprised of ten, eleven or twelve individual observables, for the BDT-GGd and BDT-GGo SRs are listed in Table 6.8 and Table 6.9, respectively.

Input variables	*BDT-GGd1*	*BDT-GGd2*	*BDT-GGd3*	*BDT-GGd4*
E_T^{miss}[GeV]	◯	-	◯	
$p_T(j)$ [GeV]	1st - 4th Jet			
$\eta(j)$	1st - 4th Jet			
Aplanarity	◯			-
m_{eff} [GeV]	◯			
Total number of input variables to BDT calculation	11	10	11	10

Table 6.8: Summary of input variables for the BDT training to obtain the BDT score in case of the BDT-GGd regions.

The preselection cuts in combination with the optimised BDT score cut, summarised in Table 6.10 for each training category define the actual BDT-GGd or BDT-GGo SRs. While BDT-GGd SRs require

[3] The TMVA parameters were specified as: *method* = "Gradient Boost", *number of trees* = 300 and *maximal depth of tree* = 3.

Input variables	*BDT-GGo1*	*BDT-GGo2*	*BDT-GGo3*	*BDT-GGo4*
$E_{\mathrm{T}}^{\mathrm{miss}}$[GeV]	-			◯
$p_T(j)$ [GeV]	1st -5th	1st - 4th	1st - 3th, 5th - 6th	1st - 4th
$\eta(j)$	1st - 5th	1st - 4th	1st - 3th, 5th - 6th	1st - 4th
Aplanarity	◯			-
m_{eff} [GeV]	◯			
Total number of input variables	12	10	12	10

Table 6.9: Summary of variables used as input for the training of the BDTs optimised for cascade gluino decays.

at least four jets, this number is increased to five and six, respectively, in case of the SRs targeting one-step decays. The common 0L preselection cuts on m_{eff} are tightened in SRs targeting signal points with a large mass-splitting. An additional requirement is placed on $E_{\mathrm{T}}^{\mathrm{miss}}/m_{\mathrm{eff}}(N_j)$ in all BDT SRs to improve the rejection of QCD background events. The BDT-GGo4 region, which targets a compressed area of the GG-onestep phase-space, uses a loosened cut on both $\Delta\phi$ variables.

Variables	*BDT-GGd1*	*BDT-GGd2*	*BDT-GGd3*	*BDT-GGd4*
N_j	≥ 4			
$\Delta\phi(j_{1,2,(3)}, \mathbf{p}_{\mathrm{T}}^{\mathrm{miss}})_{\mathrm{min}}$	≥ 0.4			
$\Delta\phi(j_{i>3}, \mathbf{p}_{\mathrm{T}}^{\mathrm{miss}})_{\mathrm{min}}$	≥ 0.4			
$E_{\mathrm{T}}^{\mathrm{miss}}/m_{\mathrm{eff}}(N_j)$	≥ 0.2			
m_{eff} [GeV]	≥ 1400		≥ 800	
BDT score	≥ 0.97	≥ 0.94	≥ 0.94	≥ 0.87
$\Delta m(\tilde{g}, \tilde{\chi}_1^0)$ [GeV]	1600 – 1900	1000 – 1400	600 – 1000	200 – 600

Variables	*BDT-GGo1*	*BDT-GGo2*	*BDT-GGo3*	*BDT-GGo4*
N_j	≥ 6		≥ 5	
$\Delta\phi(j_{1,2,(3)}, \mathbf{p}_{\mathrm{T}}^{\mathrm{miss}})_{\mathrm{min}}$	≥ 0.4			≥ 0.2
$\Delta\phi(j_{i>3}, \mathbf{p}_{\mathrm{T}}^{\mathrm{miss}})_{\mathrm{min}}$	≥ 0.4			≥ 0.2
$E_{\mathrm{T}}^{\mathrm{miss}}/m_{\mathrm{eff}}(N_j)$	≥ 0.2			
m_{eff} [GeV]	≥ 1400		≥ 800	
BDT score	≥ 0.96	≥ 0.87	≥ 0.92	≥ 0.84
$\Delta m(\tilde{g}, \tilde{\chi}_1^0)$ [GeV]	1400 – 2000	1200 – 1400	600 – 1000	200 – 400

Table 6.10: Pre-selection and BDT score for all BDT SRs. The mass-splitting $\Delta m(\tilde{g}, \tilde{\chi}_1^0)$, defining the input signal models for the training categories for the BDT-GGd (top) and BDT-GGo (bottom) channels is shown in addition.

6.2.5 Model Independent Search

The SRs in the model independent search, called discovery region (DR), are mainly based on the variation of N_j and m_{eff} following the *single-bin strategy* used in a previous version of the 0L (2-6jets) SUSY analysis [98] based on the collision data collected in 2015 and 2016 corresponding to L=36.1 fb^{-1}. Although optimised to maximise the sensitivity to the simplified SUSY models

considered in the analysis, the DRs are specifically designed to compute a model-independent statistical significance of the search results. Such model-independent interpretations are of particular importance in the recast of RPC SUSY searches in other supersymmetric or different BSM scenarios. Although feasible, such a reinterpretation would be much harder in case of the MB and BDT search. An example of a reinterpretation of the 36 fb^{-1} version of the inclusive 0L search, carried out by the ATLAS collaboration, is discussed in chapter 7 in great detail. However, the main purpose of including this simplified analysis approach, in addition to the more complex strategies described above, is to facilitate the usage of the analysis outside the collaboration.
Table 6.11 and Table 6.12 list the definitions of the individual DRs. These selections are overlapping, prohibiting a combined statistical treatment, hence the name *single-bin strategy*. The specific cuts on m_{eff} and $E_{\text{T}}^{\text{miss}}/\sqrt{H_{\text{T}}}$ were selected following closely the bin definitions applied in the MB search.

Variable	*SR2j-1600*	*SR2j-2200*	*SR2j-2800*	*SR4j-1000*	*SR4j-2200*	*SR4j-3400*
N_j	≥ 2			≥ 4		
$p_{\text{T}}(j_1)$ [GeV]	> 250	> 600	> 250	> 200		
$p_{\text{T}}(j_{i=2,\ldots,N_{j_{\text{min}}}})$ [GeV]	> 250	> 50	> 250	> 100		
$\lvert\eta(j_{i=1,\ldots,N_{j_{\text{min}}}})\rvert$	< 2.0	< 2.8	< 1.2	< 2.0		
$\Delta\phi(j_{1,2,(3)}, \mathbf{p}_{\text{T}}^{\text{miss}})_{\text{min}}$	> 0.8	> 0.4	> 0.8	> 0.4		
$\Delta\phi(j_{i>3}, \mathbf{p}_{\text{T}}^{\text{miss}})_{\text{min}}$	> 0.4	> 0.2	> 0.4	> 0.4		
Aplanarity	-			> 0.04		
$E_{\text{T}}^{\text{miss}}/\sqrt{H_{\text{T}}}[\sqrt{\text{GeV}}]$	> 16					> 10
m_{eff}[GeV]	> 1600	> 2200	> 2800	> 1000	> 2200	> 3400

Table 6.11: Summary of the DRs with a jet multiplicity of up to four.

Variable	*SR5j-1600*	*SR6j-1000*	*SR6j-2200*	*SR6j-3400*
N_j	≥ 5	≥ 6		
$p_{\text{T}}(j_1)$ [GeV]	> 600	> 200		
$p_{\text{T}}(j_{i=2,\ldots,N_{j_{\text{min}}}})$ [GeV]	> 50	> 75		
$\lvert\eta(j_i = 1,\ldots,N_{j_{\text{min}}})\rvert$	< 2.8	< 2.0		
$\Delta\phi(j_{1,2,(3)}, \mathbf{p}_{\text{T}}^{\text{miss}})_{\text{min}}$	> 0.4			
$\Delta\phi(j_{i>3}, \mathbf{p}_{\text{T}}^{\text{miss}})_{\text{min}}$	> 0.2			
Aplanarity	-	>0.08		
$E_{\text{T}}^{\text{miss}}/\sqrt{H_{\text{T}}}[\sqrt{\text{GeV}}]$	> 16			> 10
m_{eff}[GeV]	> 1600	> 1000	> 2200	> 3400

Table 6.12: Selection criteria defining DRs with high jet multiplicities.

6.3 Background Estimation

The general procedure of the background estimation was introduced in subsection 5.4.1. This section explains the different background processes and the design of the respective CRs as well as the

evaluation of the background estimation in suitable VRs in great detail.
In order to obtain an accurate and robust estimation of the SM event yields in the SRs of the different channels, a dedicated CR is assigned to each individual SR for each major background process. These CRs are constructed to be orthogonal to their associated SR creating an independent set of events for which the corresponding SM process is enhanced while the contamination from signal events is kept at a negligible level. However, it is crucial to optimise the CR definitions such that the systematic uncertainties, arising from the extrapolation of the normalised event yields in the CRs onto the SRs, are minimised while maintaining sufficient statistical precision. Therefore, the cuts on p_{T} and m_{eff} applied in the SRs are kept in the CRs where ever it is possible without significantly limiting the number of events. Four different CRs are used to predict the background contributions from the four major SM background processes in the inclusive 0L search, as summarised in Table 6.13. These processes, detailed below, result in detector signatures that mimic a hadronic SUSY signal, i.e. multiple jets associated with $E_{\mathrm{T}}^{\mathrm{miss}}$.

CR	*SR background*	*CR process*	*CR selection*
MB/BDT-CRγ	$Z(\rightarrow \nu\bar{\nu})$ + jets	γ + jets	Isolated photon
MB/BDT-CRQ	Multi-jet	Multi-jet	reversed requirements on (i) $\Delta\phi(\mathrm{j}, \boldsymbol{p}_{\mathrm{T}}^{\mathrm{miss}})$ and (ii) $E_{\mathrm{T}}^{\mathrm{miss}}/m_{\mathrm{eff}}(N_{\mathrm{j}})$ or $E_{\mathrm{T}}^{\mathrm{miss}}/\sqrt{H_{\mathrm{T}}}$
MB/BDT-CRW	$W(\rightarrow \ell\nu)$ + jets	$W(\rightarrow \ell\nu)$+jets	one lepton, 30 GeV$< m_{\mathrm{T}}(\ell, E_{\mathrm{T}}^{\mathrm{miss}}) <$ 100 GeV, b-veto
MB/BDT-CRT	$t\bar{t}$(+EW) and single top	$t\bar{t} \rightarrow b\bar{b}qq'\ell\nu$	one lepton, 30 GeV$< m_{\mathrm{T}}(\ell, E_{\mathrm{T}}^{\mathrm{miss}}) <$ 100 GeV, b-tag

Table 6.13: CR definitions targeting the main background processes in the SRs. Additionally, the processes used to model the background in the respective CR are listed. The jet p_{T} and m_{eff} requirements match those used in the corresponding SRs.

Z+jets The associated production of a Z boson plus jets contributes to the $E_{\mathrm{T}}^{\mathrm{miss}}$ via the invisible decay $Z \rightarrow \nu\bar{\nu}$. This process, which builds an irreducible background component, is estimated in the CRγ by selecting events with a photon of at least p_{T} = 150 GeV in MC samples simulating γ + jets processes. The kinematics of these processes are sufficiently similar to Z + jets if the p_{T} of the photon is larger than the mass of the Z boson. The photon is then added to the calculation of $E_{\mathrm{T}}^{\mathrm{miss}}$ representing the contribution of the undetected neutrinos.
The MC samples for both processes, Z + jets and γ + jets are produced at the same level of precision (cf. subsection 6.1.1). Nevertheless minor differences between the data-to-MC-ratios of these two samples are observed. A correction factor κ is derived for dedicated selections with up to three and at least four jets, respectively. This scaling factor is calculated as

$$\kappa = \frac{N_{CR\gamma}^{data}/N_{CR\gamma}^{MC}}{N_{VRZ}^{data}/N_{VRZ}^{MC}} \tag{6.6}$$

where VRZ is a VR enriched with Z + jets events. VRZ is constructed based on the same kinematic selections as the CRγ with an additional requirement of two leptons (e or μ). Events are selected if the invariant mass of the dilepton system lies within 25 GeV of the mass of the Z. The p_{T} of the

leptonically decaying Z is then added to the $E_{\mathrm{T}}^{\mathrm{miss}}$. Equation 6.7 states the values of the scaling factor and the statistical uncertainties for both jet-multiplicity selections.

$$\begin{aligned} N_j \leq 3: &\quad \kappa = 0.77 \pm 0.04 \\ N_j \geq 4: &\quad \kappa = 0.85 \pm 0.05 \end{aligned} \tag{6.7}$$

These scaling factors are applied to the γ + jets samples in the CRγ in order to obtain the TF for extrapolation of the background event yields onto the respective SR

$$N_{SR}^{pred}(\mathrm{Z} \to \nu\bar{\nu}) = N_{SR}^{MC}(\mathrm{Z} \to \nu\bar{\nu}) \times \frac{N_{CR\gamma}^{data}(\gamma + jets)}{\kappa . N_{CR\gamma}^{\mathrm{MC}}(\gamma + jets)}. \tag{6.8}$$

W+jets and Top Semileptonic $t\bar{t}$ and single top as well as $\mathrm{W}(\to \ell\nu)$ + jets events contribute to the $E_{\mathrm{T}}^{\mathrm{miss}}$ via processes involving the hadronic decay of a τ lepton, which is created together with a neutrino. These processes are modelled in the respective CRs by treating the high purity lepton, required in CRW and CRT, as jet. The transverse mass of this lepton and the $E_{\mathrm{T}}^{\mathrm{miss}}$, defined in Equation 6.5, is limited to a window of 30 to 100 GeV. In order to distinguish between the W and top processes, events with b-tagged jets are vetoed in the CRW, while at least one such b-jet is required in the CRT. Both CRs omit the SR requirements on $\Delta\phi$ for all BDT and MB channels. In case of the MB search the cut on $E_{\mathrm{T}}^{\mathrm{miss}}/\sqrt{H_{\mathrm{T}}}$ indicated in Table 6.4 is used to ensure a sufficient number of data events in the CRs and effectively suppress the increase of theoretical uncertainties on the background prediction caused by kinematic deviations of CR and SR. Bins with different selections on $E_{\mathrm{T}}^{\mathrm{miss}}/\sqrt{H_{\mathrm{T}}}$ are merged if they have the same cuts on N_j and m_{eff}.

The contribution of Z + jets, W + jets, top anti-top pair and single top processes to the event yields in each SR are then estimated via a combined background-only fit using the HistFitter program (cf. subsection 5.4.3). This fit, which also includes the contribution of the mutlijet background described in subsection 6.3.1, is constrained solely by the event yields in the CRs assigned to each SR assuming that no events from BSM processes contribute to these yields. It fits the prediction of all background processes to the observed yields in all CRs simultaneously, in order to obtain the respective scale factors μ(W + jets), μ(Z + jets), μ(top) and μ(QCD). These factors are then used to correct the predictions of background event yields in the individual SR.
Figure 6.2 shows the μ-factors for MC simulated background processes in all bins of the three MB channels and for all eight BDT selections. The systematic and statistical uncertainties on the scaling factors are indicated by the coloured bars depicted in the plot. These uncertainties are included in the fit as NPs constrained by Gaussian distributions. The individual contributions to the overall uncertainties are described in section 6.4. Common features of the normalisation factors are observed for all SR selections in the different analysis channels. While μ(Z + jets) and μ(W + jets) are stable with changing kinematics independently of the underlying search strategy, a general trend can be seen for μ(top). In the MB channels the top scaling factor decreases for tighter selections. A similar decrease is visible in the BDT SRs with the increase of the BDT score cut.
Even though obtained from the simultaneous background-only fit, the scaling factors of the multijet

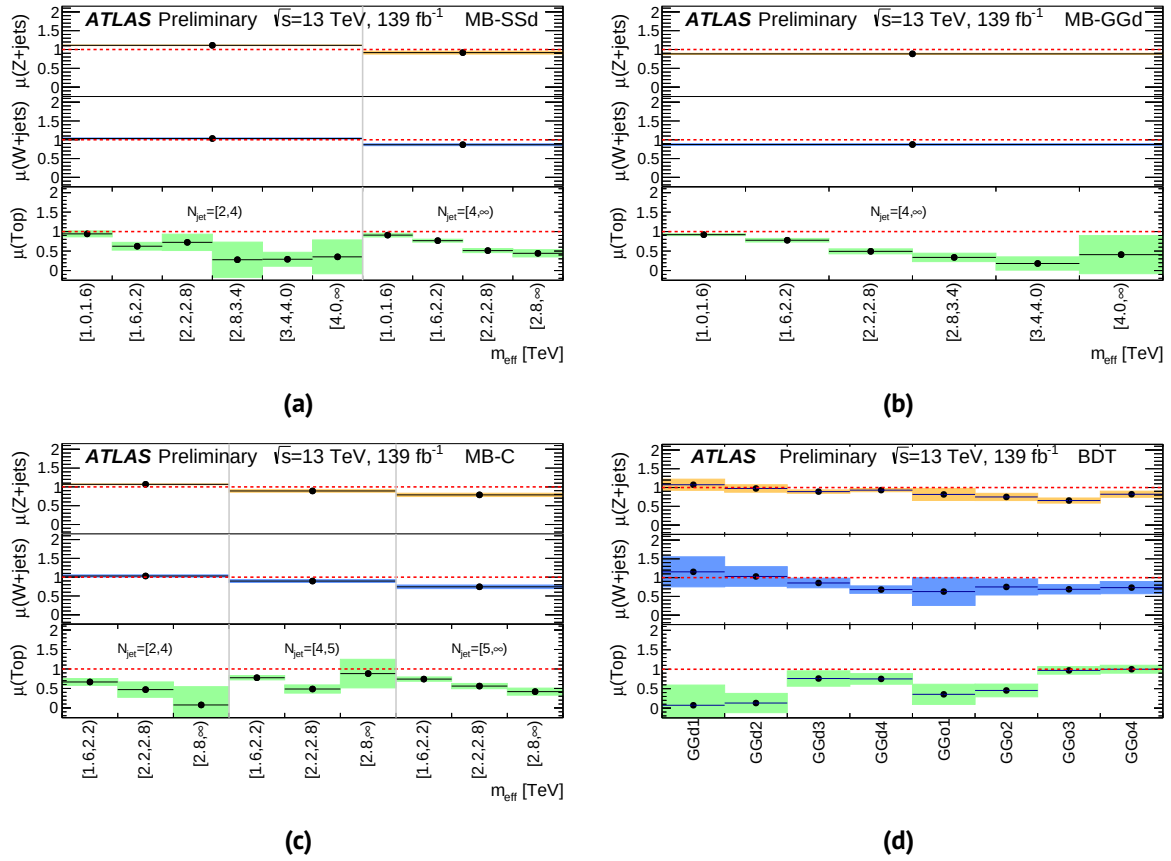

Figure 6.2: The scaling factors obtained from the background-only fit, given for each background process, modelled in MC, as a function of the SR bins in the MB-SSd (Figure 6.2a), MB-GGd (Figure 6.2b) and MB-C (Figure 6.2c) channel as well as the SRs included in the BDT-GGd and BDT-GGo searches (Figure 6.2d). The pure MC estimates are shown as dashed horizontal lines at one and the total uncertainties on the scaling factors are indicated by the vertical size of the coloured areas.

background, μ(QCD), are not shown in Figure 6.2, since the normalisation of this data-driven background estimation is arbitrary.

In case of the QCD and $t\bar{t}$ background an individual scaling factor is assigned to each bin included in the MB search, while for well modelled backgrounds like the W + jets and Z + jets a single μ-factor is derived per jet multiplicity. This specific choice of the MB fit-setup reflects in particular the mis-modelling of the top background in MC known from previous observations.

Unlike the three major background components described above, which are modelled in the CRs using MC samples, the QCD multijet background is estimated using a data-driven technique, the so called *JetSmearing*. The adaption of this method and its implementation into the 0L (2-6jets) SUSY analysis as well as the necessary optimisation studies, is one of the main contributions of the author to this analysis. Hence, subsection 6.3.1 is dedicated to the estimation of the QCD background.

6.3.1 Multijet Background Estimiation with JetSmearing

The multijet background is the only contribution to the overall background in the inclusive 0L search, which is not associated to one particular physics process, but comprises contributions from

different sources, e.g. QCD, hadronic $t\bar{t}$, etc. It does not contain any sources of real $E_{\mathrm{T}}^{\mathrm{miss}}$, except the production of neutrinos in hadronisation processes. Its major contribution comes from fake $E_{\mathrm{T}}^{\mathrm{miss}}$ of various sources:

- limited granularity of the hadronic calorimeters leads to imperfect measurement of the jet energy
- jet constituents may be lost due to interactions with non-active detector material
- not all constituents of the jet may lie within the reconstructed jet cone, resulting in a loss of energy
- punch-through jets, i.e high energetic hadronic particles, which are not stopped in the calorimetric system and reach the MS
- small areas of dead material in the calorimetric system, due to damages, service structures and electronics not included in the regions vetoed by the dead-tile cleaning

In order to effectively simulate the significant energy mis-measurement caused by detector effects, an enormous amount of simulated events has to be produced. Although such MC samples are available, it was observed that these samples suffer from severe inaccuracies - in particular for events with large $E_{\mathrm{T}}^{\mathrm{miss}}$ - due to hard-to-model features like timing dependency and JER dependencies of the jet measurement. Furthermore, the QCD background depends on the pile-up conditions and can vary greatly over the data taking periods.
The JetSmearing method [126] is a well established technique, widely used in ATLAS BSM searches, to accurately describe the multijet background in the presence of significant $E_{\mathrm{T}}^{\mathrm{miss}}$. The basic idea of this method is to modify, or "smear", the properties of jets measured in data events based on the *jet energy response* derived from simulated events.

Constructing the Energy Response The energy response R_E is defined by the ratio of the reconstructed jet energy to the energy of the particle level jet (truth jet)

$$R_E = \frac{E_{reco}}{E_{truth}}. \tag{6.9}$$

It is a measure for the intrinsic resolution associated to the reconstruction of jets with an ideal value of one. In case R_E is smaller than one, the energy of the reconstructed jet was measured too low. Similarly, the jet energy was over-measured if the response is lager than one. Figure 6.3 shows the energy response as a function of the p_{T} of the truth jet derived from multijet samples simulated with PYTHIA8 (Figure 6.3a) and b-tagged jets (Figure 6.3b), reflecting the pile-up conditions during the 2017 and 2018 data-taking period, i.e. based on MC16d samples. Similar maps are produced for the early Run 2 data using MC16a samples.
R_E is constructed selecting truth and reconstructed jets (anti-k_t jets with a cone-size of 0.4) with a p_{T} above 20 GeV. For each truth jet, the respective reconstructed jet is identified using a geometric matching procedure comprising the following steps:

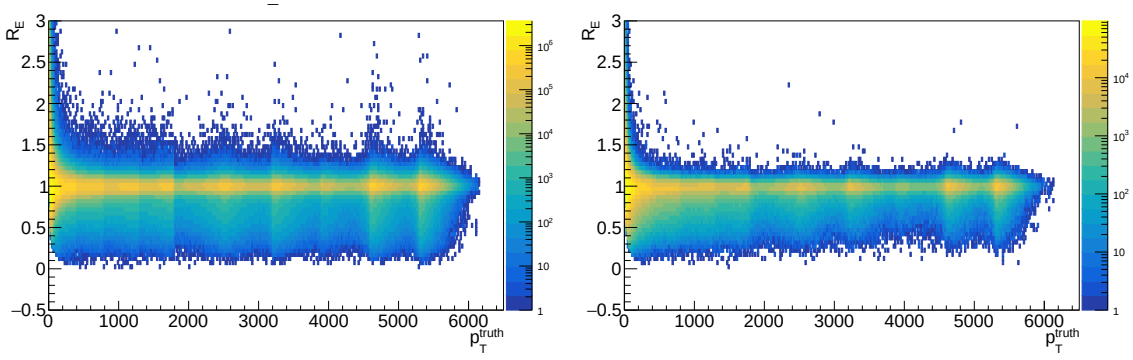

(a) (b)

Figure 6.3: The *jet response maps* for light jets (Figure 6.3a) and b-jets (Figure 6.3b) show the jet response measured from multijet events simulated with PYTHIA8 binned with respect to the truth jet p_T.

- The closest reconstructed jet to a given truth jet is the one with the minimal distance parameter ΔR. This closest reconstructed jet is considered to be the correct reconstruction of the truth jet.
- If no reconstructed jet within a cone of size $\Delta R = 0.3$ is found, the truth jet is not taken into account.
- The matching is required to be unique. Hence, a truth jet is discarded if a second reconstructed jet lies within $\Delta R < 0.6$.
- Reconstructed jets need to be isolated, i.e. no other reconstructed jet is allowed in a cone of size 0.6 around a matched reconstructed jet.
- The same isolation criteria applies to truth jets.

In order to correctly model the real E_T^{miss} contributions from neutrinos produced in the shower, neutrinos are added to the four-momentum of the truth jet if they are within $\Delta R < 0.4$. However, this contribution is rather small if no heavy-flavour decays are involved in the hadronisation process, as is the case for the decay of first and second generation squarks and gluinos, respectively.

Applying the JetSmearing Method Based on the energy response the energy of each jet in an event can be altered by modifying the four-vector of the jet. From a given hadronic data event, a so called *seed event*, containing n jets, a number of *pseudo-events* can be generated, as depicted in Figure 6.4.

To create m such pseudo-events $n \times m$ random numbers are obtained from the response map according to the p_T of the n original jets. Equation 6.10 describes the smearing of such an event

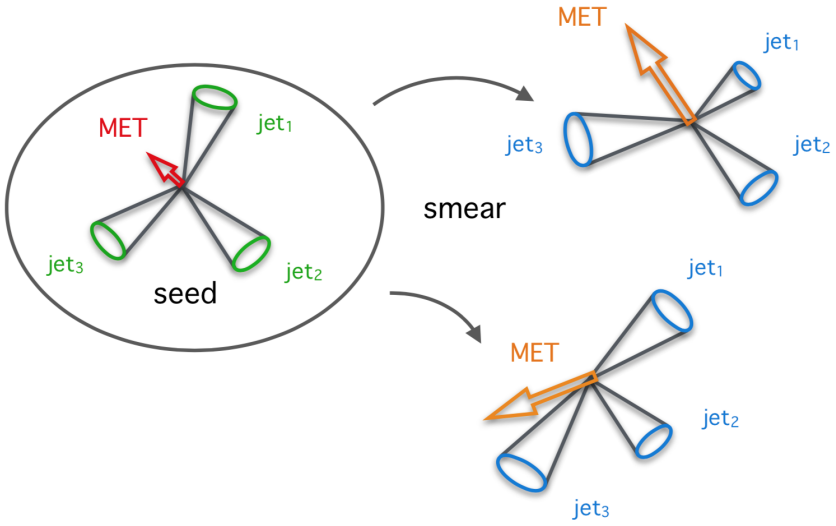

Figure 6.4: Pictorial overview of the JetSmearing method indicating jets by cones originating from the PV and $E_{\mathrm{T}}^{\mathrm{miss}}$ by the red and orange arrows, respectively.

using the random numbers $a_i, b_i, \ldots, m_i$ with $i = 1, 2, \ldots, n$ indicating the jets.

$$\begin{pmatrix} E_1 \\ \vec{p_1} \end{pmatrix} \quad \begin{pmatrix} E_2 \\ \vec{p_2} \end{pmatrix} \quad \ldots \quad \begin{pmatrix} E_n \\ \vec{p_n} \end{pmatrix} \rightarrow \begin{cases} a_1 \begin{pmatrix} E_1 \\ \vec{p_1} \end{pmatrix} & a_2 \begin{pmatrix} E_2 \\ \vec{p_2} \end{pmatrix} & \ldots & a_n \begin{pmatrix} E_n \\ \vec{p_n} \end{pmatrix} \\ b_1 \begin{pmatrix} E_1 \\ \vec{p_1} \end{pmatrix} & b_2 \begin{pmatrix} E_2 \\ \vec{p_2} \end{pmatrix} & \ldots & b_n \begin{pmatrix} E_n \\ \vec{p_n} \end{pmatrix} \\ \vdots & \vdots & & \vdots \\ m_1 \begin{pmatrix} E_1 \\ \vec{p_1} \end{pmatrix} & m_2 \begin{pmatrix} E_2 \\ \vec{p_2} \end{pmatrix} & \ldots & m_n \begin{pmatrix} E_n \\ \vec{p_n} \end{pmatrix} \end{cases} \tag{6.10}$$

In the inclusive 0L search an optimal number of smearing processes was found to be $m = 1000$. The $E_{\mathrm{T}}^{\mathrm{miss}}$ in the pseudo data events is calculated as

$$\mathbf{E}_T^{miss\prime} = \mathbf{E}_T^{miss,seed} - \sum_i \mathbf{p}_{\mathrm{T}}\prime(j_i) + \sum_i \mathbf{p}_{\mathrm{T}}(j_i), \tag{6.11}$$

where the smeared quantities are primed. $\mathbf{E}_T^{miss\prime}$ can be much larger, than the $E_{\mathrm{T}}^{\mathrm{miss}}$ in the seed event $\mathbf{E}_T^{miss,seed}$ depending on the jet directions, which are modified additionally by the $\Delta\phi$ correction, described below.

The selection of "proper" seed events is crucial for this technique to successfully describe the multijet background in the CRQ for all search channels in the analysis. Hence, the seed-selection needs to be carefully optimised in order to avoid any bias in the distributions of key variables, in particular the p_{T}, $E_{\mathrm{T}}^{\mathrm{miss}}$ and $\Delta\phi(j, E_{\mathrm{T}}^{\mathrm{miss}})$ spectra. It was found that the significance of the $E_{\mathrm{T}}^{\mathrm{miss}}$,

which is related to the calorimeter response, can be slightly modified to serve as optimal base variable for such a selection, since it is invariant under the variation of jet-multiplicity. $E_{\mathrm{T}}^{\mathrm{miss}}\,Sig$, described in subsection 6.2.1 as $E_{\mathrm{T}}^{\mathrm{miss}}/\sqrt{H_{\mathrm{T}}}$, is adjusted to account for the resolution of the soft term $E_{\mathrm{T}}^{\mathrm{miss,\,soft}}$ by means of the parameter M which is tuned to remove any residual bias in the distributions

$$E_{\mathrm{T}}^{\mathrm{miss}}\,Sig = \frac{E_{\mathrm{T}}^{\mathrm{miss}} - M}{\sqrt{\sum E_T}}. \tag{6.12}$$

An extensive optimisation study was performed in order to determine the exact values for the selection cuts, guaranteeing a sufficient modelling of the key distributions.
In addition to the variation of the soft parameter and the value for $E_{\mathrm{T}}^{\mathrm{miss}}\,Sig$, defined in Equation 6.12, a new definition of the $E_{\mathrm{T}}^{\mathrm{miss}}$ significance was tested. This variable is called object based (OB) MET significance [127] and is based on testing the hypothesis that the p_{T} of all invisible particles (p_{T}^{inv}) is non-zero against the case where all particles are detected. A LH function $\mathcal{L}(E_{\mathrm{T}}^{\mathrm{miss}}|p_{\mathrm{T}}^{inv})$ is calculated and maximised assuming $p_{\mathrm{T}}^{inv} = 0$ and $p_{\mathrm{T}}^{inv} \neq 0$. The significance of the $E_{\mathrm{T}}^{\mathrm{miss}}$ is then defined as

$$\mathcal{S}^2 = 2\,\ln\left(\frac{max_{p_{\mathrm{T}}^{inv}\neq 0}\,\mathcal{L}(E_{\mathrm{T}}^{\mathrm{miss}}|p_{\mathrm{T}}^{inv})}{max_{p_{\mathrm{T}}^{inv}=0}\,\mathcal{L}(E_{\mathrm{T}}^{\mathrm{miss}}|p_{\mathrm{T}}^{inv})}\right). \tag{6.13}$$

The $E_{\mathrm{T}}^{\mathrm{miss}}$ in this definition depends on the multiplicity and the kinematics of the involved objects, such that the soft term is already accounted for correctly.
Table 6.14 lists a few examples of event selection cuts studied in order to find the optimal seed selection.

Significance of E_T^{miss}	*Soft Parameter M*	*Condition*
$E_{\mathrm{T}}^{\mathrm{miss}}\,Sig$	0 GeV	< 0.2
$E_{\mathrm{T}}^{\mathrm{miss}}\,Sig$	8 GeV	< 0.1
$E_{\mathrm{T}}^{\mathrm{miss}}\,Sig$	8 GeV	< 1.0
OB METsig	-	< 0.1
OB METsig	-	< 0.2
OB METsig	-	< 1.0

Table 6.14: Examples for different selections, studied to optimise the seed selection cuts used in the JetSmearing method.

Distributions of key variables ($\Delta\phi(j, E_{\mathrm{T}}^{\mathrm{miss}})$, $p_T(j_1)$, $E_{\mathrm{T}}^{\mathrm{miss}}$, m_{eff}, ...) based on each seed selection were compared. Seed selections based on OB METsig generally show a significant mis-modelling in large $\Delta\phi$ tails and in soft p_{T} regions, while this overestimation can be avoided using a tight cut on $E_{\mathrm{T}}^{\mathrm{miss}}\,Sig$. Applying a requirement on the soft parameter is crucial in order to prevent overestimating the multijet background in regions of moderate p_{T} as well as large statistical fluctuations in the high $E_{\mathrm{T}}^{\mathrm{miss}}$ tails and for very hard jets. Following the result of these optimisation studies, a cut on $E_{\mathrm{T}}^{\mathrm{miss}}\,Sig$ of 0.1 $\sqrt{\mathrm{GeV}}$ with a soft parameter M = 8 GeV was chosen.

Figure 6.5 shows the p_T and E_T^{miss} spectra of preselected pseudo-events generated from a single seed event after 1000 smearing steps.

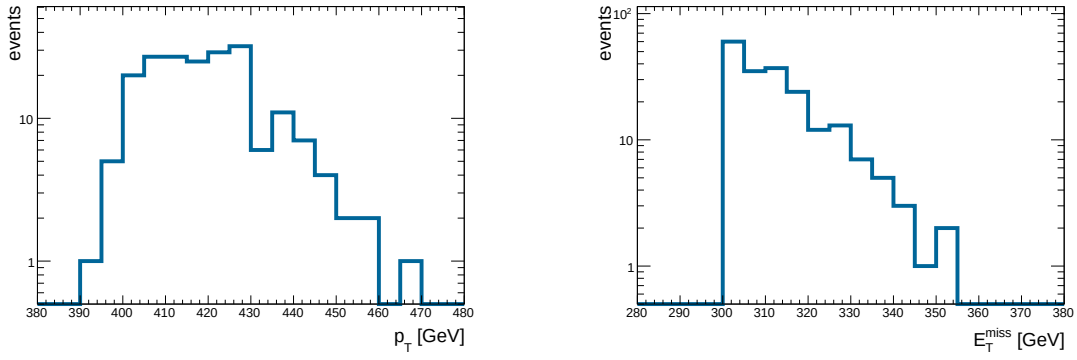

(a) **(b)**

Figure 6.5: Distribution of p_T (Figure 6.5a) and E_T^{miss} (Figure 6.5b) of preselected smeared events generated from a single seed event.

Selected seed events are not required to fulfil the preselections listed in Table 6.3, in particular the E_T^{miss} can be of the order of a few GeV, much smaller than the preselection threshold of 300 GeV. Thus, the E_T^{miss}-trigger used to select signal event candidates in the 0L (2-6jets) SUSY analysis can not be used to obtain possible seed events. Instead, a combination of single jet triggers was used for each data-taking period, as listed in Table 6.15. These HLTs are partially afflicted with very large prescale weights, depending on the jet p_T (cf. subsection 3.2.5). Hence, the overall weights of the jets in the seed events had to be calculated accordingly.

Data-taking Period	*Single Jet Triggers*
2015	HLT_j360, HLT_j260, HLT_j175, HLT_j110, HLT_j85, HLT_j60, HLT_j55, HLT_j45, HLT_j35, HLT_j25, HLT_j15
2016	HLT_j380, HLT_j360, HLT_j260, HLT_j175, HLT_j110, HLT_j85, HLT_j60, HLT_j45, HLT_j35, HLT_j25, HLT_j15
2017	HLT_j420, HLT_j400, HLT_j360, HLT_j260, HLT_j175, HLT_j110, HLT_j85, HLT_j60, HLT_j45, HLT_j35, HLT_j25, HLT_j15
2018	HLT_j420, HLT_j400, HLT_j360, HLT_j260, HLT_j175, HLT_j110, HLT_j85, HLT_j60, HLT_j45, HLT_j35, HLT_j25

Table 6.15: Summary of single jet HLTs for each Run 2 data-taking period, used to select seed events from which pseudo-events are created via the JetSmearing method.

$\Delta\phi$ Correction The mis-measurement of jets does not only alter the jet energy but can also effect the direction of the jet, i.e. the true axis of the jet cone can be mis-reconstructed. This effect needs to be accounted for, since the main variable used to suppress the QCD background in the inclusive 0L search, $\Delta\phi(j_{1,2,(3)}, \mathbf{p}_T^{miss})_{\,min}$, is based on the alignment of the directions of the jets and the missing transverse momentum. Thus, a correction is derived which is applied on pseudo-events in order to describe the widening of the $\Delta\phi(j, E_T^{miss})$ distribution.
The $\Delta\phi$ correction factor is obtained by adjusting the distribution of the azimuthal distance $\Delta\phi(j_1, j_2)$ between the two jets in well balanced dijet pseudo-events to match the distribution observed in data. Hence, events fulfilling the requirements listed in Table 6.16 are selected from data as well as

from pseudo-data. These events are used to construct the $\Delta\phi(j_1,j_2)$ distributions as a function of

N_j ($p_T > 50$ GeV, $\|\eta\| < 2.5$)	2-3
$p_T(j_1)$ [GeV]	> 100
$p_T(j_2)$ [GeV]	> 50
$\|\Delta\phi(j_1,j_2)\|$	$> \pi$-0.25
$E(j_3)$	$< E(j_1), E(j_2)$
$p_T(j_3)/\langle p_T \rangle$	< 0.1

Table 6.16: Selection of dijet events used to derive the $\Delta\phi$ correction applied in the JetSmearing method.

the average dijet p_T. The width of the distribution for data and pseudo-data events is then fitted with

$$\sigma(\Delta\phi(j_1,j_2)) = \frac{a}{p_T} + \frac{b}{\sqrt{p_T}} + c \tag{6.14}$$

by varying the arbitrary parameters a, b and c. The correct width of the ϕ resolution $\sigma_{final}(\phi)$ is derived by applying the correction via convolution of two Gaussians, $\sigma_{pseudo}(\phi)$ and $\sigma_{corr}(\phi)$

$$\sigma_{final}(\phi) = \sqrt{\sigma_{pseudo}(\phi)^2 + \sigma_{corr}(\phi)^2}. \tag{6.15}$$

The correction $\sigma_{corr}(\phi)$ is defined by the requirement that $\sigma_{final}(\Delta\phi)$ matches $\sigma_{data}(\Delta\phi)$ the observed width in data

$$\sigma_{corr}(\phi) = \frac{1}{\sqrt{2}} \sqrt{\sigma_{data}(\Delta\phi)^2 - \sigma_{pseudo}(\Delta\phi)^2}. \tag{6.16}$$

The correction corresponds to a rotation of the seed jet about the z-axis based on a random number which is created from $\sigma_{corr}(\phi)$ as function of the jet p_T. Figure 6.6a shows the distribution of azimuthal distance $\Delta\phi(j_1,j_2)$ of the dijet system obtained from dijet MC events, data and pseudo-data events for one bin of average jet p_T. The resulting Gaussian width $\sigma(\Delta\phi(j_1,j_2))$ as a function of the average p_T is shown in Figure 6.6b.

Unlike in previous productions of multijet MC samples, the JER in MC16a and MC16d samples and in the respective data-sets is found to be in good agreement. Hence, no additional corrections on the jet p_T smearing is necessary.

The pseudo-event samples obtained by the JetSmearing method are normalised in order to match the observed $\Delta\phi(j_{1,2,(3)}, \mathbf{p}_T^{\text{miss}})_{\text{min}}$ distribution in data in the QCD CRs (cf. Table 6.13) assigned to each SR in the 0L (2-6jets) SUSY analysis. Figure 6.7 shows a comparison of the $\Delta\phi(j_{1,2,(3)}, \mathbf{p}_T^{\text{miss}})_{\text{min}}$ distribution in the CRQ for the MB-SSd preselection, omitting the cut on $\Delta\phi$ itself, for normalised pseudo-data and a MC multijet sample. Additional distributions for the key variables, E_T^{miss}(Figure 6.8), m_{eff} (Figure 6.9) and the p_T of the leading jet (Figure 6.10), are shown.

These plots demonstrate, that the multijet background in the CRQ is very well modelled in pseudo-data. However, the QCD MC samples generated in the MC16a, MC16d and MC16e production

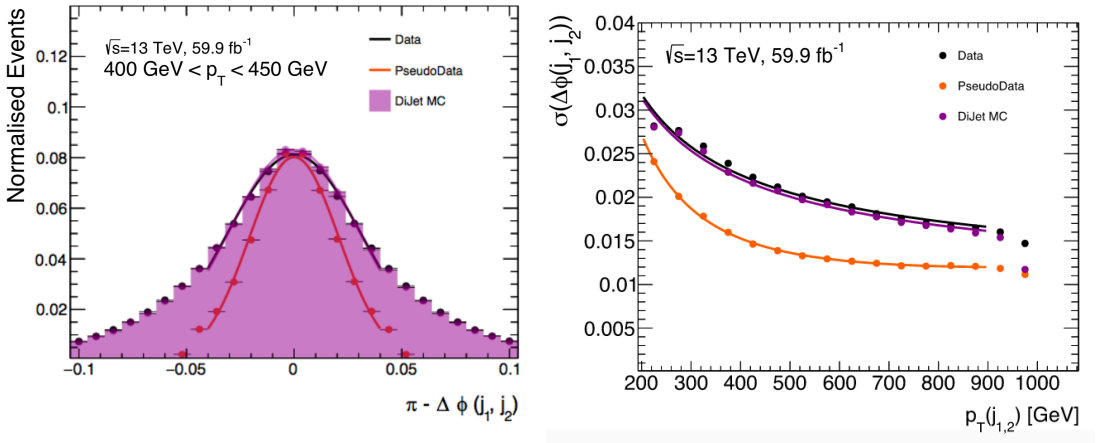

(a) (b)

Figure 6.6: The distribution of $\Delta\phi(j_1, j_2)$ for an average p_T of the dijet system between 400 and 450 GeV (Figure 6.6a) as well as $\sigma(\Delta\phi(j_1, j_2))$ as a function of the average p_T (Figure 6.6b) shown for a subset of the full Run 2 data-set corresponding to a luminosity of 59.9 fb^{-1} and the respective set of pseudo-events. Simulated dijet MC events are shown for comparison [128].

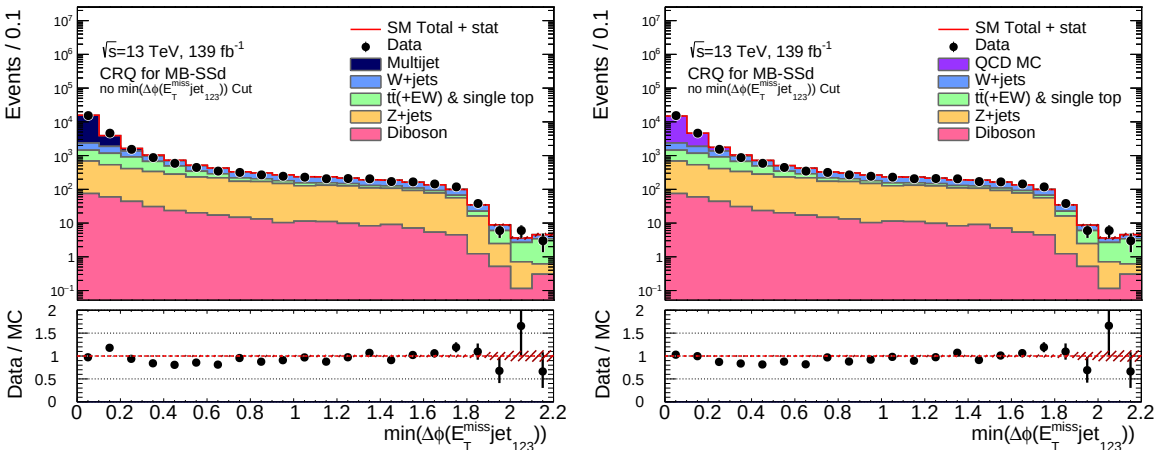

(a) (b)

Figure 6.7: The $\Delta\phi(j_{1,2,(3)}, \mathbf{p}_T^{\text{miss}})_{\text{min}}$ distribution produced from pseudo-data (Figure 6.7a) and QCD MC (Figure 6.7b) in the CRQ of the MB-SSd channel without applying the cut on $\Delta\phi(j_{1,2,(3)}, \mathbf{p}_T^{\text{miss}})_{\text{min}}$, including statistical errors only and overflow events in the last bin.

campaign are also remarkably accurate. Non of the pathological slopes, observed in previous QCD MC productions, are present. Nonetheless, the JetSmearing method provides a superior and more reliable description of the multijet background, as is apparent in Figure 6.11 and Figure 6.12. These plots, which show the same comparison of key distributions for the MB-SSd preselection, illustrate the deficiencies of the QCD MC samples. In addition to the severe lack of events in the extreme SR phase space, events with undue weights are observed in case of QCD MC, indicating problems in the simulation of QCD processes with large contributions from fake E_T^{miss} and a profound misalignment of the jets and the E_T^{miss}.

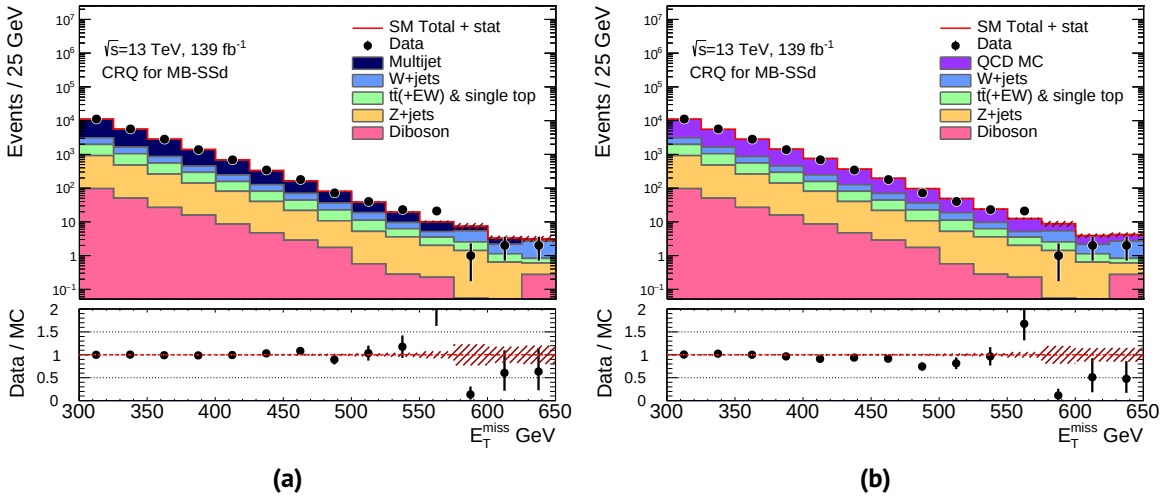

Figure 6.8: The $E_{\mathrm{T}}^{\mathrm{miss}}$ distribution produced from pseudo-data (Figure 6.8a) and QCD MC (Figure 6.8b) in the CRQ of the MB-SSd channel, including statistical errors only and overflow events in the last bin.

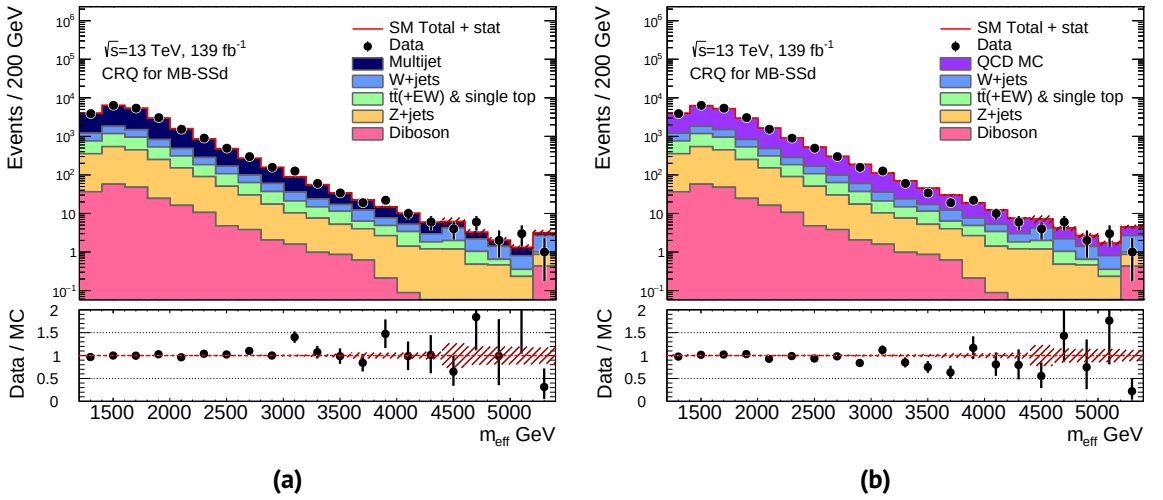

Figure 6.9: The m_{eff} distribution produced from pseudo-data (Figure 6.9a) and QCD MC (Figure 6.9b) in the CRQ of the MB-SSd, including statistical errors only and overflow events in the last bin.

In order to cover systematic uncertainties introduced by the construction of the energy response maps and the application of the $\Delta\phi$ corrections, a maximal conservative error of 100% on the pseudo-data events is assumed. This approach is justified because the multijet background gives only minor contributions in the SRs, thus having an almost negligible effect on the overall uncertainties (cf. section 6.4).

Figure 6.13 shows the distribution of m_{eff} in the four main CRs assigned to the MB-GGd preselection channels. In case of the BDT analysis the main discriminator is the BDT score instead of m_{eff}. Hence, an example of BDT score distributions in the CRs of one of the BDT search channels is given in

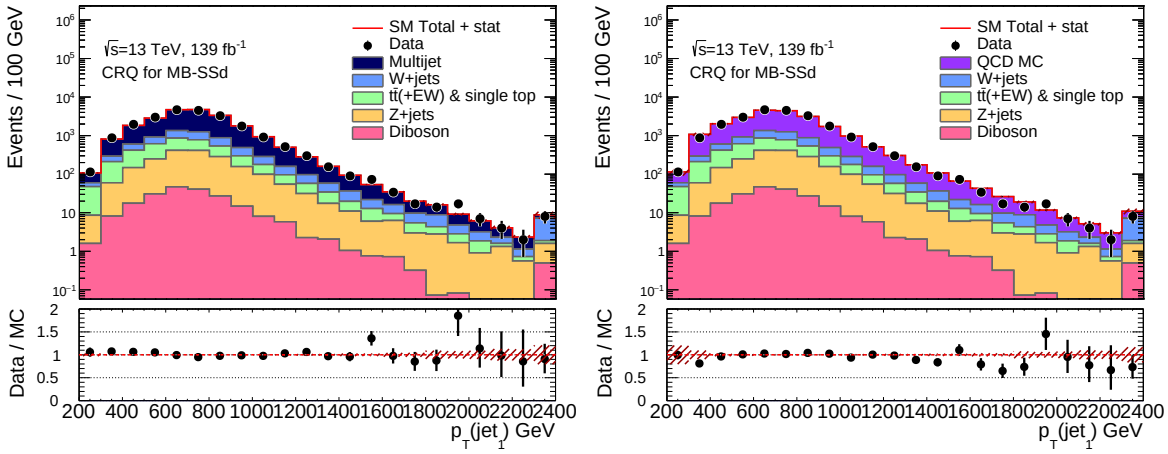

Figure 6.10: The leading jet p_{T} distribution produced from pseudo-data (Figure 6.10a) and QCD MC (Figure 6.10b) in the CRQ of the MB-SSd channel, including statistical errors only and overflow events in the last bin.

Figure 6.14. Generally, a good agreement between data and MC prediction in all CRs is observed, with the exception of the CRT, dominated by contributions from top anti-top pair and single top production. The POWHEG generator used to simulate $t\bar{t}$ events yields harder jet p_{T} spectra, resulting in harder m_{eff} spectra, than measured in data.

The production of variable distributions for various SR, CR and VR selections, such as the plots in Figure 6.13 and Figure 6.14, is a computationally challenging task. Contributions from all three MC generations (MC16a, MC16d and MC16e) scaled with respect to their associated luminosity as well as all data-sets collected during the full Run 2 data-taking are combined. Additionally, a large number of systematic uncertainties, discussed in detail in section 6.4, needs to be taken into account. The resulting size of a MC sample, describing just a single background process, is of the order of 100 GB. Depending on the region depicted, several such samples are shown in one plot, requiring sophisticated programming techniques (e.g. the parallelisation of multiple processes) in order to keep the computing time and the amount of utilised CPU memory at a reasonable level. The development of a suitable software package, interfaced with the fitting package of the analysis, as well as the production of the distribution plots was one of the author's responsibilities.

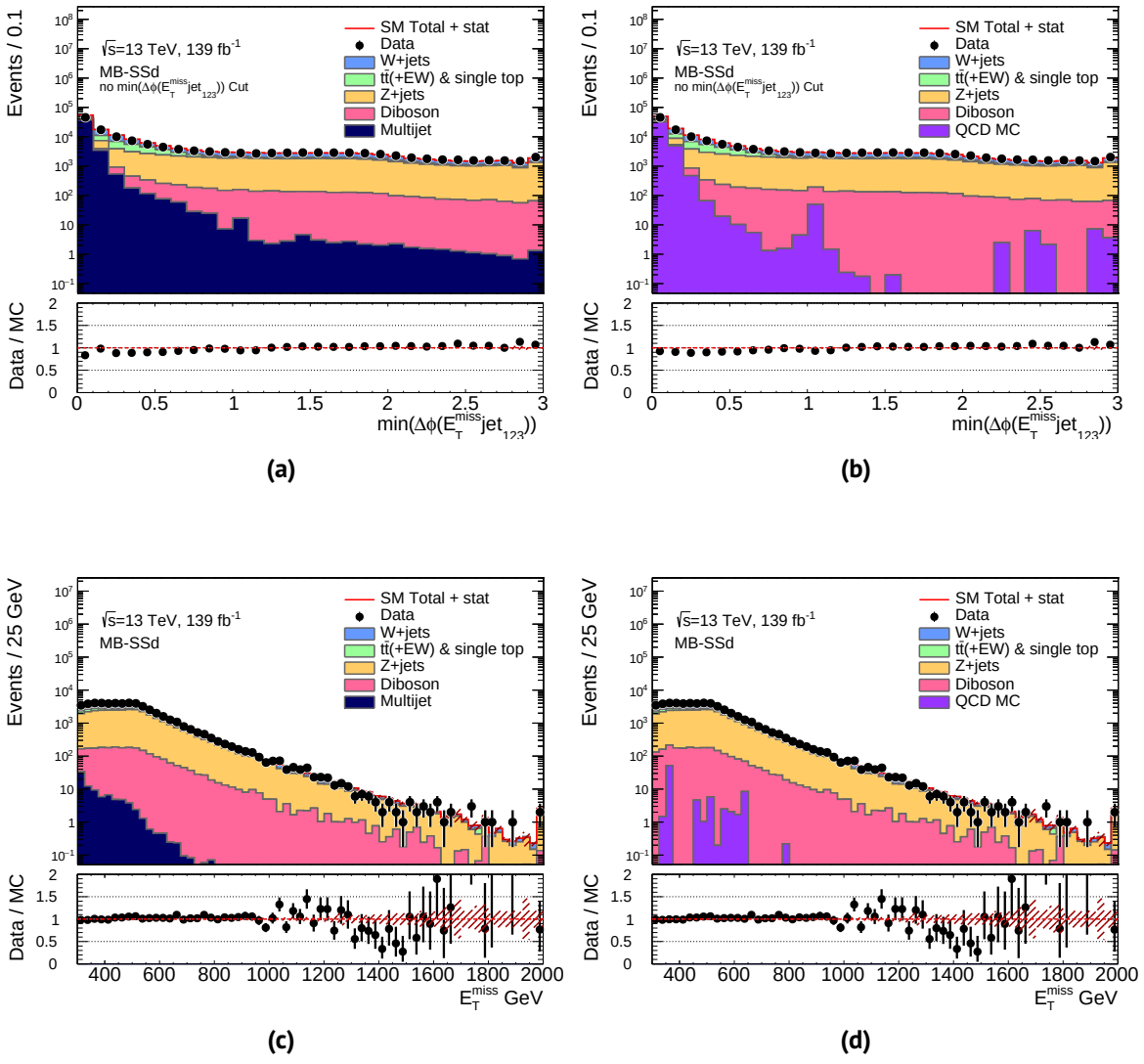

Figure 6.11: The $\Delta\phi$ and $E_{\mathrm{T}}^{\mathrm{miss}}$ distribution produced from pseudo-data (Figure 6.11a and Figure 6.11c) and QCD MC (Figure 6.11b and Figure 6.11d) in the MB-SSd channel, including statistical errors only and overflow events in the last bin.

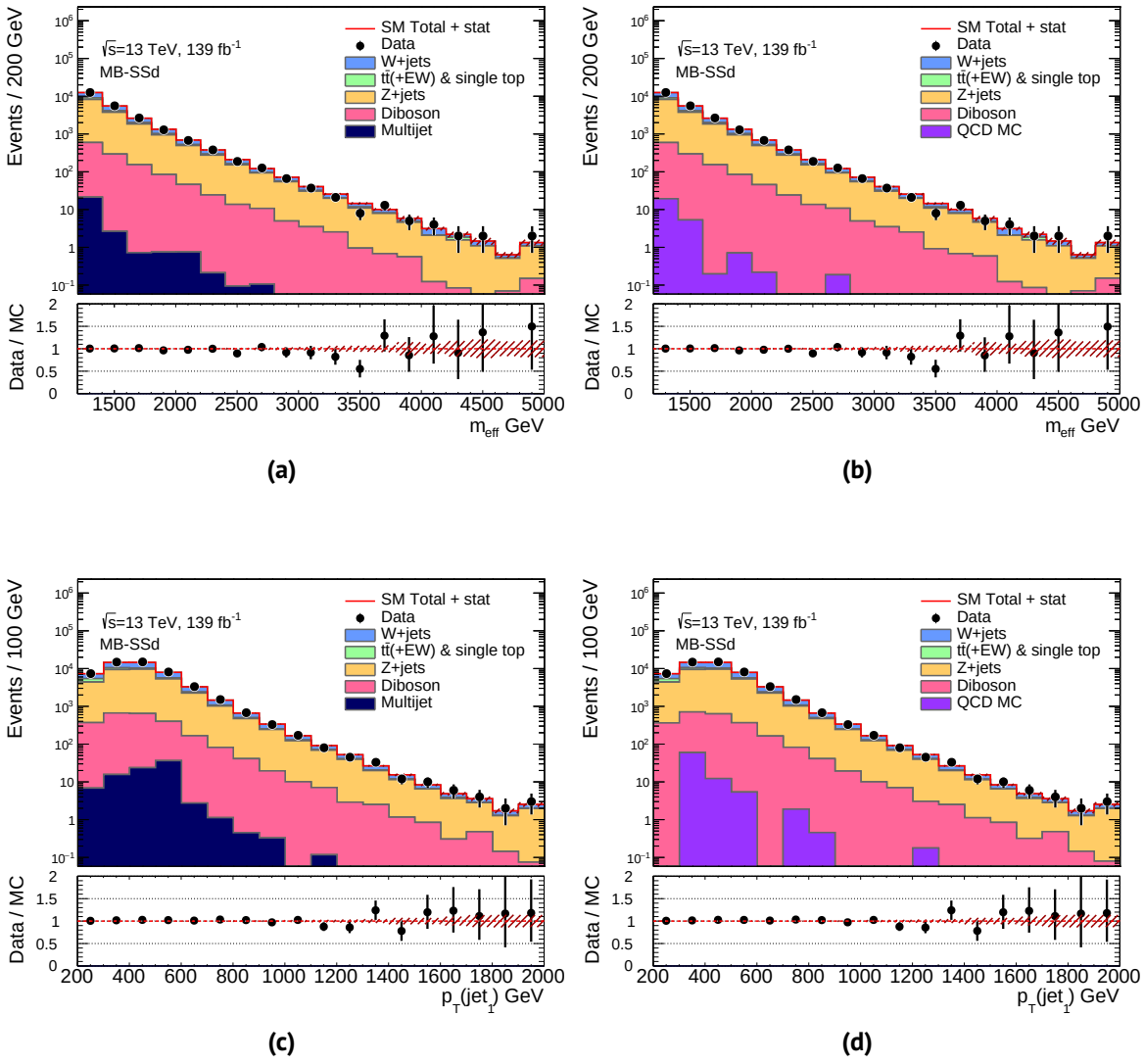

Figure 6.12: The leading jet m_{eff} and p_{T} distribution produced from pseudo-data (Figure 6.12a and Figure 6.12c) and QCD MC (Figure 6.12b and Figure 6.12d) in the MB-SSd channel, including statistical errors only and overflow events in the last bin.

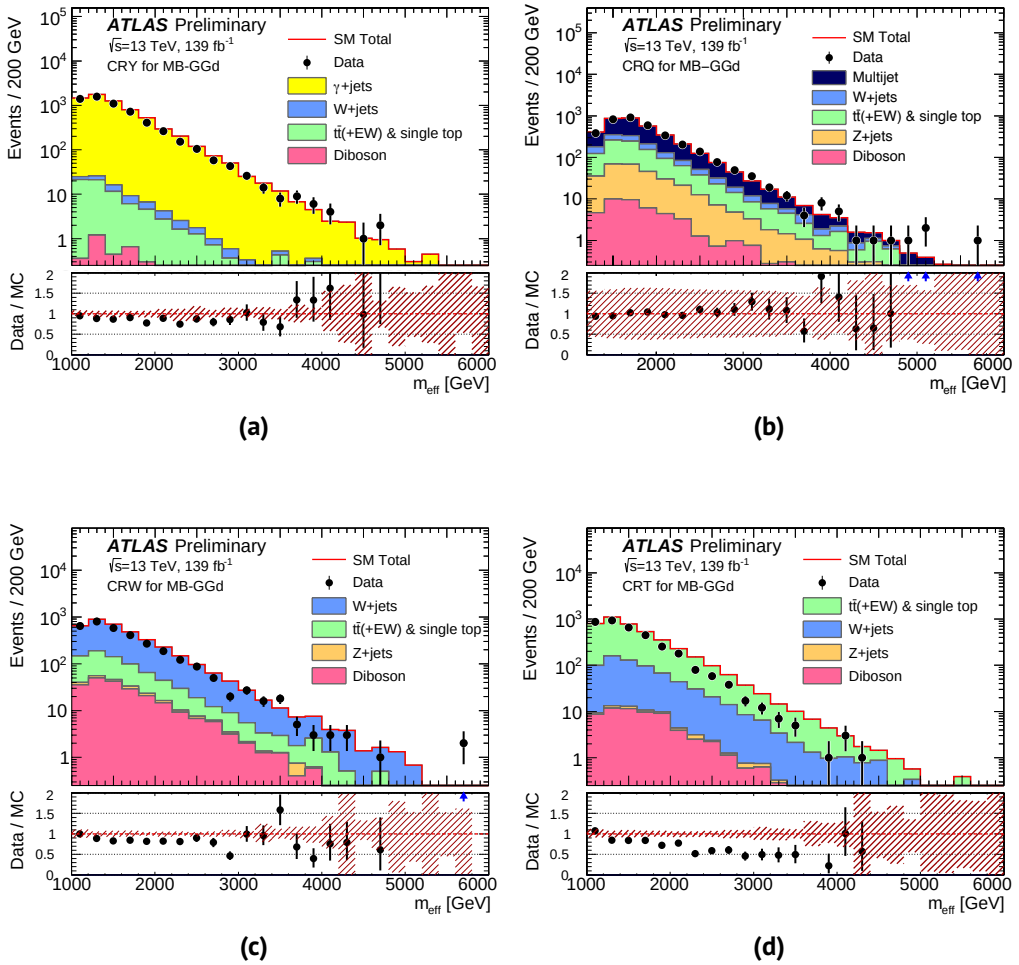

Figure 6.13: Observed m_{eff} distributions in the CRs based on the MB-GGd selection listed in Table 6.4. MB-CRγ (Figure 6.13a), MB-CRQ (Figure 6.13b), MB-CRW (Figure 6.13c) and MB-CRT (Figure 6.13d) are shown. The plots include the MC background predictions normalised solely by cross-section $\times$ luminosity and the multijet background modelled using pseudo-data normalised to data in the CRQ, respectively. For the γ + jets background an additional scaling factor κ, defined in Equation 6.6, is applied. The combined experimental and statistical uncertainties are indicated by the hatched red error bands.

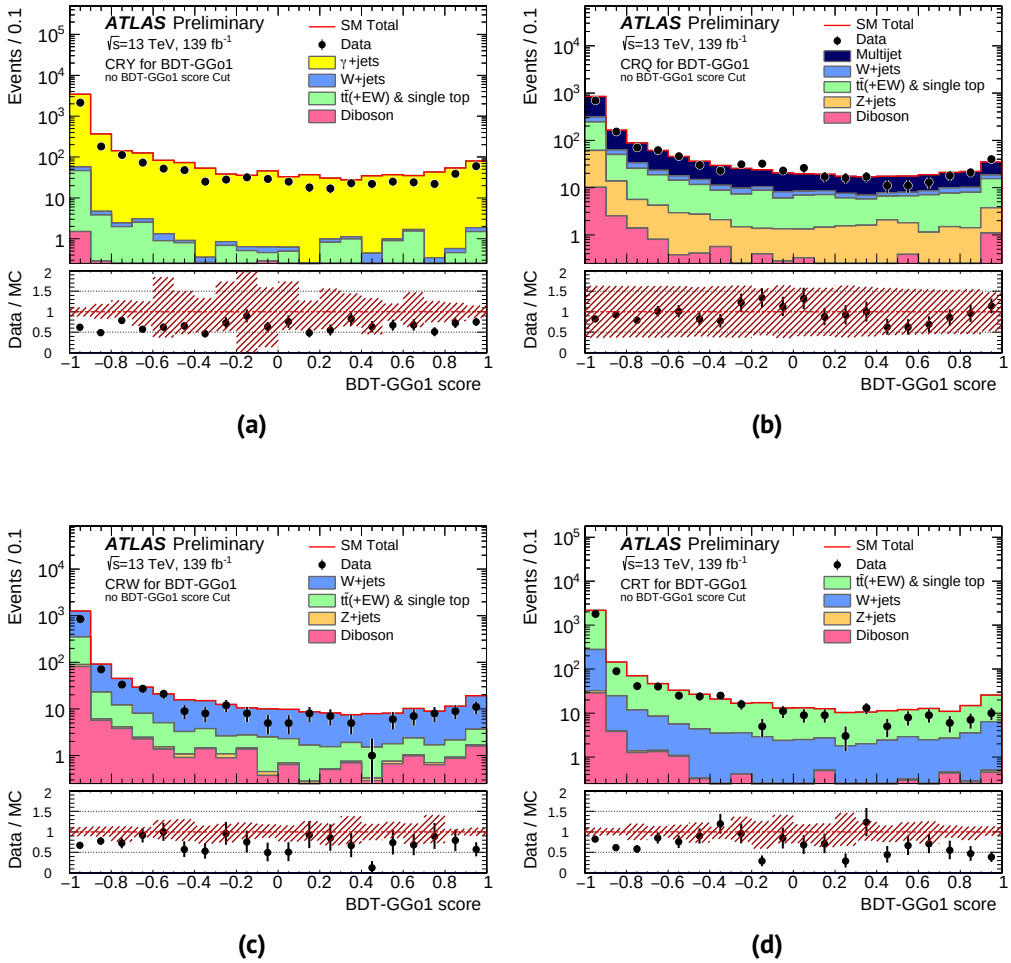

Figure 6.14: Observed BDT score distributions in the CRs based on the BDT-GGo1 selection listed in Table 6.10. BDT-CRγ (Figure 6.14a), BDT-CRQ (Figure 6.14b), BDT-CRW (Figure 6.14c) and BDT-CRT (Figure 6.14d) are shown. The plots include the MC background predictions normalised solely by cross-section $\times$ luminosity and the multijet background modelled using pseudo-data normalised to data in the CRQ, respectively. For the γ + jets background an additional scaling factor κ, defined in Equation 6.6, is applied. The combined experimental and statistical uncertainties are indicated by the hatched red error bands.

6.3.2 Evaluation of Background Estimation

The background prediction obtained from a simultaneous background-only fit in all CRs is evaluated by comparing the predicted event yields to the number of observed events in the VRs, which follow the general strategy used for the CR definitions. Though they are designed differently, the VRs are also based on final states including leptons and photons, allowing to validate the different SM background contributions with high purity while ensuring a low signal contamination. This concept is illustrated in Figure 6.15 by means of a simplified two-dimensional example based on the variables $E_{\mathrm{T}}^{\mathrm{miss}}$ and $\Delta\phi$.

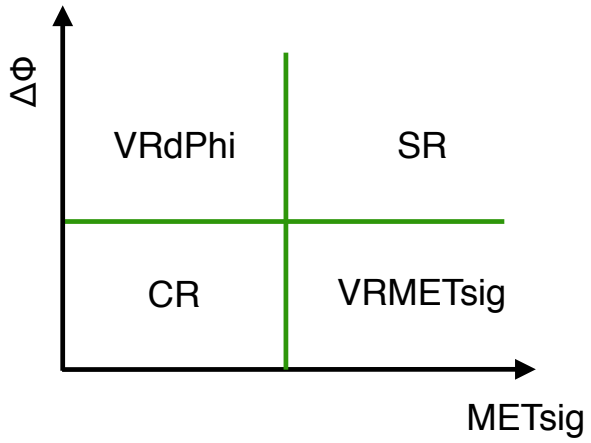

Figure 6.15: Sketch of the concept of constructing a CR and assigned VRs, validating the extrapolation over $E_{\mathrm{T}}^{\mathrm{miss}}$ and $\Delta\phi$, for a given SR.

Z+jets The evaluation of the prediction of the Z + jets contribution makes use of simulated samples describing $\mathrm{Z} \to \ell\bar{\ell}$ + jets, as briefly mentioned earlier. Events are selected containing high purity lepton pairs of opposite sign but same flavour (e, μ) with an invariant dilepton mass $m(\ell, \bar{\ell})$ within 25 GeV of the mass of the Z boson. The leptons are then added to the $E_{\mathrm{T}}^{\mathrm{miss}}$ in order to describe the energy loss due to invisible Z decay. The lower branching ratio of $\mathrm{Z} \to \ell\bar{\ell}$ in comparison to $\mathrm{Z} \to \nu\bar{\nu}$ would limit the number of events drastically introducing large statistical uncertainties. Hence, the SR selections are loosened in the respective VRZ to compensate this effect. In particular, the SR cuts on the Aplanarity and $E_{\mathrm{T}}^{\mathrm{miss}}/m_{\mathrm{eff}}(N_j)$ or $E_{\mathrm{T}}^{\mathrm{miss}}/\sqrt{H_{\mathrm{T}}}$ are omitted in the VRZ.

Individual VRs are designed to cross-check the extrapolation of the estimation of the Z + jets background from the CRγ onto the respective SR over each omitted variable, by reinstating the omitted cut. In case of the BDT search these are the VRZf, which applies the full SR selection, the VRZAp reinstating the Aplanarity cut and the VRZL. The VRZL is equivalent to the VRZf but the cut on the BDT score is loosened to ensure that at least ten events are selected. The extrapolation over $E_{\mathrm{T}}^{\mathrm{miss}}/\sqrt{H_{\mathrm{T}}}$ onto the MB SRs is validated in the VRZMETsig. Both searches use a VRZdPhi evaluating the cut on $\Delta\phi$.

W+jets and Top A similar approach is used to validate the estimation of the W + jets and top anti-top pair and single top background contributions. The VRW and VRT apply the same selections as used in the CRW and CRT, respectively. Individual variable extrapolations are tested in the BDT channels using VRWf, VRWAp and VRWL or VRTf, VRTAp and VRTL and in the MB search using VRWMETsig or VRTMETsig. The extrapolation over $\Delta\phi$ is evaluated for both analysis approaches by means of the VRWdPhi and VRTdPhi, respectively.

Multijet The validation of the multijet background prediction is again based on the selection applied in the CRQ with reinstated cuts on $E_{\mathrm{T}}^{\mathrm{miss}}/\sqrt{H_{\mathrm{T}}}$ (in MB channels), $E_{\mathrm{T}}^{\mathrm{miss}}/m_{\mathrm{eff}}(N_j)$ (in BDT channels) and $\Delta\phi$, realised in the regions VR0LMETsig, VR0LMETMeff and VR0LdPhi. These VRs are used to generally evaluate the background prediction of all SM processes in 0L channels, where the QCD contribution can be arbitrarily small.
The result of the comparison of observation and prediction is exemplified for the VR0LMETsig and VR0LMETMeff, respectively, in Figure 6.16 and for VR0LdPhi in Figure 6.17. Both figures show the evaluation of the QCD background prediction as a function of the respective SR selections, i.e. all bins of the three MB channels MB-SSd, MB-GGd and MB-C as well as all eight BDT SRs. The deviation of prediction and observation is quantified using the LHR method introduced in subsection 5.4.2 and described in detail in [129]. The systematic uncertainties, detailed in section 6.4, are included in the calculation as NPs.

The largest over-all discrepancy in the MB search is 2.6σ found in the VR0LMETsig for the MB-SSd selection with N_j = [2, 3], m_{eff}= [2.8 TeV, 3.4 TeV) and $E_{\mathrm{T}}^{\mathrm{miss}}/\sqrt{H_{\mathrm{T}}}$ = [16 GeV$^{1/2}$, 22 GeV$^{1/2}$). While in case of the BDT analysis it is 2.4σ in the VRTL of the BDT-GGo2.

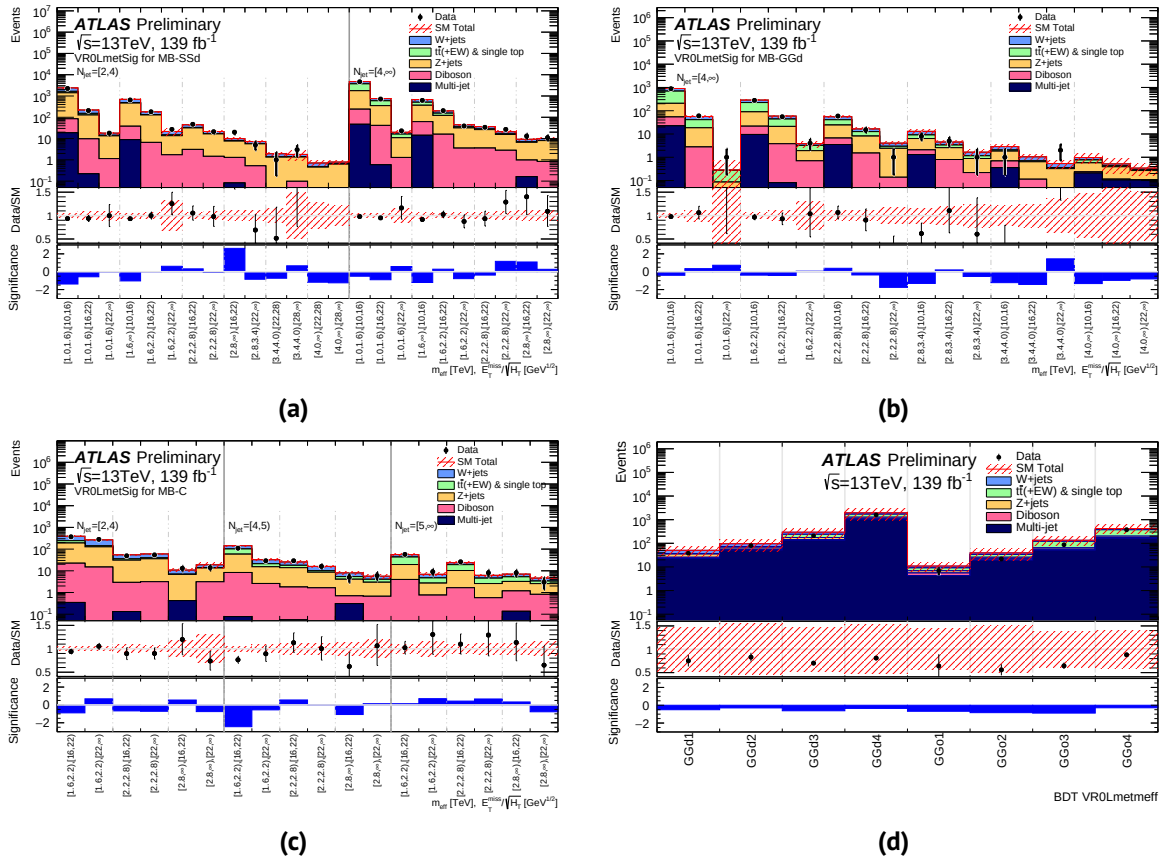

Figure 6.16: Comparison of the number of observed events in data and the estimated contributions from SM background processes for VR0LMETsig assigned to MB-SSd (Figure 6.16a), MB-GGd (Figure 6.16b) and MB-C (Figure 6.16c) selections as well as for VR0LMETMeff (Figure 6.16d) in the BDT search. If the observation exceeds the predicted event yield a positive significance computed following the LHR method is shown. In case the background is over-estimated, the same procedure gives a negative significance.

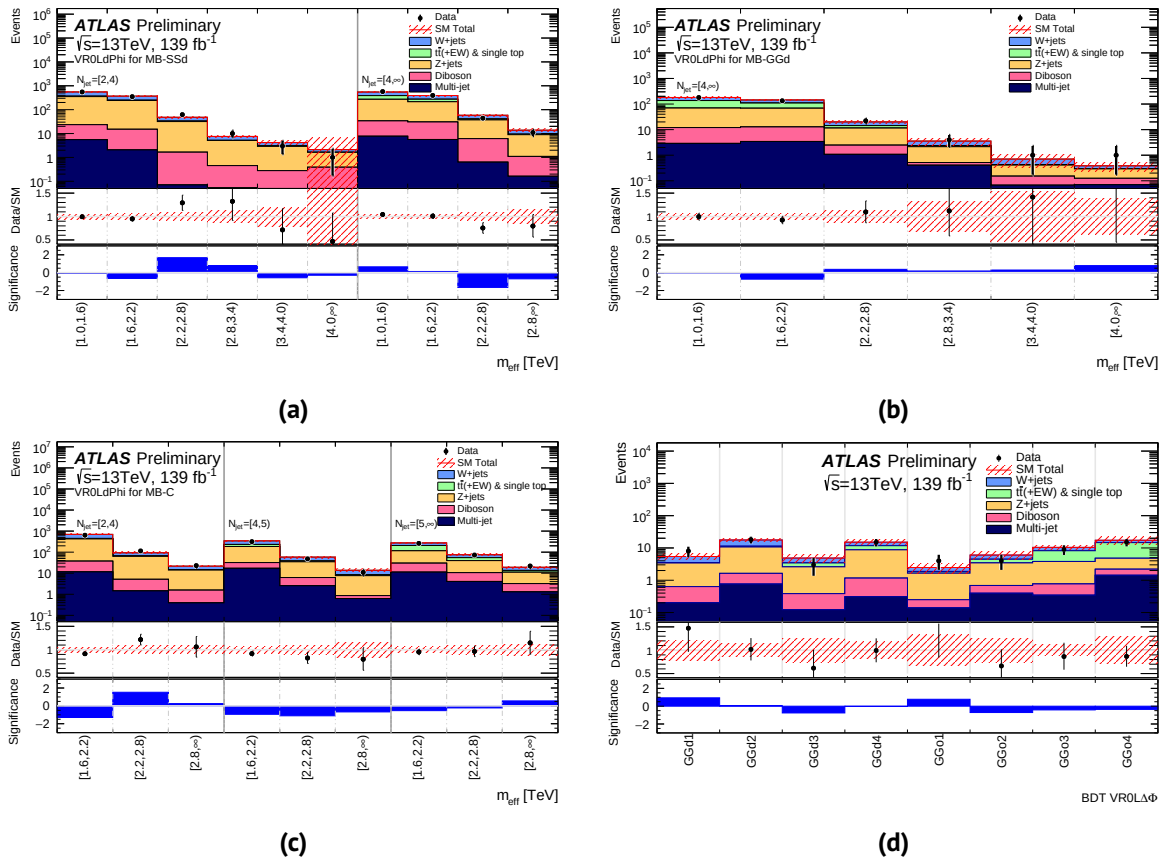

Figure 6.17: Comparison of the number of observed events in data and the estimated contributions from SM background processes for VR0LdPhi assigned to MB-SSd (Figure 6.17a), MB-GGd (Figure 6.17b) and MB-C (Figure 6.17c) selections and all SRs in the BDT search (Figure 6.16d). If the observation exceeds the predicted event yield a positive significance computed following the LHR method is shown. In case the background is over-estimated, the same procedure gives a negative significance.

6.4 Statistical Treatment and Systematic Uncertainties

The fit procedure used to compute and interpret the results in the 0L (2-6jets) SUSY analysis was introduced in a generalised way in subsection 5.4.3 and is described in more detail in this section. All three different fits (background-only, discovery and exclusion fit) are based on the LH function

$$L(\boldsymbol{n} \,|\, \boldsymbol{\mu}, \boldsymbol{s}, \boldsymbol{b}, \boldsymbol{\theta}) \;=\; P_{\mathrm{SR}} \times P_{\mathrm{CRW}} \times P_{\mathrm{CRT}} \times P_{\mathrm{CR}\gamma} \times P_{\mathrm{CRQ}} \times C_{syst}\,, \tag{6.17}$$

where the P_r denote the Poissonian distributions describing the event yields in the SR and the CRs for the main background processes, that are W + jets, $t\bar{t}$, Z + jets and QCD, and C_{syst} represents the systematic errors taken into account. The LH function depends on

- the numbers of observed events in each region $\boldsymbol{n}$
- the predicted numbers of background events from various SM sources (V + jets, $t\bar{t}$, multijet and diboson processes) in the different regions $\boldsymbol{b}$
- the expected number of signal events $\boldsymbol{s}$, set to zero in the background-only fit, obtained from a generic BSM model in case of the discovery fit and taken from MC simulation for the topologies considered in this analysis in the exclusion fit
- free normalisation factors $\boldsymbol{\mu}$ for the main background processes and for the signal, referred to as signal strength parameter μ_s which is set to zero except in the exclusion fit
- NPs representing the uncertainties $\boldsymbol{\theta}$

The total uncertainties on the background prediction and the signal estimation in the inclusive 0L search comprise the statistical errors, due to limited event yields and systematic uncertainties. The systematics include theoretical uncertainties introduced by the MC modelling of signal and background processes and the experimental uncertainties from the reconstruction and calibration of the physics objects used in the analysis.
As described in subsection 5.4.2, the systematic uncertainties are incorporated in the LH fits as NPs constrained by Gaussian distributions. The PDF of the overall uncertainties $C_{syst}(\boldsymbol{\theta}^0, \boldsymbol{\theta})$ can be described as a product of (unit) Gaussians G for each individual uncertainty j included in the set of all systematics SU

$$C_{syst}(\boldsymbol{\theta}^0, \boldsymbol{\theta}) = \prod_{j \in SU} G(\theta_j^0, \theta_j), \tag{6.18}$$

where $\boldsymbol{\theta}^0$ holds the nominal predictions, i.e. the means of the Gaussians, around which the θ_j are varied, e.g. when maximising the likelihood, defining the size of the respective uncertainty.
The NPs can be treated as:

- fully correlated across regions and physics processes, like the uncertainties on the luminosity, the $E_{\mathrm{T}}^{\mathrm{miss}}$, etc.
- independent for different processes but correlated across CRs and SRs, respectively, e.g. theoretical uncertainties from MC modelling

- completely uncorrelated

The systematic uncertainties on the background prediction are evaluated on the TFs used to extrapolate the estimation in the CRs onto the SR for the main background processes and on the MC description for the modelling of the minor backgrounds. Correlations between the individual NPs are taken into account where appropriate.

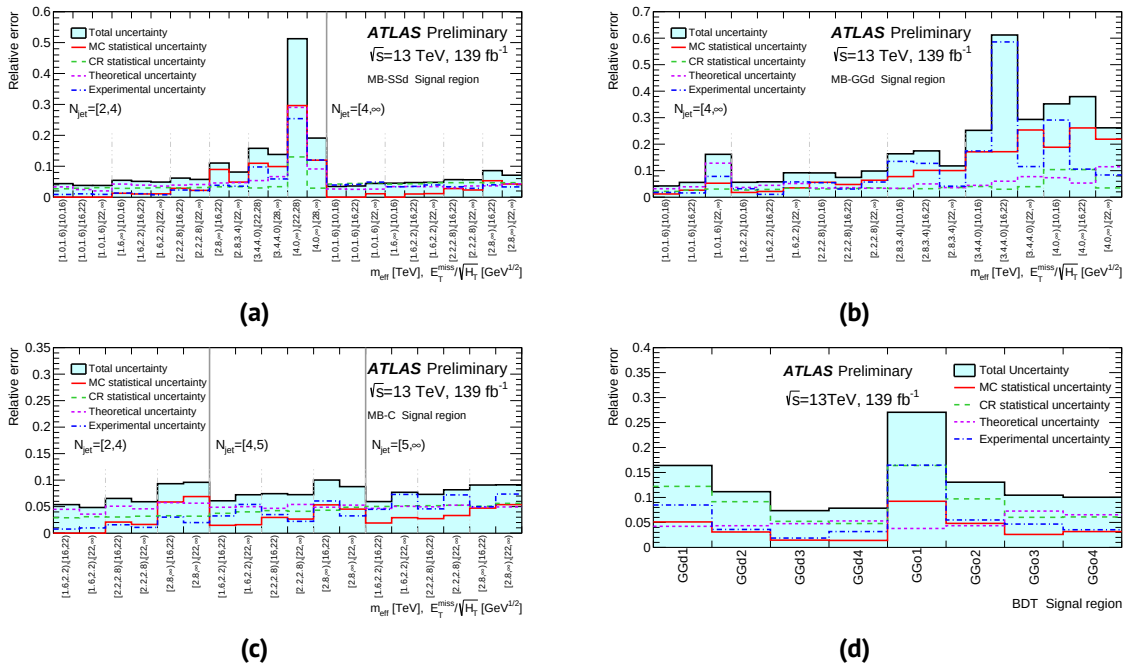

Figure 6.18: Breakdown of the main systematic uncertainties on the background prediction in the SRs for all MB-SSd (Figure 6.18a), MB-GGd (Figure 6.18b), MB-C (Figure 6.18c) bins and the BDT search channels (Figure 6.18d). Correlations between the uncertainties can lead to a total uncertainty on the background which differs from the quadratic sum of the individual components.

Figure 6.18 shows the overall uncertainties on the background prediction as a function of the SR bins for the three MB channels and the BDT SRs, respectively. The total uncertainties are lowest (5%) in many MB-SSd bins and can be as large as 60% for tight MB-GGd selections. In case of the BDT channels they reach from 8% in the BDT-GGd3 up to 28% in the BDT-GGo1 SR.
In addition, the combination of the individual contributions to each uncertainty group (experimental, theoretical, statistical and data-driven) are shown in Figure 6.18. These contributions are discussed in more detail below.

6.4.1 Experimental Systematics

The primary source of experimental uncertainties for MC modelled background estimations and signal processes are the uncertainties arising from the calibration of JES and JER, detailed in section 5.3 and from the reconstruction of the $E_{\mathrm{T}}^{\mathrm{miss}}$. The experimental uncertainties are obtained following the official recommendations using the *GlobalReduction* schema composed of 20 NPs for the JES and the *StrongReduction* schema with 8 NPs for the calculation of the JER uncertainties.

The combined experimental systematics on the background prediction range from 1% of the total background in the loosest MB selections up to 60% for the bins with the tightest selections on m_{eff} and $E_{\text{T}}^{\text{miss}}/\sqrt{H_{\text{T}}}$, staying comparably low in the BDT channels, where they lie between 1% and 15%.
For signal processes these uncertainties stay below a few percent for most of the topologies.
Systematic errors arising from the lepton reconstruction and the tagging of b-jets are generally negligible in the 0L (2-6jets) SUSY analysis.

6.4.2 Theoretical Uncertainties

The basic procedure to estimate the theoretical uncertainties arising from the MC modelling of the main background processes is to compare different generators and vary the renormalisation and factorisation scales.

Vector bosons plus jets The W + jets and Z + jets processes are the dominant source of SM background in the inclusive 0L search. Uncertainties on the modelling of these processes are derived considering different merging and resummation scales by means of alternative samples. PDF uncertainties are taken into account as well as variations of α_s and variations of renormalisation and factorisation scales in the matrix elements using 7-point scale variations.

Top anti-top pair and single top Theoretical systematics on the modelling of this background are obtained via comparison of the nominal sample, given in Table 6.2 with two different alternative samples:

- Samples produced with MG5_aMC@NLO interfaced with PYTHIA8 are used to estimate uncertainties on the modelling of the hard scatter process.
- POWHEG-BOX interfaced with Herwig7 is used to produce alternative samples which allow to obtain uncertainties arising from fragmentation and hadronisation processes.

Uncertainties on ISR and FSR, variations in the shower radiation and of factorisation and renormalisation scales are included in the event weights of the nominal sample.

Diboson The production of two SM vector bosons associated with jets is only a minor background in the analysis. Uncertainties on this background are estimated similarly to the procedure used in case of the vector bosons plus jets background.

The combined theoretical systematics on the background prediction, represented in Figure 6.18 by the purple line, are between 3% and 30% for loose and tight MB selections, respectively, and vary from 3% up to only 8% in the BDT search. In the majority of channels, these theoretical systematics are larger than or compatible with the experimental uncertainties.
In case of the signal processes, systematic uncertainties arising form the MC modelling are estimated following a similar method. Uncertainties on the computation of the cross-sections are derived from

the changes under variation of the strong coupling constant, the factorisation and renormalisation scales and the PDFs, while uncertainties on ISR and FSR are estimated by varying the generator tunes used in the simulation and the scales in the matrix generator. The latter, accounting for the shape of signal spectra, are evaluated as function of the mass splitting between the initial and final SUSY particle $\Delta m(\tilde{g}/\tilde{q}, \tilde{\chi}_1^0)$ reaching up to 10% for compressed spectra and decreasing to be negligible for $\Delta m > 200$ GeV[4].

6.4.3 Statistical Uncertainties and Systematics from Data-Driven Methods

The statistical errors on the MC event counts are described by completely uncorrelated NPs. The combined contribution of the MC statistical uncertainties is show in Figure 6.18 as solid red line and reaches a maximum of 30% in tight MB-SSd selections and of 8% in the BDT-GGo1 channel.
Data-driven methods are applied to correct the prediction of the Z + jets background in the CRγ and to estimated the QCD background.
Uncertainties arising from the correction based on the κ-factor in the CRγ are labelled CR statistical uncertainties and indicated by the green line in Figure 6.18. They range from 3% to 14% in the MB search and from 5% to 16% in case of the BDT analysis.
The prediction of the multijet background using the JetSmearing technique is afflicted with a conservative estimation of 100% uncertainty on the event yields from QCD processes. Nevertheless, this particular systematic is below 1% due to the contribution of the multijet background being negligible in all SRs.

6.5 Results and Interpretation

The thoroughly validated background prediction in each SR is compared to the event yields obtained by subjecting the full Run 2 data-set to the respective selection cuts defined in subsection 6.2.4, subsection 6.2.3 and subsection 6.2.5, in order to compute upper limits on the number of BSM signal events.
Figure 6.19 (Figure 6.20) shows the comparison of the distribution of m_{eff} ($E_{\text{T}}^{\text{miss}}/\sqrt{H_{\text{T}}}$) for data events and MC events normalised to the theoretical cross-section, for the preselection of the three MB search channels. Each plot additionally shows the expected distribution of signal events for an example signal grid point, i.e. a specific mass configuration of the simplified model topology the respective search channel was optimised for. Similarly, the distribution of example BDT score cuts are shown in Figure 6.21 for the BDT-GGd1 and BDT-GGo1 selections.
Although the background prediction prior to the normalisation obtained from the background-only fit is used for these comparisons, the prediction and observation agree within the given uncertainties.
A detailed list of the exact observed event counts and the expected number of background events obtained from the background-only fit is given in Table 6.17 for the MB-SSd, in Table 6.18 for the

[4] These shape uncertainties, which are known to have only a minor effect, were originally computed in the L=36.1 fb^{-1} version of the analysis and applied in the full Run 2 search, due to time constraints.

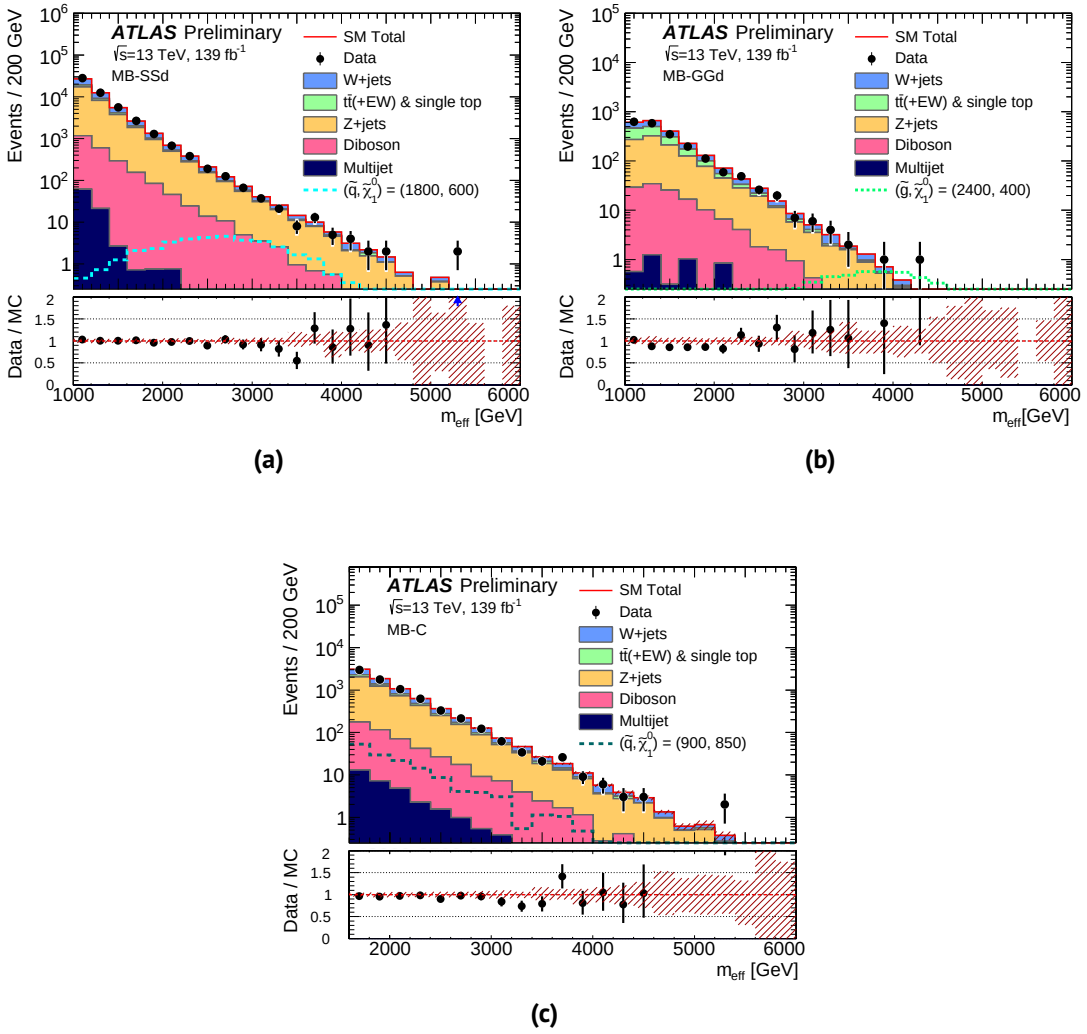

Figure 6.19: Observed m_{eff} distributions for the MB-SSd (Figure 6.19a), MB-GGd (Figure 6.19b) and MB-C (Figure 6.19c) preselections, defined in Table 6.4. The MC based background estimation prior to the background-only fit, only normalised to the theoretical cross-sections weighted by the integrated luminosity together with the multijet background modelled using pseudo-data normalised to data in the CRQ is given by the histograms. The combination of statistical and systematic uncertainties is indicated by the red, hatched error bands. Expected distributions for benchmark signal points with indicated mass configurations given in GeV, are shown for comparison.

MB-GGd and in Table 6.19 for the MB-C bins, in Table 6.20 for all BDT selections and in Table 6.21 for the DR selections.

A pictorial overview of these results is given in Figure 6.22 showing the number of observed and predicted event counts for each SR selection of the MB and BDT search as well as for the DRs in the model-independent search. Additionally, the ratio of observation and prediction is shown in the bottom part of these plots as well as the quantification of the agreement, computed via a model-independent fit. This discovery fit, as described in subsection 5.4.3, uses the event yields in the CRs to constrain the background prediction in the SRs, similar to the background-only fit. In a second step, the event yields in the SRs are included in the LH functions with an additional NP

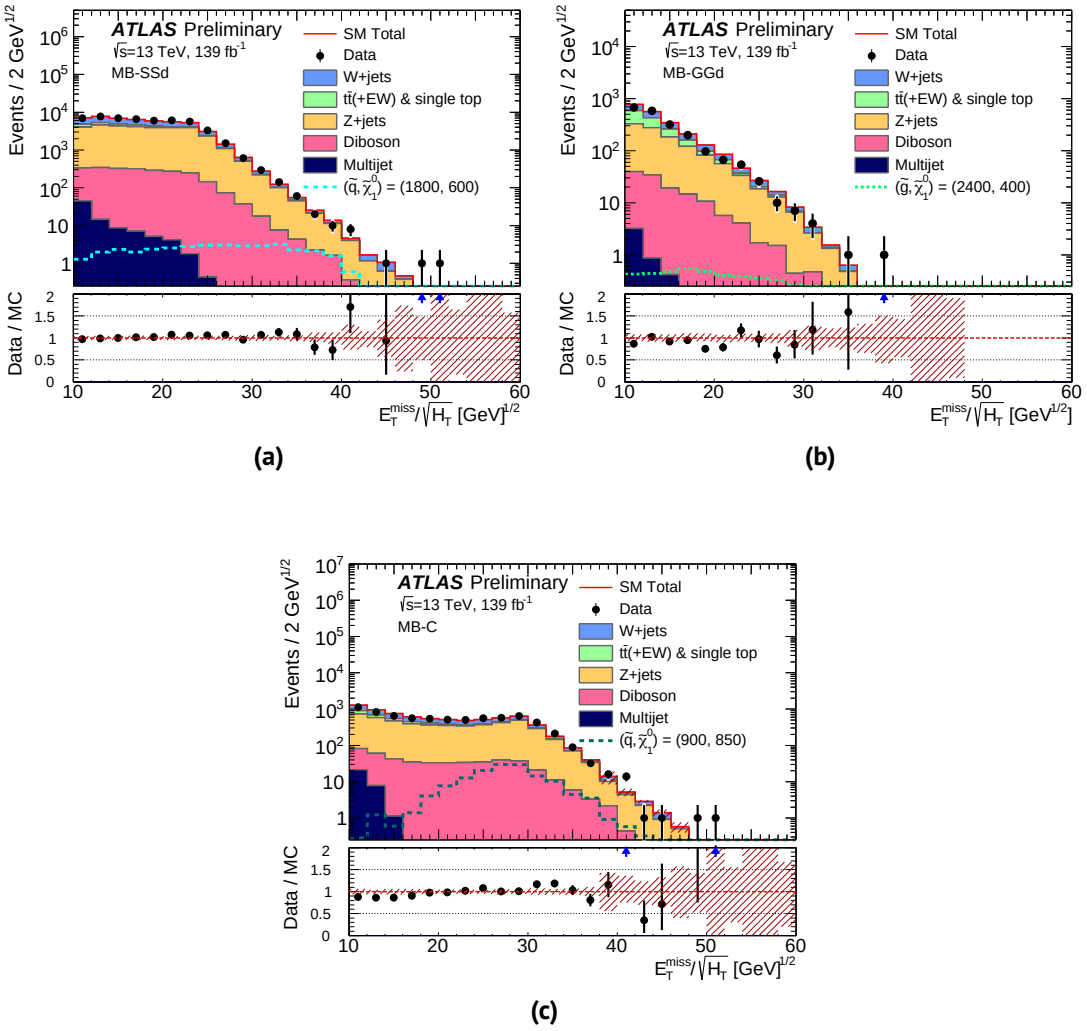

Figure 6.20: Observed $E_{\mathrm{T}}^{\mathrm{miss}}/\sqrt{H_{\mathrm{T}}}$ distributions for the MB-SSd (Figure 6.20a), MB-GGd (Figure 6.20b) and MB-C (Figure 6.20c) preselections, defined in Table 6.4. The MC based background estimation prior to the background-only fit, only normalised to the theoretical cross-sections weighted by the integrated luminosity together with the multijet background modelled using pseudo-data normalised to data in the CRQ is given by the histograms. The combination of statistical and systematic uncertainties is indicated by the red, hatched error bands. Expected distributions for benchmark signal points with indicated mass configurations given in GeV, are shown for comparison.

accounting for potential contribution from a generic BSM process. This method allows to compute ULs at *95% CL* on the number of BSM events n_{BSM} in each SR, which can be translated into ULs on the visible cross-section σ_{vis}, following the CL_s prescription. Furthermore, one-sided p-values are computed to test the background-only hypothesis H_0, in order to quantify the significance of any possible excess above the SM prediction. These p-values as well as the ULs on the visible cross-section and on the number of observed and expected signal events are also shown in the event count lists given in Table 6.20 for the BDT selections and in Table 6.21 for the DR selections. No statistically significant excess was found in any of the searches considered in the 0L (2-6jets) SUSY analysis.

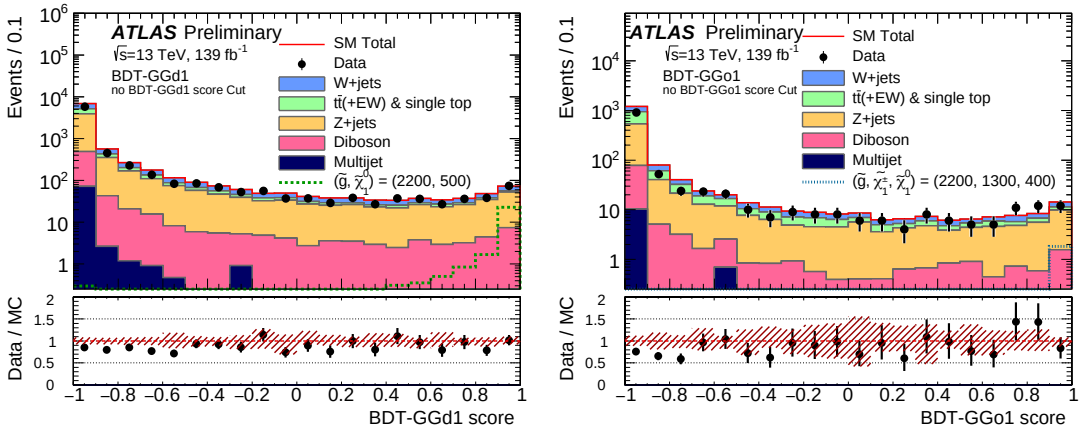

Figure 6.21: Observed BDT score distributions for the BDT-GGd1 (Figure 6.21a) and the BDT-GGo1 (Figure 6.21b) preselections, defined in Table 6.10. The MC based background estimation prior to the background-only fit, only normalised to the theoretical cross-sections weighted by the integrated luminosity together with the multijet background modelled using pseudo-data normalised to data in the CRQ is given by the histograms. The combination of statistical and systematic uncertainties is indicated by the red, hatched error bands. Expected distributions for benchmark signal points with indicated mass configurations given in GeV, are shown for comparison.

In the absence of any sign of new physics, BSM searches typically set limits on the BSM models the analysis is designed for. Hence, a model-dependent fit is used to derive exclusion limits for the simplified model topologies described in section 6.2. This exclusion fit, introduced in subsection 5.4.3, is similar to the model-independent fit not only including the signal yields in the SRs but also potential signal contamination in the CRs using signal MC predictions. Systematic uncertainties on the signal events are included via additional NPs and correlations between signal and background uncertainties are taken into account accordingly. This method is used to derive observed and expected *95% CL* ULs on the specific SUSY models in all MB and BDT regions. Both searches are combined to obtain the final exclusion limit per signal grid point taken from the SR providing the best expected CL_s value. The results of the exclusion fit are presented as *exclusion lines* given in the two dimensional parameter space investigated for each signal process, as discussed in detail below.

SS-direct Exclusion limits on the squark pair production with subsequent direct decay $\tilde{q} \rightarrow q\tilde{\chi}_1^0$ are shown in the $m(\tilde{q})$-$m(\tilde{\chi}_1^0)$ mass plane. In this specific scenario, only MB SRs provide the best expected CL_s, thus limits shown in Figure 6.23 are obtained solely from the MB analysis. The plot shows the observed and expected exclusion contour for this specific topology as well as the limits obtained previously in the inclusive 0L search based on an early Run 2 data-set, corresponding to L=36.1 fb^{-1}. Neutralino masses are found to be excluded below 800 GeV for $m(\tilde{q}) < 1200$ GeV. In case the LSP is massless, squark masses can be excluded below 1900 GeV.

MB-SSd regions								
Signal Region	**2-1000-10**	**2-1000-16**	**2-1000-22**	**2-1600-10**	**2-1600-16**	**2-1600-22**	**2-2200-16**	**2-2200-22**
Fitted background events								
Diboson	210 ± 50	81 ± 18	44 ± 10	36 ± 8	26 ± 6	29 ± 7	2.7 ± 0.7	7.6 ± 2.2
Z/γ^*+jets	4360 ± 280	1760 ± 90	930 ± 50	580 ± 40	366 ± 25	443 ± 28	45.1 ± 3.5	104 ± 7
W+jets	2178 ± 100	702 ± 25	294 ± 9	245 ± 13	131 ± 6	131 ± 5	16.1 ± 0.8	29.2 ± 1.3
$t\bar{t}$(+EW) + single top	133 ± 28	48 ± 10	16 ± 4	11.3 ± 2.3	5.2 ± 1.4	5 ± 4	1.3 ± 1.0	$1.51^{+1.74}_{-1.51}$
Multi-jet	12 ± 12	1.5 ± 1.5	0.24 ± 0.24	0.7 ± 0.6	0.09 ± 0.09	0.02 ± 0.02	0.01 ± 0.1	0.02 ± 0.02
Total bkg (pre-fit)	6570.36	2424.38	1201.77	851.26	509.44	575.91	62.24	135.99
Total bkg	6890 ± 300	2589 ± 100	1290 ± 50	870 ± 50	528 ± 27	608 ± 30	65 ± 4	142 ± 8
Observed	6986	2537	1289	926	526	638	55	146

Signal Region	**2-2800-16**	**2-2800-22**	**2-3400-22**	**2-3400-28**	**2-4000-22**	**2-4000-28**	**4-1000-10**	**4-1000-16**
Fitted background events								
Diboson	0.45 ± 0.14	1.6 ± 0.8	0.12 ± 0.04	$0.83^{+0.85}_{-0.83}$	0.07 ± 0.03	0.23 ± 0.1	432 ± 22	282 ± 18
Z/γ^*+jets	10.6 ± 1.4	27.3 ± 2.6	2.47 ± 0.34	8.8 ± 1.1	0.65 ± 0.29	2.7 ± 0.5	3520 ± 240	2210 ± 140
W+jets	2.8 ± 0.4	5.4 ± 0.4	0.9 ± 0.4	1.6 ± 0.4	0.08 ± 0.06	1.0 ± 0.4	2119 ± 100	970 ± 50
$t\bar{t}$(+EW) + single top	$0.09^{+0.13}_{-0.09}$	$0.03^{+0.05}_{-0.03}$	0.01 ± 0.1	$0.18^{+0.44}_{-0.18}$	$0.10^{+0.27}_{-0.10}$	–	1470 ± 90	550 ± 50
Multi-jet	–	–	–	–	–	–	29 ± 29	4 ± 4
Total bkg (pre-fit)	13.68	33.89	3.30	11.18	1.16	3.93	8467.25	4486.63
Total bkg	14.0 ± 1.5	34.3 ± 2.8	3.5 ± 0.6	11.4 ± 1.6	0.9 ± 0.5	4.0 ± 0.8	7570 ± 260	4010 ± 140
Observed	17	29	3	6	1	5	7769	4286

Signal Region	**4-1000-22**	**4-1600-10**	**4-1600-16**	**4-1600-22**	**4-2200-16**	**4-2200-22**	**4-2800-16**	**4-2800-22**
Fitted background events								
Diboson	65 ± 4	66 ± 17	48 ± 12	40 ± 10	5.8 ± 1.7	12.7 ± 3.4	1.5 ± 0.5	4.5 ± 1.2
Z/γ^*+jets	528 ± 30	466 ± 32	290 ± 19	299 ± 18	45.1 ± 3.2	82 ± 5	8.9 ± 0.9	24.3 ± 1.8
W+jets	174 ± 13	224 ± 9	114 ± 7	87 ± 4	14.2 ± 1.0	21.3 ± 1.1	2.8 ± 0.3	6.5 ± 0.6
$t\bar{t}$(+EW) + single top	55 ± 15	101 ± 14	43 ± 5	24 ± 6	2.8 ± 0.5	3.4 ± 1.4	0.26 ± 0.1	1.4 ± 0.8
Multi-jet	0.24 ± 0.24	1.7 ± 1.7	0.16 ± 0.16	0.1 ± 0.1	0.02 ± 0.02	0.05 ± 0.05	–	–
Total bkg (pre-fit)	899.55	982.49	556.41	511.78	78.64	135.43	15.60	43.23
Total bkg	820 ± 40	860 ± 40	494 ± 23	450 ± 22	68 ± 4	120 ± 7	13.4 ± 1.2	36.7 ± 2.6
Observed	858	819	461	485	71	113	17	31

Table 6.17: Numbers of observed event counts compared with background expectations obtained from the background-only fit in the bins of the MB-SSd channel. Statistical and systematic uncertainties are included in the errors stated. If cells are left empty, the corresponding estimates are below 0.01 events.

GG-direct Similarly, the exclusion limits for the simplified model considering pair-produced directly decaying gluinos ($\tilde{g} \to q\bar{q}\tilde{\chi}_1^0$) are shown in Figure 6.24. The free parameters in the GG-direct model are the mass of the $\tilde{g}$ and the LSP. Hence, limits are derived as a function of $m(\tilde{g})$ and $m(\tilde{\chi}_1^0)$. Limits placed on the gluino masses are stronger than the ones for the squark masses, due to the larger production cross-section for the gluinos. Directly decaying gluinos are excluded up to 2350 GeV for a very light LSP, while $m(\tilde{\chi}_1^0) < 950$ GeV can be excluded for 1 TeV gluinos and in compressed mass spectra.

Limits are obtained combining the optimised MB and BDT channels, where the MB-C has the highest sensitivity close to the diagonal, as expected. The individual contours from the MB and BDT search are shown additionally as purple and green lines, respectively.

SS-onestep Figure 6.25 shows the exclusion limits for pair produced squarks decaying via an intermediate $\tilde{\chi}_1^\pm$ ($\tilde{q} \to q\tilde{\chi}_1^\pm \to qW^\pm\tilde{\chi}_1^0$), the so called SS-onestep model. Exclusion contours are shown for the two signal grids constructed for this model, described in subsection 6.1.1. Limits as a function of $m(\tilde{q})$ and $m(\tilde{\chi}_1^0)$ are presented in Figure 6.25a excluding squark masses up to 600 GeV for compressed mass spectra (close to the diagonal) where MB-C has the largest sensitivity and squark masses up to almost 1.3 TeV for a massless LSP. Figure 6.25b shows the exclusion line

MB-GGd regions						
Signal Region	**4-1000-10**	**4-1000-16**	**4-1000-22**	**4-1600-10**	**4-1600-16**	**4-1600-22**
Fitted background events						
Diboson	67 ± 18	17 ± 5	2.3 ± 0.8	17 ± 5	11.4 ± 2.9	4.0 ± 1.5
Z/γ^*+jets	500 ± 40	132 ± 10	16.9 ± 1.7	107 ± 9	57 ± 4	28.2 ± 2.6
W+jets	296 ± 25	60 ± 5	6.1 ± 1.3	59 ± 5	22.9 ± 2.0	8.3 ± 0.8
$t\bar{t}$(+EW) + single top	391 ± 24	46 ± 7	$2.68^{+3.56}_{-2.68}$	49 ± 5	11.3 ± 2.2	2.1 ± 1.6
Multi-jet	1.9 ± 1.9	0.12 ± 0.12	0.01 ± 0.1	2.3 ± 2.3	–	0.02 ± 0.02
Total bkg (pre-fit)	1365.21	279.03	29.97	266.07	114.40	47.23
Total bkg	1250 ± 50	256 ± 14	28 ± 5	234 ± 13	102 ± 6	43 ± 4
Observed	1281	240	35	228	95	44
Signal Region	**4-2200-10**	**4-2200-16**	**4-2200-22**	**4-2800-10**	**4-2800-16**	**4-2800-22**
Fitted background events						
Diboson	2.5 ± 1.0	2.5 ± 1.0	1.5 ± 0.5	0.68 ± 0.24	0.68 ± 0.24	0.11 ± 0.1
Z/γ^*+jets	13.7 ± 1.2	13.7 ± 1.2	11.2 ± 1.3	2.6 ± 0.5	2.6 ± 0.5	3.0 ± 0.4
W+jets	4.4 ± 0.6	4.4 ± 0.6	3.23 ± 0.32	0.87 ± 0.21	0.87 ± 0.21	1.1 ± 0.15
$t\bar{t}$(+EW) + single top	0.74 ± 0.19	0.74 ± 0.19	0.24 ± 0.15	0.1 ± 0.09	0.1 ± 0.09	0.13 ± 0.07
Multi-jet	–	–	–	–	–	–
Total bkg (pre-fit)	24.74	24.74	18.85	5.01	5.01	5.33
Total bkg	21.3 ± 1.6	21.3 ± 1.6	16.2 ± 1.6	4.3 ± 0.8	4.3 ± 0.8	4.3 ± 0.5
Observed	23	23	15	5	5	8
Signal Region	**4-3400-10**	**4-3400-16**	**4-3400-22**	**4-4000-10**	**4-4000-16**	**4-4000-22**
Fitted background events						
Diboson	$0.11^{+0.23}_{-0.11}$	$0.11^{+0.23}_{-0.11}$	0.16 ± 0.13	–	–	0.07 ± 0.1
Z/γ^*+jets	0.35 ± 0.27	0.35 ± 0.27	1.09 ± 0.3	0.07 ± 0.03	0.07 ± 0.03	0.21 ± 0.06
W+jets	0.21 ± 0.12	0.21 ± 0.12	$0.12^{+0.17}_{-0.12}$	0.05 ± 0.1	0.05 ± 0.1	0.06 ± 0.02
$t\bar{t}$(+EW) + single top	$0.01^{+0.01}_{-0.01}$	$0.01^{+0.01}_{-0.01}$	$0.00^{+0.00}_{-0.00}$	$0.00^{+0.00}_{-0.00}$	$0.00^{+0.00}_{-0.00}$	$0.00^{+0.03}_{-0.00}$
Multi-jet	–	–	–	$0.04^{+0.04}_{-0.04}$	$0.04^{+0.04}_{-0.04}$	–
Total bkg (pre-fit)	0.92	0.92	1.52	0.14	0.14	0.39
Total bkg	0.7 ± 0.4	0.7 ± 0.4	1.4 ± 0.4	0.15 ± 0.06	0.15 ± 0.06	0.34 ± 0.09
Observed	1	1	0	0	0	1

Table 6.18: Numbers of observed event counts compared with background expectations obtained from the background-only fit in the bins of the MB-GGd channel. Statistical and systematic uncertainties are included in the errors stated. If cells are left empty, the corresponding estimates are below 0.01 events.

in case the neutralino mass is fixed at 60 GeV, where the excluded squark mass is found to be as large as 1350 GeV.

GG-onestep The results of the exclusion fit using a signal with pair produced gluinos, which decay via the cascade $\tilde{g} \to q\bar{q}\tilde{\chi}_1^{\pm} \to q\bar{q}W^{\pm}\tilde{\chi}_1^0$ are also presented in two different planes with $m(\tilde{g})$ on the x-axis and on the y-axis $m(\tilde{\chi}_1^0)$ (Figure 6.26a) and $x = \Delta m(\tilde{\chi}_1^{\pm}, \tilde{\chi}_1^0)/\Delta m(\tilde{g}, \tilde{\chi}_1^0)$ (Figure 6.26b), respectively. LSP masses are found to be excluded up to 900 GeV in the region near the kinematic limit, targeted by the MB-C SRs. If the mass of the neutralino vanishes, the exclusion limit for $m(\tilde{g})$ reaches almost 2.2 TeV for the most favourable values of the x parameter.

Phenomenological squark-gluino Production Limits are also set on a less simplified model, which includes several production and decay modes, as detailed in subsection 6.1.1. For this topology limits are provided as a function of $m(\tilde{q})$ and $m(\tilde{g})$ for three different masses of the lightest neutralino: 0 GeV, 995 GeV and 1495 GeV, depicted in Figure 6.27. In this scenario the on-shell decays $\tilde{q} \to q\tilde{g}$ and $\tilde{g} \to q\tilde{q}$ are included, if kinematically possible. The best exclusion was found assuming a massless LSP (Figure 6.27a) where a lower limit for equal squark and gluino masses can be placed at 3 TeV.

MB-C regions						
Signal Region	**2-1600-16**	**2-1600-22**	**2-2200-16**	**2-2200-22**	**2-2800-16**	**2-2800-22**
Fitted background events						
Diboson	45 ± 10	108 ± 22	5.5 ± 1.4	25 ± 6	1.1 ± 0.4	5.6 ± 1.6
Z/γ^*+jets	580 ± 50	1400 ± 90	78 ± 7	274 ± 21	17.2 ± 2.0	65 ± 7
W+jets	239 ± 13	429 ± 19	28.5 ± 1.8	71 ± 4	5.7 ± 0.6	17.8 ± 1.7
$t\bar{t}$(+EW) + single top	22.6 ± 3.4	33 ± 9	1.0 ± 0.8	2.3 ± 1.0	$0.07^{+0.28}_{-0.07}$	$0.06^{+0.21}_{-0.06}$
Multi-jet	0.14 ± 0.14	0.35 ± 0.35	0.01 ± 0.1	0.05 ± 0.05	$0.09^{+0.09}_{-0.09}$	$0.02^{+0.02}_{-0.02}$
Total bkg (pre-fit)	867.04	1908.27	109.06	360.02	23.89	86.02
Total bkg	890 ± 50	1969 ± 100	113 ± 7	373 ± 22	24.2 ± 2.3	89 ± 8
Observed	908	2108	107	406	37	85
Signal Region	**4-1600-16**	**4-1600-22**	**4-2200-16**	**4-2200-22**	**4-2800-16**	**4-2800-22**
Fitted background events						
Diboson	21 ± 6	21 ± 5	3.6 ± 1.0	12 ± 4	1.4 ± 0.5	3.6 ± 1.0
Z/γ^*+jets	148 ± 15	125 ± 12	34 ± 4	57 ± 5	7.5 ± 0.9	18.6 ± 1.9
W+jets	71 ± 5	47 ± 4	14.9 ± 0.9	18.3 ± 1.5	2.74 ± 0.27	6.7 ± 0.8
$t\bar{t}$(+EW) + single top	32.1 ± 3.0	12.1 ± 1.8	1.7 ± 0.6	2.6 ± 0.9	0.37 ± 0.17	1.9 ± 1.1
Multi-jet	0.05 ± 0.05	0.04 ± 0.04	0.03 ± 0.03	0.03 ± 0.03	$0.06^{+0.06}_{-0.06}$	–
Total bkg (pre-fit)	323.81	248.05	64.73	103.69	13.60	34.22
Total bkg	273 ± 17	204 ± 15	54 ± 4	91 ± 7	12.0 ± 1.2	30.8 ± 2.7
Observed	274	213	54	98	16	25
Signal Region	**5-1600-16**	**5-1600-22**	**5-2200-16**	**5-2200-22**	**5-2800-16**	**5-2800-22**
Fitted background events						
Diboson	11.6 ± 3.0	5.4 ± 1.4	6.8 ± 1.9	5.5 ± 1.7	2.0 ± 0.5	2.1 ± 0.8
Z/γ^*+jets	58 ± 6	26.8 ± 2.7	29.4 ± 3.5	24.1 ± 2.5	8.2 ± 0.9	13.8 ± 1.4
W+jets	32.5 ± 2.5	11.7 ± 1.0	12.7 ± 0.9	8.2 ± 0.7	3.5 ± 0.4	3.8 ± 0.4
$t\bar{t}$(+EW) + single top	27.4 ± 2.7	4.4 ± 1.1	5.9 ± 0.9	3.6 ± 0.7	1.06 ± 0.27	1.15 ± 0.32
Multi-jet	$0.04^{+0.04}_{-0.04}$	–	0.04 ± 0.04	0.02 ± 0.02	$0.21^{+0.21}_{-0.21}$	–
Total bkg (pre-fit)	176.28	67.04	74.09	59.02	20.62	30.13
Total bkg	129 ± 8	48 ± 4	55 ± 4	41.3 ± 3.4	15.0 ± 1.4	20.8 ± 1.9
Observed	126	51	57	47	15	24

Table 6.19: Numbers of observed event counts compared with background expectations obtained from the background-only fit in the bins of the MB-C channel. Statistical and systematic uncertainties are included in the errors stated. If cells are left empty, the corresponding estimates are below 0.01 events.

BDT regions				
Signal Region	**GGd1**	**GGd2**	**GGd3**	**GGd4**
Fitted background events				
Diboson	3.0 ± 0.9	4.9 ± 1.4	21 ± 5	26 ± 7
Z/γ^*+jets	20 ± 4	33 ± 5	139 ± 14	180 ± 18
W+jets	7.0 ± 2.6	13.2 ± 3.5	48 ± 8	52 ± 9
$t\bar{t}$(+EW) + single top	$0.1^{+0.3}_{-0.1}$	$0.6^{+0.8}_{-0.6}$	16 ± 5	39 ± 11
Multi-jet	$0.1^{+0.1}_{-0.1}$	$0.1^{+0.1}_{-0.1}$	$0.1^{+0.1}_{-0.1}$	$0.1^{+0.1}_{-0.1}$
Total bkg (pre-fit)	29	56	253	348
Total bkg	30 ± 5	52 ± 6	223 ± 17	298 ± 23
Observed	34	68	227	291
$\langle \epsilon\sigma \rangle^{95}_{obs}$ [fb]	0.13	0.25	0.33	0.36
S^{95}_{obs}	19	34	46	50
S^{95}_{exp}	16^{+6}_{-5}	22^{+8}_{-5}	43^{+17}_{-12}	54^{+20}_{-15}
p_0 (Z)	0.30 (0.52)	0.05 (1.60)	0.44 (0.15)	0.50 (0.00)
Signal Region	**GGo1**	**GGo2**	**GGo3**	**GGo4**
Fitted background events				
Diboson	0.6 ± 0.2	2.2 ± 0.6	6.6 ± 2.2	6.8 ± 2.1
Z/γ^*+jets	3.8 ± 1.3	10.9 ± 1.9	35 ± 6	39 ± 7
W+jets	0.9 ± 0.5	3.8 ± 1.3	16 ± 4	27 ± 6
$t\bar{t}$(+EW) + single top	0.2 ± 0.2	1.3 ± 0.8	28 ± 6	85 ± 14
Multi-jet	–	–	$0.1^{+0.1}_{-0.1}$	$0.5^{+0.5}_{-0.5}$
Total bkg (pre-fit)	7	25	111	178
Total bkg	5.5 ± 1.5	18.3 ± 2.4	85 ± 9	159 ± 16
Observed	6	25	80	135
$\langle \epsilon\sigma \rangle^{95}_{obs}$ [fb]	0.05	0.12	0.16	0.18
S^{95}_{obs}	7	17	22	25
S^{95}_{exp}	$6.6^{+2.5}_{-1.8}$	11^{+5}_{-2}	25^{+10}_{-7}	37^{+14}_{-10}
p_0 (Z)	0.41 (0.22)	0.10 (1.28)	0.50 (0.00)	0.50 (0.00)

Table 6.20: Numbers of observed event counts compared with background expectations obtained from the background-only fit in the BDT-GGd and BDT-GGo channels. Statistical and systematic uncertainties are included in the errors stated. If cells are left empty, the corresponding estimates are below 0.01 events. Additionally, p-values (p_0) for the background-only hypothesis and their translation into Gaussian standard deviations (Z) obtained from the model-independent fit are quoted, giving the probability of the respective observation being consistent with the background prediction. These p-values are truncated at 0.5 if the observed number of events is lower than expected. Furthermore, ULs at *95% CL* on the visible cross-section ($\langle \epsilon\sigma \rangle^{95}_{obs}$) and on the visible number of observed (S^{95}_{obs}) and expected (S^{95}_{exp}) signal events are shown for the given number of predicted background events (and $\pm 1\sigma$ excursions of the expectation).

Model independent regions					
Signal Region	**SR-2j-1600**	**SR-2j-2200**	**SR-2j-2800**	**SR-4j-1000**	**SR-4j-2200**
Fitted background events					
Diboson	130 ± 29	74 ± 17	5.8 ± 1.7	44 ± 12	6.3 ± 1.7
Z/γ^*+jets	1510 ± 120	670 ± 40	64 ± 7	282 ± 22	35 ± 4
W+jets	500 ± 50	225 ± 16	15.4 ± 2.4	144 ± 12	15.4 ± 1.9
$t\bar{t}$(+EW) + single top	44 ± 9	14 ± 4	1.4 ± 0.8	67 ± 14	2.4 ± 0.9
Multi-jet	0.22 ± 0.22	0.32 ± 0.32	–	0.17 ± 0.17	$0.03^{+0.03}_{-0.03}$
Total bkg (pre-fit)	2120	979	82	610	71
Total bkg	2190 ± 130	980 ± 50	87 ± 8	536 ± 31	60 ± 5
Observed	2111	971	78	535	60
$\langle \epsilon\sigma \rangle^{95}_{obs}$ [fb]	1.46	0.78	0.13	0.54	0.14
S^{95}_{obs}	204	108	19	75	19
S^{95}_{exp}	246^{+91}_{-67}	114^{+43}_{-31}	24^{+10}_{-7}	76^{+27}_{-23}	19^{+8}_{-5}
p_0 (Z)	0.50 (0.00)	0.50 (0.00)	0.50 (0.00)	0.50 (0.00)	0.50 (0.00)
Signal Region	**SR-4j-3400**	**SR-5j-1600**	**SR-6j-1000**	**SR-6j-2200**	**SR-6j-3400**
Fitted background events					
Diboson	0.74 ± 0.24	36 ± 9	1.8 ± 0.6	$0.33^{+0.80}_{-0.33}$	0.07 ± 0.02
Z/γ^*+jets	3.3 ± 0.8	170 ± 16	9.3 ± 1.8	2.4 ± 0.6	0.32 ± 0.19
W+jets	1.6 ± 0.4	80 ± 7	7.2 ± 1.6	1.6 ± 0.5	0.41 ± 0.31
$t\bar{t}$(+EW) + single top	$0.09^{+0.12}_{-0.09}$	33 ± 6	2.7 ± 1.5	0.38 ± 0.3	$0.03^{+0.04}_{-0.03}$
Multi-jet	$0.05^{+0.05}_{-0.05}$	0.23 ± 0.23	–	–	–
Total bkg (pre-fit)	6.5	427	29	7.0	1.1
Total bkg	5.7 ± 1.0	319 ± 19	21.0 ± 2.9	4.6 ± 1.0	0.8 ± 0.4
Observed	4	320	25	5	0
$\langle \epsilon\sigma \rangle^{95}_{obs}$ [fb]	0.04	0.36	0.11	0.04	0.02
S^{95}_{obs}	5	50	15	6	3
S^{95}_{exp}	$6.1^{+2.9}_{-1.2}$	50^{+11}_{-13}	12^{+5}_{-4}	$5.8^{+2.8}_{-1.3}$	$3.0^{+1.2}_{-0.1}$
p_0 (Z)	0.50 (0.00)	0.48 (0.05)	0.24 (0.71)	0.48 (0.04)	0.50 (0.00)

Table 6.21: Numbers of observed event counts compared with background expectations obtained from the background-only fit in the DRs from the model-independent search. Statistical and systematic uncertainties are included in the errors stated. If cells are left empty, the corresponding estimates are below 0.01 events. Additionally, p-values (p_0) for the background-only hypothesis and their translation into Gaussian standard deviations (Z) obtained from the model-independent fit are quoted, giving the probability of the respective observation being consistent with the background prediction. These p-values are truncated at 0.5 if the observed number of events is lower than expected. Furthermore, ULs at *95% CL* on the visible cross-section ($\langle \epsilon\sigma \rangle^{95}_{obs}$) and on the visible number of observed (S^{95}_{obs}) and expected (S^{95}_{exp}) signal events are shown for the given number of predicted background events (and $\pm 1\sigma$ excursions of the expectation).

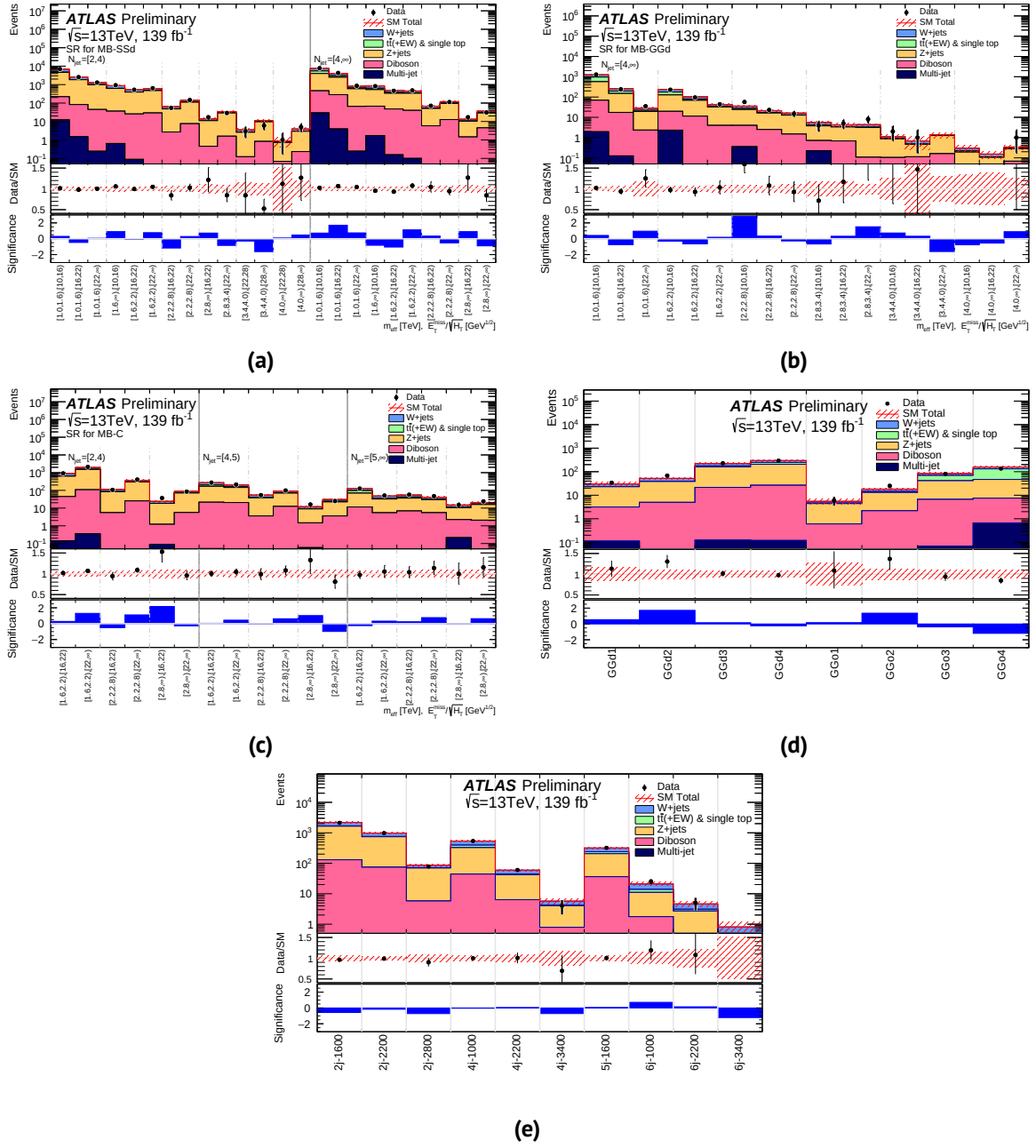

Figure 6.22: Observed and expected event yields as a function of the individual bins in the MB-SSd (Figure 6.22a), MB-GGd (Figure 6.22b) and MB-C (Figure 6.22c) channels as well as of the SRs in the BDT search (Figure 6.22d) and of the DRs in the model-independent search (Figure 6.22e). The significance of the discrepancy between observation and prediction, shown in the lower part of the plots, is computed following the profile likelihood method described in [129] in the case where the observed yield exceeds the prediction, and using the same expression with an overall minus sign if the yield is below the prediction. Hatched red error bands represent the combined systematic and statistical uncertainties.

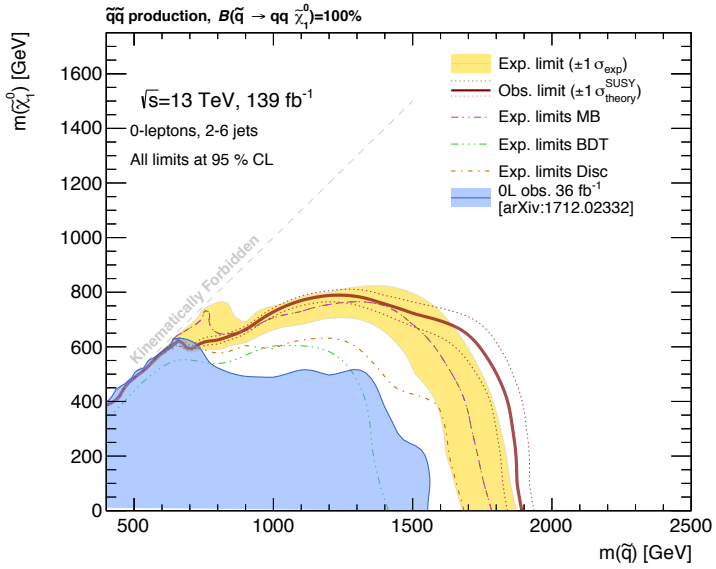

Figure 6.23: Exclusion limits in the mass plane of the SS-direct signal grid - $m(\tilde{q})$ against $m(\tilde{\chi}_1^0)$ - obtained from the optimised MB SR providing the best expected sensitivity at each point. The pink, green and orange dashed lines show the expected limits at *95% CL* obtained from the MB, BDT and model independent search, respectively. The yellow band indicates the 1σ excursions due to experimental and background-only theoretical uncertainties. The red solid contour represents the nominal observed limit, while the dotted red lines show the effect of the theoretical signal uncertainties. The results from the previous 0L (2-6jets) SUSY analysis [98] is shown for comparison. Signal cross-sections are corrected with respect to the results presented in [97].

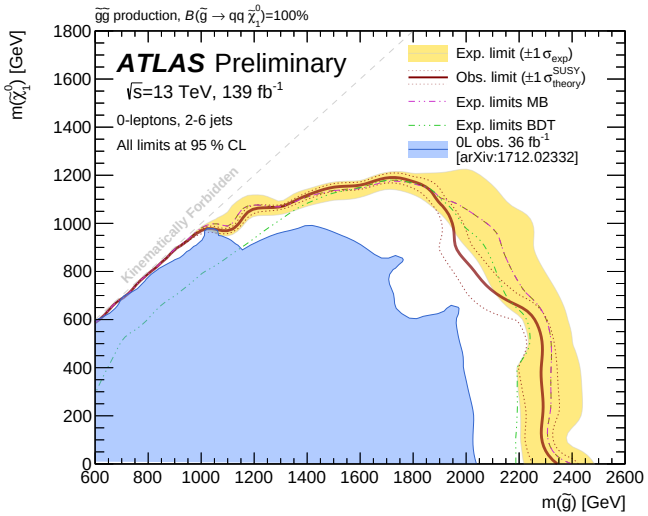

Figure 6.24: Exclusion limits in the mass plane of the GG-direct signal grid - $m(\tilde{g})$ against $m(\tilde{\chi}_1^0)$ - obtained from a combination of MB-C, MB-GGd and BDT-GGd SRs providing the best expected sensitivity at each point.The pink and green dashed lines show the expected limits at *95% CL* obtained from the MB and BDT, respectively. The yellow band indicates the 1σ excursions due to experimental and background-only theoretical uncertainties. The red solid contour represents the nominal observed limit, while the dotted red lines show the effect of the theoretical signal uncertainties. The result from the previous 0L (2-6jets) SUSY analysis [98] is shown for comparison as well as the individual expected exclusion lines derived in the MB and BDT analysis.

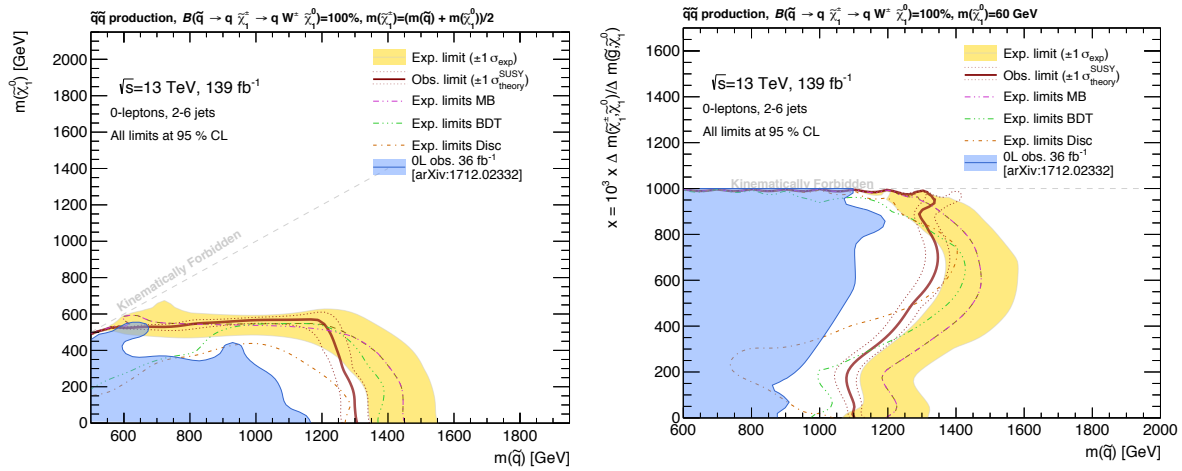

(a) **(b)**

Figure 6.25: Exclusion limits in the mass planes of the SS-onestep signal grid - $m(\tilde{q})$ against $m(\tilde{\chi}_1^0)$ for fixed chargino mass $m(\tilde{\chi}_1^{\pm}) = 1/2\,(m(\tilde{q}) + m(\tilde{\chi}_1^0))$ (Figure 6.25a) and $m(\tilde{q})$ against $x = \Delta m(\tilde{\chi}_1^{\pm}, \tilde{\chi}_1^0)/\Delta m(\tilde{q}, \tilde{\chi}_1^0)$ for fixed neutralino mass $m(\tilde{\chi}_1^0)$ = 60GeV (Figure 6.25b) - obtained from combined MB and BDT SRs providing the best expected sensitivity at each point. The pink, green and orange dashed lines show the expected limits at *95% CL* obtained from the MB, BDT and model independent search, respectively. The yellow bands indicate the 1σ excursions due to experimental and background-only theoretical uncertainties. The red solid contour represents the nominal observed limit, while the dotted red lines show the effect of the theoretical signal uncertainties. The results from the previous 0L (2-6jets) SUSY analysis [98] are shown for comparison as well as the individual expected exclusion lines derived in the MB and BDT analysis. Signal cross-sections are corrected with respect to the results presented in [97].

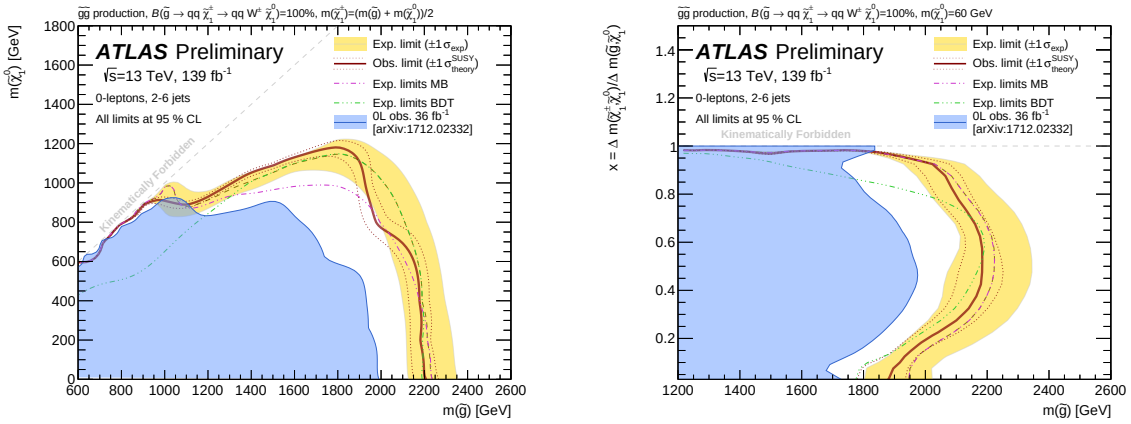

(a) **(b)**

Figure 6.26: Exclusion limits in the mass planes of the GG-onestep signal grid - $m(\tilde{g})$ against $m(\tilde{\chi}_1^0)$ for fixed chargino mass $m(\tilde{\chi}_1^{\pm}) = 1/2\,(m(\tilde{g}) + m(\tilde{\chi}_1^0))$ (Figure 6.26a) and $m(\tilde{g})$ against $x = \Delta m(\tilde{\chi}_1^{\pm}, \tilde{\chi}_1^0)/\Delta m(\tilde{g}, \tilde{\chi}_1^0)$ for fixed neutralino mass $m(\tilde{\chi}_1^0)$ = 60GeV (Figure 6.25b) - obtained from combined MB and BDT SRs providing the best expected sensitivity at each point. The pink and green dashed lines show the expected limits at *95% CL* obtained from the MB and BDT search, respectively. The yellow bands indicate the 1σ excursions due to experimental and background-only theoretical uncertainties. The red solid contour represents the nominal observed limit, while the dotted red lines show the effect of the theoretical signal uncertainties. The results from the previous 0L (2-6jets) SUSY analysis [98] are shown for comparison as well as the individual expected exclusion lines derived in the MB and BDT analysis.

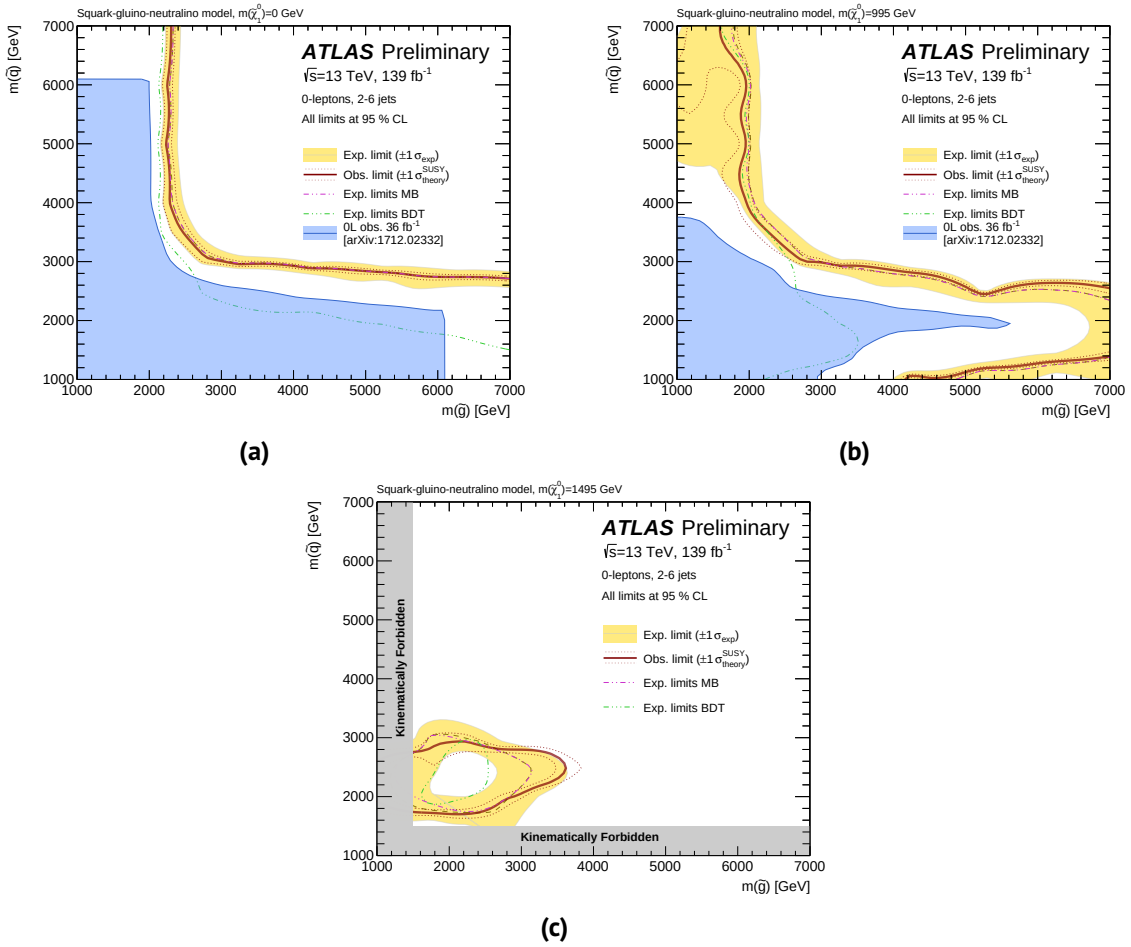

Figure 6.27: Exclusion limits in the $m(\tilde{q})$-$m(\tilde{g})$ plane for a signal model assuming inclusive squark-gluino production obtained from combined MB and BDT SRs providing the best expected sensitivity at each point are shown for three different assumptions on the mass of the LSP: $m(\tilde{\chi}_1^0)$ = 0 GeV (Figure 6.27a), $m(\tilde{\chi}_1^0)$ = 995 GeV (Figure 6.27b) and $m(\tilde{\chi}_1^0)$ = 1495 GeV (Figure 6.27c). The pink and green dashed lines show the expected limits at *95% CL* obtained from the MB and BDT search, respectively. The yellow bands indicate the 1σ excursions due to experimental and background-only theoretical uncertainties. The red solid contour represents the nominal observed limit, while the dotted red lines show the effect of the theoretical signal uncertainties. The results from the previous 0L (2-6jets) SUSY analysis [98] are shown for comparison as well as the individual expected exclusion lines derived in the MB and BDT analysis.

7 Search for Squarks and Gluinos with Varying RPV Coupling Strength

The previous chapter presented the 0L (2-6jets) SUSY analysis, a search specifically designed to target supersymmetric particles with vanishing lifetime and a stable LSP in the context of the RPC MSSM. This analysis is one out of many in the ATLAS SUSY search program. Figure 7.1 gives an overview of this program, grouping the individual searches with respect to their basic underlying model assumptions. The first three categories, which include the majority of SUSY analyses, target promptly decaying sparticles in RPC scenarios (inclusive searches, searches for third generation squarks and for eweakinos), while the second, much smaller group targets models including LL sparticles and RPV processes.

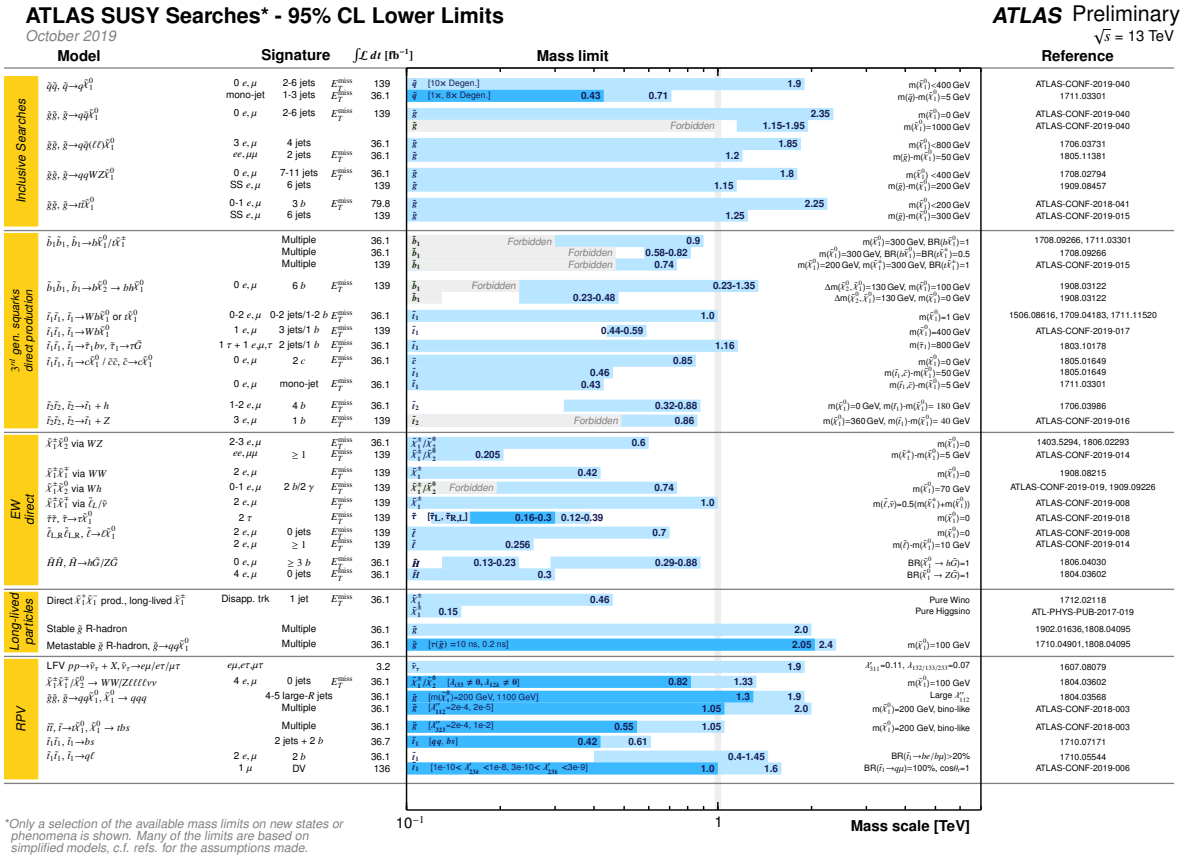

Figure 7.1: Summary of the ATLAS SUSY search program depicting the mass range of sparticles excluded by a representative selection of available results. Exclusion limits are based on the nominal cross-sections and displayed in a parameter space representing the respective model each search was designed for [130].

Analyses included in the first group and those included in the RPV category can be distinguished in particular by their underlying assumption about the R-parity, which is maximally violated in the latter and strictly conserved in the first group. However, many possible realisations of SUSY allow for intermediate scenarios, as explained in subsection 2.2.2. Hence, the ATLAS collaboration decided to investigate the "gap" in phase space between these two extreme scenarios by reinterpreting

a selection of analyses from both groups in scenarios with variable sparticle life times and RPV coupling strengths. The reinterpretation, often referred to as *RPC-meets-RPV analysis* [131], is based on the idea, that searches designed for specific scenarios might also be sensitive to different SUSY models which include similar final states. This chapter is dedicated to the RPC-meets-RPV analysis.

Models describing the production of gluinos and stops decaying into a LL LSP are constructed as well as a pure RPC model featuring a LL gluino. These models and their MC simulation are detailed in section 7.1. An overview of the set of analyses contributing to the reinterpretation is given in section 7.2 and the final results are discussed in section 7.4.

This chapter mainly focuses on the reinterpretation of the L=36.1 fb^{-1} version of the 0L (2-6jets) SUSY analysis, since the author was the main analyser. Furthermore, the inclusive 0L search plays a special role in the RPC-meets-RPV analysis being the only search reinterpreted in the variable RPV and the LL gluino scenarios. Additionally, Jet Energy Scale (JES) and Jet Energy Resolution (JER) uncertainties arising from the displacement of the decays of LL particles, which have to be taken into account in all contributing analyses, were assessed in the context of the 0L (2-6jets) SUSY analysis. This study was made public separately [132] and is detailed in section 7.3.

7.1 SUSY Models

Both scenarios considered in the RPC-meets-RPV analysis are described via simplified models. The variable RPV scenario comprises three different sets of simplified models, based on the variation of the baryon-number-violating RPV coupling λ''_{ijk} from Equation 2.29. The model predicting LL gluinos, forming R-hadrons, is based on a Split-SUSY scenario, as described in subsection 2.2.2. The main characteristics of both scenarios are summarised in Table 7.1 and detailed below.

Model name	Gqq	Gtt	Stop	R-hadron
Coupling	λ''_{112}	λ''_{323}	λ''_{323}	–
Decay	$\tilde{g} \to qq\tilde{\chi}_1^0$ $\tilde{g} \to qq\tilde{\chi}_1^0(\to qqq)$ $\tilde{g} \to qqq$	$\tilde{g} \to tt\tilde{\chi}_1^0$ $\tilde{g} \to tt\tilde{\chi}_1^0(\to tbs)$ $\tilde{g} \to tbs$	$\tilde{t}_1 \to t\tilde{\chi}_1^0$ $\tilde{t}_1 \to t\tilde{\chi}_1^0(\to tbs)$ $\tilde{t}_1 \to bs$	$\tilde{g} \to qq\tilde{\chi}_1^0$
Other coloured sparticle masses	$m(\tilde{q})$ = 3 TeV $m(\tilde{t}/\tilde{b})$ =5 TeV	$m(\tilde{q})$ = 5 TeV $m(\tilde{t}/\tilde{b})$ =2.4 TeV	$m(\tilde{q}/\tilde{g})$ = 3 TeV $m(\tilde{t}_2/\tilde{b})$ = 3 TeV	$m(\tilde{q}/\tilde{t}/\tilde{b}) \approx$ PeV
LSP	The LSP is bino-like, $m(\tilde{\chi}_1^0)$ = 200 GeV			$m(\tilde{\chi}_1^0)$ = 100 GeV

Table 7.1: Summary of signal models in the variable RPV and the LL gluino scenario. Light-flavoured squark masses are assumed to be degenerate ($\tilde{q} = \tilde{u}, \tilde{d}, \tilde{s}, \tilde{c}$) as well as the left- and right-handed sparticles ($\tilde{q} = \tilde{q}_1, \tilde{q}_2$). In case of the stop model, the right-handed stop is assumed to be lighter.

7.1.1 Variable RPV Models

All sets of simplified models included in this scenario assume that the lepton-number-violating RPV couplings λ and λ' are zero, guaranteeing the stability of the proton. Just one particular λ'' out of all possible combinations of i, j and k is chosen to be non-zero, respecting the antisymmetry condition $\lambda''_{ijk} = -\lambda''_{ijk}$ (cf. subsection 2.2.1).

The choice of the nature of the LSP not only affects the complexity of the expected processes - the potential presence of charginos in the particle spectrum would open additional decay channels for squarks and gluinos - but also the lifetime of the LSP. To simplify the possible signal processes, the LSP in all three sets of topologies is assumed to be a pure bino $\widetilde{\chi}_1^0$ with a mass of 200 GeV in order to allow for decays of the LSP into top quarks. Its lifetime, described in terms of decay length L, depends not only on the mass eigenstate of the $\widetilde{\chi}_1^0$ (Equation 2.34) but also on the masses of the squarks and the value of the coupling strength

$$L(cm) = \frac{0.9\beta\gamma}{\lambda''^2} \left(\frac{m(\tilde{q})}{100\ \text{GeV}} \right)^4 \left(\frac{1\ \text{GeV}}{m(\widetilde{\chi}_1^0)} \right)^5 . \tag{7.1}$$

Hence, in order to construct the signal grids in the RPV scenario, the free parameters of each category are the mass of the initial SUSY particle as well as the coupling strength λ'' and with it the neutralino lifetime and branching ratio of the neutralino decay channels. SPheno 4.0.2 [133, 134] in combination with SARAH 4.12.0 [135] is used to compute the lifetime and branching ratio for the chosen squark masses, stated in Table 7.1.

The three different categories describe a pair-production of gluinos decaying into light-flavoured quarks (Gqq model) or top quarks (Gtt model) and a potentially LL LSP and the production of $\widetilde{t}$ (Stop model), depicted in Figure 7.2. The RPV coupling strength is increased from left to right, changing the branching ratio of the possible decay channels. For very small values of λ'' the neutralino is stable and the intial sparticle decays promptly. With growing coupling strength, the LSP is rendered a LL particle, giving rise to cascade decays with increasing branching ratio. The diagrams in the middle of Figure 7.2 assume 100% branching ratio for the decay depicted. For even higher values of λ'' the branching ratio for the prompt, maximally R-parity violating decay of the initial sparticle (right column) becomes large until it reaches 100% for λ'' = 1.

The three sets of simplified models considered in the RPC-meets-RPV analysis are detailed below.

Gqq model The variable RPV coupling in case of the Gqq model is λ''_{112}. This model contains light gluinos produced in pairs and decaying via $\widetilde{g} \to qq\widetilde{\chi}_1^0$ into first and second generation quarks and the LSP which is stable for $\lambda''_{112} \to 0$ (the RPC limit). With increased value of the RPV coupling strength the LSP decays into three quarks ($\widetilde{\chi}_1^0 \to qqq$). In the RPV limit, where the λ''_{112} reaches its maximal value, the lifetime of the neutralino vanishes allowing for a direct decay of the gluino $\widetilde{g} \to qqq$. The additional squark masses are set to 3 TeV in case of the first and second generation and are assumed to exceed 5 TeV for all other sparticles including stop and sbottom.

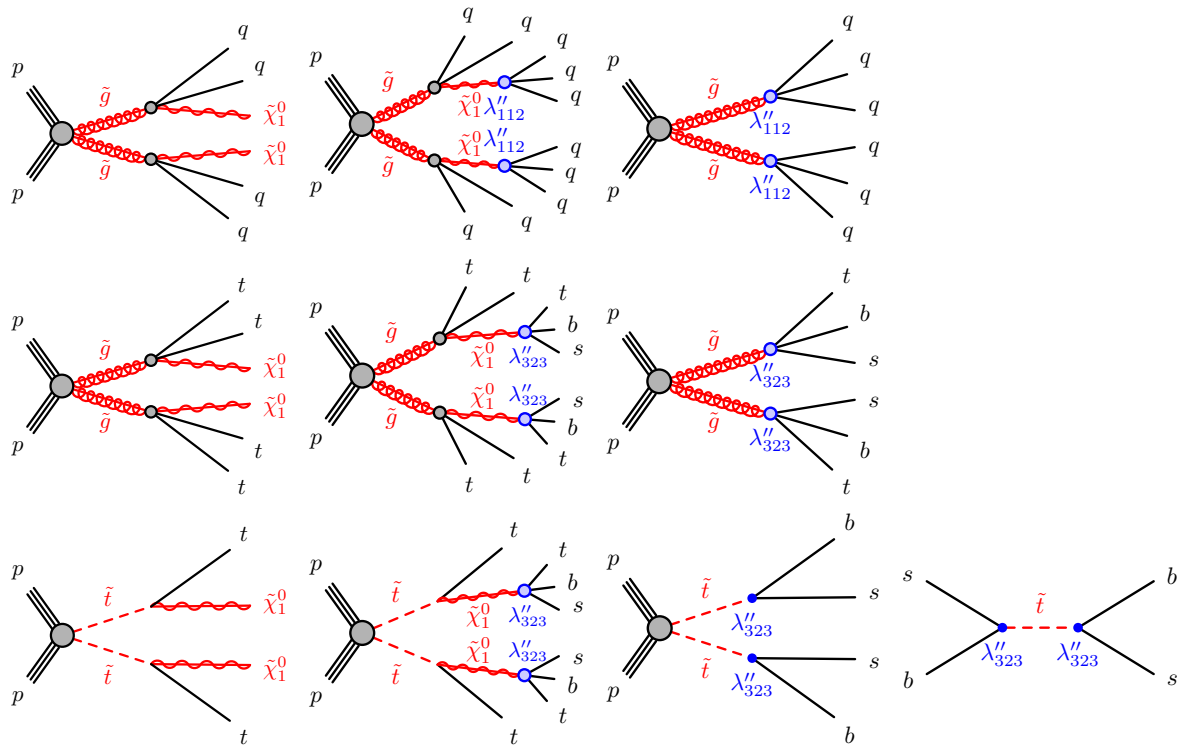

Figure 7.2: Sets of simplified models considered in the RPV scenario. The top row shows the Gqq model, the Gtt model is depicted in the middle row, and Stop model is shown in the bottom row. For each model, the graphs on the left represent the RPC limit where the $\widetilde{\chi}_1^0$ is stable, the middle graphs are the dominant process for moderate values of λ'' and the processes on the right depict the RPV limit of the model, describing a prompt decay of $\widetilde{g}$ and $\widetilde{t}$, respectively.

Gtt model Similarly to the Gqq model, the Gtt model describes the pair production of gluinos with a subsequent decay into top quarks and the LSP. The non-zero coupling constant in this model is the λ''_{323}, a scenario which is favoured under MFV (cf. subsection 2.2.2). The gluinos are assumed to decay via off-shell stops into tops and the LSP ($\widetilde{g} \to tt\widetilde{\chi}_1^0$), whereby the masses of stop and sbottom are set to 2.4 TeV and all other sparticles (including light-flavoured squarks) are heavier than 5 TeV. For low values of the RPV coupling the LSP decays as $\widetilde{\chi}_1^0 \to tbs$, while the neutralino vanishes for large values of λ''_{323} giving rise to a direct gluino decay of the form $\widetilde{g} \to tbs$.

The masses of the (off-shell) squarks involved in the decay processes are chosen differently than in the Gqq model given that in the Gtt model only two light squarks (the right-handed $\widetilde{t}$ and $\widetilde{b}$) are present and the decays considered in this model are suppressed due to the top mass being much larger than the masses of the first and second generation quarks.

Stop model This model is also based on the variation of λ''_{323} but unlike the Gtt model, the Stop model describes the pair-production of stops which decay directly into a top quark and a stable LSP in the RPC limit ($\widetilde{t}_1 \to t\widetilde{\chi}_1^0$). While moderate values of the coupling strength give rise to a decay via an intermediate neutralino, which subsequently decays via $\widetilde{\chi}_1^0 \to tbs$. For large values of λ''_{323} the stop decays directly into bottom and strange ($\widetilde{t}_1 \to bs$) but can also be produced resonantly ($pp \to \widetilde{t}_1 \to bs$). This resonant single stop production allows to set much stronger limits on the

mass of the $\widetilde{t}$, since the cross-section for this production mode evolves with $(\lambda''_{323})^2$ and is much larger than for the pair-production, e.g. two orders of magnitude for λ''_{323} = 1 and $m(\widetilde{t})$ = 500 GeV.

The different signal grids in the RPC-meets-RPV analysis are generated with MG5_aMC@NLO2.3.3 [72] interfaced with PYTHIA8.210. Up to two additional partons in the matrix element are considered. The A14 [107] tune is used for the UE parameters and the NNPDF23LO PDF set [106]. Pile-up collisions are simulated with PYTHIA8.186 [114] using the A2 tune [136] and the MSTW2008LO [137] PDF set. GEANT4 is used to describe the detector response to the signal events.
The respective cross-sections for models assuming pair-production are calculated at NLO in the strong coupling constant α_s with additional resummation of soft gluon emission at next-to-leading-logarithmic order (NLL), often referred to as (NLO+NLL) [119–122, 138]. Uncertainties on the calculated cross-sections are obtained from varying the PDF sets as well as the factorisation and renormalisation scales [139]. Possible contributions from the t- and u-channel for gluino pair-production and from the $\widetilde{g}\widetilde{q}$ production mode are not included, even tough squark masses are specified. In case of the resonant single stop production included in the Stop model, the cross-section is derived at NLO precision [140, 141].
The range in which λ'' is varied is well motivated and constrained by theoretical ULs. These limits are obtained considering the Renormalisation Group Equations (RGE) of the superpotential parameters in Equation 2.29. Additionally, it is required that $\lambda''(M_{GUT}) < \sqrt{4\pi}$, i.e. the RPV couplings behave perturbatively up to the scale of the GUT. The values of these ULs, found in literature, are $\lambda''_{112} < 1.25$ [142] and $\lambda''_{323} < 1.07$ [143].

Consequences of the finite neutralino lifetime The impact of the variation of the neutralino lifetime in the RPV scenario on the main variables used to define SR selections in the contributing analysis, detailed below, was investigated. The distribution of the multiplicity of jets and b-jets, $E_{\mathrm{T}}^{\mathrm{miss}}$ and m_{eff} as a function of the $\widetilde{\chi}_1^0$ lifetime are shown in Figure 7.3.
Several effects are visible in these plots:

- The jet multiplicity increases for $\widetilde{\chi}_1^0$ lifetimes short enough to allow for decays taking place in the calorimetric system where the decay products can be reconstructed.
- The number of b-tagged jets shows a similar behaviour but the b-tagging efficiency tunes this observable such that it is increased for small but non-zero lifetimes. For larger lifetimes on the other hand, the b-jet multiplicity decreases due to the negative effect of the increased decay length on the tagging efficiency.
- The distribution of the $E_{\mathrm{T}}^{\mathrm{miss}}$ largely depends on the lifetime of the neutralino. In case of short lifetimes, i.e. large values of λ'', the $\widetilde{\chi}_1^0$ decays significantly reduce the amount of $E_{\mathrm{T}}^{\mathrm{miss}}$. However, for sufficiently large lifetimes the decay of the LSP takes place outside the sensitive detector volume, resulting in signatures with significant $E_{\mathrm{T}}^{\mathrm{miss}}$, increasing the sensitivity of dedicated RPC searches.
- The scalar sum of the p_{T} of the hadronic decay products of the LSP is generally larger than its contribution to the $E_{\mathrm{T}}^{\mathrm{miss}}$. Hence, m_{eff} is increased for larger neutralino lifetimes.

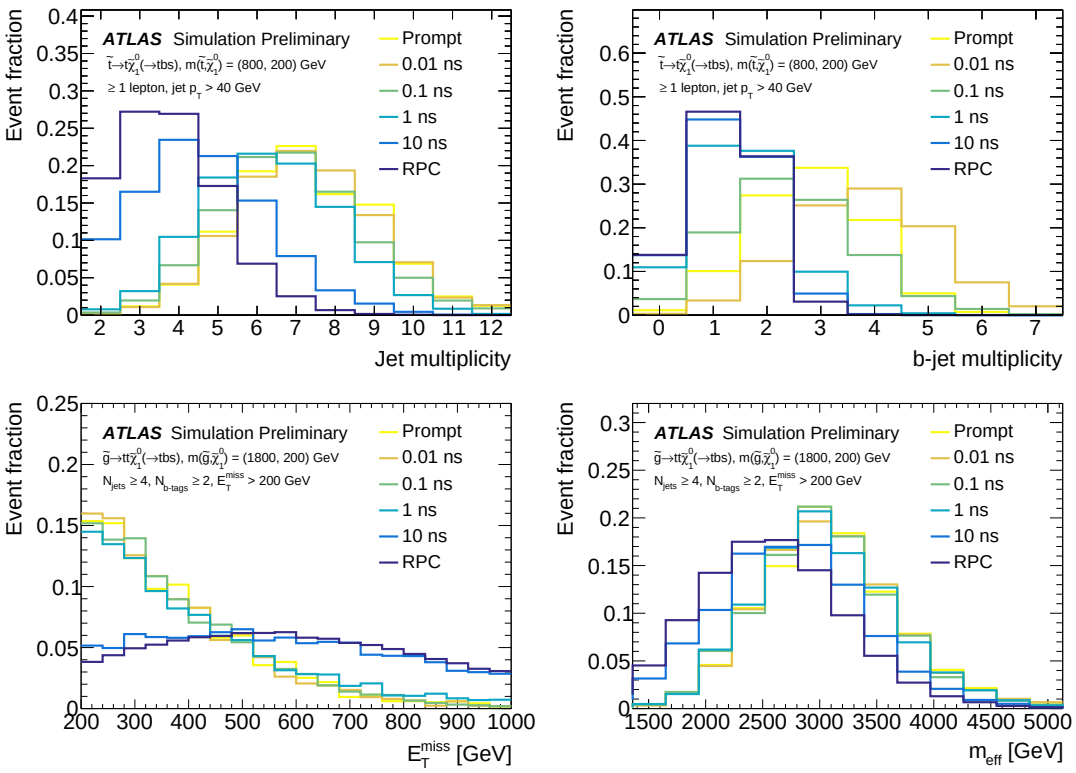

Figure 7.3: Distribution of the number of jets and b-tagged jets in the Gtt model as well as E_T^{miss}, and m_{eff} in the Gqq model for various neutralino lifetimes at reconstruction level based on the full simulation of the ATLAS detector.

7.1.2 R-hadron Model

Based on the idea of Split-SUSY, a simplified model is constructed describing the pair-production of LL gluinos which can hadronise into highly virtual, colour-singlet states, the so called *R*-hadrons. As described in subsection 2.2.2, the metastability of gluinos in this particular SUSY model is a consequence of the large squark masses, which are of the order of PeV. The characteristics of the hadronic states - the mass, the lifetime, possible decay channels, etc. - are largely determined by the initial gluino.

The intermediate *R*-hadrons decay further into light-flavoured quarks and a stable LSP with a chosen mass of 100 GeV, fully conserving *R*-parity [144–146] leading to signatures with multiple displaced jets and E_T^{miss}. Hence, the free parameters in the *R*-hadron model are the mass and the lifetime of the gluino.

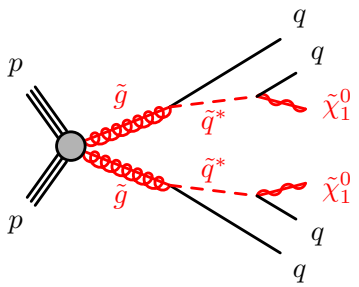

Figure 7.4: Diagram illustrating the LL gluino model.

Figure 7.4 shows the Feynman diagram for the simplified *R*-hadron model in case the lifetime of the initial gluino exceeds the hadronisation timescale of the order of 10^{-23} sec. If the gluino lifetime is below this threshold, no bound-state can be formed and the respective process is

represented by the first graph in Figure 7.2. The signal grid is produced with PYTHIA6.428, using the AUET2B tune [136] to obtain the parameters for the UE and the CTEQ6L1 [147] PDF set. Dedicated routines [146, 148, 149] which describe the hadronisation of heavy coloured particles, were used to simulate the production process of the R-hadrons. In order to simulate the response of the ATLAS detector to such non-standard processes, a specified simulation implemented in GEANT4 [145] was used to correctly describe the interactions of the R-hadrons with the active detector material.

7.2 Analyses

Out of all ATLAS searches included in Figure 7.1 for which results based on a partial set of the Run 2 data were available, a set of nine analyses showing the highest sensitivity to the processes described in section 7.1, were reinterpreted in the context of the RPC-meets-RPV analysis. These searches together with their main SR selections and the models they are most sensitive to, are listed in Table 7.2 and discussed in greater detail in this section focusing in particular on the 0L (2-6jets) SUSY analysis in subsection 7.2.1. If not stated otherwise below, all contributing analyses are based on the same Run 2 data-subset, corresponding to an integrated luminosity of L=36.1 fb^{-1}.

Analysis name	Leptons	Jets	b-tags	$E_{\mathrm{T}}^{\mathrm{miss}}$ requirement	Representative cuts	Model targeted
RPC 0-lepton, 2-6 jets [98]	0	≥ 4	–	$E_{\mathrm{T}}^{\mathrm{miss}}/m_{\mathrm{eff}} > 0.2$	$m_{\mathrm{eff}} > 3000$ GeV	Gqq, R-hadron
RPC 0-lepton, 7-11 jets [150]	0	≥ 7 ≥ 11	– ≥ 2	$E_{\mathrm{T}}^{\mathrm{miss}}/\sqrt{H_{\mathrm{T}}} > 5$ GeV$^{1/2}$	–	Gqq Gtt
RPC multi-b [151]	0 1	≥ 7 ≥ 5	≥ 3 ≥ 3	$E_{\mathrm{T}}^{\mathrm{miss}} > 350$ GeV $E_{\mathrm{T}}^{\mathrm{miss}} > 500$ GeV	$m_{\mathrm{eff}} > 2600$ GeV $m_{\mathrm{eff}} > 2200$ GeV	Gtt
RPV 1-lepton [152]	1	≥ 10	≥ 3 0	–	–	Gtt, stop
RPC Stop 0-lepton [153]	0	≥ 4	≥ 2	$E_{\mathrm{T}}^{\mathrm{miss}} > 400$ GeV	$m_{\mathrm{jet,R=1.2}} > 120$ GeV	stop
RPC Stop 1-lepton [154]	1	≥ 4	≥ 1	$E_{\mathrm{T}}^{\mathrm{miss}} > 250$ GeV	$m_T > 160$ GeV	stop
RPC and RPV same-sign and three leptons [155]	2 SS or 3	≥ 6 ≥ 6	≥ 2 ≥ 2	$E_{\mathrm{T}}^{\mathrm{miss}}/m_{\mathrm{eff}}$>0.15 –	$m_{\mathrm{eff}} > 1800$ GeV $m_{\mathrm{eff}} > 2000$ GeV	Gtt, stop
RPV stop dijet pairs [156]	–	≥ 4	≥ 2	–	$\mathcal{A} < 0.05$	stop
Dijet and TLA [157, 158]	–	≥ 2	–	–	$\lvert y^* \rvert < 0.6$	stop

Table 7.2: Summary of the main characteristics of the most sensitive SRs for each contributing analysis, showing only a subset of the cuts defining the SR. Variables which are not used in the respective analysis are marked with a dash (–).

RPC 0L (7-11jets) The so called RPC multijet search targets gluinos which decay via long cascades generating final states with a high jet multiplicity and very soft neutralino LSPs causing only

moderate $E_{\mathrm{T}}^{\mathrm{miss}}$. Its main discriminating variable is $E_{\mathrm{T}}^{\mathrm{miss}}/\sqrt{H_{\mathrm{T}}}$. Although this search is not designed specifically for the topologies considered in the RPC-meets-RPV analysis, it might gain some sensitivity to the Gqq model and Gtt model in case a sufficiently short lifetime of the neutralino leads to decays inside the detector increasing the jet multiplicity, while moderate values of $E_{\mathrm{T}}^{\mathrm{miss}}$ can be obtained from jet mis-reconstruction, due to displaced decays.

RPC multi-b This analysis searches for pair-produced gluinos which decay into top quarks and a stable LSP equivalent to the RPC limit of the Gtt model. It uses a hard cut on m_{eff}, a moderate one on the $E_{\mathrm{T}}^{\mathrm{miss}}$ and requires a high jet and b-jet multiplicity in regions with zero or one leptons. These SR selections are optimised to maximise the sensitivity based on a two-dimensional shape fit of N_j and m_{eff}.

RPC stop 0L and RPC stop 1L Both analyses search for pair-produced stops in the RPC limit of the Stop model. While the RPC stop 0L targets $t\bar{t}$ + $E_{\mathrm{T}}^{\mathrm{miss}}$ events where the tops decay solely hadronically, the RPC stop 1L requires one top to decay leptonically. Large radius jets, obtained via jet reclustering, are used in these searches to reconstruct the boosted hadronic decay products of the top.

RPC and RPV SS/3L The main requirement in this analysis is the presence of two same-sign or three leptons, which effectively suppresses the SM background processes making it sensitive to RPC as well as RPV processes. Hence, SRs are constructed with and without a $E_{\mathrm{T}}^{\mathrm{miss}}$ requirement to target all three simplified models included in the Gtt model and the RPV limit of the Stop model.

RPV 1L This search is designed to target pure RPV scenarios describing the production of gluinos and stops. Event selections require at least one lepton and either the absence of b-jets or the presence of many b-jets, final states which are similar to the RPV limits of the Gtt and the Stop model.

RPV stop dijet pairs Based on a Run 2 data subset corresponding to an integrated luminosity of L=37 fb^{-1}, this search presents limits on the mass of the stop of about 650 GeV. The model targeted describes a pair-production of stops, which decay into b and s, similar to the Stop model in the RPC-meets-RPV analysis for large values of λ''. Final states are selected containing two heavy and well balanced jet pairs, i.e. large masses with a small mass asymmetry $\mathcal{A}$.

RPV dijet and RPV TLA These two analyses are originally designed to search for an excess in the dijet mass spectrum in early Run 2 data sets corresponding to luminosities of L=36.1 fb^{-1} and L=3.4 fb^{-1}, respectively. The offline RPV dijet search and the Trigger Level Analysis (TLA) are reinterpreted targeting the resonant production of a single stop, included in the Stop model.
Unlike in typical SUSY analyses, RPV dijet and RPV TLA do not make use of simulated signal samples to interpret their results. Instead limits on Gaussian resonances are reinterpreted [159] based on the computation of signal acceptances taken from [141].

7.2.1 RPC inclusive 0L search

The 0L (2-6jets) SUSY analysis [98] reinterpreted in the RPC-meets-RPV analysis is very similar to the latest version of this analysis based on the full Run 2 dataset described in detail in chapter 6, with the exception that neither a MB nor a BDT search was used. Instead the RPC 0L (2-6jets) makes use of a plethora of single bin SRs, similar to the DRs described in subsection 6.2.5, as well as the so called recursive jigsaw reconstruction. This technique is used to construct regions targeting mainly compressed mass spectra. Hence, only the m_{eff} based single bin selections are reinterpreted in the context of the Gqq model and R-hadron scenario, where the mass difference between the initial sparticle and the LSP is rather large.

The event cleaning cuts, used in the RPC 0L (2-6jets) to suppress events from Non-Collision Background (NCB), are based on the jet charged particle fraction, i.e. the ratio of the scalar sum of the p_{T} of the tracks associated with the jet and the jet p_{T}. These requirements were found to significantly reduce the efficiency in LL decays where jets produced in displaced vertices are likely to miss associated tracks. Hence, these cuts were modified in order to gain sensitivity in such scenarios. Additionally, the requirement on the energy weighted jet timing had to be removed, since displaced jets can have significantly shifted positive timing.

Modification of the Non-Collision Background Cleaning The NCB is generally negligible in all SRs in the inclusive 0L search. Hence, this background is not included in the original fitting procedure to obtain the analysis results. Event yields from NCB are estimated using a template fit method. The non-collision template requires a ratio of the total charge fraction $chargeFrac$ of the first two leading jets (j_1 and j_2) and the maximal fraction of energy in one layer of the calorimeter F_{max} below 0.1,

$$\frac{chargeFrac(j_1,j_2)}{F_{max}(j_1,j_2)} < 0.1. \tag{7.2}$$

The collision template selects predominantly back-to-back jet events. The difference between the results of fitting data with both templates gives an estimate for the NCB contribution.

In order to avoid the inefficiencies to LL signals introduced by this method, the requirement in Equation 7.2 is replaced by

$$F_{max}(j_1,j_2) < 0.8 \quad and \quad F_{EM}(j_1,j_2) < 0.96, \tag{7.3}$$

based on the longitudinal calorimeter-sampling profile of the two leading jets. F_{EM} denotes the fraction of energy in the EMcal, i.e. less than 96% of the energy of the two leading jets is deposited in the EMcal and less than 80% in one single layer of the calorimeter.

These NCB cuts are used in ATLAS searches for long-lived particles [160], where they were found to be very efficient. However, the effect of the modification of the NCB cleaning and of the removal of the original jet timing requirement (-4 ns $< timing <$ 4 ns) on the results of the RPC 0L (2-6jets) was investigated.

Figure 7.5 illustrates a comparison of the distribution of the energy weighted jet timing

$$timing = \frac{timing(j_1)E(j_1) + timing(j_2)E(j_2)}{E(j_1) + E(j_2)} \tag{7.4}$$

for different configurations of the NCB cleaning. Figure 7.5a and Figure 7.5b give the yields of collision and non-collision events using the original and the modified cleaning on a very loose pre-selection ($p_T(j_1) > 200$ GeV, $p_T(j_2) > 50$ GeV, $m_{\text{eff}} > 800$ GeV), showing how the contribution from NCB is increased due to the cleaning modification. The mis-modelling of the positive tails visible in Figure 7.5b can be compensated by reintroducing a loosened requirement on the timing of the first two jets ($timing(j_1, j_2) < 20$ ns), as shown in Figure 7.5c. However, it was decided to renounce this correction, since the events in the positive tail, which are mainly NCB events from the next bunch-crossing[1], vanish in case of a phase-space more similar to the SR selections in the RPC 0L (2-6jets), exemplified in Figure 7.5d.

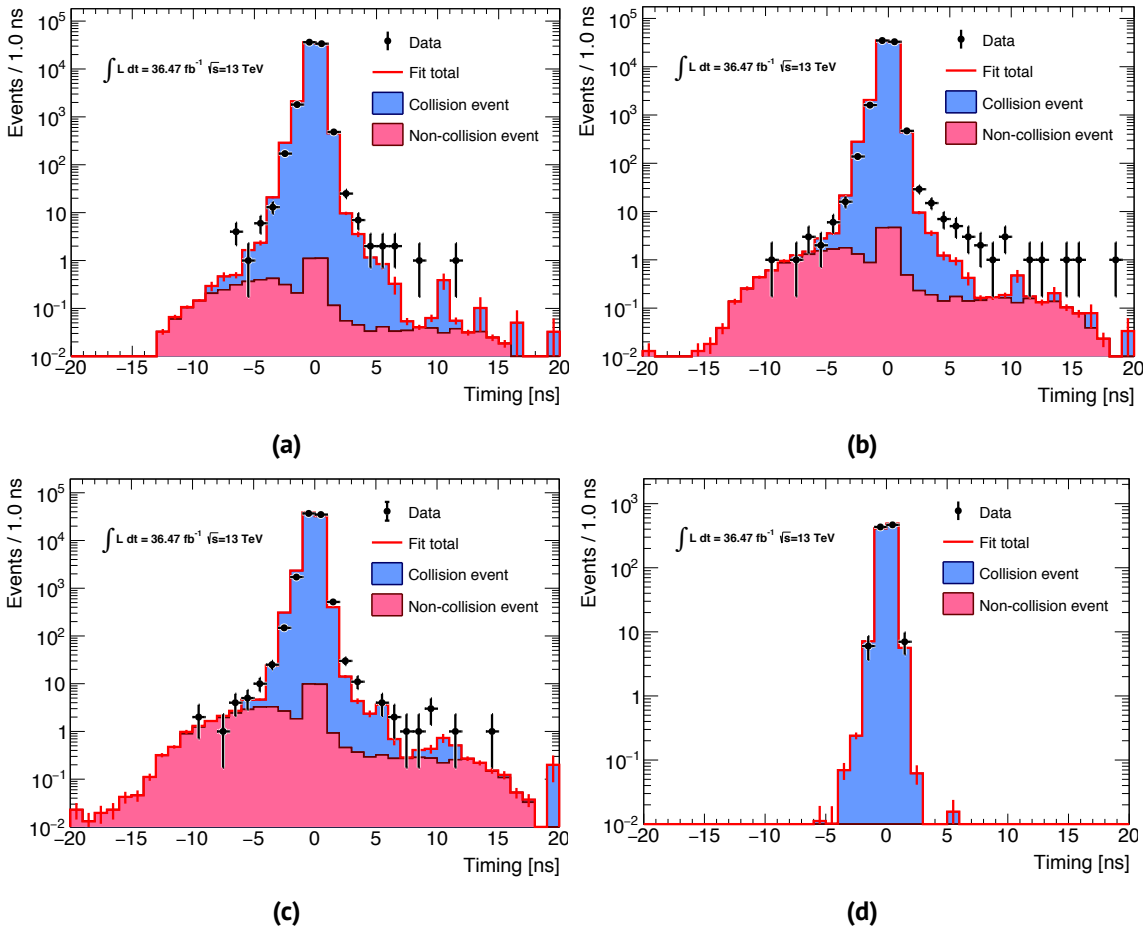

Figure 7.5: Result of the template fit on data showing the energy weighted jet timing of the dijet system defined in Equation 7.4. The original (Figure 7.5a) and the modified NCB cleaning without and with a requirement placed on the jet timing (Figure 7.5b and Figure 7.5c) is applied to preselected events. Results using the modified cleaning in a tighter, more SR like scenario (Figure 7.5d) are also shown [161].

The results of the background-only fit are reproduced using the modified cleaning cuts, in order to

[1] the bunch-spacing during Run 2 is 25 ns

proof that no significant change in the yields in the SRs is introduced. Figure 7.6 shows the event yields as a function of the SR selections as published and reproduced with modified NCB cuts.

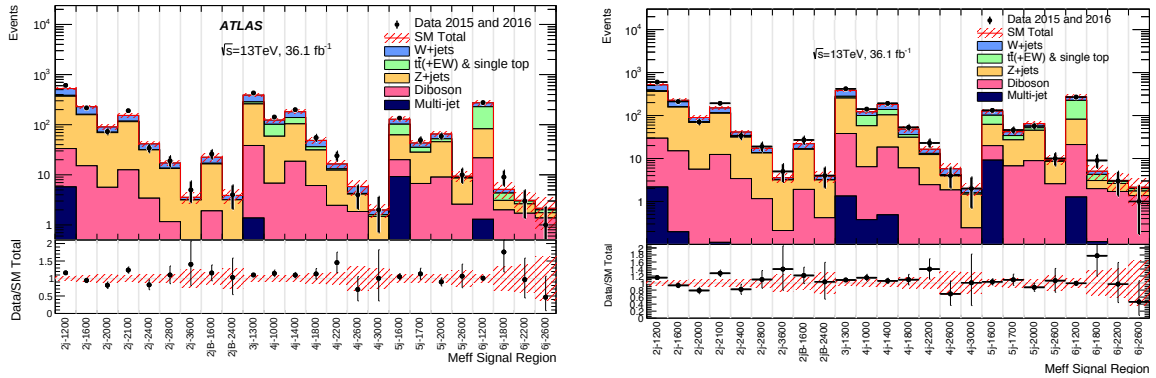

Figure 7.6: Comparison of observed and expected event yields as a function of SR selections in the RPC 0L (2-6jets) search published in [98] (Figure 7.6a) and reproduced using the modified NCB cleaning (Figure 7.6b) [161].

The signal and background yields in all SRs and CRs taken into account, were found to change only minimally. Deviations from the published results are below 2% to 4% for most regions.
Having only a minor effect on the analysis results in the original RPC scenario, the modifications of the NCB cuts are immensely important in LL scenarios, improving the expected exclusion limits, in particular in the R-hadron model, by more than two orders of magnitude in sparticle lifetime.
The analysis setup was also used to study the impact of the finite sparticle lifetimes, resulting in displaced decays, on the kinematic uncertainties on the jets and the $E_{\mathrm{T}}^{\mathrm{miss}}$. Detailed studies on these additional uncertainties are discussed in subsection 7.3.1 and subsection 7.3.2.

7.3 Estimating the Uncertainties

In each analysis reinterpreted in the context of the RPC-meets-RPV analysis the total set of individual uncertainties, described in the respective publication, is applied.
Generally, the contribution from pile-up is suppressed in the analyses, by requiring jets within $|\eta| < 2.4$ to satisfy a loose requirement on JVT [82], corresponding to a working point with an efficiency of 94% for a p_{T} of 40 GeV and almost 100% for jets with $p_{\mathrm{T}} \geq 60$ GeV produced in the hard scatter. The JVT requirement is applied to all jets up to 60 GeV, except in the RPV 1L, where it is applied independently of the jet p_{T}. The lepton definitions used in the individual searches rely on the impact parameters in the final states, as described in subsection 5.1.3 and subsection 6.1.2. Hence, the contributing analyses are sensitive to displaced jets but ignore displaced leptons.
Searches, which are sensitive to hadronic signals with a substantial lifetime, need to take into account additional uncertainties arising from the jet displacement. In particular two dedicated uncertainties are considered, accounting for potential differences in the modelling of LL signals in data and MC simulation, due to effects of the displacement on the performance of the jet reconstruction and calibration as well as b-tagging algorithms.

These uncertainties, detailed below, are applied solely to the respective LL signal samples, since the background processes in all contributing analyses are prompt.

7.3.1 Uncertainties on the Jet Energy Scale

The analyses reinterpreted in the RPC-meets-RPV analysis are specifically designed to search for promptly decaying sparticles with vanishing lifetime. The hadronic decay products of such sparticles are reconstructed and calibrated as jets using the standard procedure described in subsection 5.1.2. The LL SUSY particles in the variable RPV and the R-hadron scenario, on the other hand, potentially decay far from the centre of the detector in a Displaced Vertex (DV). Therefore, it is vital to asses the sensitivity of the contributing analyses in displaced scenarios by studying the transverse momentum response and reconstruction efficiency for displaced jets.
Ideally these studies should be based on a comparison of the behaviour of displaced jets in MC simulated samples and data. However, no data containing events with strongly displaced jets is available, thus a purely MC based strategy is employed instead. Uncertainties are estimated from the comparison of displaced and promptly produced jets in simulation. This procedure guarantees an extremely conservative estimate, since the jet displacement is expected to result in similar trends in data as well as in MC.
The transverse momentum response, or p_T response, is defined as the p_T ratio of the leading reconstructed jet to its associated truth jet, the particle jet constructed from the decay products of the LL particles. It was studied in the R-hadron as well as in the Gqq scenario, in order to understand the effects of jet displacement on JES and JER. A representative subset of signal samples, summarised in Table 7.3, was used in this MC based study.

Scenario	Mass of the Gluino	Mass of the Neutralino	Lifetime of the LL particle
Gqq model	1 TeV, 1.6 TeV and 2 TeV	200 GeV	0.01 ns to 50 ns
R-hadron	1 TeV and 2 TeV	100 GeV	0.01 ns to 100 ns

Table 7.3: Summary of the representative signal samples used to study the p_T response of displaced jets in both LL scenarios.

Detector level jets are reconstructed and selected similar to the procedure described in subsection 6.1.2 with the exception of specific tracking requirements, in particular the GSC, which were omitted in this study. Truth jets contain all decay products of the respective LL mother particle as well as particles produced in prompt decays. They are reconstructed from these particles prior to the detector simulation following the same procedure. Signal jets - reconstructed and truth - are required to have $|\eta| < 2.8$ as well as a $p_T \geq 50$ GeV and $p_T \geq 20$ GeV, respectively.
The p_T response is constructed based on geometric matching using the distance parameter ΔR, similar to the procedure described in subsection 6.3.1. The closest truth jet, i.e. the one with the minimal ΔR, is associated to the reconstructed jet, with the truth four-momentum given relative to the DV.
Truth jets considered as possible matches need to be labelled as decay products of the respective

LL particle. Hence, only truth jets, which are matched to a LL mother particle, are selected as input. This tagging procedure follows the geometric matching principle described above. The minimal distance between the candidate truth jet and the LL particle ΔR is required to be below 0.3 in case of the Gqq model and depends on the p_{T} of the LL particle in the R-hadron model, indicated by the red lines in Figure 7.7 and summarised in Table 7.4.

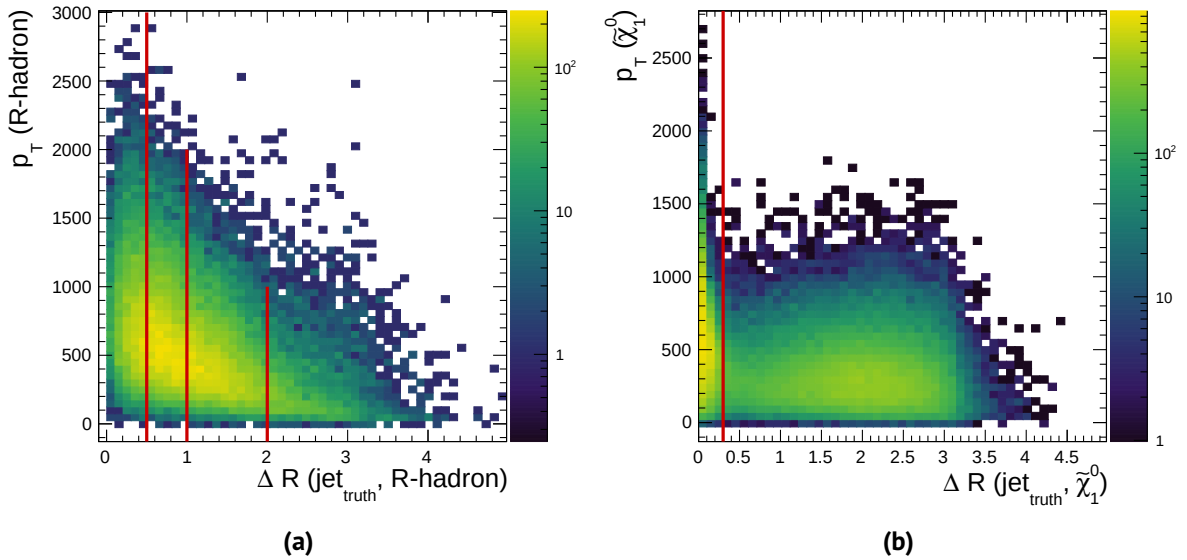

(a) (b)

Figure 7.7: Distance between the respective LL particle and the leading truth jet as a function of the particle p_{T} in the R-hadron model (Figure 7.7a) and the Gqq model (Figure 7.7b). The thresholds for the ΔR requirement are indicated by the red lines.

LL particle	*kinematic selection*	*matching condition*
$\tilde{\chi}_1^0$	–	$\Delta R < 0.3$
R-hadron	$p_{\mathrm{T}} < 1000$ GeV	$\Delta R < 2$
	1000 GeV $< p_{\mathrm{T}} <$ 2000 GeV	$\Delta R < 1$
	2000 GeV $< p_{\mathrm{T}}$	$\Delta R < 0.5$

Table 7.4: Summary of p_{T} selections and upper thresholds of the distance parameter ΔR between the respective LL particle and the truth jet, used in the truth tagging procedure.

The standard reconstruction algorithms, employed in the RPC 0L (2-6jets) search, assume that jets are produced in the PV rather than in their truth origin, the DV, sketched in Figure 7.8. Hence, the ΔR based matching of reconstructed and truth jets is aggravated with increased jet displacement.

In order to compensate these matching inefficiencies and to improve the (θ dependent) p_{T} response, a geometric correction to θ and ϕ of the fully calibrated detector level jet is applied, such that the corrected reconstructed jet points at the DV $(x_{\mathrm{DV}}, y_{\mathrm{DV}}, z_{\mathrm{DV}})$ rather than the PV. These angular

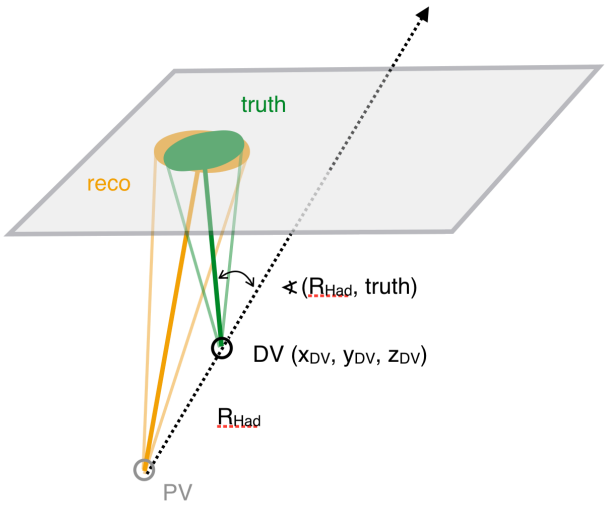

Figure 7.8: Illustration of the correction of the default axis of the reconstructed jet. The truth jet is defined relative to the DV at which the R-hadron decays. The detector level jet is initially reconstructed as being produced from the PV [132].

corrections

$$\theta_{corr} = \arccos\left(\frac{C_R\cos\theta - z_{\mathrm{DV}}}{\sqrt{C_R^2 + x_{\mathrm{DV}}^2 + y_{\mathrm{DV}}^2 + z_{\mathrm{DV}}^2 - 2\,C_R(x_{\mathrm{DV}}\sin\theta\cos\phi + y_{\mathrm{DV}}\sin\theta\sin\phi + z_{\mathrm{DV}}\cos\theta)}}\right) \tag{7.5}$$

and

$$\phi_{corr} = \arctan\left(\frac{C_R\sin\theta\sin\phi - y_{\mathrm{DV}}}{C_R\sin\theta\cos\phi - x_{\mathrm{DV}}}\right) \tag{7.6}$$

are based on the jet's energy-weighted centre-of-gravity, or centroid $C_R = \sqrt{C_x^2 + C_y^2 + C_z^2}$, calculated from its constituent topoclusters [162].

Figure 7.9 shows the positive impact of these corrections on the distance between the leading reconstructed jet, to the closest truth jet, exemplified in the R-hadron scenario.

The leading jet response is studied as a function of the radial (R_{DEC}) and longitudinal (z_{DV}) decay position of the respective LL particle, that is the transverse and longitudinal distance of the DV from the centre of the detector, respectively.

Figure 7.10 (Figure 7.11) compares the response distributions, derived in several bins of R_{DEC} in the LL neutralino (gluino) scenario, using un-isolated jets to construct the jet response (Figure 7.10a and Figure 7.11a) and using isolated jets (Figure 7.10b and Figure 7.11b). Large non-Gaussian tails of the jet response in both LL scenarios are observed, though they are less severe in case of the R-hadron model. Depending on the jet displacement, these tails are removed, if the p_{T} response is constructed from an isolated reconstructed jet, in order to ensure a clean matching. This isolation, which allows only one truth jet to lie within a cone of ΔR = 1.0 and no additional reconstructed jet within ΔR = 0.6, is applied on the leading jet only. Placing such isolation criteria on the sub-leading

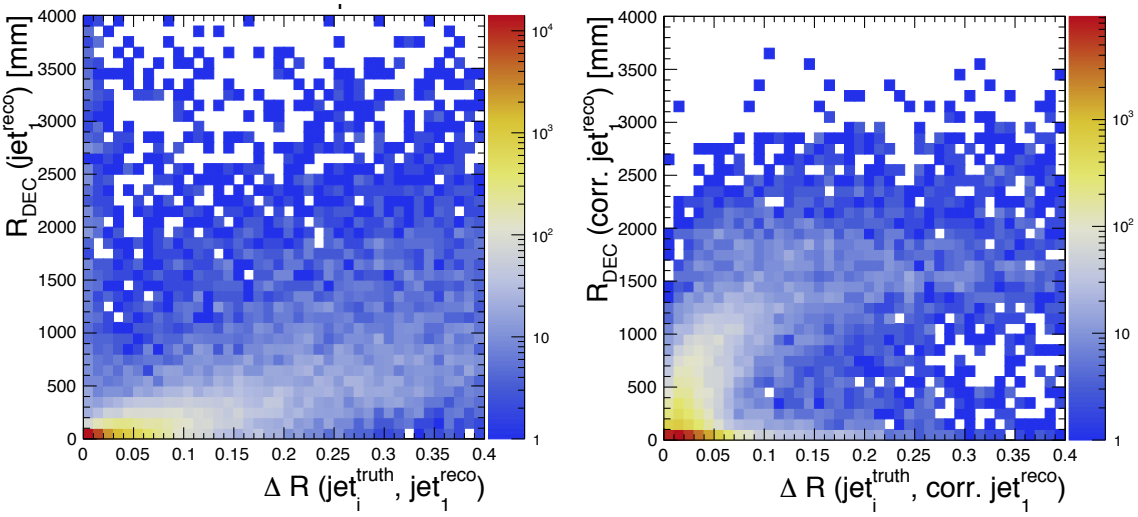

(a) (b)

Figure 7.9: Comparison of the distance between the leading reconstructed jet and the closest truth jet as function of the displaced vertex position of the R-hadron associated to truth jet without (Figure 7.9a) and with (Figure 7.9b) applying the correction on the direction of the reconstructed jet.

jet heavily reduces the number of available signal events, thus was not applied in the construction of the p_T response. For the same reason, the isolation cuts on the leading jet had to be loosened in the variable RPV scenario.

Figure 7.12 shows the p_T response, ranging from 0 to 3, in the LL gluino (Figure 7.12a) and LL neutralino (Figure 7.12b) scenario, fit with a Gaussian and normalised to unity in each bin of R_{DEC}. Similarly, the p_T response in slices of longitudinal decay position is shown in Figure 7.13. The solid red line indicates the unit response, expected in a prompt scenario and the difference to the fitted mean, given by the grey dots, is interpreted as a measure for the additional uncertainties on the JES, while the width of the Gaussian distribution, indicated by the error bars, represents additional uncertainties on the JER.

In case of the R-hadron scenario this deviation of the mean of the jet response from unity is negligible for $R_{DEC} < 1.4$ m (approaching the outermost part of the inner solenoid) and for $|z_{DV}| < 1.5$ m, whereas significant deviations are observed in the Gqq model. For decay radii above 200 mm a linearly increasing upwards shift of the response is found, which jumps up to a maximal value of about 30% around $R_{DEC} = 1$ m, corresponding to the outermost layer of the ID. A possible explanation for this significant shift, which is driven by the large non-Gaussian tails, present in the p_T response distribution (cf. Figure 7.10b), is the large multiplicity of hadronic decay products of the LL $\tilde{\chi}_1^0$. Such a highly populated environment - the Gqq model includes ten jets for moderate lifetimes, while final states in the R-hadron model have a jet multiplicity of four - gives rise to additional nearby jet activity leading to inaccurate matching between reconstructed and truth jets which cannot be cured by applying isolation criteria. Moreover, the reconstruction of jets assuming their origin in the PV introduces the possibility of additional particles being erroneously clustered into these jets.

Additionally, the jet reconstruction efficiency in the R-hadron scenario was studied in order to asses

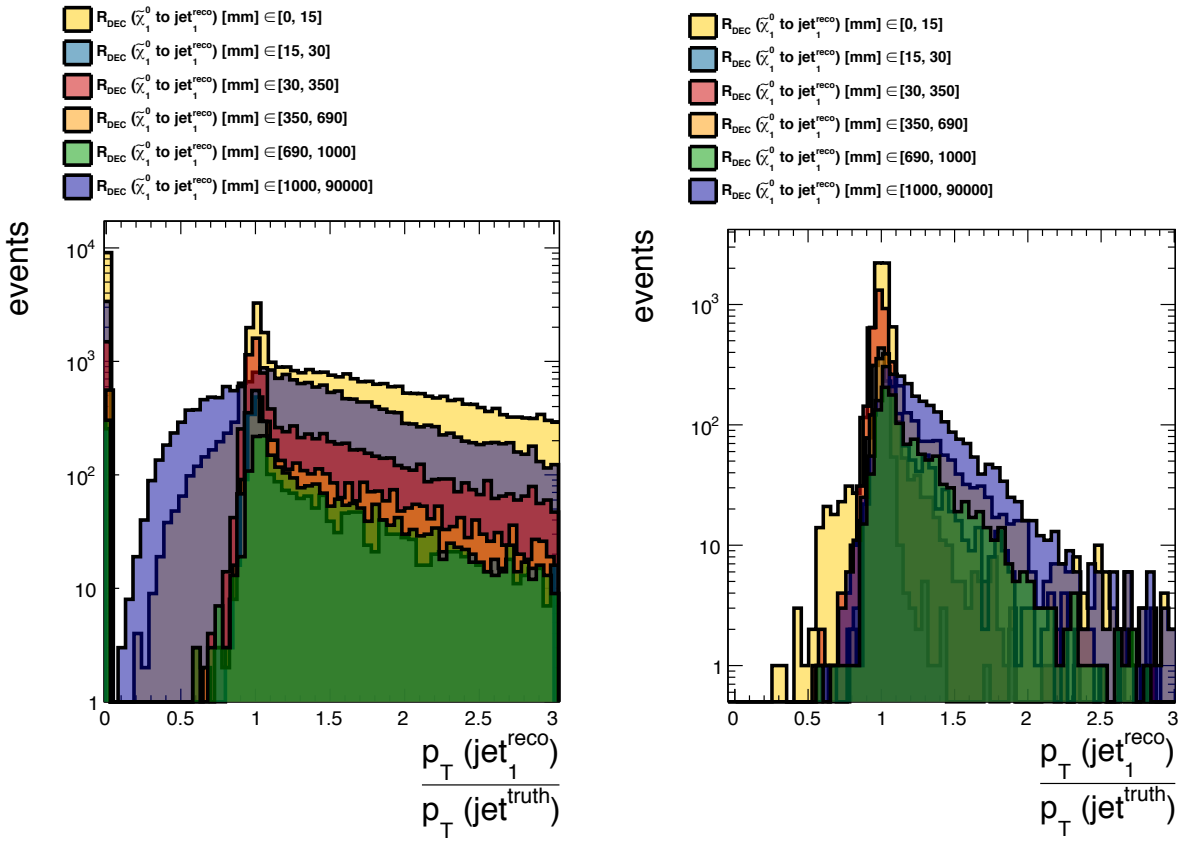

Figure 7.10: Comparison of the jet response function binned with respect to the decay radius of the LL neutralino associated to the matched truth jet without (Figure 7.10a) and with (Figure 7.10b) applied isolation in the matching of reconstructed and truth jets.

the optimal form and magnitude of the supplementary kinematic uncertainties on jets implemented in all searches included in the RPC-meets-RPV analysis. The reconstruction efficiency is defined as the fraction of events in which the leading truth jet was successfully matched to a reconstructed jet within a cone of $\Delta R = 0.3$. Since no isolation criteria are placed on the jets, to avoid limitations due to statistical fluctuations, effects of failed matching caused by the near-by jet activity are included in the reconstruction efficiency, shown in Figure 7.14.

The input signal samples are separated into groups according to the average sparticle lifetime, leading to decays in different regions of the detector (cf. section 3.2). If the radial displacement of the decay is less than 30 mm, the DV lies within the beam pipe. Decays with $R_{\text{DEC}} < 1000$ mm occur entirely within the ID, which has an outer radius of 1082 mm. DVs with $R_{\text{DEC}} > 1500$ mm are located beyond the inner layer of the LAr calorimeter with an inner radius of 1500 mm.

For soft jets ($p_{\text{T}} < 200$ GeV) produced within the ID the reconstruction efficiency is about 70%, increasing rapidly with the jet p_{T}. It reaches a plateau of almost 100% for jets originating from DVs in the beam pipe. For large p_{T} jets ($p_{\text{T}} > 1.5$ TeV) the efficiency drops again to not less than 90% for $R_{\text{DEC}} < 1500$ mm. Jets produced in vertices in the calorimetric system can not be reconstructed efficiently.

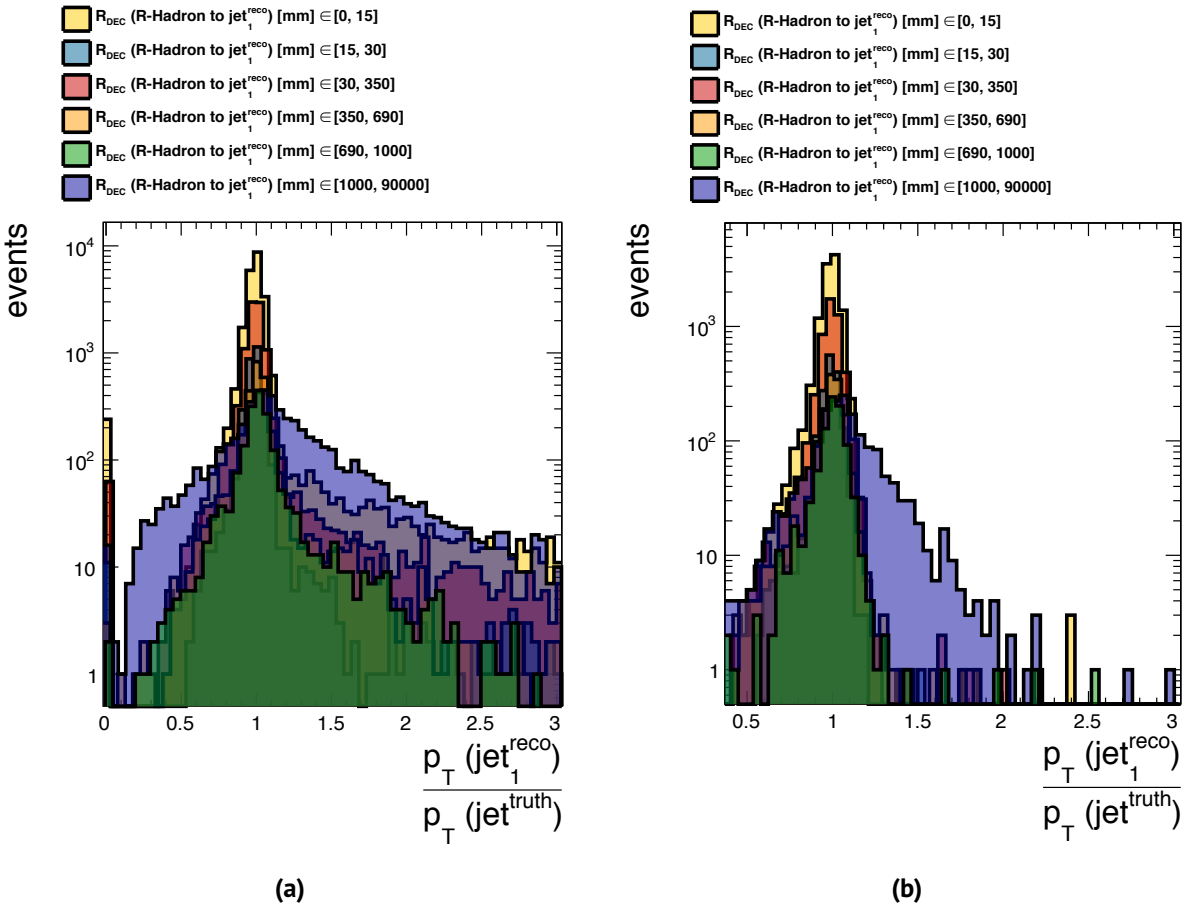

Figure 7.11: Comparison of the jet response function binned with respect to the decay radius of the R-hadron associated to the matched truth jet without (Figure 7.11a) and with (Figure 7.11b) applied isolation in the matching of reconstructed and truth jets.

Following the results from studying the p_T response and the reconstruction efficiency, the deviation of the response from unity is parametrised as a function of the decay position, to describe an additional systematic uncertainty. The form of this systematic, which is applied in the R-hadron and the variable RPV model, is shown in Figure 7.15. It is negligible for LL gluinos and neutralinos produced in DVs with decay radii below 1 m and increases linearly to a maximum of 30% for decays, which occur entirely within the calorimeter ($R_{\text{DEC}} \geq 1.6$ m). For R_{DEC} approaching the outside of the calorimeter the reconstruction efficiency decreases rapidly. Hence, if the decay radius is larger than the radius of the calorimeter, jets are no longer reconstructed and no uncertainties are needed.

Uncertainties of this form, following to a large extent the observations in the R-hadron scenario, are applied in all contributing analyses. Although the uncertainties should, in principle, be evaluated for each jet, depending on its displacement, such an approached was found to be infeasible, due to the difficulties in determining the exact origin of the final state jets. Hence, a more simplified, yet conservative approach was chosen. The average R_{DEC} is calculated from all LL sparticles decaying within the detector volume and the corresponding uncertainty, obtained from the parametrisation indicated in Figure 7.15 is applied to all signal jets present in an event.

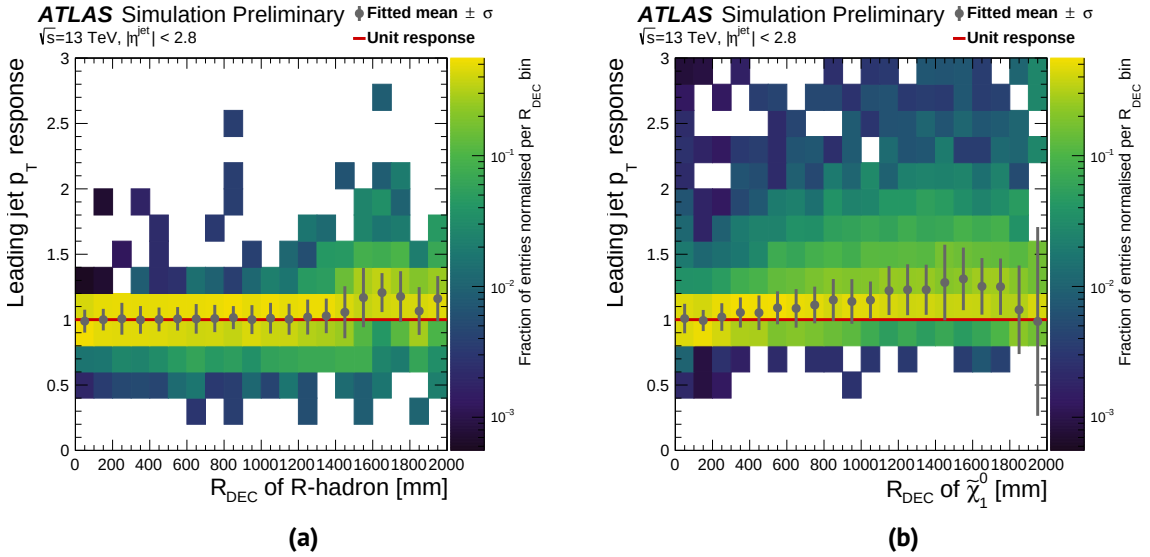

Figure 7.12: Leading jet response as function of the decay radius R_{DEC} of the respective LL particle in the R-hadron scenario (Figure 7.12a) and the Gqq model (Figure 7.12b). A fit with a Gaussian distribution is performed in each normalised R_{DEC} bin. The grey dots indicate the fitted mean and the error bars the width of the fit [132].

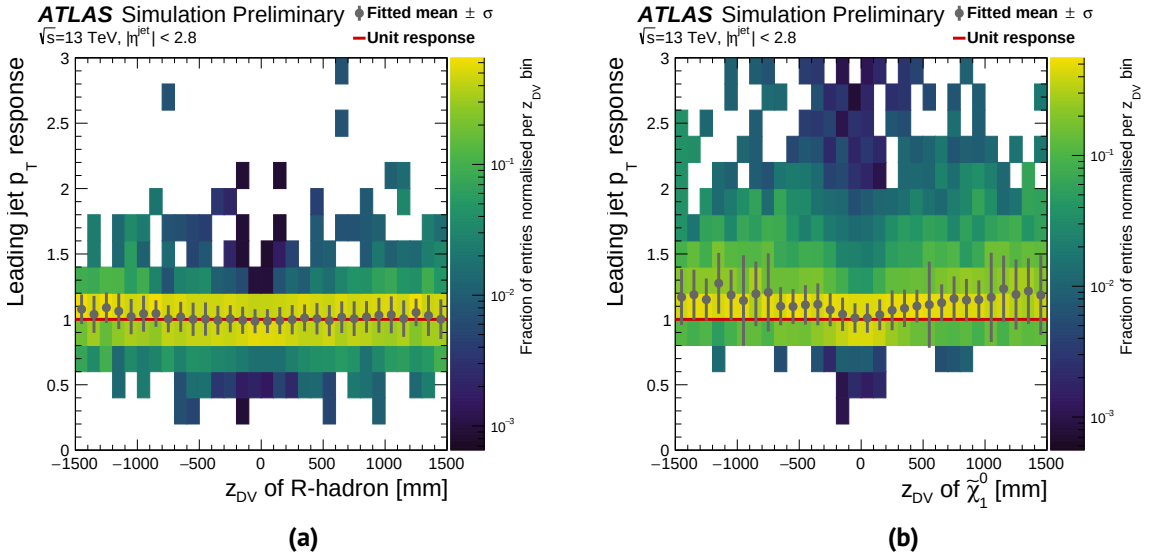

Figure 7.13: Leading jet response as function of the longitudinal decay position z_{DV} of the respective LL particle in the R-hadron scenario (Figure 7.13a) and the Gqq model (Figure 7.13b). A fit with a Gaussian distribution is performed in each normalised z_{DV} bin. The grey dots indicate the fitted mean and the error bars the width of the fit [132].

This choice is maximal conservative, given that the usual procedure to estimate uncertainties on the JES uses the difference between the response in data and MC only (cf. subsection 5.1.2). Nevertheless, these uncertainties have just a minor impact on the sensitivity of the individual searches included in the RPC-meets-RPV analysis.

Additionally, the evolution of the width of the p_{T} response as function of the origin vertex displacement, indicated by the error bars in Figure 7.12 and Figure 7.13, was investigated, in order to cover

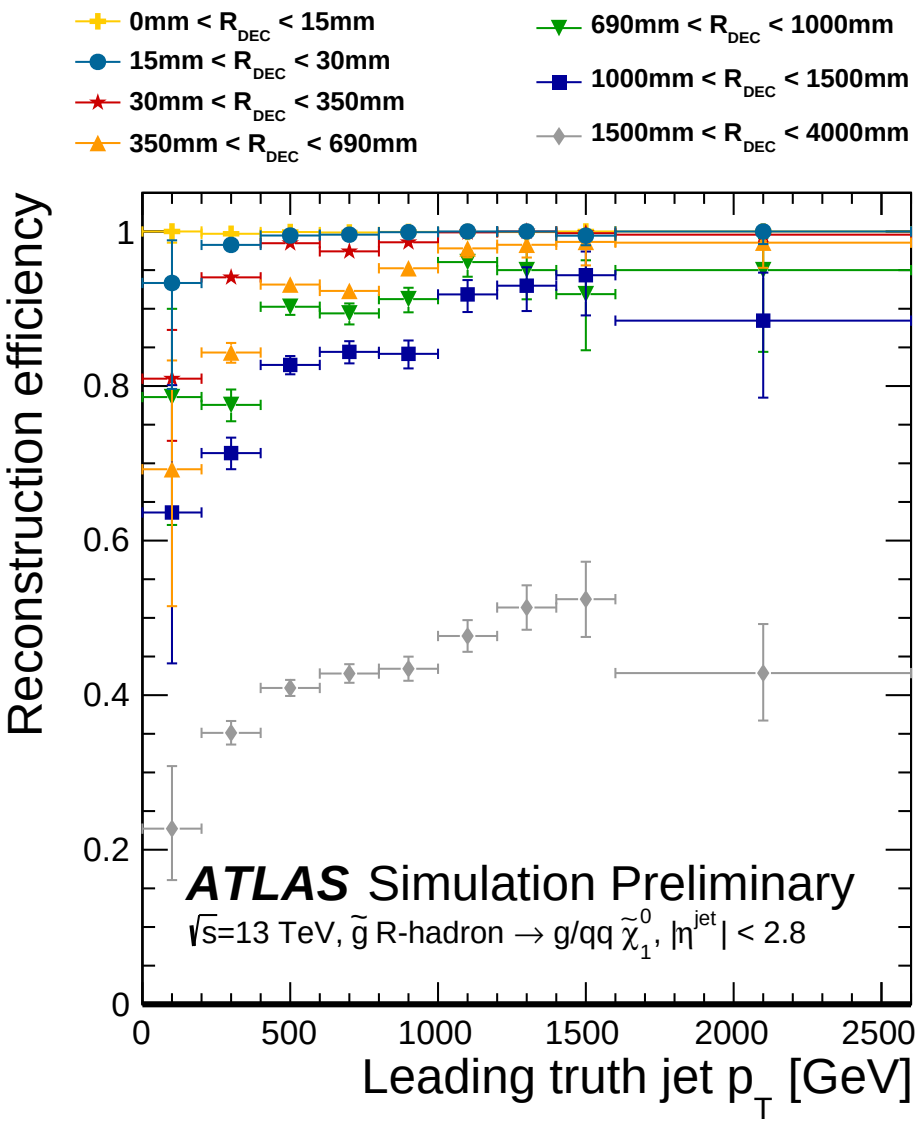

Figure 7.14: Jet reconstruction efficiency as a function of p_T for the leading truth jet in the *R*-hadron scenario for decays in different areas of the ATLAS detector [132].

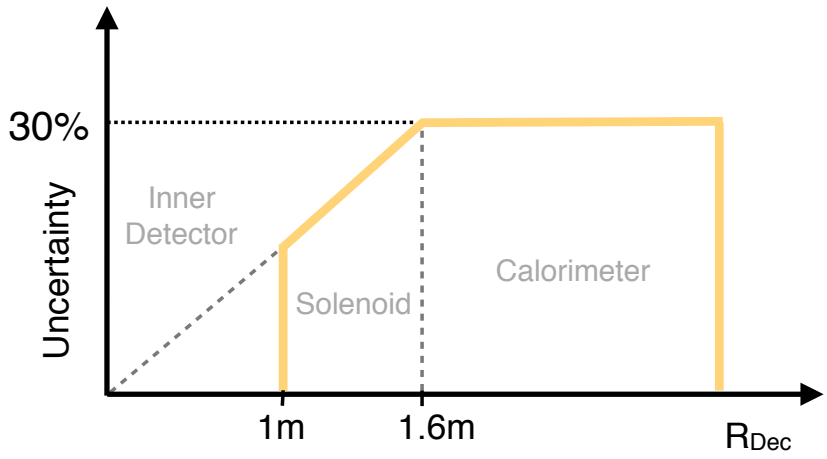

Figure 7.15: Sketch of the schematic course of the systematics representing the additional kinematic uncertainties on the JES as a function of the decay radius in the LL gluino and neutralino scenario.

the impact of the jet displacement on the JER. Even though a slight increase of the width of the response was observed, this effect was not taken into account in the reinterpretations. Neglecting this effect is a reasonable choice, given that the official uncertainties on the JER applied in all early Run 2 searches are based on a very conservative extrapolation from Run 1 studies.

7.3.2 Uncertainties on the E_T^{miss}

As detailed in subsection 5.1.4, the E_T^{miss} is composed of several terms, including in particular the contribution of jets and a soft term built from high-quality tracks associated with the PV. Systematic uncertainties on the hard objects contributing to the calculation of the E_T^{miss} are propagated to the uncertainties on the E_T^{miss} itself, including the additional scale uncertainties arising from the jet displacement, discussed above. Uncertainties on the soft term, on the other hand, are not effected by the displacement of the decay products.

The composition of the E_T^{miss} was studied in the context of the RPC 0L (2-6jets) analysis as a function of the lifetime of the LL gluino in the R-hadron model and compared to a prompt scenario. No sizeable difference in the composition of the E_T^{miss} was found. Hence, no additional uncertainties on the E_T^{miss} are required.

Searches originally designed to target pure RPC scenarios, rely on a E_T^{miss}-trigger to pre-select potential signal events. The performance of this trigger and its dependency on the lifetime of the LL particle was evaluated in MC simulation. No impact of the displacement of the decay vertex on the trigger efficiency turn-on was observed. No additional trigger systematics are applied in the RPC-meets-RPV analysis, since no significant differences in the online and offline E_T^{miss} definitions were found in scenarios with prompt and displaced jets.

7.3.3 Uncertainties on the b-tagging

The b-tagging efficiency is expected to be affected by the additional displacement of the origin vertex due to the finite sparticle lifetime, as is also indicated by the b-jet multiplicity shown in Figure 7.3. It was studied in the LL neutralino scenario in models including the production of b-jets (Gtt model and Stop model).
The b-tagging is most efficient for decay lengths of the order of millimetres, i.e. DVs located inside the beam pipe and the inner most layer of the IBL (cf. subsection 3.2.2). Larger displacement leads to a rapid decrease of the efficiency.
b-jets originating from displaced decays in signal events with an average LL sparticle lifetime of 0.01 ns, are correctly tagged with an efficiency of about 85%, while also 20% of the light-flavoured jets are tagged. A comparison to MC simulated $t\bar{t}$ events, where the efficiency is 77% for b-jets and below 1% for light jets, shows that the contribution from mis-tagging of light jets needs to be taken into account in the RPC-meets-RPV analysis.
The systematics covering this dependency of the b-tagging efficiency on the vertex displacement are assessed following a bottom-up approach. Underlying tracking observables, like the impact-parameter resolution, the track reconstruction efficiency and the fake-rate, are tuned in MC simulation, to reflect the measurements in data. The resulting effect is then propagated onto the observables relevant in the b-tagging procedure, i.e. the b-tagging algorithm is applied to the adjusted MC samples and the efficiency is re-computed. The additional b-tagging uncertainty is then given by the difference between the nominal and the adjusted efficiencies, increasing as a function of the lifetime of the LSP. Given an average neutralino lifetime of 1 ns, this additional systematic is about 10% (20%) in SRs requiring at least 2 (4) b-jets.

7.4 Results and Discussion

The results of the reinterpretations of the nine searches included in the RPC-meets-RPV analysis, are provided separately for the three models with variable RPV coupling strength and the Split-SUSY based model featuring LL gluinos. Individual limits from each analysis are presented, since the SR and CR selections in the searches potentially overlap, such that no statistical combination can be performed.
Results are derived in the form of ULs at *95% CL* on the respective sparticle masses, using the CL_s prescription, explained in subsection 5.4.2 and section 6.5, except the reinterpretation of the RPV dijet and RPV TLA searches, where a Bayesian procedure is applied to set 95% credibility-level upper limits on generic Gaussian resonances [157]. In the following, these results are discussed in detail for each model.

Gqq model Observed and expected limits in the Gqq model are given in Figure 7.16 as a function of the mass of the gluino and the lifetime of the neutralino ($\tau(\tilde{\chi}_1^0)$) and coupling strength λ''_{112}, respectively. Gluino masses up to 2 TeV are excluded for $\tau(\tilde{\chi}_1^0)$ = 100 ns and up to 1 TeV for $\tau(\tilde{\chi}_1^0)$ = 1 ns.

The strongest ULs in this model are provided by the RPC 0L (2-6jets) analysis in the RPC limit, where the gluino decays promptly into multiple jets and a stable LSP and for low values of the RPV coupling strength. This analysis relies on a substantial amount of $E_{\mathrm{T}}^{\mathrm{miss}}$, in order to effectively separate signal and background. Hence, its sensitivity to the Gqq signals drops rapidly with decreased lifetime of the $\widetilde{\chi}_1^0$, due to the increasing probability of the process $\widetilde{\chi}_1^0 \rightarrow qqq$.
The RPC 0L (7-11jets) analysis has also some sensitivity in the Gqq model, though it is designed to target final states with a large jet-multiplicity. Due to a lack of hadronic final state objects for large $\tau(\widetilde{\chi}_1^0)$ in this scenario and due to the decrease of the $E_{\mathrm{T}}^{\mathrm{miss}}$ for larger values of λ''_{112}, the analysis is less efficient than the RPC 0L (2-6jets) and the limits provided are much weaker.

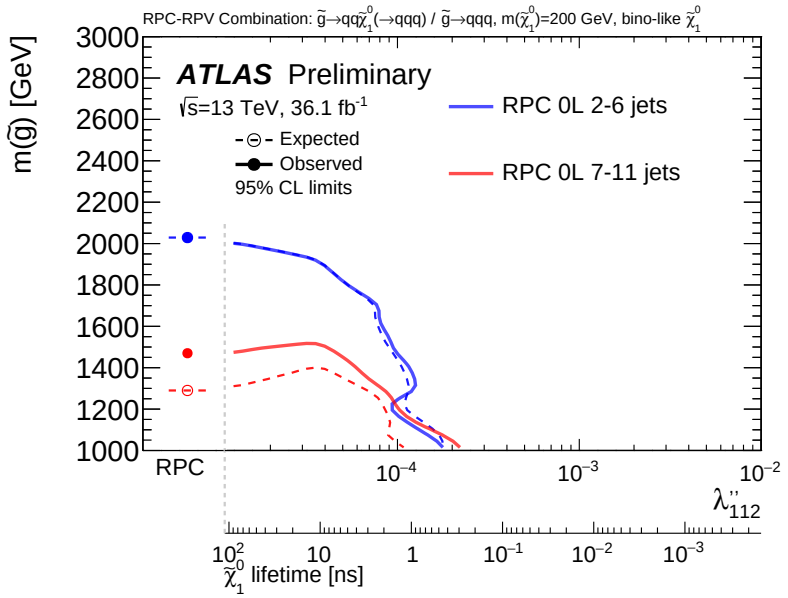

Figure 7.16: Expected (dashed lines) and observed (solid lines) exclusion limits for the Gqq model as a function of λ''_{112} and $m(\widetilde{\mathrm{g}})$. The coupling strength λ''_{112} increases, $\tau(\widetilde{\chi}_1^0)$ decreases from left to right. The dots on the very left represent the ULs provided by the analyses in the RPC limit of the Gqq model.

The results can also be interpreted as limits on the coupling strength λ''_{112}, excluding values up to 10^{-4}. However, it is possible to place stronger limits on λ''_{112} from different experimental methods. In particular,

$$\lambda''_{112} \lesssim 5 \cdot 10^{-7} \left(\frac{m(\tilde{q}_R)}{1\ \mathrm{TeV}}\right)^2 \left(\frac{m(\tilde{g})}{1\ \mathrm{TeV}}\right)^{1/2} \tag{7.7}$$

was found by means of low-energy di-nucleon decay measurements [163, 164], which can be translated into a limit on the gluino mass of about 5 TeV for $m(\widetilde{\chi}_1^0)$ = 200 GeV. However, the RPC 0L (2-6jets) does not place any requirements on b-tagged jets. Hence, even though λ''_{112} was used to generate the signal samples in the Gqq model, the limits on the coupling strength obtained in the RPC-meets-RPV analysis can also be interpreted for different choices of ijk, provided that $i \neq 3$.
Models with $\lambda''_{112} \gtrsim 10^{-4}$ could not be excluded in the RPC-meets-RPV analysis. However, previous ATLAS searches specifically designed to target 0L channels in pure RPV scenarios provide limits on $m(\widetilde{\mathrm{g}})$ of 1.2 TeV assuming a gluino decay of the form $\widetilde{\mathrm{g}} \rightarrow qq\widetilde{\chi}_1^0(\rightarrow qqq)$ with a promptly decaying LSP [165] and of 0.9 TeV considering a prompt and direct gluino decay to multiple light-flavoured

jets ($\widetilde{g} \to qqq$) [166].

Gtt model Figure 7.17 shows the expected and observed exclusion contours in the Gtt model given as a function of the gluino mass and $\tau(\widetilde{\chi}_1^0)$, the gluino branching ratio and λ''_{323}, respectively. The entire range of coupling strength λ''_{323} is effectively covered, with the largest $m(\widetilde{g})$ exclusion in the RPC limit and for a coupling strength of about $3{\cdot}10^{-2}$.
In the RPC and low coupling regime the RPC multi-b search provides the strongest limits on $m(\widetilde{g})$. This analysis looses sensitivity in the Gtt scenario with increased coupling strength, leading to a decrease in E_T^{miss}, due to the decreasing lifetime of the LSP. However, unlike the dedicated RPC analyses used in the Gqq model, the RPC multi-b has some efficiency up to large values of λ'', thanks to the E_T^{miss}, created in leptonic decays of the multiple tops in the final states. This large top multiplicity is reduced with increasing branching ratio of $\widetilde{g} \to tbs$ changing the preferred gluino decay from a cascade via an intermediate LL neutralino, $\widetilde{g} \to tt\widetilde{\chi}_1^0(\to tbs)$, to a direct decay.
With increased λ''_{323} the RPV 1L search takes over and provides the strongest ULs on $m(\widetilde{g})$ for intermediate and large values of the coupling strength. In this regime the analysis is highly efficient, since it was optimised to target processes with a large final state multiplicity from gluino cascade decays. Hence, it is most sensitive where the branching ratio for $\widetilde{g} \to tt\widetilde{\chi}_1^0(\to tbs)$ is maximal. The enhanced b-tagging efficiency in this region further improves the limits, excluding gluino masses of almost 2.2 TeV for $\tau(\widetilde{\chi}_1^0) = 10^{-2}$ ns. For small values of λ''_{323} the ULs are weakened by the reduction in multiplicity, due to displaced decays allowing final state objects to escape detection.
The weakest limits in this scenario occur for $\lambda''_{323} \approx 3{\cdot}10^{-3}$ corresponding to a moderate neutralino lifetime, giving rise to displaced signatures, which are not targeted by the analyses reinterpreted in the Gtt model and for $\lambda''_{323} = 1$, where the strongly reduced jet multiplicity in the final states hampers the separation of signal and background.

Stop model Unlike in the Gqq and Gtt model, the correlation between the RPV coupling strength and the neutralino lifetime and stop decay branching ratio, respectively, depends on the mass of the $\widetilde{t}_1$. Hence, exclusion limits in this model are given in the $m(\widetilde{t}_1)$-λ''_{323} plane and contours indicating $\tau(\widetilde{\chi}_1^0)$ and the branching ratio are overlaid in Figure 7.18.
The weakest limits in this scenario occur in the transition regions between the areas covered by the individual analyses, while the strongest limits on the mass of the stop reach as high as 2.4 TeV in the regime of maximal RPV, provided by the RPV dijet analysis.
In the RPC limit and for low values of λ''_{323}, the RPC stop 0L and RPC stop 1L searches are most efficient and provide the strongest ULs. Their sensitivity drops quickly with a growing coupling strength, since both analyses rely on a E_T^{miss} requirement in the SR definitions.
The RPV 1L has the largest sensitivity in case of moderate values of the coupling strength and excludes stop masses of about 1.1 TeV for $\lambda''_{323} \approx 10^{-2}$.
For large values of the RPV coupling strength ($\lambda''_{323} \to 1$), weak limits on $m(\widetilde{t})$ are set by the RPV stop dijet pairs search, while the RPV dijet and TLA, which gain access to the single stop resonant production in this region, provide extremely strong limits, due to the large cross-section of this particular process.

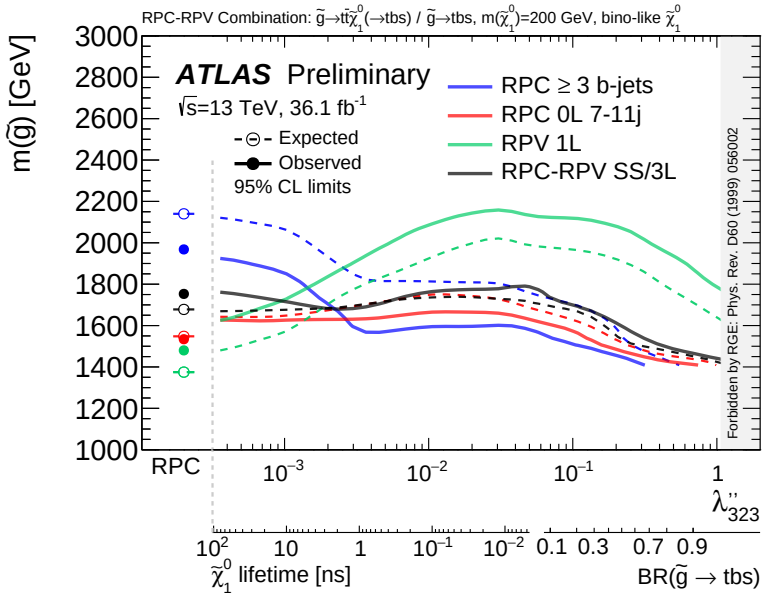

Figure 7.17: Expected (dashed lines) and observed (solid lines) exclusion limits for the Gtt model as a function of λ''_{323} and $m(\tilde{g})$. The coupling strength λ''_{323} and the branching ratio for the direct RPV gluino decay increases, $\tau(\tilde{\chi}^0_1)$ decreases from left to right. The dots on the very left represent the ULs provided by the analyses in the RPC limit of the Gtt model and the rightmost area ($\lambda''_{323} > 1.07$) is forbidden by theoretical constraints on the coupling strength.

The gap visible in Figure 7.18 between the regions covered by dedicated RPC and RPV analyses could potentially be closed by new searches, which specifically target signatures featuring DVs or displaced leptons.

R-hadron model Figure 7.19 shows the observed and expected exclusion limits on the mass of the gluino obtained from the reinterpretation of the RPC 0L (2-6jets) analysis in the R-hadron model. ULs are given as a function of the gluino lifetime and respective decay length, increasing from left to right. Additionally, results from a dedicated ATLAS search for DV plus $E_{\mathrm{T}}^{\mathrm{miss}}$ signatures [160], a search based on large ionisation loss dE/dx in the pixel detector [167] and analyses targeting stopped gluinos, decaying out of time [168] and stable charged R-hadrons [169] are shown in this ATLAS summary plot.
The RPC 0L (2-6jets) search places the strongest limits on $m(\tilde{g})$ for promptly decaying gluinos and very low gluino lifetimes and provides strong limits for even larger lifetimes until the displacement of the decays moves the origin of the jet production into the calorimeter. The sensitivity of the inclusive 0L search in this scenario is not affected by the nature of the gluino hadronisation, i.e. the R-hadron spectrum (cf. subsection 2.2.2), unlike it is the case for searches targeting direct R-hadron interactions.
Gluinos in the R-hadron model are excluded up to 1.6 TeV over the full range of R-hadron lifetime.

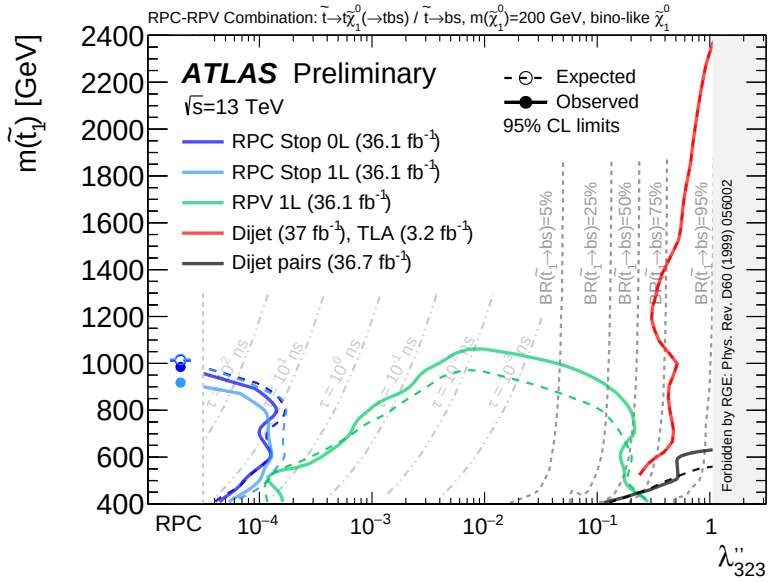

Figure 7.18: Expected (dashed lines) and observed (solid lines) exclusion limits for the Stop model as a function of λ''_{323} and $m(\tilde{t}_1)$. The coupling strength λ''_{323} increases from left to right and the grey contours indicate the $\tau(\tilde{\chi}^0_1)$ and stop decay branching ratio, respectively. The dots on the very left represent the ULs provided by the analysis in the RPC limit of the Stop model and the rightmost area ($\lambda''_{323} > 1.07$) is forbidden by theoretical constraints on the coupling strength. Only observed limits are shown in case of the RPV dijet and TLA searches.

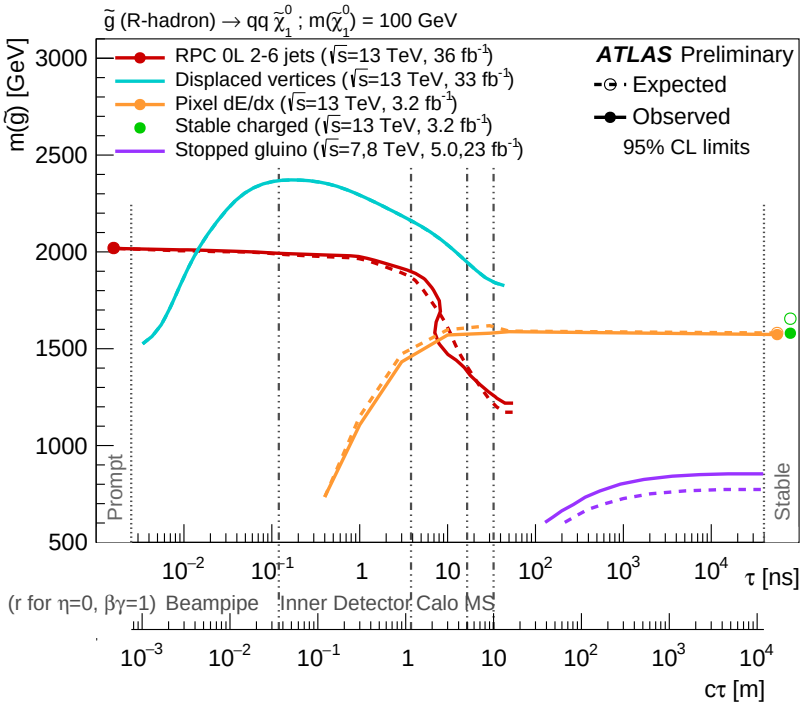

Figure 7.19: ATLAS summary plot for searches for meta-stable gluinos showing expected (dashed lines) and observed (solid lines) exclusion limits in the *R*-hadron model as a function of gluino lifetime and mass. The lifetime and respective decay length increases from left to right. The dots represent the ULs for models assuming prompt decays or stable particles, i.e. particles which escape the detector.

8 Conclusion

This thesis presents two searches for supersymmetric particles, based on different SUSY models assuming vanishing or variable R-parity violating couplings and promptly decaying or metastable gluinos.

The 0L (2-6jets) SUSY analysis targets promptly decaying squarks and gluinos predicted in the RPC MSSM assuming a stable neutralino LSP, selecting events with multiple jets, missing transverse momentum ($E_{\mathrm{T}}^{\mathrm{miss}}$) and no leptons. The full Run 2 pp collision dataset recorded with the ATLAS detector at $\sqrt{s}$ = 13 TeV, corresponding to a total integrated luminosity of L=139 fb^{-1}, was analysed employing three different search strategies. The multi-bin (MB) approach includes three different signal region (SR) selections, optimised to be sensitive to pair-produced, directly decaying squarks and gluinos as well as in compressed scenarios. Each of these search channels contains several orthogonal exclusive selections, which are combined in the final fit. The other two analysis approaches - the boosted decision tree (BDT) search and the model independent search - are based on a *cut and count* strategy using a single-bin fit to obtain the final results. SR definitions in the BDT analysis include the optimised BDT score cut, targeting gluino direct and cascade decays.

Even though the contribution of hadronic events with fake $E_{\mathrm{T}}^{\mathrm{miss}}$ is effectively reduced by the substantial amount of $E_{\mathrm{T}}^{\mathrm{miss}}$ and the alignment of $E_{\mathrm{T}}^{\mathrm{miss}}$ and jets required in the analysis, a reliable prediction of this multijet background contribution is needed. Despite being just a minor background, its estimation is among the most challenging ones. Unlike other SM background processes it cannot be modelled sufficiently using MC predictions. Hence, a data-driven technique, the *JetSmearing* method, is implemented in the inclusive 0L search. The multijet prediction obtained by this technique is evaluated in dedicated validation regions and is found to provide a satisfactory description of data.

No significant excess above the SM background in any of the search channels is found in data. Exclusion limits are derived in terms of simplified models describing light-flavoured squark and gluino production with subsequent direct or one-step decays. Gluino masses are excluded at *95% CL* up to 2.35 TeV assuming a direct decay into a massless neutralino. In a simplified model describing mass-degenerate first and second generation squarks subsequently decaying into massless LSPs, squark masses are excluded below 1.94 TeV. Additionally, limits are provided in models with pair-produced squarks and gluinos, which decay via an intermediate chargino into one or two light quarks, a W boson and the LSP, excluding squark masses up to 1.3 TeV and gluino masses below 2.19 TeV, in case of massless neutralinos. A lower limit of 3 TeV for equal squark and gluino masses is set in a less simplified model, including the production of squark-squark, squark-anti-squark, gluino-gluino and squark-gluino, with subsequent decays into massless LSPs. Thanks to the two new sophisticated analysis approaches - the MB and the BDT search - these results significantly surpass the exclusion limits set by previous analyses.

The introduction of non-zero RPV couplings into the superpotential of the MSSM renders the LSP a metastable particle, thus allowing to investigate the phase-space between regions probed by ATLAS SUSY searches designed for pure RPC or pure RPV models. In RPC Split-SUSY scenarios gluino decays are suppressed due to large squark masses resulting in non-negligible gluino lifetimes and

the formation of displaced decaying R-hadrons.
A reinterpretation of several early Run 2 ATLAS searches, based on pp collision data at $\sqrt{s}$ = 13 TeV recorded in 2015 and 2016, in scenarios with a long-lived (LL) neutralino LSP is presented. The RPC-meets-RPV analysis additionally covers the reinterpretation of the inclusive 0L search in a scenario featuring metastable gluinos. The assessment of the impact of the jet displacement on the Jet Energy Scale (JES) and the Jet Energy Resolution (JER) is one of the main challenges and requires detailed studies of the transverse momentum response and the reconstruction efficiency. The results of these studies are used to estimate additional uncertainties on the JES implemented in all searches incorporated in the RPC-meets-RPV analysis and were made public independently.
Individual limits are reported from each contributing analysis in simplified models describing three scenarios with variable RPV couplings. The exclusion limits are presented as function of the initial sparticle mass and the value of the respective coupling strength λ'' and the corresponding neutralino lifetime, respectively. The variation of λ'' leads to a multitude of possible final states in each scenario, thus a large variation in sensitivity is observed as a function of coupling strength. Gluino masses are excluded up to 1.8 TeV over the full range of λ'' in a simplified model spectrum describing pair-produced gluinos with large branching fractions to top quarks. In a scenario with gluinos decaying into first and second generation quarks, limits on the gluino mass are set at 2.0 TeV in the region where a large neutralino lifetime results in final states with substantial $E_{\mathrm{T}}^{\mathrm{miss}}$. For large coupling values no limits are obtained in this scenario. Large variations of coverage are also observed in a scenario of pair-produced or resonantly produced stops, where stop masses are excluded up to 2.4 TeV at large coupling strength. No limits can be established in a region corresponding to a neutralino lifetime of about 1 ns, equivalent to $\lambda'' \approx 10^{-4}$.
The reinterpretation of the L=36.1 fb^{-1} 0L (2-6jets) SUSY analysis in the R-hadron scenario provides limits on the mass of the LL gluino about 2 TeV for gluino lifetimes below around 3 ns, exceeding the results of other ATLAS R-hadron searches, which are less sensitive in this region. The sensitivity of the inclusive 0L search drops rapidly, once the large displacement of the R-hadron decay leads to jets produced in the calorimeter.
In the light of these results, the planning phase of an updated iteration of the RPC-meets-RPV reinterpretation effort using the full Run 2 data-set has already begun. Major improvements in the coverage of the investigated phase-space are expected from the incorporation of searches specifically targeting LL SUSY particles and exotic scenarios including for instance resonant single production of new particles. Additionally, the expansion of the probed phase-space by including new benchmark scenarios, e.g. production of eweakinos or leptoquarks (colour-triplet bosons carrying lepton and baryon number), are discussed.

Despite the absence of experimental evidence for BSM signals, the remarkable results of the 0L (2-6jets) SUSY analysis and the RPC-meets-RPV analysis represent an important contribution to the hunt for SUSY at the LHC, significantly extending the parameter-space tested for the existence of supersymmetric particles.
The search for new physics, in particular in more challenging regions of the supersymmetric phase-space, will be continued not only within the ATLAS collaboration but also in other collaborations at CERN and elsewhere, pushing forward the frontier of our knowledge.

Bibliography

[1] G. A. *et al.*, *Observation of a new particle in the search for the Standard Model Higgs boson with the ATLAS detector at the LHC*, Physics Letters B **716** (2012) 1 – 29.

[2] S. C. *et al.*, *Observation of a new boson at a mass of 125 GeV with the CMS experiment at the LHC*, Physics Letters B **716** (2012) 30 – 61.

[3] M. A. Levinson and D. E. Kaplan, *Particle Fever*, http://particlefever.com/. Accessed 30th November 2019.

[4] D. H. Perkins, *Introduction to High Energy Physics*. Cambridge University Press, 4 ed., 2000.

[5] M. L. Mangano, *Introduction to QCD*, https://cds.cern.ch/record/454171.

[6] E. Fermi, *Tentativo di una Teoria Dei Raggi β*, Il Nuovo Cimento (1924-1942) **11** (2008) 1.

[7] S. L. Glashow, *Partial-symmetries of weak interactions*, Nuclear Physics **22** (1961) 579 – 588.

[8] A. Salam, *Weak and Electromagnetic Interactions*, Originally printed in *Svartholm: Elementary Particle Theory, Proceedings Of The Nobel Symposium Held 1968 At Lerum, Sweden*, Stockholm 1968, 367-377.

[9] S. Weinberg, *A Model of Leptons*, Phys. Rev. Lett. **19** (1967) 1264–1266.

[10] N. Cabibbo, *Unitary Symmetry and Leptonic Decays*, Phys. Rev. Lett. **10** (1963) 531–532.

[11] F. Englert and R. Brout, *Broken Symmetry and the Mass of Gauge Vector Mesons*, Phys. Rev. Lett. **13** (1964) 321–323.

[12] P. W. Higgs, *Broken Symmetries and the Masses of Gauge Bosons*, Phys. Rev. Lett. **13** (1964) 508–509.

[13] J. Lykken and M. Spiropulu, *The future of the Higgs boson*, Physics Today **66** (2013) 28.

[14] ATLAS and CMS Collaborations, *Combined Measurement of the Higgs Boson Mass in pp Collisions at $\sqrt{s} = 7$ and 8 TeV with the ATLAS and CMS Experiments*, Phys. Rev. Lett. **114** (2015) 191803, arXiv:1503.07589 [hep-ex].

[15] ATLAS Collaboration, *Measurement of the Higgs boson mass in the $H \to ZZ^* \to 4\ell$ and $H \to \gamma\gamma$ channels with $\sqrt{s} = 13$ TeV pp collisions using the ATLAS detector*, Phys. Lett. **B784** (2018) 345–366, arXiv:1806.00242 [hep-ex].

[16] S.-K. Collaboration, *Evidence for Oscillation of Atmospheric Neutrinos*, Phys. Rev. Lett. **81** (1998) 1562–1567, https://link.aps.org/doi/10.1103/PhysRevLett.81.1562.

[17] Z. Maki, M. Nakagawa, and S. Sakata, *Remarks on the Unified Model of Elementary Particles*, Progress of Theoretical Physics **28** (1962) 870–880.

[18] F. Zwicky, *On the Masses of Nebulae and of Clusters of Nebulae*, Astrophysical Journal (1937) .

[19] V. C. Rubin and J. Ford, W. Kent, *Rotation of the Andromeda Nebula from a Spectroscopic Survey of Emission Regions*, Astrophysical Journal **159** (1970) 379.

[20] NASA, *Detailed Dark Matter Map Yields Clues to Galaxy Cluster Growth.*, https://www.nasa.gov/mission_pages/hubble/science/dark-matter-map.html. Accessed 13th December 2019.

[21] J. R. Brownstein and J. W. Moffat, *The Bullet Cluster 1E0657-558 evidence shows Modified Gravity in the absence of Dark Matter*, Mon. Not. Roy. Astron. Soc. **382** (2007) 29–47, arXiv:astro-ph/0702146 [astro-ph].

[22] H. Miyazawa, *Baryon Number Changing Currents*, Prog. Theor. Phys. **36 (6)** (1966) 1266.

[23] P. Ramond, *Dual Theory for Free Fermions*, Phys. Rev. D **3** (1971) 2415.

[24] Y. A. Golfand and E. P. Likhtman, *Extension of the Algebra of Poincare Group Generators and Violation of p Invariance*, JETP Lett. **13** (1971) 452, Pisma Zh. Eksp. Teor. Fiz.

[25] A. Neveu and J. H. Schwarz, *Factorizable dual model of pions*, Nucl. Phys. B **31** (1971) 86.

[26] A. Neveu and J. H. Schwarz, *Quark Model of Dual Pions*, Phys. Rev. D **4** (1971) 1109.

[27] J. Gervais and B. Sakita, *Field theory interpretation of supergauges in dual models*, Nucl. Phys. B **34** (1971) 632.

[28] D. V. Volkov and V. P. Akulov, *Is the Neutrino a Goldstone Particle?*, Phys. Lett. B **46** (1973) 109.

[29] J. Wess and B. Zumino, *A Lagrangian Model Invariant Under Supergauge Transformations*, Phys. Lett. B **49** (1974) 52.

[30] J. Wess and B. Zumino, *Supergauge Transformations in Four-Dimensions*, Nucl. Phys. B **70** (1974) 39.

[31] S. P. Martin, *A Supersymmetry primer*, Adv.Ser.Direct.High Energy Phys. **21** (2010) 1–153, arXiv:hep-ph/9709356 [hep-ph].

[32] S James Gates, Jr, *Sticking with SUSY.*, http://live.iop-pp01.agh.sleek.net/2014/09/25/sticking-with-susy/. Accessed 3rd December 2019.

[33] P. Fayet, *Supersymmetry and Weak, Electromagnetic and Strong Interactions*, Phys. Lett. B **64** (1976) 159.

[34] V. Magerl, *Constraining low fine tuned supersymmetric models with simplified models spectra results based on CMS and ATLAS searches*, http://katalog.ub.tuwien.ac.at/AC12404710, August, 2015.

[35] H. K. Dreiner, *An Introduction to explicit R-parity violation*, Adv. Ser. Direct. High Energy Phys. **21** (1997) 565, arXiv:hep-ph/9707435 [hep-ph].

[36] R. Barbier et al., *R-parity violating supersymmetry*, Phys. Rept. **420** (2005) 1–202, arXiv:hep-ph/0406039 [hep-ph].

[37] G. D'Ambrosio, G. F. Giudice, G. Isidori, and A. Strumia, *Minimal flavor violation: An Effective field theory approach*, Nucl. Phys. **B645** (2002) 155–187, arXiv:hep-ph/0207036 [hep-ph].

[38] C. Csaki, Y. Grossman, and B. Heidenreich, *MFV SUSY: A Natural Theory for R-Parity Violation*, Phys. Rev. D **85** (2012) 095009, arXiv:1111.1239 [hep-ph].

[39] G. F. Giudice and A. Romanino, *Split supersymmetry*, Nucl. Phys. **B699** (2004) 65–89, arXiv:hep-ph/0406088 [hep-ph], Erratum: Nucl. Phys.B706,487(2005).

[40] ATLAS Collaboration, ATLAS, *Generation and Simulation of R-Hadrons in the ATLAS Experiment*, Tech. Rep. ATL-PHYS-PUB-2019-019, CERN, Geneva, May, 2019. http://cds.cern.ch/record/2676309.

[41] LHC SUSY Cross Section Working Group, *Cross-section plots*, https://twiki.cern.ch/twiki/bin/view/LHCPhysics/SUSYCrossSections. Accessed 6th December 2019.

[42] ATLAS Collaboration, H. Okawa, *Interpretations of SUSY Searches in ATLAS with Simplified Models*, in *Particles and fields. Proceedings, Meeting of the Division of the American Physical Society, DPF 2011, Providence, USA, August 9-13, 2011*. 2011. arXiv:1110.0282 [hep-ex].

[43] O. S. Brüning, P. Collier, P. Lebrun, S. Myers, R. Ostojic, J. Poole, and P. Proudlock, *LHC Design Report*. CERN Yellow Reports: Monographs. CERN, Geneva, 2004. https://cds.cern.ch/record/782076.

[44] *LEP design report*. CERN, Geneva, 1984. https://cds.cern.ch/record/102083. Copies shelved as reports in LEP, PS and SPS libraries.

[45] ALICE Collaboration, *The ALICE experiment at the CERN LHC*, JINST **3** (2008) S08002.

[46] ATLAS Collaboration, *The ATLAS Experiment at the CERN Large Hadron Collider*, JINST **3** (2008) S08003.

[47] CMS Collaboration, *The CMS experiment at the CERN LHC*, JINST **3** (2008) S08004.

[48] LHCb Collaboration, *The LHCb Detector at the LHC*, JINST **3** (2008) S08005.

[49] E. Mobs, *The CERN accelerator complex - August 2018. Complexe des accélérateurs du CERN - Août 2018*, https://cds.cern.ch/record/2636343, General Photo.

[50] ATLAS Collaboration, *ATLAS inner detector: Technical Design Report, 1*. CERN, Geneva, 1997. https://cds.cern.ch/record/331063.

[51] ATLAS Collaboration, S. Haywood, L. Rossi, R. Nickerson, and A. Romaniouk, *ATLAS inner detector: Technical Design Report, 2.* CERN, Geneva, 1997. https://cds.cern.ch/record/331064.

[52] ATLAS Collaboration, *ATLAS liquid-argon calorimeter: Technical Design Report.* CERN, Geneva, 1996. http://cds.cern.ch/record/331061.

[53] ATLAS Collaboration, *ATLAS tile calorimeter: Technical Design Report.* CERN, Geneva, 1996. https://cds.cern.ch/record/331062.

[54] ATLAS Collaboration, *ATLAS muon spectrometer: Technical Design Report.* CERN, Geneva, 1997. https://cds.cern.ch/record/331068.

[55] F. Kuger, *Signal Formation Processes in Micromegas Detectors and Quality Control for large size Detector Construction for the ATLAS New Small Wheel.* PhD thesis, Wurzburg U., 2017. arXiv:1708.01624 [physics.ins-det]. https://opus.bibliothek.uni-wuerzburg.de/frontdoor/index/index/searchtype/simple/query/%2A%3A%2A/browsing/true/doctypefq/doctoralthesis/start/7/rows/100/institutefq/Physikalisches+Institut/yearfq/2017/docId/15249.

[56] ATLAS Collaboration, K. Potamianos, *The upgraded Pixel detector and the commissioning of the Inner Detector tracking of the ATLAS experiment for Run-2 at the Large Hadron Collider*, Tech. Rep. ATL-PHYS-PROC-2016-104, CERN, Geneva, Aug, 2016. http://cds.cern.ch/record/2209070. EPS-HEP 2015 Proceedings.

[57] A Ruiz Martínez and ATLAS Collaboration, *The Run-2 ATLAS Trigger System*, Journal of Physics: Conference Series **762** (2016) 012003, http://stacks.iop.org/1742-6596/762/i=1/a=012003.

[58] ATLAS Collaboration, *Luminosity Public Results for Run-1*, https://twiki.cern.ch/twiki/bin/view/AtlasPublic/LuminosityPublicResults#Integrated_luminosity_summary_pl, 2013. Accessed 15th December 2019.

[59] ATLAS Collaboration, *Luminosity Public Results for Run-2*, https://twiki.cern.ch/twiki/bin/view/AtlasPublic/LuminosityPublicResultsRun2#Multiple_Year_Collision_Plots, 2018. Accessed 15th December 2019.

[60] V. N. Gribov and L. N. Lipatov, *Deep inelastic ep scattering in perturbation theory*, Sov. J. Nucl. Phys. **15** (1972) 438, Yad. Fiz.15,781(1972).

[61] Y. L. Dokshitzer, *Calculation of the Structure Functions for Deep Inelastic Scattering and e^+ e^- Annihilation by Perturbation Theory in Quantum Chromodynamics.*, Sov. Phys. JETP **46** (1977) 641–653, Zh. Eksp. Teor. Fiz.73,1216(1977).

[62] G. Altarelli and G. Parisi, *Asymptotic Freedom in Parton Language*, Nucl. Phys. **B126** (1977) 298–318.

[63] S. Dulat, T.-J. Hou, J. Gao, M. Guzzi, J. Huston, P. Nadolsky, J. Pumplin, C. Schmidt, D. Stump, and C.-P. Yuan, *New parton distribution functions from a global analysis of quantum chromodynamics*, Phys. Rev. D **93** (2016) 033006, https://link.aps.org/doi/10.1103/PhysRevD.93.033006.

[64] S. Höche, *Introduction to parton-shower event generators*, 2015. arXiv:1411.4085 [hep-ph].

[65] ATLAS Collaboration, *Pileup Interactions and Data Taking Efficiency Public Results for Run-2*, https://twiki.cern.ch/twiki/bin/view/AtlasPublic/LuminosityPublicResultsRun2#Pileup_Interactions_and_Data_Tak. Accessed 15th December 2019.

[66] D. Amati and G. Veneziano, *Preconfinement as a property of perturbative QCD*, Physics Letters B **83** (1979) 87 – 92, http://www.sciencedirect.com/science/article/pii/0370269379908967.

[67] J. Bellm et al., *Herwig 7.0/Herwig++ 3.0 release note*, Eur. Phys. J. C **76** (2016) 196, arXiv:1512.01178 [hep-ph].

[68] E. Bothmann, G. S. Chahal, S. Höche, J. Krause, F. Krauss, S. Kuttimalai, S. Liebschner, D. Napoletano, M. Schönherr, H. Schulz, S. Schumann, and F. Siegert, *Event Generation with Sherpa 2.2*, SciPost Phys. **7** (2019) 34, https://scipost.org/10.21468/SciPostPhys.7.3.034.

[69] B. Andersson and G. Gustafson and G. Ingelman and T. Sjöstrand, *Parton fragmentation and string dynamics*, Physics Reports **97** (1983) 31 – 145, http://www.sciencedirect.com/science/article/pii/0370157383900807.

[70] T. Sjöstrand, S. Ask, J. R. Christiansen, R. Corke, N. Desai, P. Ilten, S. Mrenna, S. Prestel, C. O. Rasmussen, and P. Z. Skands, *An Introduction to PYTHIA 8.2*, Comput. Phys. Commun. **191** (2015) 159, arXiv:1410.3012 [hep-ph].

[71] S. Alioli, P. Nason, C. Oleari, and E. Re, *A general framework for implementing NLO calculations in shower Monte Carlo programs: the POWHEG BOX*, JHEP **06** (2010) 043, arXiv:1002.2581 [hep-ph].

[72] J. Alwall, R. Frederix, S. Frixione, V. Hirschi, F. Maltoni, et al., *The automated computation of tree-level and next-to-leading order differential cross sections, and their matching to parton shower simulations*, JHEP **07** (2014) 079, arXiv:1405.0301 [hep-ph].

[73] D. J. Lange, *The EvtGen particle decay simulation package*, Nucl. Instrum. Meth. A **462** (2001) 152.

[74] GEANT4 Collaboration, S. Agostinelli et al., *GEANT4: A Simulation toolkit*, Nucl. Instrum. Meth. A **506** (2003) 250.

[75] The ATLAS Collaboration, *The ATLAS Simulation Infrastructure*, The European Physical Journal C **70** (2010) 823–874, https://doi.org/10.1140/epjc/s10052-010-1429-9.

[76] R. Reece and K. Cranmer, *The big-picture of the flow of ATLAS data*, https://reece.scipp.ucsc.edu/, 2017. Accessed 15th December 2019.

[77] ATLAS Collaboration, T. Cornelissen, M. Elsing, S. Fleischmann, W. Liebig, E. Moyse, and A. Salzburger, *Concepts, Design and Implementation of the ATLAS New Tracking (NEWT)*, Tech. Rep. ATL-SOFT-PUB-2007-007. ATL-COM-SOFT-2007-002, Geneva, Mar, 2007. https://cds.cern.ch/record/1020106.

[78] B. Isildak, *Measurement of the differential dijet production cross section in proton-proton collisions at* $\sqrt{s} = 7$ *TeV*. PhD thesis, Bogazici U., 2011. arXiv:1308.6064 [hep-ex].

[79] M. Cacciari, G. P. Salam, and G. Soyez, *The anti-k_t jet clustering algorithm*, JHEP **04** (2008) 063, arXiv:0802.1189 [hep-ph].

[80] M. Cacciari, G. P. Salam, and G. Soyez, *FastJet User Manual*, Eur. Phys. J. C **72** (2012) 1896, arXiv:1111.6097 [hep-ph].

[81] M. Cacciari and G. P. Salam, *Pileup subtraction using jet areas*, Phys. Lett. **B659** (2008) 119–126, arXiv:0707.1378 [hep-ph].

[82] ATLAS Collaboration, *Tagging and suppression of pileup jets with the ATLAS detector*, ATLAS-CONF-2014-018, 2014, https://cds.cern.ch/record/1700870.

[83] ATLAS Collaboration, *Jet energy scale measurements and their systematic uncertainties in proton–proton collisions at* $\sqrt{s} = 13$ *TeV with the ATLAS detector*, Phys. Rev. D **96** (2017) 072002, arXiv:1703.09665 [hep-ex].

[84] ATLAS Collaboration, P. O. Hansson Adrian, *The ATLAS b-Jet Trigger*, Tech. Rep. arXiv:1111.4190, CERN, Geneva, Nov, 2011. https://cds.cern.ch/record/1397942. Comments: 4 pages, 6 figures, conference proceedings for PIC2011.

[85] ATLAS Collaboration, *Optimisation of the ATLAS b-tagging performance for the 2016 LHC Run*, ATL-PHYS-PUB-2016-012, 2016, https://cds.cern.ch/record/2160731.

[86] ATLAS Collaboration, *Performance of b-jet identification in the ATLAS experiment*, Journal of Instrumentation **11** (2016) P04008–P04008, https://doi.org/10.1088%2F1748-0221%2F11%2F04%2Fp04008.

[87] W. Lampl et al., *Calorimeter Clustering Algorithms: Description and Performance*, http://inspirehep.net/record/807147.

[88] ATLAS Collaboration, *Performance of missing transverse momentum reconstruction with the ATLAS detector in the first proton–proton collisions at* $\sqrt{s} = 13$ *TeV*, ATL-PHYS-PUB-2015-027, 2015, https://cds.cern.ch/record/2037904.

[89] ATLAS Collaboration, *Characterisation and mitigation of beam-induced backgrounds observed in the ATLAS detector during the 2011 proton–proton run*, JINST **8** (2013) P07004, arXiv:1303.0223 [hep-ex].

[90] ATLAS Collaboration, *Muon reconstruction performance of the ATLAS detector in proton–proton collision data at* $\sqrt{s} = 13$ *TeV*, Eur. Phys. J. C **76** (2016) 292, arXiv:1603.05598 [hep-ex].

[91] ATLAS Collaboration, *Electron reconstruction and identification in the ATLAS experiment using the 2015 and 2016 LHC proton–proton collision data at* $\sqrt{s}$ = 13 *TeV*, submitted to Eur. Phys. J. (2019), arXiv:1902.04655 [hep-ex].

[92] ATLAS Collaboration, *Jet energy scale measurements and their systematic uncertainties in proton-proton collisions at* $\sqrt{s} = 13$ *TeV with the ATLAS detector*, Phys. Rev. **D96** (2017) 072002, arXiv:1703.09665 [hep-ex].

[93] ATLAS Collaboration, *Jet energy resolution in 2017 data and simulation*, https://atlas.web.cern.ch/Atlas/GROUPS/PHYSICS/PLOTS/JETM-2018-005/.

[94] A. L. Read, *Presentation of search results: the* CL_S *technique*, J. Phys. G **28** (2002) 2693.

[95] G. Cowan, K. Cranmer, E. Gross, and O. Vitells, *Asymptotic formulae for likelihood-based tests of new physics*, Eur. Phys. J. C **71** (2011) 1554, arXiv:1007.1727 [physics.data-an].

[96] M. Baak, G. J. Besjes, D. Côte, A. Koutsman, J. Lorenz, and D. Short, *HistFitter software framework for statistical data analysis*, Eur. Phys. J. **C75** (2015) 153, arXiv:1410.1280 [hep-ex].

[97] ATLAS Collaboration, *Search for squarks and gluinos in final states with jets and missing transverse momentum using 139* fb^{-1} *of* $\sqrt{s}$ *=13 TeV* pp *collision data with the ATLAS detector*, Tech. Rep. ATLAS-CONF-2019-040, CERN, Geneva, Aug, 2019. http://cds.cern.ch/record/2686254.

[98] ATLAS Collaboration, *Search for squarks and gluinos in final states with jets and missing transverse momentum using* $36 fb^{-1}$ *of* $\sqrt{s} = 13$ *TeV* pp *collision data with the ATLAS detector*, Phys. Rev. D **97** (2018) 112001, arXiv:1712.02332 [hep-ex].

[99] A. Hoecker et al., *TMVA - Toolkit for Multivariate Data Analysis*, 2007, arXiv:physics/0703039 [physics.data-an].

[100] T. Gleisberg, S. Höche, F. Krauss, M. Schönherr, S. Schumann, et al., *Event generation with SHERPA 1.1*, JHEP **02** (2009) 007, arXiv:0811.4622 [hep-ph].

[101] R. Gavin, Y. Li, F. Petriello and S. Quackenbush, *FEWZ 2.0: A code for hadronic Z production at next-to-next-to-leading order*, Comput. Phys. Commun. **182** (2011) 2388–2403, arXiv:1011.3540 [hep-ph].

[102] NNPDF Collaboration, R. D. Ball et al., *Parton distributions for the LHC Run II*, JHEP **04** (2015) 040, arXiv:1410.8849 [hep-ph].

[103] S. Höche, F. Krauss, S. Schumann, and F. Siegert, *QCD matrix elements and truncated showers*, JHEP **05** (2009) 053, arXiv:0903.1219 [hep-ph].

[104] M. Czakon, P. Fiedler, and A. Mitov, *Total Top-Quark Pair-Production Cross Section at Hadron Colliders Through* $O(\alpha_S^4)$, Phys. Rev. Lett. **110** (2013) 252004, arXiv:1303.6254 [hep-ph].

[105] M. Czakon and A. Mitov, *Top++: A Program for the Calculation of the Top-Pair Cross-Section at Hadron Colliders*, Comput. Phys. Commun. **185** (2014) 2930, arXiv:1112.5675 [hep-ph].

[106] R. D. Ball et al., *Parton distributions with LHC data*, Nucl. Phys. B **867** (2013) 244, arXiv:1207.1303 [hep-ph].

[107] ATLAS Collaboration, *ATLAS Pythia 8 tunes to* 7 *TeV data*, ATL-PHYS-PUB-2014-021, 2014, https://cds.cern.ch/record/1966419.

[108] N. Kidonakis, *Two-loop soft anomalous dimensions for single top quark associated production with a W- or H-*, Phys. Rev. D **82** (2010) 054018, arXiv:1005.4451 [hep-ph].

[109] N. Kidonakis, *Next-to-next-to-leading-order collinear and soft gluon corrections for t-channel single top quark production*, Phys. Rev. D **83** (2011) 091503, arXiv:1103.2792 [hep-ph].

[110] M. Aliev et al., *HATHOR: HAdronic Top and Heavy quarks crOss section calculatoR*, Comput. Phys. Commun. **182** (2011) 1034–1046, arXiv:1007.1327 [hep-ph].

[111] P. Kant et al., *HatHor for single top-quark production: Updated predictions and uncertainty estimates for single top-quark production in hadronic collisions*, Comput. Phys. Commun. **191** (2015) 74–89, arXiv:1406.4403 [hep-ph].

[112] A. Lazopoulos, T. McElmurry, K. Melnikov and F. Petriello, *Next-to-leading order QCD corrections to* $t\bar{t}Z$ *production at the LHC*, Phys. Lett. B **666** (2008) 62–65, arXiv:0804.2220 [hep-ph].

[113] J. M. Campbell and R. K. Ellis, $t\bar{t}W^{\pm}$ *production and decay at NLO*, JHEP **07** (2012) 052, arXiv:1204.5678 [hep-ph].

[114] T. Sjostrand, S. Mrenna, and P. Z. Skands, *A Brief Introduction to PYTHIA 8.1*, Comput. Phys. Commun. **178** (2008) 852–867, arXiv:0710.3820 [hep-ph].

[115] W. Beenakker, C. Borschensky, M. Krämer, A. Kulesza, and E. Laenen, *NNLL-fast: predictions for coloured supersymmetric particle production at the LHC with threshold and Coulomb resummation*, JHEP **12** (2016) 133, arXiv:1607.07741 [hep-ph].

[116] W. Beenakker, C. Borschensky, M. Krämer, A. Kulesza, E. Laenen, V. Theeuwes, and S. Thewes, *NNLL resummation for squark and gluino production at the LHC*, JHEP **12** (2014) 023, arXiv:1404.3134 [hep-ph].

[117] W. Beenakker, T. Janssen, S. Lepoeter, M. Krämer, A. Kulesza, E. Laenen, I. Niessen, S. Thewes, and T. Van Daal, *Towards NNLL resummation: hard matching coefficients for squark and gluino hadroproduction*, JHEP **10** (2013) 120, arXiv:1304.6354 [hep-ph].

[118] W. Beenakker, S. Brensing, M. Krämer, A. Kulesza, E. Laenen, and I. Niessen, *NNLL resummation for squark-antisquark pair production at the LHC*, JHEP **01** (2012) 076, arXiv:1110.2446 [hep-ph].

[119] W. Beenakker et al., *Soft-gluon resummation for squark and gluino hadroproduction*, JHEP **12** (2009) 041, arXiv:0909.4418 [hep-ph].

[120] A. Kulesza and L. Motyka, *Soft gluon resummation for the production of gluino-gluino and squark-antisquark pairs at the LHC*, Phys. Rev. D **80** (2009) 095004, arXiv:0905.4749 [hep-ph].

[121] A. Kulesza and L. Motyka, *Threshold resummation for squark-antisquark and gluino-pair production at the LHC*, Phys. Rev. Lett. **102** (2009) 111802, arXiv:0807.2405 [hep-ph].

[122] W. Beenakker et al., *Squark and gluino production at hadron colliders*, Nucl. Phys. B **492** (1997) 51–103, arXiv:hep-ph/9610490.

[123] A. Djouadi, M. Muhlleitner, and M. Spira, *Decays of supersymmetric particles: The Program SUSY-HIT (SUspect-SdecaY-Hdecay-InTerface)*, Acta Phys. Polon. **B 38** (2007) 635–644, arXiv:hep-ph/0609292 [hep-ph].

[124] ATLAS Collaboration, *Measurement of the photon identification efficiencies with the ATLAS detector using LHC Run-1 data*, Eur. Phys. J. C **76** (2016) 666, arXiv:1606.01813 [hep-ex].

[125] C. Chen, *New approach to identifying boosted hadronically decaying particles using jet substructure in its center-of-mass frame*, Phys. Rev. D **85** (2012) 034007, https://link.aps.org/doi/10.1103/PhysRevD.85.034007.

[126] ATLAS Collaboration, S. Owen, *Data-driven estimation of the QCD multijet background to SUSY searches with jets and missing transverse momentum at ATLAS using jet smearing*, 2011. ATL-COM-PHYS-2011-1066.

[127] ATLAS Collaboration, *Object-based missing transverse momentum significance in the ATLAS Detector*, ATLAS-CONF-2018-038, 2018, https://cds.cern.ch/record/2630948.

[128] C. Macdonald, *Private study on $\Delta\Phi$ corrections in the context of the JetSmearing method*, 2019.

[129] R. D. Cousins, J. T. Linnemann, and J. Tucker, *Evaluation of three methods for calculating statistical significance when incorporating a systematic uncertainty into a test of the background-only hypothesis for a Poisson process*, Nucl. Instrum. Meth. A **595** (2008) 480–501, arXiv:physics/0702156 [physics.data-an].

[130] ATLAS Collaboration, *SUSY October 2019 Summary Plot Update*, Tech. Rep. ATL-PHYS-PUB-2019-044, CERN, Geneva, Oct, 2019. http://cds.cern.ch/record/2697155.

[131] ATLAS Collaboration, *Reinterpretation of searches for supersymmetry in models with variable R-parity-violating coupling strength and long-lived R-hadrons*, ATLAS-CONF-2018-003, 2018, https://cds.cern.ch/record/2308391.

[132] ATLAS Collaboration, *Transverse momentum response and reconstruction efficiency for jets from displaced decays in the ATLAS detector*, tech. rep., CERN.

[133] W. Porod, *SPheno, a program for calculating supersymmetric spectra, SUSY particle decays and SUSY particle production at e+ e- colliders*, Comput. Phys. Commun. **153** (2003) 275–315, arXiv:hep-ph/0301101 [hep-ph].

[134] W. Porod and F. Staub, *SPheno 3.1: Extensions including flavour, CP-phases and models beyond the MSSM*, Comput. Phys. Commun. **183** (2012) 2458–2469, arXiv:1104.1573 [hep-ph].

[135] F. Staub, *SARAH 4 : A tool for (not only SUSY) model builders*, Comput. Phys. Commun. **185** (2014) 1773–1790, arXiv:1309.7223 [hep-ph].

[136] ATLAS Collaboration, *Further ATLAS tunes of* Pythia *6 and Pythia 8*, ATL-PHYS-PUB-2011-014, 2011, https://cds.cern.ch/record/1400677.

[137] A. Sherstnev and R. S. Thorne, *Parton Distributions for LO Generators*, Eur. Phys. J. C **55** (2008) 553, arXiv:0711.2473 [hep-ph].

[138] W. Beenakker et al., *Squark and gluino hadroproduction*, Int. J. Mod. Phys. A **26** (2011) 2637–2664, arXiv:1105.1110 [hep-ph].

[139] C. Borschensky, M. Kramer, A. Kulesza, M. Mangano, S. Padhi, T. Plehn, and X. Portell, *Squark and gluino production cross sections in pp collisions at $\sqrt{s}$ = 13, 14, 33 and 100 TeV*, Eur. Phys. J. C **74** (2014) 3174, arXiv:1407.5066 [hep-ph].

[140] T. Plehn, *Single stop production at hadron colliders*, Phys. Lett. B **488** (2000) 359–366, arXiv:hep-ph/0006182 [hep-ph].

[141] A. Monteux, *New signatures and limits on R-parity violation from resonant squark production*, JHEP **03** (2016) 216, arXiv:1601.03737 [hep-ph].

[142] J. L. Goity and M. Sher, *Bounds on $\Delta B = 1$ couplings in the supersymmetric standard model*, Phys. Lett. B **346** (1995) 69–74, arXiv:hep-ph/9412208 [hep-ph].

[143] B. C. Allanach, A. Dedes, and H. K. Dreiner, *Two loop supersymmetric renormalization group equations including R-parity violation and aspects of unification*, Phys. Rev. D **60** (1999) 056002, arXiv:hep-ph/9902251 [hep-ph].

[144] R. Mackeprang and A. Rizzi, *Interactions of Coloured Heavy Stable Particles in Matter*, Eur. Phys. J. C **50** (2007) 353–362, arXiv:hep-ph/0612161.

[145] R. Mackeprang and D. Milstead, *An Updated Description of Heavy-Hadron Interactions in GEANT-4*, Eur. Phys. J. C **66** (2010) 493–501, arXiv:0908.1868 [hep-ph].

[146] A. C. Kraan, *Interactions of heavy stable hadronizing particles*, Eur. Phys. J. C **37** (2004) 91–104, arXiv:hep-ex/0404001.

[147] J. Pumplin et al., *New generation of parton distributions with uncertainties from global QCD analysis*, JHEP **07** (2002) 012, arXiv:hep-ph/0201195.

[148] G. R. Farrar and P. Fayet, *Phenomenology of the Production, Decay, and Detection of New Hadronic States Associated with Supersymmetry*, Phys. Lett. B **76** (1978) 575.

[149] M. Fairbairn, A. C. Kraan, D. A. Milstead, T. Sjostrand, P. Z. Skands, and T. Sloan, *Stable massive particles at colliders*, Phys. Rept. **438** (2007) 1–63, arXiv:hep-ph/0611040 [hep-ph].

[150] ATLAS Collaboration, *Search for new phenomena with large jet multiplicities and missing transverse momentum using large-radius jets and flavour-tagging at ATLAS in 13 TeV pp collisions*, JHEP **12** (2017) 034, arXiv:1708.02794 [hep-ex].

[151] ATLAS Collaboration, *Search for supersymmetry in final states with missing transverse momentum and multiple b-jets in proton–proton collisions at $\sqrt{s} = 13$ TeV with the ATLAS detector*, JHEP **06** (2018) 107, arXiv:1711.01901 [hep-ex].

[152] ATLAS Collaboration, *Search for new phenomena in a lepton plus high jet multiplicity final state with the ATLAS experiment using $\sqrt{s} = 13$ TeV proton–proton collision data*, JHEP **09** (2017) 088, arXiv:1704.08493 [hep-ex].

[153] ATLAS Collaboration, *Search for a scalar partner of the top quark in the jets plus missing transverse momentum final state at $\sqrt{s} = 13$ TeV with the ATLAS detector*, JHEP **12** (2017) 085, arXiv:1709.04183 [hep-ex].

[154] ATLAS Collaboration, *Search for top-squark pair production in final states with one lepton, jets, and missing transverse momentum using $36\,fb^{-1}$ of $\sqrt{s} = 13$ TeV pp collision data with the ATLAS detector*, JHEP **06** (2018) 108, arXiv:1711.11520 [hep-ex].

[155] ATLAS Collaboration, *Search for supersymmetry in final states with two same-sign or three leptons and jets using $36\,fb^{-1}$ of $\sqrt{s} = 13$ TeV pp collision data with the ATLAS detector*, JHEP **09** (2017) 084, arXiv:1706.03731 [hep-ex].

[156] ATLAS Collaboration, *A search for pair-produced resonances in four-jet final states at $\sqrt{s} = 13$ TeV with the ATLAS detector*, Eur. Phys. J. C **78** (2018) 250, arXiv:1710.07171 [hep-ex].

[157] ATLAS Collaboration, *Search for new phenomena in dijet events using $37\,fb^{-1}$ of pp collision data collected at $\sqrt{s} = 13$ TeV with the ATLAS detector*, Phys. Rev. D **96** (2017) 052004, arXiv:1703.09127 [hep-ex].

[158] ATLAS Collaboration, *Search for light dijet resonances with the ATLAS detector using a Trigger-object Level Analysis in LHC pp collisions at $\sqrt{s} = 13$ TeV*, ATLAS-CONF-2016-030, 2016, https://cds.cern.ch/record/2161135.

[159] ATLAS Collaboration, *Search for new phenomena in the dijet mass distribution using pp collision data at $\sqrt{s} = 8$ TeV with the ATLAS detector*, Phys. Rev. D **91** (2015) 052007, arXiv:1407.1376 [hep-ex].

[160] ATLAS Collaboration, *Search for long-lived, massive particles in events with displaced vertices and missing transverse momentum in $\sqrt{s}$ = 13 TeV pp collisions with the ATLAS detector*, arXiv:1710.04901 [hep-ex].

[161] Z. Rurikova, *Private study on non-collision background and jet timing in the context of the 0L (2-6jets) SUSY analysis, reinterpreted in a metastable gluino scenario*, 2018.

[162] ATLAS Collaboration, *Topological cell clustering in the ATLAS calorimeters and its performance in LHC Run 1*, Eur. Phys. J. C **77** (2017) 490, arXiv:1603.02934 [hep-ex].

[163] N. Zwane, *Long-Lived Particle Searches in R-Parity Violating MSSM*, J. Phys. G **44** (2017) 105003, arXiv:1505.03479 [hep-ph].

[164] Super-Kamiokande Collaboration Collaboration, M. Litos et al., *Search for Dinucleon Decay into Kaons in Super-Kamiokande*, Phys. Rev. Lett. **112** (2014) 131803.

[165] ATLAS Collaboration, *Search for R-parity-violating supersymmetric particles in multi-jet final states produced in pp collisions at $\sqrt{s} = 13$ TeV using the ATLAS detector at the LHC*, Phys. Lett. B **785** (2018) 136, arXiv:1804.03568 [hep-ex].

[166] ATLAS Collaboration, *Search for massive supersymmetric particles decaying to many jets using the ATLAS detector in pp collisions at $\sqrt{s} = 8$ TeV*, Phys. Rev. D **91** (2015) 112016, arXiv:1502.05686 [hep-ex].

[167] ATLAS Collaboration, *Search for metastable heavy charged particles with large ionization energy loss in pp collisions at $\sqrt{s} = 13$ TeV using the ATLAS experiment*, Phys. Rev. D **93** (2016) 112015, arXiv:1604.04520 [hep-ex].

[168] ATLAS Collaboration, *Search for heavy long-lived charged R-hadrons with the ATLAS detector in $3.2\,fb^{-1}$ of proton–proton collision data at $\sqrt{s} = 13$ TeV*, Phys. Lett. B **760** (2016) 647, arXiv:1606.05129 [hep-ex].

[169] ATLAS Collaboration, *Search for long-lived stopped R-hadrons decaying out of time with pp collisions using the ATLAS detector*, Phys. Rev. D **88** (2013) 112003, arXiv:1310.6584 [hep-ex].

List of Figures

List of Tables

List of Publications

The author of this document is a member of the ATLAS collaboration, thus the work presented in this thesis is typically based on contributions from many different groups. Material labelled with "***ATLAS***", "***ATLAS*** *Preliminary*" or "***ATLAS*** *Simulation Preliminary*" was approved by the collaboration and published as paper, conference note or public note. Unlabelled figures and plots are privately produced by the author if not indicated otherwise in the respective figure caption.
Contributions of the author to the analyses presented in this thesis are detailed in the text. A summary of these publications is given here:

- *Search for squarks and gluinos in final states with jets and missing transverse momentum using 36 fb^{-1} of $\sqrt{s} = 13$ TeV pp collision data with the ATLAS detector* [98]:
  - Studies and optimisation of *boosted signal regions*, i.e. event selections targeting signal processes including boosted W bosons in the final state, based on jet reclustering techniques.
  - Request of MC production of signal samples and production of HEPData material.

- *Reinterpretation of searches for supersymmetry in models with variable R-parity-violating coupling strength and long-lived R-hadrons* [131]:
  - Reinterpretation of the 0L (2-6jets) SUSY analysis, listed above, in the context of the two long-lived models.
  - Studies on supplementary uncertainties on the jet energy scale and jet energy resolution, arising from the displacement of jets in long-lived scenarios.
  - Presenting the analysis in the ATLAS approval process.

- *Transverse momentum response and reconstruction efficiency for jets from displaced decays in the ATLAS detector* [132]:
  - The note summarises the studies on the jet response and reconstruction efficiency performed by the author in the context of the reinterpretation listed above.
  - Being the sole contributor to the note, the author of this thesis was responsible for writing and editing the text as well as the entire approval process.

- *Search for squarks and gluinos in final states with jets and missing transverse momentum using 139 fb^{-1} of $\sqrt{s}$ =13 TeV pp collision data with the ATLAS detector* [97]:
  - Production of preselected input samples for the analysis.
  - Studies on and implementation of the JetSmearing method, employed to obtain the multijet background estimation.

– Development of a software package for creating distribution plots incorporating background, signal and data samples of all three MC campaigns and data-taking periods, respectively, as well as all statistical and systematic uncertainties.

In addition to these publications, the author contributed to the collaboration as part of the *ATLAS Jet and E_T^{miss} Combined Performance Group*, providing the MC based computation of the jet mass scale calibration of small radius anti-k_t jets (built from EM topological clusters and from the particle flow) used as input for jet reclustering in searches for boosted signatures.

Acknowledgement

First of all, I would like to thank *Prof. Dr. Gregor Herten* and *Prof. Dr. Ulrich Landgraf* for all their support and for the opportunity to do my PhD in Freiburg as part of the Graduiertenkolleg as well as *Chris Skorek* for all her help in organising administrative matters.
Thank you to the entire group: *Fabio*, *Tomas* and *Manfredi* for helping me a lot in my very first month, *Andrea* for guiding me through the qualification, *Martina* for sharing the office and your experience, *Andrea* for all your advice and for proofreading this thesis, *Patrick*, *Jürgen*, *Bernhard*, ...all of you, who made these past years so enjoyable!
A big thank you to *Zuzana* for all the work we did together, for being a great analysis contact, for all your support and advice not only regarding physics, for your help and not least for all your time and patience improving and correcting this thesis.
Furthermore I would like to thank the ZeroLepton anlysis team - *Yu*, *Kenta*, *Christina*, *Nikola*, *Marija*, *Paul* and many more - for the great collaboration and for making this work possible.
Thank you also to *Thor*, for all your help in particular in understanding the German bureaucracy but also with the thesis and much more.
Thanks to *Simone* and *Manuel* for sharing the office in Freiburg and Geneva and for hugging the koalas together.
Peter, grazie mille for everything: your help and support, your jokes, your company on many travels and for joining my "excesses" whenever it was needed ...also my apologies for not letting you get enough sleep.
Thank you so much, *Giulia* and *Simona* for our shared lunches (the sunny and the sad ones), for our travels together, for sharing the most stressful times and for the girl power that kept me going.
My dear *Savonas*, there are not enough words to express all my gratitude, so I just say thank you, danke, grazie, 고마워 to all of you - *Sunga*, *Riccardo*, *Maria*, *Vlad*, *Stefano*, *Vale*, *Costanza*, *Giacomo*, *Eduardo*, *Tazio*, *Lisa*, *Danny*, ... - for being friends and always making me feel welcome.
Mama und *Papa*, tausend Dank für alles, eure Unterstützung egal wobei und dafür, dass ihr immer für mich da seid. Vielen Dank liebe *Kinderkiste* - *Andi*, *Uli*, *Resl*, *Sasha* - für Kost und Logis und überhaupt für alles.
Und natürlich danke *Michi*, dass du dich auf dieses Abenteuer eingelassen hast, dass du dich immer um mich kümmerst und für jeden Unfug zu haben bist. Danke, dass du vernüftig bist und ich es deswegen nicht sein muss und danke für die vielen Jahre zu zweit und bald zu dritt.